Designing Sorbent-Containing Electrospun Fibers For Dilute Chemical Separations

by

Mitchell Armstrong

A Dissertation Presented in Partial Fulfillment
of the Requirements for the Degree
Doctor of Philosophy

Approved March 2018 by the
Graduate Supervisor Committee:

Bin Mu, Chair
Matthew Green
Julianne Holloway
Klaus Lackner
Don Seo

ARIZONA STATE UNIVERSITY

May 2018

ABSTRACT

An urgent need for developing new chemical separations that address the capture of dilute impurities from fluid streams are needed. These separations include the capture of carbon dioxide from the atmosphere, impurities from drinking water, and toxins from blood streams. A challenge is presented when capturing these impurities because the energy cost for processing the bulk fluid stream to capture trace contaminants is too great using traditional thermal separations. The development of sorbents that may capture these contaminants passively has been emphasized in academic research for some time, producing many designer materials including metal-organic frameworks (MOFs) and polymeric resins. Scaffolds must be developed to effectively anchor these materials in a passing fluid stream. In this work, two design techniques are presented for anchoring these sorbents in electrospun fiber scaffolds.

The first technique involves imbedding sorbent particles inside the fibers: forming particle-embedded fibers. It is demonstrated that particles will spontaneously coat themselves in the fibers at dilute loadings, but at higher loadings some get trapped on the fiber surface. A mathematical model is used to show that when these particles are embedded, the polymeric coating provided by the fibers may be designed to increase the kinetic selectivity and/or stability of the embedded sorbents. Two proof-of-concept studies are performed to validate this model including the increased selectivity of carbon dioxide over nitrogen when the MOF ZIF-8 is embedded in a poly(ethylene oxide) and Matrimid polymer blend; and that increased hydrothermal stability is realized when the water-sensitive MOF HKUST-1 is embedded in polystyrene fibers relative to pure HKUST-1 powder.

The second technique involves the creation of a pore network throughout the fiber to increase accessibility of embedded sorbent particles. It is demonstrated that the removal of a blended highly soluble polymer additive from the spun particle-containing fibers leaves a pore network behind without removing the embedded sorbent. The increased accessibility of embedded sorbents is validated by embedding a known direct air capture sorbent in porous

electrospun fibers, and demonstrating that they have the fastest kinetic uptake of any direct air capture sorbent reported in literature to date, along with over 90% sorbent accessibility.

ACKNOWLEDGMENTS

First I'd like to acknowledge support from Erin, my mom, my dad, and the rest of my family who have been encouraging and supportive over the last four years.

I'd also like to acknowledge support from my PhD advisor, Dr. Bin Mu, and the rest of my PhD committee who have each contributed ideas, resources, and questions that have aided in the progress of this work.

Support from the faculty and staff of the School of Engineering for Matter Transport and Energy including Fred Pena, Dr. Lenore Dai, Susan Terkelson, Christine Quintero, Gayla Ruark has been highly appreciated, along the professors that have provided financial support through teaching assistant positions- Dr. Dave Nielsen, Dr. Veronica Burrows, and Dr. Brent Nannenga.

The facilities provided by the LeRoy Eyring Center for Solid State Science made the characterization possible, and training from Karl Wiess, Emmanual Hoigard, and Dewight Williams is greatly appreciated.

I'd also like to thank the other lab members, both past and present, of the Nanoporous Materials Research lab including Bohan Shan, Christopher Balzer, and Korinthia Yuriar-Arredondo.

Those working for research facilities provided by the Ira A. Fulton School of Engineering have also enabled this research including Myrna Martinez and those at Engineering Technical Services group including Chris, Darien, Matt, and Dale.

Finally, I'd like to acknowledge those who had helped me decide to pursue graduate school including Dr. John Corbett and Dr. John Barrett.

TABLE OF CONTENTS

Page

CHAPTER Page

CHAPTER Page

CHAPTER Page

LIST OF TABLES

Table Page

LIST OF FIGURES

Figure Page

Figure Page

Figure Page

Figure Page

Figure Page

Figure Page

Figure Page

Figure Page

Figure Page

CHAPTER 1.

GENERAL INTRODUCTION

1.1 Chemical Separations

Improving the efficiency of chemical separations has a tremendous potential to improve the quality of life for all of humanity. The National Academy of Engineering has published a list of the 14 Grand Challenges of the 21st Century, and three of these challenges are dependent on chemical separations: provide access to clean water, develop carbon sequestration techniques, and managing the nitrogen cycle. Other challenges also incorporate secondary needs for chemical separations including development of personalized medicine -in which advances in dialysis needed. In 2016, a complementary list of, “Seven Chemical Separations that Could Change the World,” was published, which lists: hydrocarbons from crude oil, uranium from seawater, alkenes from alkanes, greenhouse gases from dilute emissions, rare-earth metals from ores, benzene derivatives from each other, and trace contaminates from water.(Sholl & Lively, 2016) Each chemical separation is different, and each present their own set of challenges, however, a common theme throughout most of these current challenges is the fact that a highly dilute substance must be efficiently separated from a bulk fluid stream.

Sherwood’s rule states that the cost of a chemical separation scales linearly with the concentration of desirable species in the bulk phase.(Sherwood, 1959) This means that separating a more dilute species requires more energy per quantity than a more concentrated species. Many of these new separations are challenging because the species to be captured is very dilute. For example, removing greenhouse gases from dilute streams typically means atmospheric CO_2, which is currently around 400 ppm. Rare earth elements in ore are also at ppm levels, uranium concentration in seawater and dilute species in water are both at ppb levels. Sherwood’s Rule, however, only applies to the processing of the bulk phase. Therefore, strategies to overcome this obstacle must be aimed at reducing the energy expended on processing the bulk phase.

To address this issue, the development of more energy efficient separation technologies is needed.(Sholl & Lively, 2016) Of the many currently understood separation processes, membrane separations and sorption separations are among the most highly studied for these separation challenges because they are able to minimize the energy usage, and may be implemented on both large and small scales (Figure 1.1.1).(Department of Energy, 2005)

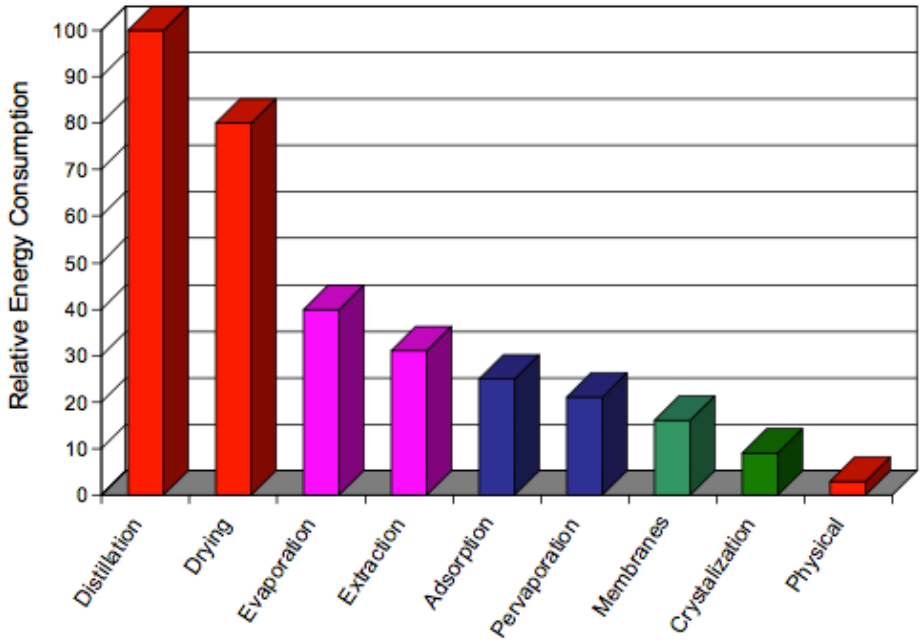

Figure 1.1.1. Relative Energy Consumption for various separation technologies as predicted by the Department of Energy, adapted from a Department of Energy report from 2003.(Department of Energy, 2005)

Membrane separations function via pressurizing the bulk fluid to drive it past a surface that allows one species through while rejecting others. Sorption uses materials with active sites that passively collect targeted chemical species, deferring energetically intense reactivation until after the targeted chemical is concentrated on the active sites of the material. Currently, each of these separation technologies are primarily driven by new material design.(Department of Energy, 2005)

1.2 Research Strategy

In this work, we primarily focus on new sorbent materials. A passive collection scheme minimizes the energy consumption of processing the bulk solution, making the design of these systems flexible and viable for many of these separation challenges with the design of a sorbent with carefully designed active sites. Developing new tools for incorporating microscopic sorbents into composite macroscale materials is the focus of this work. By determining predictive models and synthesis-property relationships among these new composites along with providing proof-of-concept work is expected to increase the portfolio of materials and strategies for designing materials for these chemical separations that have potential for improving quality of life on this planet.

Structuring of MOFs –and other sorbents- on the macroscale is important for real-world applications, and this is often done by incorporating them into composite materials.(Furukawa, Reboul, Diring, Sumida, & Kitagawa, 2014) Composite structures composed of adsorbents (principally MOFs) and electrospun fibers are studied in this work. MOFs and electrospun fibers are each highly studied for a variety of applications due to their tunability. They have strong overlap in chemically selective applications including sensing, drug delivery, separations, and catalysis (Figure 1.2.1).

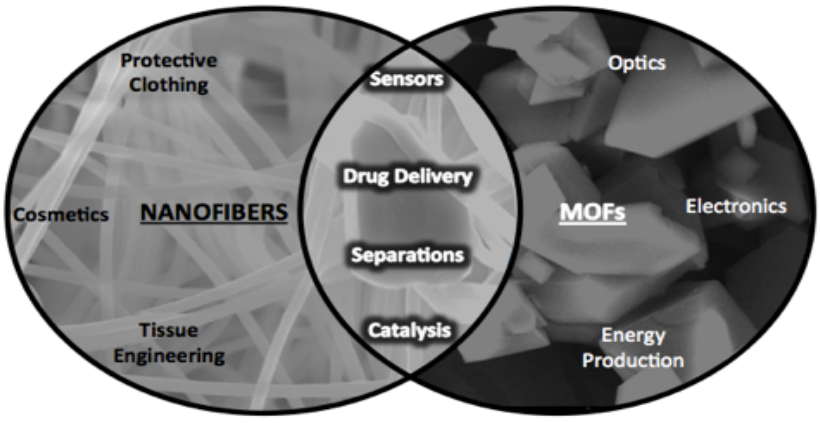

Figure 1.2.1. Venn diagram of some applications for both MOFs and electrospun nanofibers along with an overlap with adsorption based applications.

MOFs add value to chemical separations due to the ability to tailor functional groups, pore sizes, and surface areas for specific separations. Drawbacks of MOFs –and most adsorbents- are the need to shape them into a macroscopic material before use, and fouling. Nanofibers are complimentary to these needs. They typically lack the high functionality provided by adsorbent particles, however, they provide a macroscopic platform that is readily implemented into separation elements. They are studied individually for separation applications due to their high surface area and processability on the macroscale.(Bhardwaj & Kundu, 2010)

Three ideal particle-fiber morphologies are considered: Particle embedded fibers, particle-containing porous fiber, and particle-covered fibers. These three structures are displayed in Figure 1.2.2.

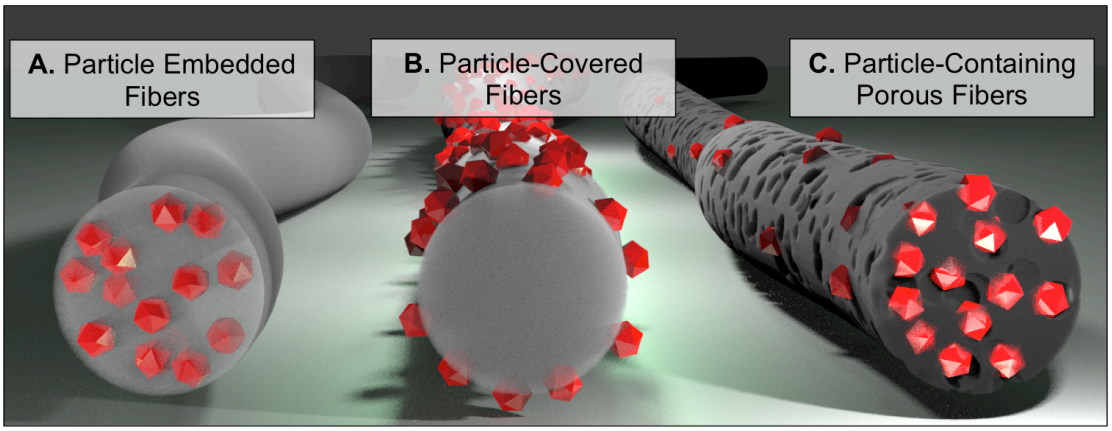

Figure 1.2.2. An illustration of three different ideal fiber morphologies considered for this work. These include (A) Particle embedded fibers, (B) particle-covered fibers, and (C) particle-containing porous fibers.

It is expected that one of these three particle-fiber morphologies will be the ideal case depending on the objective separation and embedded sorbent. When using particle embedded fibers, the fluid must pass through the polymer layer before reaching the adsorbent, which then may allow the polymer to be designed to add either additional protection or separation properties before reaching the adsorbent. Particle-containing porous fibers allow for simultaneously maximizing the adsorbent: polymer ratio and adsorbent exposure to a fluid stream. Particle-coated fibers sacrifice loading potential, and possibly adhesion, but avoid the need for fiber

penetration. This may prove useful for applications where particles embedded inside the fiber may have diminished properties such as fluorescent sensing.

With a near limitless list of MOFs, polymers, and design tools available, a rational design process for selecting and targeting MOF-embedded electrospun fiber composite design is needed. To effectively construct a framework for the rational design of these composite materials, a three-pronged approach is undertaken. (1) Tools for the fabrication of these three ideal structures must be understood and developed, (2) predictive structure-property relationships must be established to guide composite design, and (3) proof-of-concept must be verified through case studies to demonstrate the advantages of each approach.

The two morphologies that are expected to have the broadest impact are particle-embedded fibers and particle-containing porous fibers, and because of this they are the primary focus of this effort.

1.3 Structure of Thesis

The first chapter of this thesis introduces chemical separations and the overall goal of developing rational design procedures and fabrication strategies for adsorbent-embedded electrospun fibers. Chapter 2 introduces relevant background and methodology on the adsorption process, metal-organic-frameworks, electrospun fibers and fiber fabrication techniques, and characterization techniques used in multiple chapters. The background section is not necessary for those with previous background in any of these areas since each are simply a literature review, but is presented if further understanding is desired. Chapter 3 contains a consolidated materials and methods section.

Chapters 4 explore how electrospinning may be used as a tool to design either particle-embedded fibers or particle-covered fibers based on the electrospinning solution. Chapter 5 contains the derivation of design criteria for particle-embedded fibers and a validation against finite-element models. Chapters 6 and 7 are presented to provide experimental evidence of enhanced selectivity and stability, respectively, as predicted by the model in chapter 5. Chapter 8 demonstrates a strategy for designing particle-containing porous fibers, and Chapter 9 provides a

case-study for particle-containing porous fibers for the application of direct air capture. Chapter 10 contains overall conclusions from this work as well as recommendations for future research directions.

CHAPTER 2.

BACKGROUND

2.1. Adsorption

Adsorption is the process of a fluid component concentrating at an interface to reduce the surface energy of that interface. When a material, in this case called an adsorbent, is in vacuum the molecules at the surface are at a higher energy state than the molecules inside the solid because they are missing chemical bonds (Figure 2.1.1 a). When this adsorbent is placed into a fluid- either a gas, liquid, or atmosphere- molecules in that fluid stream will spontaneously concentrate at the surface to reduce this excess surface energy as well as the energy of the entire system (Figure 2.1.1 b).

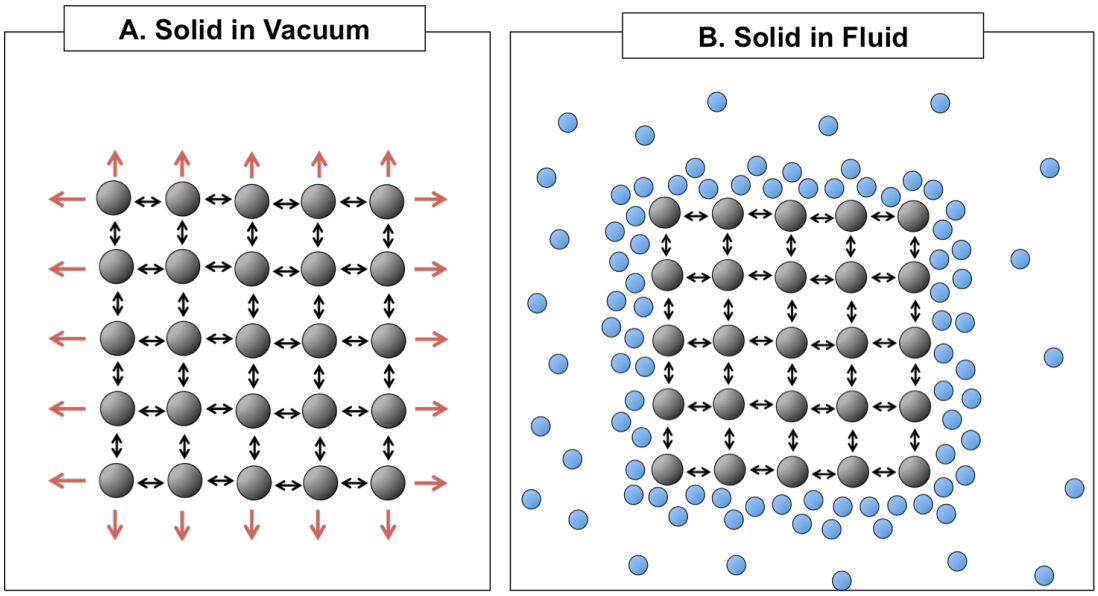

Figure 2.1.1. (A) A solid in vacuum demonstrating that molecules on the surface are missing bonds, leading to a higher surface energy. (B) When these molecules are put in a fluid, adsorption of fluid species will spontaneously concentrate at the solids surface.

This adsorbent may be designed to preferentially adsorb specific molecules from the fluid stream, and this quantity adsorbed may be manipulated by adjusting the temperature, pressure, or chemical environment of the system. A cyclic capture and release process may be designed to result in chemical separations. To design an effective adsorption process a holistic view must be taken incorporating the necessary adsorption phenomena at the adsorbent surface, the

adsorbent itself, and the cyclic process. Key points to the process are provided here, while some of these other considerations are discussed throughout this thesis. Section 2.1.1 describes how the quantity of species adsorbed at the surface may be measured (thermodynamics); section 2.1.2 lists some common sorbents that will be considered in this work along with future work.

2.1.1. The thermodynamics of adsorption. When a gas is exposed to a surface at a specified concentration, some will be adsorbed. Various routes have been demonstrated to show this relationship, including through kinetic equilibrium calculations, thermodynamic equations of states, and statistical probabilities.(Do, 1998) The relationship between concentration (or partial pressure) and the quantity adsorbed at a given temperature is called an isotherm. The international union of pure and applied chemistry (IUPAC) has defined a variety of isotherm types, as shown in Figure 2.1.1.1.(Thommes et al., 2015)

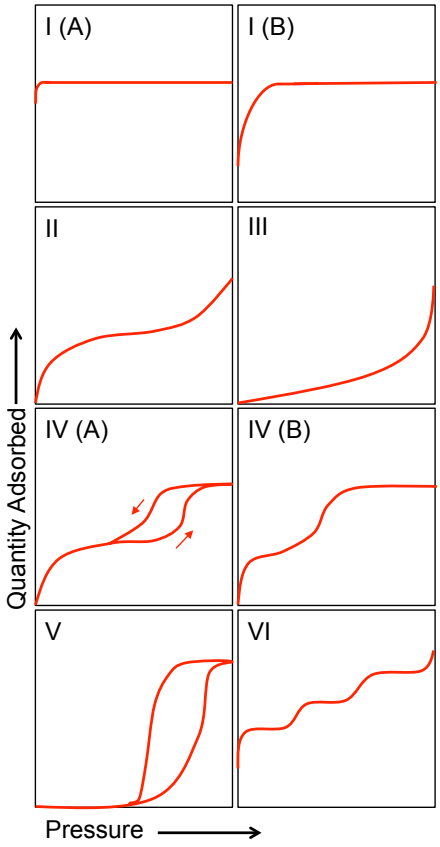

Figure 2.1.1.1. Isotherms types according to IUPAC.(Thommes et al., 2015)

Type I isotherms result from systems where a single layer of molecules adsorb to the surface. This may occur from either a chemical adsorption process where a secondary layer is not favorable (typically representative of Type I (a)), or a porous structure where only a single layer fits inside the pores (typically representative of Type II (b)). These isotherms and assumptions fit the Langmuir isotherm:

$$\theta_i = \frac{KP_i}{1+KP_i} \quad (2.1)$$

where P_i is the partial pressure of gas i, K is an adsorption equilibrium constant, and θ_i is the uptake of gas i.

Each of the other isotherm types allow for multilayer adsorption. Type II isotherms are composed of surfaces with favorable adsorbate-adsorbent interactions, and Type III isotherms have unfavorable adsorbate-adsorbent interactions.

The last four isotherm types each contain complex geometries or surfaces that add extra features to the isotherms. Hysteresis loops, in which the adsorption process differs from the adsorption process, occur when capillary forces or pores change the geometry of adsorption and desorption. A variety of other isotherm models are available for fitting various isotherms, and some will be discussed in future chapters.

These isotherms, by definition, neglect the temperature effect on the adsorption phenomena. Often terms in the isotherm are assigned temperature dependence. Multiple isotherms may be taken at different temperatures and correlated to determine this relationship.

2.1.2. Adsorbents. Adsorbents must be designed to take into account the thermodynamics, kinetics, and overall adsorption process. High surface areas allow for more active sites, porosity both increases surface areas and may include size-exclusion at specific sizes. Incorporating highly active groups may increase quantity adsorbed, but it may be at the tradeoff of either selectivity or adsorbent stability. With large tradeoffs between components that effect the final properties of the adsorbent system, many different adsorbent materials have been used and are

under research. Each class of adsorbents offer there own set of advantages and disadvantages for adsorption applications. A few that are likely to be considered for current and future application-specific work are outlined here.

Metal-organic-frameworks (MOFs) are a relatively new class of porous materials composed of metal nodes connected by ligand struts. These materials are highly tunable but tend to suffer from stability issues relative to other adsorbents. They will be discussed further in the next section.

Zeolites are porous crystals that are traditionally composed of silica, alumina, and oxygen into tetragonal building blocks to form porous crystals.(Baerlocher, McCusker, & Olson, 2007) Some zeolite structures are of significant economic importance for adsorption-based applications, however, a limited number of structures are available without modification. This limitation has not impeded their use and further functionalization for adsorption applications, however, and a combination of cheap manufacturing and high stability relative to MOFs many advantages.

Porous aromatic frameworks and covalent organic frameworks each represent classes of porous crystals intended to overcome the weak coordination bonds in MOFs with covalent carbon-carbon bonds,(Ben et al., 2009) yet to date they do not have the same functionality as MOFs, however they may emerge as more viable options industrially in the near future.

Templated porous carbons formed by pyrolysis of precursor structures are also highly studied for adsorption due to advantages posed by traditional activated carbon yet containing more uniform pore structures and sizes.(Sakintuna & Yürüm, 2005)

Other carbons based on benzene structures such as carbon nanotubes, graphene, fullerines, and their functionalized derivatives have many applications in adsorption as well due to low reactivity, high surface areas, reusability, and low cost. These materials have lower adsorptive properties than other materials without extensive modification, but are leading sorbents for heavy metal removal from water streams and have potential to compete in other adsorption fields as well.(Chawla, Kumar, & Kaur, 2015)

Nanosized metal oxides are a final sorbent to be listed here. They are typically either spherical or cylindrical materials with high adsorptivity due to a size-quantization effect.

Drawbacks include agglomerations, stability issues, and difficulty separating from the fluid stream.(Hua et al., 2012)

2.2 Materials: Metal-Organic Frameworks (MOFs)

Metal-Organic Frameworks, (MOFs) are a class of adsorbents brimming with potential that find their roots in Tempe, Arizona. Originally synthesized and presented in 1989,(Hoskins & Robson, 1989) Omar Yaghi placed a spotlight on these materials by presenting MOF-5 to the academic community in 1995, while also revealing the extraordinary potential these materials possess.(Containing & Rectangular, 1995) For decades crystalline MOFs have been touted as potentially transformative materials in the fields of catalysis, sensing, chemical storage and chemical separations. Unprecedented surface areas and a theoretically infinite set of metal/ ligand combinations allow MOFs to be finely tuned in terms of functional groups, aperture sizes and pore geometries. This expansive design potential is indeed a strong argument for this excitement, however, with over tens of thousands of MOFs synthesized over the past 30 years, none have made a significant industrial impact.(Vaughan, 2014) This absence of industrial impact is rooted in the metal-organic chemistry at the core of MOFs. There exists an inherent tradeoff between performance, stability, and cost that researchers have not yet overcome. In this section we discuss the chemistry and synthesis of MOFs, why these crystals have great potential, and how they may eventually be realized on a commercial scale.

2.2.1. The anatomy of MOFs. The true definition of a MOF comes with controversy. The quick adoption by multiple scientific disciplines led to several incompatible interpretations. In 2012 a poll was taken on what the definition should be and no answer received more than a 33% endorsement.(Batten et al., 2012) Notable chemists lobbied to adopt a definition that strictly followed traditional organometallic chemistry nomenclature.(Tranchemontagne, Mendoza-Cortes, O'Keeffe, & Yaghi, 2009) However, citing years of broader usage of the term MOF, in 2013, the International Union of Pure and Applied Chemistry (IUPAC) recommending a more relaxed definition: "*A metal-organic framework, abbreviated to MOF, is a coordination network with*

organic ligands containing potential voids."(Batten et al., 2013) The implications of this definition are that MOFs are (1) a subset of coordination polymers and coordination networks, (2) composed of metal nodes connected by organic ligands, (3) potentially dynamic systems changing as a result of external stimuli, and (4) not required to be porous or crystalline in nature.(Batten et al., 2013) Presently, the IUPAC also endorsed the usage of nicknames for commonly used MOFs to enhance recognition (e.g ZIF-8 for zeolitic immidazolate framework-8 or HKUST-1 for Hong Kong University of Science and Technology-1) due to the absence of a universally accepted naming scheme. This work refers to MOFs as a particular subset of the class of materials exhibiting both crystallinity and porosity, and uses the commonly accepted nicknames for MOFs.

MOFs are constructed from metal nodes connected by organic linkers. The organic linkers are often composed of multiple carboxylic acid groups, but may also use imidazolate-metal or cation-anion interactions to sustain the network. A set of typical ligands are demonstrated. The metal nodes sometimes are composed of individual metal atoms, however, it is much more common for a metal-containing complex called a secondary building unit (SBU) to act as the node. A figure of some common ligands, SBUs, and how they arrange are demonstrated in Figure 2.2.1.1.(Howarth, Liu, Li, Li, Wang, & Farha, 2016)

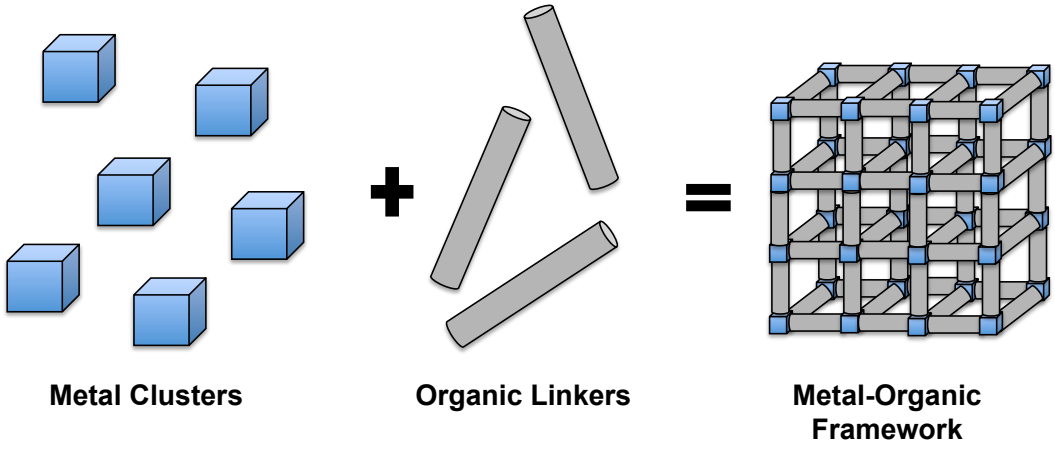

Figure 2.2.1.1. A demonstration of how metal nodes may be attached to organic linkers to form metal-organic framework. Adapted From Howarth and coworkers.(Howarth, Liu, Li, Li, Wang, Hupp, et al., 2016)

MOFs of interest in this work are both porous and crystalline, meaning that they contain a repeating structure through space.

2.2.2. ZIF-8 and other archetypal MOFs. When searching the keyword metal-organic framework and/or MOF in the Web of Science there are over 40,000 hits. Research on MOF structures is not equal. Only a handful of MOFs are at the center of most of these works. In this work we loosely define archetypal MOFs as MOFs listed as the topic of over 800 papers in the Web of Science database- a significant drop off in this metric is observed below 800. Figure 2.2.2.1 contains a survey of MOFs and the number of times that each of these is listed as a topic in Web of Science; ZIF-8, Mil-101, MOF-5, HKUST-1, and UiO-66 each meet this definition of archetypal MOFs. Each of these MOFs contains some combination of the following attributes that have naturally qualified them for the increased attention: easy synthesis, high relative stability, and/or benchmark properties in one or more applications. Each of these MOFs has unique traits, synthesis considerations, and structural analogs deserving of independent consideration.

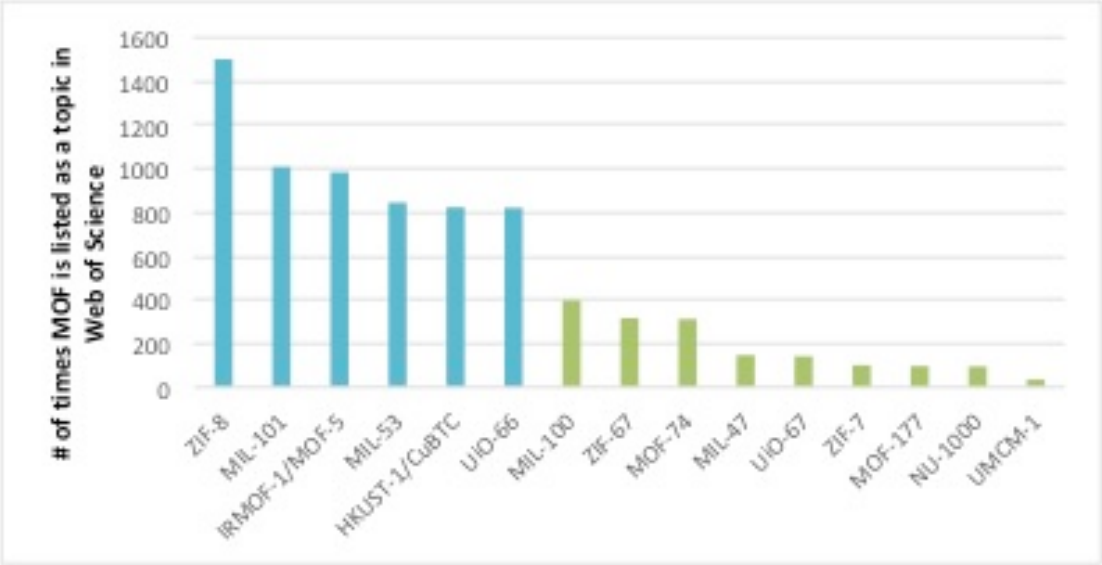

Figure 2.2.2.1. A selection of MOFs and the number of times each is listed as the topic to a paper in the Web of Science. Blue bars indicate benchmark MOFs, and green bars represent other MOFs.

Ultimately, because we are studying the fundamental relationships resulting from MOF containing fibers in this study, these highly studied MOFs are used in this work. HKUST-1 is the MOF selected for studying water-sensitivity since the water sensitivity of this MOF is well documented, it is briefly discussed in the chapter that it is used, Chapter 7, and the synthesis of HKUST-1 is explored in the appendix. UiO-66 is the focus of some studies in the appendix, and is also expected to be the focus of studies going forward when this research direction transitions into water-based applications. ZIF-8 is used throughout most of this work due to its well-understood properties and morphology control. Its structure is discussed here.

ZIF-8 (zeolitic immidazolate framework-8) has a sodalite topology and is composed of stacked cages. A single cage is composed of zinc nitrate tetragonal nodes coordinated to 2-methlimadazole linkers to form a 6-membered and 4-membered aperture. This results in pore diameters of 11.6 Å with pore apertures of 3.4 Å,(James, Wang, Meng, & Lin, 2017) however, the effective pore aperture is found to be nearer to 4.2 Å due to framework flexibility.(C. Zhang et al., 2012). A representation of ZIF-8 is given in Figure 6.2.2.1, which is adapted from a previous publication.(M. R. Armstrong, Shan, Maringanti, Zheng, & Mu, 2016)

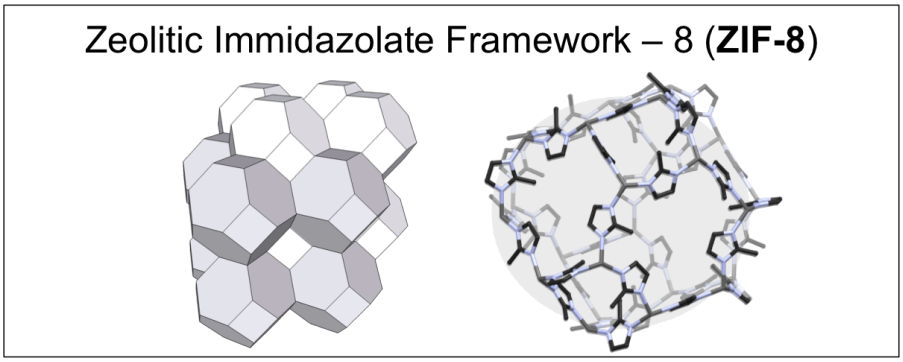

Figure 6.2.2.1. A representation of the metal-organic-framework (MOF) zeolitic-imidazolate-framework-8 (ZIF-8) showing The cage structure of ZIF-8 was generated from crystallographic data provided by Park and coworkers.(Park et al., 2006). Image adapted from a previous publication.(M. R. Armstrong et al., 2016)

2.2.3. Synthesis and activation of MOFs. Many routes are available for the synthesis of MOFs, and after synthesis, they must be activated- the process of removing residual solvent from pores- and often shaped into forms that may be used for processes later. Commonly explored synthesis methods include solvothermal synthesis, sonochemical synthesis, mechanical milling, microwave synthesis. (Y.-R. Lee et al., 2015) Each of these methods has a tendency to produce crystals of different size and crystallinity. Typically solvothermal synthesis is used to synthesize MOFs, however, this technique does not always provide suitable control over particle size and particle size distributions. For this reason specialized techniques including Cravillon's room temperature synthesis method,(Cravillon et al., 2011) and sonochemistry are also used to create particles of smaller size and tighter distributions than their solvothermal counterparts.

After synthesis, the solvent must be removed from the pores to leave behind a porous structure. This is routinely done through a solvent-exchange to a more volatile solvent, followed by heating in a vacuum oven to clear the pores. A further step that is required for industrial processes yet is largely unexplored is the next step: shaping. MOFs must be pelletized or produced in a functional form that allows them to be used in their intended application. Desantis et. al. explore the economic impact of two more methods- solventless methods such as milling and aqueous phase MOF synthesis- that have potential for high-throughput, cheap synthesis of MOFs that have potential for synthesizing MOFs at commercially acceptable prices, their potential industrial process workflows are shown in Figure 2.2.2.1.(Desantis et al., 2017)

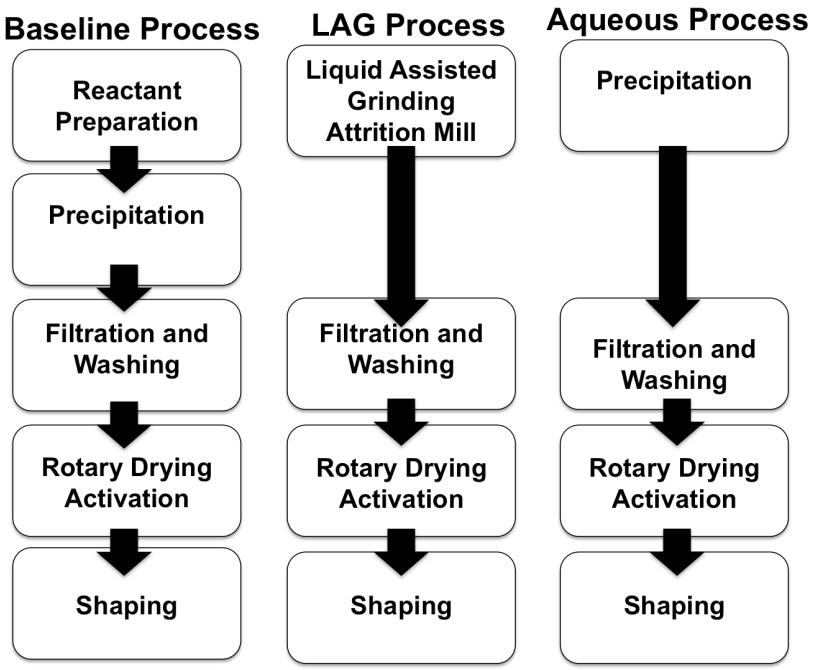

Figure 2.2.2.1. The current baseline process for lab scale MOF synthesis and two other MOF fabrication techniques with potential for industrial scale production including liquid assisted grinding or an aqueous phase precipitation process.

2.3 Materials: Fibers and Electrospinning

Fibers are important. The original manufacturers of fibers -silk worms- provoked wars, built fortunes for aristocrats, and laid the foundation for dynasties. Today they are ubiquitous to many technologies. Fiber optic cables span the ocean, Lightweight carbon fiber and Kevlar enable lightweight durable composites, hollow-fiber membranes produce drinkable water, non-woven fiber mats provide breathable air, and after thousands of years fibers still the foundation of the textile industry. The high aspect ratio of fibers allows their length to span space (making them highly processable), yet the smaller dimensions add strength and functionality. With a strong historical and present-day importance, it is unsurprising that there are both highly mature fiber fabrication technologies as well as emerging technologies of academic intrigue. In this section the geometric implications of fibers are discussed, followed by an overview of some mature technologies. Electrospinning – an emerging technology used throughout this thesis- is discussed, and next generation electrospinning technologies are also mentioned.

2.3.1. The geometry and vocabulary of fibers. Fibers are defined as solid, flexible materials that are 1000× longer in length than in all other dimensions. The term aspect ratio is used to describe the ratio of a materials longest dimension divided by the materials shortest dimension, therefore, an alternative definition of a fiber is a material with an aspect ratio over 1000:1.(Ko & Wan, 2014) Since fibers are typically fabricated along their length, it is convenient to discuss fibers in terms of cylindrical coordinates (Figure 2.3.1.1).

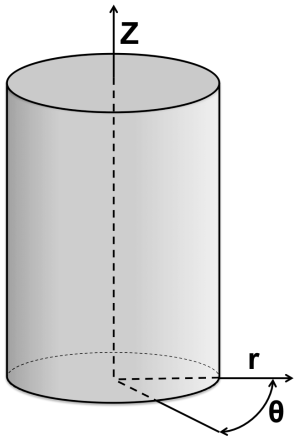

Figure 2.3.1.1. An illustration of the cylindrical coordinate system.

The z-axis contains the length or height of the fiber, it is called the longitudinal or axial direction. The r-axis contains the fiber radius and diameter; it is called the radial direction. The θ-axis is called the angular or azimuthal position.

The relationship between the external surface area of a fiber (**SA**, in cm^2/g) and the fiber diameter (**D**, in cm) and density (**ρ**, in cm^3/g) may be defined for fibers that may be approximated as cylinders by neglecting the contribution of the fiber ends as:

$$SA = \frac{4}{\rho D} \quad (2.2)$$

Neglecting the ends of the fibers is considered a valid approximation because of the high aspect ratio in fibers.

Fibers of small dimensions are interesting in part due to their extreme surface areas. Along with a higher surface area, fibers of smaller diameters also have an increased polymer chain alignment, which may also result in increased mechanical strength.(Ko & Wan, 2014) A

stringent requirement for the use of the term nanofiber requires diameters less than 100 nm, however, it is generally practice to describe any fiber below 1000 nm as a nanofiber.

Spinning fibers is the most common approach to fiber fabrication. Other methods exist such as self-assembly, chemical vapor deposition, phase separation and template synthesis.(Ko & Wan, 2014) Spinning is done by extruding a polymer dope through a spinneret (which is typically a needle, die, or hole) followed by a solidification process. The diameter of the final fiber is described by the drawdown ratio, which is the ratio of the final diameter of the fiber versus the diameter of the spinneret. To further decrease the fiber diameter a drawing process may be used in which the solidified fiber is pulled to increase the drawdown ratio by further extending the fiber during the solidification process. A review of some fiber spinning techniques is presented in the next section.

2.3.2. Fiber fabrication. Table 2.3.2.1 contains a summary of fiber spinning techniques, which is adapted from a review presented by Luo and coworkers.(Luo, Stoyanov, Stride, Pelan, & Edirisinghe, 2012)

Table 2.3.2.1.
Fiber Spinning Techniques

Process	**Minimum Fiber Diameter**	**Dope**	**Solidification**
Melt Spinning	Macro	Melt	Cooling
Melt Blowing	Nano	Melt	Cooling
Conjugate Spinning	Nano	Melt	Cooling
Film Splitting	Micro	Melt	Cooling
Wet Spinning	Nano	Solution	Coagulation
Dry Spinning	Nano	Solution	Heating or Evaporation
Gel Spinning	Micro	Solution	Cooling, Evaporation, or Coagulation
Emulsion Spinning	Macro	Emulsion	Phase Separation
Centrifugal Spinning	Nano	Melt, Solution	Cooling
Electrospinning	Nano	Melt, Solution, or Emulsion	Cooling, Evaporation, or Coagulation

The first cluster of processes is characterized by the cooling of a molten polymer, which may be called melt spinning. The first and most basic is melt spinning, where either polymer pellets, granules or raw material is heated and extruded through a dye, and solidify as they cool. Melt blowing adds a strong air stream that draws the fibers to smaller dimensions. Conjugate spinning involves making nano-dimensioned fibers through a templating method; two different polymers are spun together in an island-in-sea orientation where small dimension fibers (islands) are embedded in a larger polymer fiber (sea), and the sea polymer is dissolved away to leave behind a bundles of nanofibers. Film splitting is a method by which ribbons or sheets are extruded, and the fiber form is made by cutting these films along the longitudinal axis to form fibers.

Next are solution-spinning techniques. These processes require a dope in which the polymer is dissolved in a solvent while extruded through a spinerette. In wet spinning the solution is extruded into a bath of non-solvent bath to induce solidification, In dry spinning the solution is extruded into a heated chamber in which the polymer is solidified through solvent evaporation. Gel spinning (also called wet-dry spinning) is a hybrid between wet and dry spinning in which polymers with a low solvent content are extruded while still retaining a portion of the solvent in a gel form that may be drawn or processed further. Emulsion spinning is a technique in which a

non-melting and non-soluble polymer is suspended in another polymer solution, extruded, and the soluble polymer is removed leaving behind the non-soluble polymer in fiber form.

Centrifugal spinning is either a solution or melt spinning process in which the dope is fed through a spinerette in the center of a drum rotating at a high angular velocity. The fiber is extruded and drawn out by centrifugal forces before being collected on the drum.

Electrospinning is often a solution spinning technique (although may be melt or emulsion spinning) in which a high direct current voltage is applied to the spinerette, which draws the fiber onto a grounded substrate. This method is further explained in the following two sections.

2.3.3. Electrospinning overview. Electrospinning, in its most common form, is conducted by passing a polymer solution through a needle with a syringe pump. This needle is connected to a high voltage power supply delivering a direct current to the needle at some working distance from a grounded collector. An illustration of this process is shown in Figure 2.3.3.1.

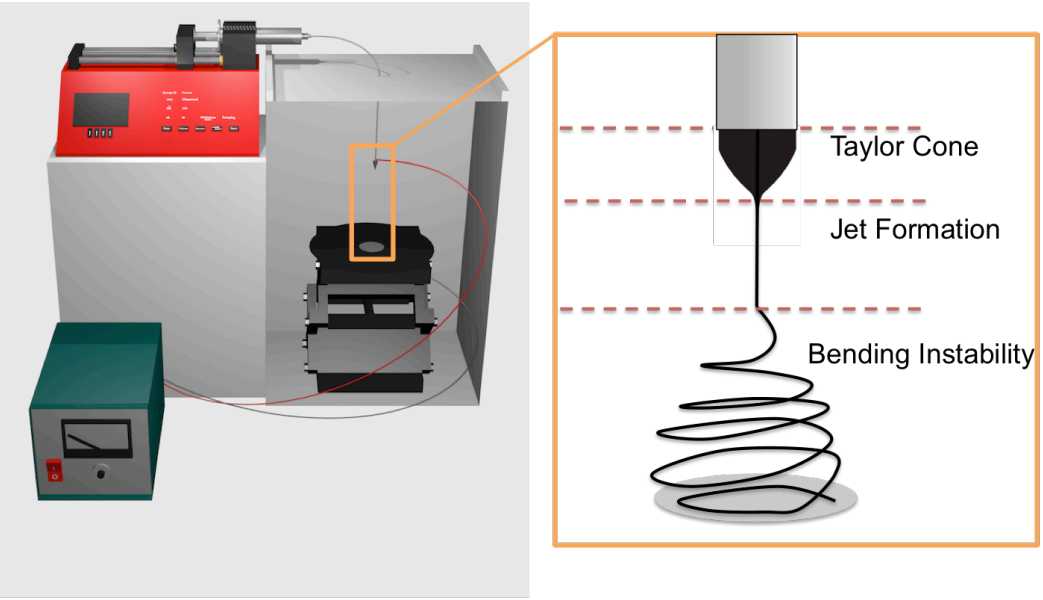

Figure 2.3.3.1. Electrospinning apparatus with important electrospinning regimes including the Taylor cone formation, jet formation, and the onset of bending instabilities.

The inset image shows the regimes of a polymer fluid being electrospun. Initially after leaving the needle a Taylor Cone is formed, which results from the balance between surface

tension forces and electrostatic repulsion forces. This shape results in a virtual orifice at the end of the Taylor cone which is smaller than the actual spinneret orifice used. This initial elongation both increases the drawdown ratio and allows needle-less electrospinning to be used, allowing spinning processes to be performed without a spinneret. An examples of this includes electrospinning fibers from a helical wire rotating through a polymer solution.(Han, Nurwaha, Li, & Wang, 2014)

A polymer jet is ejected from the end of the Taylor cone. This jet is initially straight, however, the electrostatic forces eventually induce bending instabilities which initiates a whipping region where the polymer fluid drastically reduces its diameter until the solvent evaporates and the polymer solidifies.

Parameters used to control the electrospinning process may be divided into solution parameters, operating parameters, and environmental parameters. A list of these parameters is given in Table 2.3.2.2.(Stranger, Jon, Tucker, Nick, and Staiger, 2009)

Table 2.3.2.2.
Electrospinning Parameters

Solution Parameters	**Process Parameters**	**Environmental Parameters**
Concentration	Electrostatic Potential	Temperature
Viscosity	Electric Field Potential	Humidity
Surface Tension	Electrostatic Field Shape	Local Atmospheric Flow
Conductivity	Working Distance	Atmospheric Composition
Dielectric Constant	Feed Rate	Pressure
Solvent Volatility	Orifice Diameter	
Molecular Weight	Spinning Angle	

In general, increasing solution concentration/ viscosity increases fiber diameter, decreasing surface tension increases longitudinal uniformity of the fiber, and increased molecular weight leads to easier spinnability. Increasing working distance and decreasing voltage have been shown to decrease fiber diameter. Increased humidity has been shown to induce pores on the fiber.(Ko & Wan, 2014) The interplay between these parameters and the electrospinning regions is described further in the next section.

2.3.4. Electrospinning balances and phenomena. During the process of electrospinning multiple phenomena must occur. First, a Taylor Cone is made and maintained at the spinerette tip. A jet is expelled from this tip, and whipping is induced. The electrical charge may migrate radially through the fiber, and evaporation at the surface of the fiber occurs. Each of these are discussed here.

The Taylor cone formation occurs due to a balance between surface tension forces and electrostatic repulsion. For this cone to become the favorable geometry, a critical voltage ($\mathbf{V_{crit}}$) must be surpassed. This equation is given as:

$$V_{Crit}^2 = 4\frac{H^2}{L^2}\left(ln\frac{2L}{R} - \frac{3}{2}\right)(0.117\pi\gamma R) \quad (2.3)$$

where H is the working distance between electrodes, L is the length of the spinneret, R is the spinneret radius and γ is the surface tension.(Stranger, Jon, Tucker, Nick, and Staiger, 2009) This model is believed to be oversimplified and only true in particular cases, yet it serves as a good illustration and sufficient estimation for most cases. A more extensive model is discussed by Yarin,(Yarin & Reneker, 2001) and Rutledge.(Shin, Hohman, Brenner, & Rutledge, 2001) An illustration of the forces that lead to Taylor Cone formation is given by Cann and coworkers.(Wu, Oleschuk, & Cann, 2012)

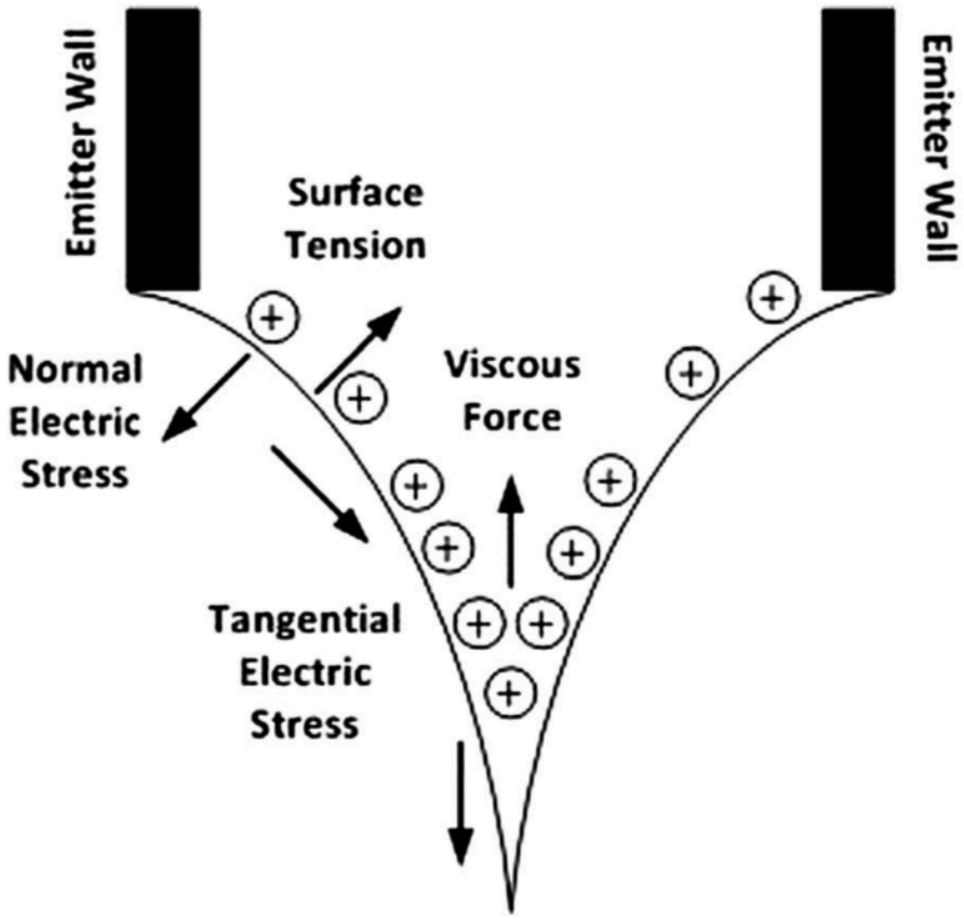

Figure 2.3.4.1. The forces that lead to Taylor cone formation and the jet that produces electrospun fibers. From Cann and coworkers.(Wu et al., 2012)

The movement of electrical charge is not entirely understood in electrospinning as of yet. It is hypothesized by Kornev that the charge initially starts within the volume of the polymer fluid, migrates towards the surface of the polymer fluid during the electrospinning process, and that higher solution dielectric coefficients slow this charge migration process.(Kornev, 2011) Collins and coworkers hypothesize that charge is delivered to the polymer solution through a field emission mechanism such that the charge originates in the center of the fluid passing through the spinneret, and that throughout the electrospinning process charge is lost through the corona effect at the spinneret tip, through loss to humidity, through losses by electro-spraying, carried

away by evaporating solvent, charge transferred to the grounded collector, and residual charge left over in solidified fiber.(Collins et al., 2012)

Electrostatic instabilities eventually induce whipping during the flight of the fluid jet. Charge repulsion will elongate the viscoelastic fluid jet to accommodate the charge as seen in Figure 2.3.4.2, which was originally presented by Yarin.(Reneker & Yarin, 2008)

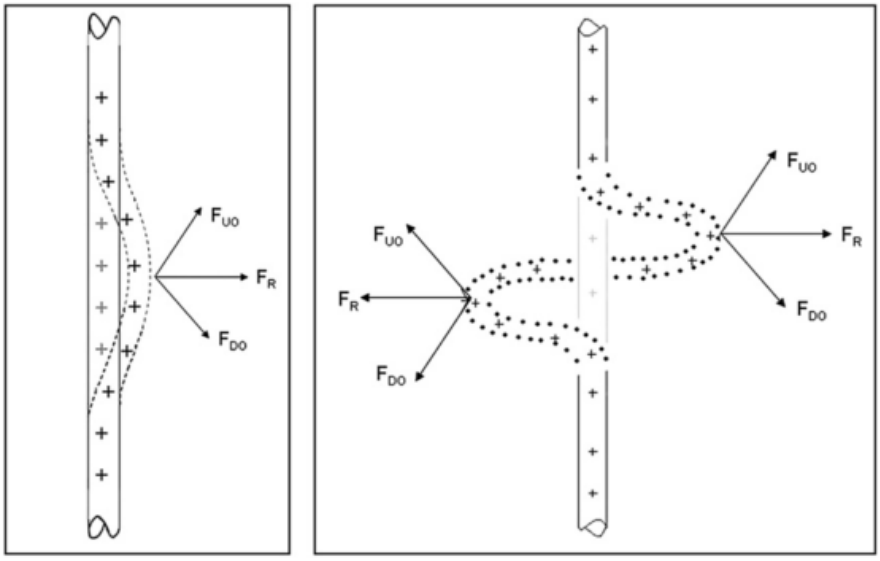

Figure 2.3.4.2. A figure from Yarin,(Reneker & Yarin, 2008) illustrating how charge repulsion induces a whipping motion during electrospinning elongates and thins the polymer fluid to create fine fibers.

Models to properly characterize this whipping are elusive since it occurs in a chaotic, random manner, however in general adopts a conical helix shape.(J. Guerrero, Rivero, Gundabala, Perez-saborid, & Fernandez-nieves, 2014)

The evaporation of solvent during the electrospinning process is what generates the transition between the viscous fluid into a solid fiber. In general, evaporation may be described by the Langmuir evaporation equation:(Langmuir, 1932)

$$\mu = 2.65\times10^{19}\frac{p}{\sqrt{MT}} \qquad (2.4)$$

Where **p** is the partial pressure of the solvent in the gas phase, **M** is the molecular weight of the solvent, **T** is the temperature, and **μ** is local evaporation rate. The total evaporation rate is

then the product of the surface area and **μ**. Therefore; the evaporation rate is a function of the changing fiber surface area and solvent volatility. The changing fiber surface area is generally inverse to solvent volatility since increased solvent in the polymer fluid increases the rate of expanding surface.

CHAPTER 3.

MATERIALS AND METHODS

3.1 Chemicals Used

Polymers. Poly(ethylene oxide) ("PEO", M_V = 400,000) and Polystyrene ("PS", M_W = 250,000 g/mol) was purchased from Sigma-Aldrich. Matrimid 5218 ("MAT", M_W 80,000) was provided by Huntsman.

Gases. Carbon dioxide (CO_2), nitrogen (N_2), and helium (He) were purchased from Prax-air, each at ultra-high purity grade.

MOF precusors. Zinc nitrate ($Zn(NO_3)_2$, purity 98%) copper (II) Nitrate ($(CuNO_3)_2 \cdot 6H_2O$, 98%), trimesic acid (BTC, 98%), and 2-methyl immidazolate ($CH_3C_3H_2NH$, purity 99%) were purchased from Sigma-Aldrich.

Solvents. Methanol (CH_2OH, 99.8%) dimethyl formamide (DMF, 99.9%), ultra-pure water (H_2O, 99.9%), ethanol (EtOH, 99.8%) and dichloromethane (CH_2Cl_2, 99.5%) were purchased from Sigma-Aldrich

All chemical were used as purchased without further purification.

3.2 Characterization Techniques

3.2.1. Porosimetry. Nitrogen porosimetry at 77K was performed on a Micrometrics Tristar II porosimeter in a liquid nitrogen bath. Carbon dioxide isotherms were collected at 273 K by immersion in ice slurry. Void volume was measured with helium before each run.

High-pressure sorption experiments were performed on a Quantachrome iSorb HP2 machine. Helium void fractions were taken before each measurement. Default equations of state recommended by Quantachrome software were used for each gas: Helmholtz for CO_2 and N_2, and the mBWR-Jacobsen for He. A maximum equilibrium for CO_2 and N_2 was set to 3 minutes in chapter 4. Initial activation was performed at 55 °C for 72 hours under vacuum, and activation between each run was performed at 55 °C for 12 hours under vacuum.

3.2.2. Microscopy. Scanning electron microscopy (SEM) was performed on a Zeiss EVO MA 10 microscope with an applied voltage of 15 kV on samples after gold sputtering.

Bright-field transmission electron spectroscopy (TEM) was performed on a Phillips CM200-FEG microscope on carbon coated samples.

Scanning transmission electron microscopy (STEM) was performed on a Titan Krios microscope under low-dose mode at 200 kV using a high angle annular dark field detector (HAADF).

3.2.3 Other Characterization Techniques. Diffuse reflectance Fourier transform infrared spectroscopy (DRIFT) was performed on a Nicolet iS50 FTIR spectrometer with a DTGS KBR detector, 100 scans averaged per spectra, and baseline corrections.

Thermal gravimetric analysis (TGA) was performed on an TA TGA Q500 instrument at a 10 °C ramp rate from 50 °C to 500 °C with N_2 gas flowing at 40 mL/min (Chapter 7) or TGA was performed on a TA Instruments SDT Q600 Thermal Gravimetric Analyzer under dry air flowing at 25 mL/min with a 20°C/min ramp rate from 30°C to 600 °C (Chapter 4)

Powder X-ray diffraction (PXRD) analysis of the UiO-66 and secondary growth samples were performed using an X-ray diffractometer (P'ANalytical) at 40 kV with a Cu-Kα X-ray tube with a nickel filter.

CHAPTER 4.

INFLUENCE OF PARTICLE SIZE AND LOADING ON PARTICLE ACCESSIBILITY IN MOF-EMBEDDED ELECTROSPUN FIBERS

4.1. Introduction

The properties of particle containing fibers are most importantly determined by two different radial locations of the particle along the fiber: on the surface (type B: particle-coated fibers, from Figure 1.2.2) or imbedded in the bulk (Type A: particle-embedded fibers, from Figure 1.2.2). Both may be the desirable case for different applications. Work by Kim, Hadjiargyrou, and coworkers demonstrate an application in which antibiotics inside fibers for controlled release, and that excess antibiotic at the surface resulted in an undesirable burst release.(Kim et al., 2004) In the case of using the embedded particles for catalytic applications, it is important to have particles located along the surface to enhance availability.(Lõpez-Maya et al., 2015) For this reason, we investigate the influence of particle size and particle loading on the availability of nanoparticles at an electrospun fiber interface. We use the polymer poly(ethylene oxide) since it has previously been reported to be impenetrable to nitrogen when measuring isotherms at 77 K,(Ostermann, Cravillon, Weidmann, Wiebcke, & Smarsly, 2011) and embed a metal-organic-framework, ZIF-8, in the fibers since it is a highly studied crystal of high surface area with well-established properties.(C. Zhang & Koros, 2015) The combination of these two materials allow us to exclusively probe the resulting composite fibers for accessible ZIF-8 along the surface, since embedded ZIF-8 will not provide any nitrogen uptake.

We find from this chapter that at ZIF-8 loadings near 10 wt%, nearly all particles are wrapped by the fiber for both ZIF-8 particles around 12.5μm and 200 nm in diameter. However, when using ZIF-8 particles of 200 nm, increasing loading demonstrates that particles eventually are forced into exposed states along the surface of the fiber. This occurs at loadings as low as 33 wt% (42 vol%), which suggests that particles are being kinetically trapped at the surface before being able to settle into available positions inside the fiber.

4.2 Results and Discussion

4.2.1. Materials synthesized. Table 4.2.1.1 contains a list of the materials synthesized for this study.

Table 4.2.1.1.
Samples synthesized and relevant properties

Sample	Sample name	ZIF-8 diameter (d) (μm)	Fiber diameter (D) (μm)	Weight % ZIF-8	Volume% ZIF-8	Figure Color Label
A	μZIF-8	12.5 ±3	-	100	100	Grey
B	nZIF-8	0.18 ±0.3	-	100	100	Black
C	PEO	-	2.8 ±0.4	0	0	Brown
D	10%μ	12.5 ±3	0.7 ±0.2	12.0 ±2.3	13.0 ±2.9	Orange
E	10%n	0.18 ±0.03	1.2 ±0.2	9.1 ±2.1	11.2 ±2.6	Purple
F	25%n	0.18 ±0.03	2.6 ±0.8	22.8 ±2.6	27.2 ±3.1	Green
G	33%n	0.18 ±0.03	1.3 ±0.3	31.9 ±2.7	37.2 ±3.2	Blue
H	50%n	0.18 ±0.03	1.9 ±0.7	50.1 ±3.0	56.0 ±3.4	Red

ZIF-8 was synthesized by 2 different methods. To create nano-sized ZIF-8 (***nZIF-8***), a method adapted from Cravillon and coworkers was used.(Cravillon et al., 2011) To synthesize micron-sized ZIF-8 (***μZIF-8***), a method adopted from Zhang and coworkers was used.(C. Zhang et al., 2012)

To form fibers, solutions of 200 mg PEO in 10 mL DCM were prepared. nZIF-8 at varying weight percentages (wt%) with respect to PEO including 10, 25, 33, and 50 wt%, along with 10 wt% μZIF-8 were suspended in individual 200mg PEO solutions to form a series of electrospinning solutions. Each solution was passed through a 21 gauge stainless steel needle at a flow rate of 0.2 mL/min using a syringe pump under an applied voltage of 15 kV onto grounded aluminum foil 15 cm from the needle. The electrospinning process was performed at room temperature (25°C) and at humidity levels below 20%. The collected non-woven mats were dried at 50°C under vacuum for 48 hours before characterization. Final weight percentages of ZIF-8 in

the fibers were confirmed through thermal gravimetric analysis (TGA) (Figure 4.2.1.1). The expected weight percentage was within the uncertainty of the TGA confirmed weight percentages for each case.

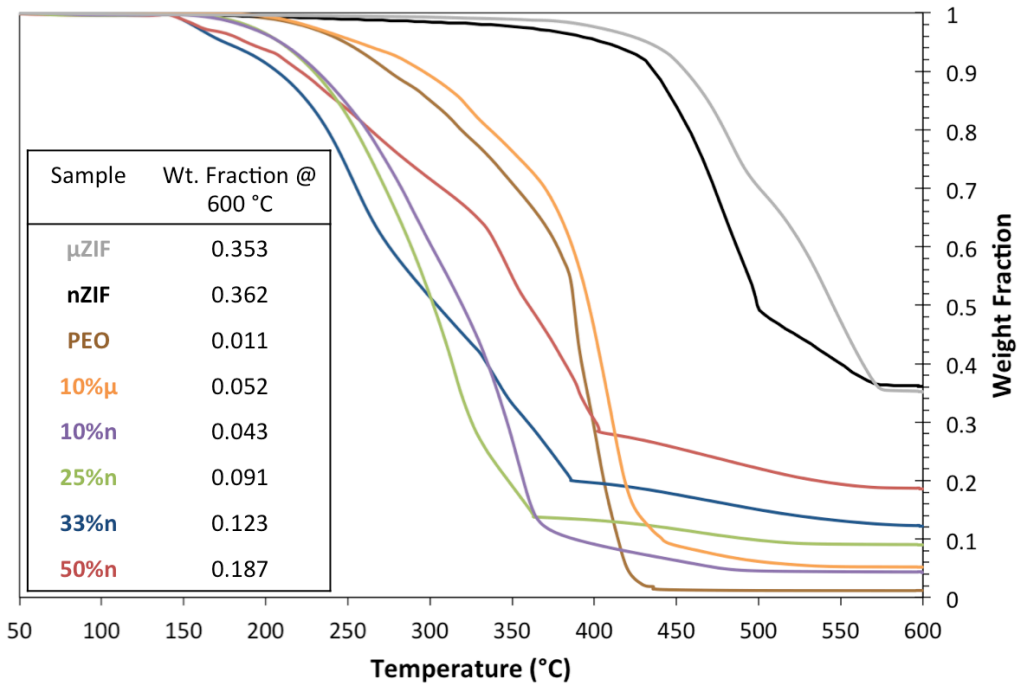

Figure 4.2.1.1. TGA decomposition curve for each sample tested in this work at a ramp rate of 20 °C/min and an air flow rate of 25 mL/min. The inset table contains sample names, color labels, and final weight fractions remaining after reaching a temperature of 600 °C.

The volume percentage of ZIF-8 was calculated using a PEO density of 1.2 g/mL (reported by Sigma-Aldrich) and ZIF-8 density of 0.95g/mL (reported by Tan and Cheetham) (J. Tan, Bennett, & Cheetham, 2010). Uncertainties from diameter measurements are the standard deviation of 50 measurements, uncertainties in the weight and volume percent come from propagation of an approximated uncertainty of 1% during TGA. Diameters are measured from the insets of each image shown in Figure 4.2.1.2, alongside other microscopic images.

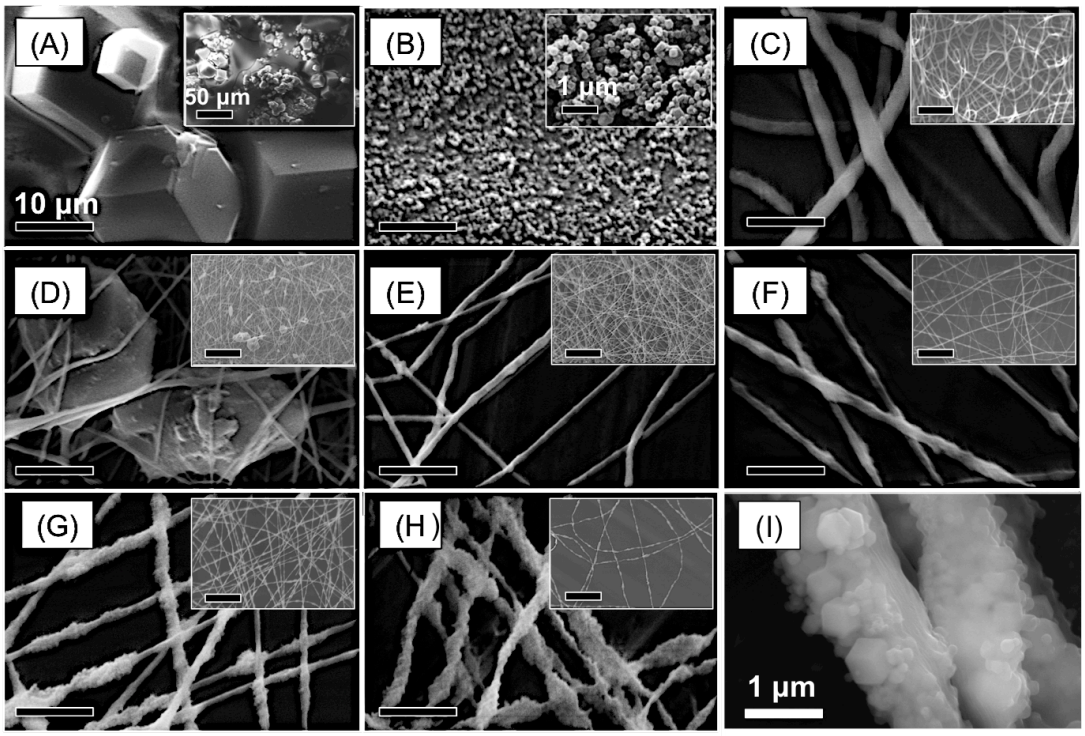

Figure 4.2.1.2. The scale bar for all main SEM images is 10 µm unless otherwise noted, and the scale bar for all inset SEM images is 50 µm unless otherwise noted. (A) SEM images of µZIF-8 (B) SEM images of nZIF-8 where the SEM inset image has a scale bar of 1 µm. (C) SEM images of pure PEO fibers (D) SEM images of 10%µ fibers (E) SEM images of 10%n fibers. (F) SEM images of 25%n fibers. (G) SEM image of 33%n fibers. (H) SEM image of 50%n fibers. (I) High magnification SEM image of 50%n fibers with a scale bar of 1 µm.

These images show that when particles are introduced to the fibers, the diameter drops in each case. For loadings of 33% and 50% it appears that nZIF-8 particles appear at the surface due to a rougher texture relative to fibers at lower loadings. Variations in size and roughness axially along these fibers exist that are likely due to instabilities during the electrospinning process induced by high levels of discrete particles influencing the solution surface tension during the electrospinning process. The µZIF-8 in the 10%µ fibers in Figure 4.2.1.1(D) appear to show that the PEO expands to encapsulate the particles before retracting again to a normal fiber diameter due to the loss in facet sharpness seen in comparison to the µZIF-8 particles in Figure 4.2.1.1 (A). A similar wrapping phenomena is observed in the high magnification image of the 50%n fibers in Figure 4.2.1.1 (I). In this image, most of the particles appear to be wrapped by fiber due to an observed loss of facet sharpness, however, some particles appear to be exposed at the surface

as well. Furthermore, optical images of the 33%n fibers suspended over a ringstand are shown in Figure 4.2.1.3 to demonstrate that they are readily removed from the aluminum foil substrate and may be handled.

*Figure 4.2.1.3***.** Optical images of 33%n fibers suspended over a 3" ringstand.

4.2.2. Influence of particle size. Two cases were explored in which different particle sizes were embedded into electrospun fibers through the electrospinning of suspensions at 10 wt%. In case I, the particle diameter (**d**) is smaller than the fiber diameter (**D**) (i.e. **d/D** < 1). In case II, **d** is larger than **D** (i.e. **d/D** >1). Both of these cases have been realized experimentally by embedding either nZIF-8 or μZIF-8 inside PEO fibers forming 10%n and 10%μ fibers, respectively. To probe for ZIF-8 accessible at the surface of these composite fibers, nitrogen adsorption isotherms were collected at 77K and are shown in Figure 4.2.2.1 along with calculated pore size distributions for both ZIF-8 embedded fibers. The pure components PEO, nZIF-8, and μZIF-8 are also investigated for reference.

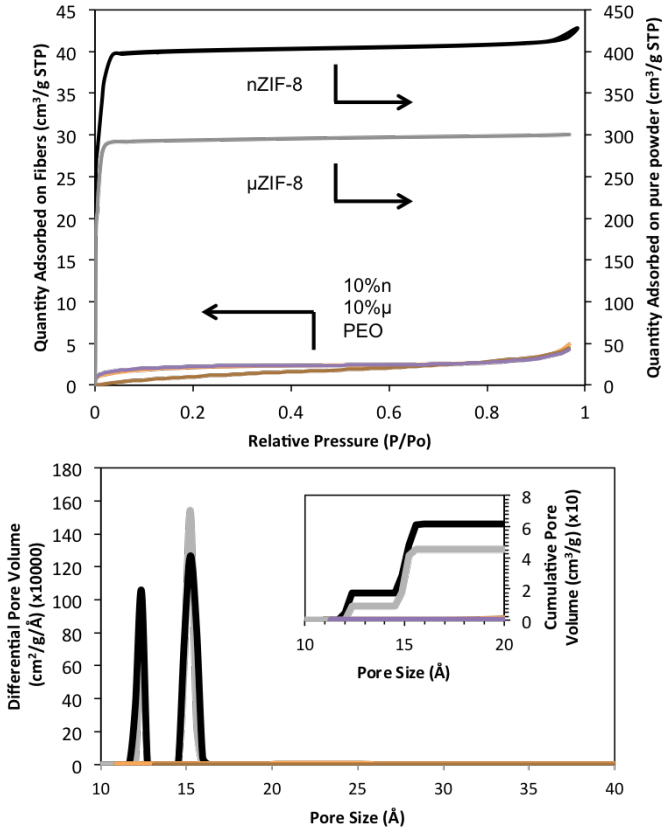

Figure 4.2.2.1. (Top) Nitrogen isotherms at 77 K. From top to bottom the samples are nZIF-8 (black), μZIF-8 (grey), 10%n fibers (purple), 10%μ fibers (orange), and PEO fibers (brown). nZIF-8 and μZIF-8 have quantity adsorbed shown on the right axis, 10%n, 10%μ, and PEO fibers have quantity adsorbed on the left axis. (bottom) Differential pore size distributions generated from the nitrogen isotherms for each material tested along with the cumulative pore volume reported from 10 to 20 angstroms in the inset graph with the same color scheme. All three fibers show no visible porosity and overlap along the baseline.

As seen in the calculated pore volumes, both nZIF-8 and μZIF-8 fibers at 10 wt% loading in fibers appear to take up no nitrogen, resulting in near complete nanoparticle blockage. This result means that during the electrospinning process, all particles at 10 wt% appear to be embedded inside the fiber, in agreement with the SEM images. The bimodal pore size distribution for ZIF-8 in Figure 4.2.2.1 is routinely observed in literature, and is attributed to either framework flexibility or a phase change in nitrogen (C. Zhang et al., 2012).

4.2.3. Theoretical framework for particle wrapping inside electrospun fibers. The thermodynamically favorable location of a particle inside along a fluid surface is determined by interplay between the energy of adhesion ($\mathbf{E_{ad}}$) and the energy of fiber stretching ($\mathbf{E_{St}}$). This model was originally derived by Dietrich, Angelova, and Pouligny for latex spheres being encapsulated by spherical vesicles for the full range of **d/D** and non-equilibrium fluid surface excess energies (Dietrich, Angelova, & Pouligny, 1997). It is adapted here for our system. Their model defines the total energy of the system, and we adapt it here (**E**) as:

$$E = E_0 + E_{AD} + E_{St} \tag{4.1}$$

Where we introduce the term $\mathbf{E_0}$ is the initial energy state, arbitrarily defined as the state in which no adhesion between the particle and fiber occurs. The relationship between these energies is illustrated in Figure 4.2.3.1.(Deserno & Bickel, 2003)

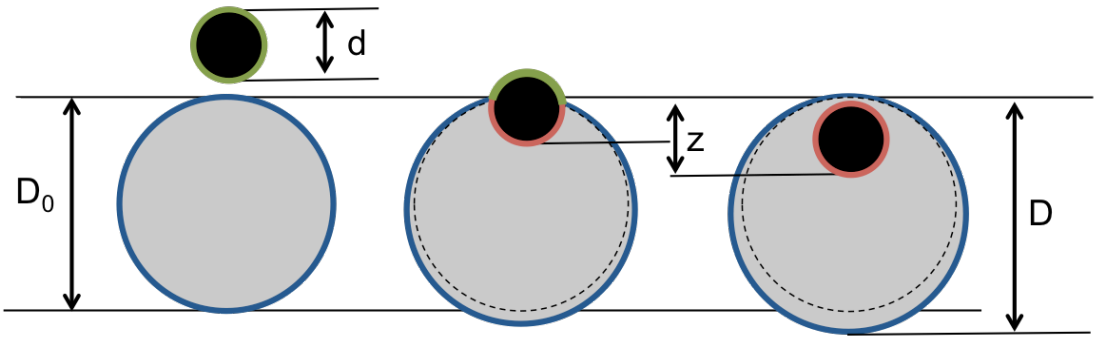

Figure 4.2.3.1. Cartoon depicting interplay of the energy of adhesion ($\mathbf{E_{ad}}$) and energy of bending ($\mathbf{E_{Be}}$). The fiber (grey) has a fluid-vapor interface (blue), the particle (black) has a solid-vapor interface (green), and when the fiber starts to wrap the particle a fluid-solid interface emerges (red).

As the fluid starts to penetrate the fluid surface two changes to interfacial areas takes place. (1) Some solid-vapor interface and fluid-vapor interface combine to become a solid-fluid interface, which is accounted for in $\mathbf{E_{AD}}$. (2) More fluid-vapor interface is simultaneously generated due to volume conservation and the particle stretching the fluid, which is accounted for in $\mathbf{E_{St}}$. $\mathbf{E_0}$, the initial energy state, is defined as the left image in which no adhesion has occurred.

For the limit of **d/D** < 0.2 Dietrich demonstrated that the fluid could be treated as a flat sheet, allowing curvature of the fiber and volume change of the fiber to be considered negligibly small. This approximation, along with approximating our ZIF-8 particles as spheres of uniform surface energy, that the fiber surface energy is constant with changing surface area, equation 4.1 becomes:

$$E = E_0 + (k_{AD} S_{AD})_{AD} + \left(\gamma_{FV,eff}(\Delta S_{Fiber})\right)_{S\square} \quad (4.2)$$

Where $\mathbf{k_{AD}}$ is the work of adhesion, $\mathbf{S_{AD}}$ is the surface area of the adhered particle-fiber interface, $\mathbf{\Delta S_{Fiber}}$ is the change in fiber surface area, and $\mathbf{\gamma_{FV,eff}}$ is the effective surface energy of the fluid-vapor interface. We consider $\mathbf{\gamma_{FV,eff}}$ to be an effective surface energy because, during electrospinning, this value will be a balance between attractive viscoelastic forces and repulsive electrostatic forces.(Stranger, Jon, Tucker, Nick, and Staiger, 2009) During electrospinning it is necessary for electrostatic forces to overcome these viscoelastic forces forcing this interface into an actively expanding state, (Reneker & Yarin, 2008) requiring $\mathbf{\gamma_{FV,eff}}$ to be either negative or nearly zero.

$\mathbf{k_{AD}}$ may be represented by the Dupree equation:

$$k_{AD} = \gamma_{SF} - \gamma_{SV} - \gamma_{FV,eff} \quad (4.3)$$

where $\mathbf{\gamma_{SV}}$ is the surface energy of the solid-vapor interface and $\mathbf{\gamma_{SF}}$ is the surface energy of the solid-fluid interface. All interfacial surface energy terms are constants. Each surface area term ($\mathbf{S_{AD}}$, $\mathbf{\Delta S_{Fiber}}$) may be defined in terms of the particle diameter, **d**, and the fractional particle immersion depth, **z,** where the total penetration depth is **zd** and **z** is a value between 0 and 1. $\mathbf{E_0}$, the initial energy state, is independent of particle penetration, and treated as a constant. It may be defined as:

$$E_0 = \gamma_{SF}\pi d^2 + \gamma_{FV,eff}\pi D_0^2 \quad (4.4)$$

where $\mathbf{D_0}$ is the diameter of the fiber without any adhesion.

Taking the derivative of **E** with respect to **z**, we find a relationship that describes the minimum energy of the system is found to be:

$$k_{AD} = -\gamma_{FV,eff} \quad (4.5)$$

Therefore, it may be expected if $\mathbf{k_{AD}}$ is greater than – $\boldsymbol{\gamma_{FV,eff}}$ that full wrapping will occur, and if it is less than - $\boldsymbol{\gamma_{FV,eff}}$, no wrapping will occur. By expanding $\mathbf{k_{AD}}$ with the Dupree equation (equation 4.3) and expressing this equation as an inequality, a final condition for full wrapping is given by:

$$\gamma_{SF} > \gamma_{SV} \tag{4.6}$$

For ENNCs composed of crystalline particles such as ZIF-8, $\mathbf{k_{AD}}$ is expected to be highly favorable since fluid solutions tend to wet high-energy crystalline substrates missing chemical bonds along their surface. In case I, where **d/D** < 1, as long as the particle is entirely wrapped, all positions inside the fiber are energetically equivalent in this treatment. Control over radial charge distributions has been postulated, which may introduce variance in energetic positions inside the fiber,(Kornev, 2011) however that is outside the scope of this work.

For case II when **d/D** > 1, the model for this energy balance becomes substantially more complex. However, equation 4.1 has been solved computationally by Raatz, Lipowsky, and Weikl without the constraints used at the limit of a small **d/D** (Raatz, Lipowsky, & Weikl, 2014). They show that the optimum location for a series of large spherical particles inside a thin, tensionless, cylindrical fluid is along the central axis of the fiber, and that the fluid will expand to wrap the particle in a thin coating before returning to its original diameter. The approximation of a tensionless fluid fiber is considered accurate due to the balance of electrostatic and viscoelastic forces during electrospinning bringing $\boldsymbol{\gamma_{FV,eff}}$ towards zero.

The experimental results from both case I and II appear to follow the expected theoretical results of a system reaching a minimum energy state with negligible fluid surface tension limit and favorable adhesive forces. When **d/D** was small, particles appeared to be entirely wrapped by the fiber from negligible availability of ZIF-8 at the surface to adsorb N_2. SEM images confirm the expected morphology for particles strung along a cylinder of negligible surface tension where the large particles appear coated in a film, and negligible adsorption is observed. A cartoon of the calculated minimum energy states for both the large **d/D** case and small **d/D** case is shown in **Figure 4.2.3.2** for the limit of a fluid of negligible surface energy. For the small **d/D** case the results come from equation 4.6, and for the case of large **d/D** we produce an illustration of the

results found computationally by Raatz and coworkers solving equation 4.1 computationally.(Raatz et al., 2014)

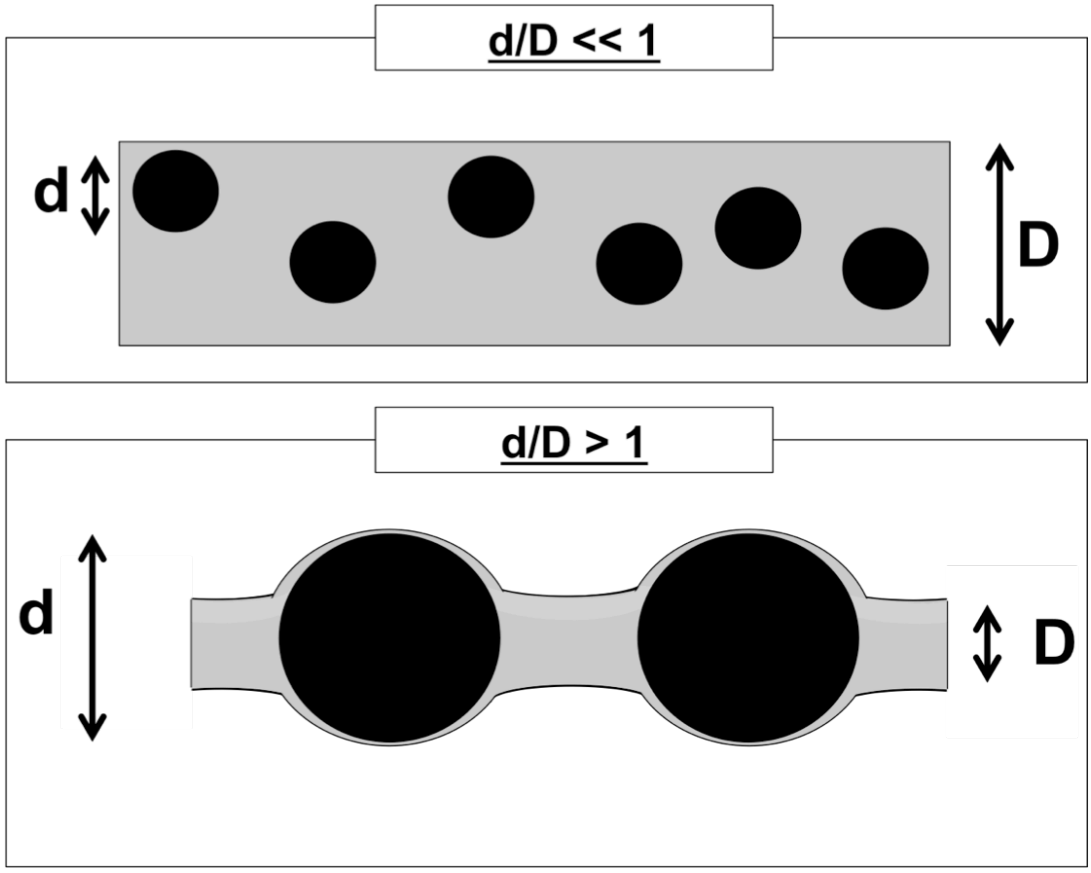

Figure 4.2.3.2. Cartoon depiciting the theoretical minimum energy state for both the case od d/D << 1 and d/D >1 in the limit of negligible surface tension in the fluid. The calculation for d/D>1 comes from work by Raatz and coworkers.(Raatz et al., 2014)

4.2.4 Influence of loading. Although nZIF-8 at 10% loading did not show signs of MOF exposure due to being imbedded inside the fibers since all particles had access to sites of lowest energy inside the fibers: a dilute particle case. It is expected that significant amounts of ZIF-8 should be exposed upon much higher loadings when these sites become unavailable. When packing spheres into a cubic system, it is readily calculated that for an ideal hexagonal close-packed system that the maximum loading volume is 74%. However, it has also been shown that the way in which the packing occurs may lower the actual loading volume (Torquato, Truskett, & Debenedetti, 2000), and a maximum packing for a randomly loose packed system is typically

around 56% (Jaeger & Nagel, 1992). In cubic systems, jamming theory also predicts spheres experience even lower volume fractions for weakly attractive colloidal particles due to kinetic trapping upon a fluid-to-solid transition that leads to a non-equilibrium packing density dependent on concentration, temperature, and stress (Trappe, Prasad, Cipelletti, Segre, & Weitz, 2001). A further limit applicable to our system is that maximum packing inside a cylinder only decreases even further when adopting an ideal FCC structure when **d/D** > 0.33 due to the relevance of edge effects (Mughal, Chan, Weaire, & Hutzler, 2012), which we may neglect it in the limit of small **d/D**.

Thus, dependent on the nature of how the particles are jammed together in our system, the volume necessary to facilitate the particles will change due to how efficiently the particles are packed. If the volume necessary to facilitate the particles exceeds the volume of polymer necessary to coat them, sites inside of the fiber that minimize the surface energy of the particles will no longer be available, necessitating the particles to sit along the surface of the fiber in the undesirable higher energy states. To investigate this phenomenon, ZIF-8 embedded fibers with low **d/D** were fabricated with varying ZIF-8 loadings (10%n, 25%n, 30%n, and 50%n). These fibers were analyzed with N_2 porosimetry at 77K to find exposed nZIF-8 at the surface in the same manner used previously, seen in Figure 4.2.4.1.

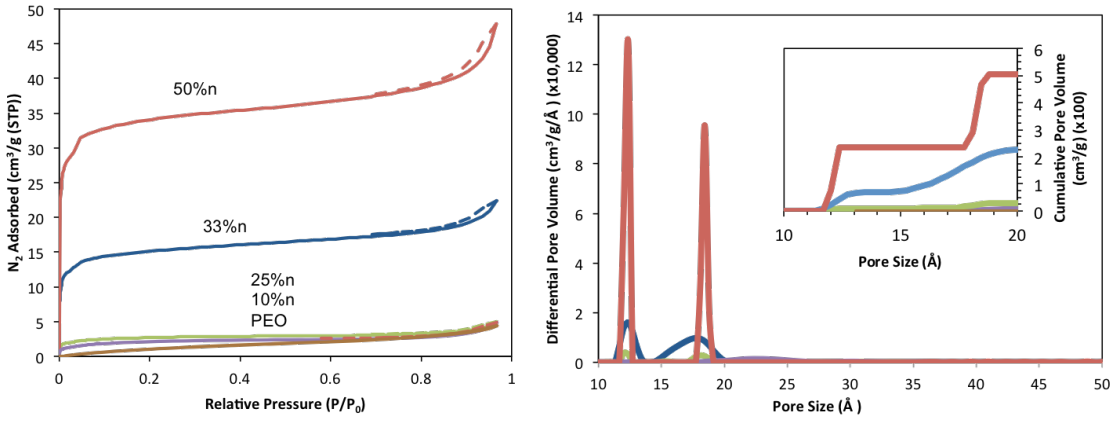

Figure 4.2.4.1. The left chart contains N_2 isotherms at 77K of composite fibers including PEO imbedded with nanosized ZIF-8 particles at loading ratio of 50% (red), 25% (blue), 33% (green), 25% (purple), and pure PEO fibers (brown). The right chart contains the pore size distributions generated from these isotherms, where the main figure contains the differential pore volumes and the inset image contains the cumulative pore volumes up to 20 Angstroms. These are in the same order from top to bottom as the isotherms.

These isotherms and corresponding pore size distributions show that nearly no extra nitrogen is taken up in the composite fibers with 10% or 25% loading of nanosized ZIF-8 particles relative to the pure PEO fibers. However, high loadings with 33% and 50% start to show significant rises in N_2 uptake, which is in agreement with SEM images in Figure 4.2.1.1 showing the emergence of nZIF-8 along the fiber surface. Also noteworthy is the shift of the second peak in the pore size distribution from 15 for the pure powder to ~18 Angstroms, which may be an artifact attributed to PEO attenuating the flexibility or condensation of N_2 to a slightly higher partial pressure.

Even though a significant amount of N_2 is adsorbed for n33% and n50% fibers, the ZIF-8 accessible is only 12% and 16%, respectively, when comparing the observed cumulative pore volume at 20 Å to the expected values if all nZIF-8 was available. Since a significant number of particles are trapped at the surface for n33% fibers, which have a nZIF-8 volume fraction of 42%, it appears that the particles become kinetically trapped before reaching a random close packed equilibrium loading near 56%. Notable is the drastic increase in surface availability between the n25% and n33% fibers (with an increase of 10%). This suggests that a threshold is passed between these values in which the increased loading significantly affects the ability for the particles to find minimum energy states- a transition between a dilute and saturated loading regime. By observing SEM images in Figure 4.2.1.1 this becomes obvious due to preferential clumping of nZIF-8 particles in some areas of fiber and smooth areas in others. The n50% fibers, with a volume fraction of 63%, which rests in between ideal random close packing and ideal FCC packing, have far more uniform clumps of nZIF-8 particles along the fibers relative to n33% out of necessity to put the particles somewhere, and provide even more nZIF-8 at the surface.

4.3 Conclusion

In this chapter we proposed a model to describe the wrapping of nanoparticles by electrospun fibers that predicts the formation of particle-embedded fibers during the electrospinning process if the surface energy of the particle is higher than that of the polymeric fluid. This is experimentally

validated for low loadings of both small and large particles, a regime we name the dilute regime. At higher loadings a combination of particles are found at the surface and embedded in the fiber, which deviates from the simple analytical model. This deviation is expected to be due to either kinetic forces or more complex thermodynamic relationships. At the conclusion of this chapter we have determined that particle-embedded fibers may be expected for smaller loadings, and that more sophisticated tool or control must be used to fabricate particle-coated fibers or particle-embedded fibers at higher loadings.

CHAPTER 5.

A MODEL FOR GAS UPTAKE IN MOF-EMBEDDED ELECTROSPUN FIBERS FOR ESTABLISHING PREDICTIVE DESIGN CRITERIA

5.1 Introduction

In Chapter 4 the idea that particles were nearly all embedded in fibers over the dilute loading regime was presented. Techniques for creating core-shell MOF particles through a variety of means has been a highly sought-after in recent years to either provide increased selectivity or stability. Strategies to increase selectivity and/or attenuate water uptake by forming a protective shell on the external surfaces of a MOF core are emerging, and a survey of these techniques is given in Table 5.1.1. These studies show that widespread implementation of MOF sorbents in a core-shell orientation containing a highly selective nano-dimensional shell surrounding a MOF core may be feasible if this barrier is able to provide enhanced protection and increased selectivity through either a molecular sieving or solution-diffusion bottlenecking mechanism, yet allow desirable molecules to pass through the barrier over acceptable timescales.

When designing core-shell sorbents, the shell must be thin enough to allow the desirable sorbate to reach the core in a reasonable time. Even micrometer thick polymer shells have been shown to slow sorption kinetics enough to effectively block nearly all adsorption in some cases.(Carné-Sánchez et al., 2015) Along with those mentioned previously, another enabling technology for reproducibly creating nanometer scale polymer coatings over MOFs is electrospinning.(M. Armstrong, Balzer, Shan, & Mu, 2017a)

Table 5.1.1.
Survey of core-shell MOF composites in literature

Method	Shell*	MOF core	Comments
Solvothermal Secondary Growth	bio-MOF-14	bio-MOF-11	Selectivity/ capacity properties greater than either individual MOF for CO_2/N_2 adsorption, some water protection(T. Li, Sullivan, & Rosi, 2013)
Epitaxial Secondary Growth	$Zn(ADC)_2$	$Zn(BDC)_2$	Selectivity/ capacity properties greater than either individual MOF for cetane / isocetane liquid separation(Hirai et al., 2011)
Spray Drying Microspheres	PS	HKUST-1	Tradeoff between water protection and accessibility based on loading/ thickness(Carné-Sánchez et al., 2015)
Bath Sonication	organosilicone	ZIF-67 HKUST-1 NH_2-MIL-125	Coating method that increases water resistance that may be applied to many MOFs(Qian et al., 2017)
Silicone Vapor Deposition	PDMS	MOF-5 ZnBT HKUST-1	Water protection observed, both surface area and crystallinity of MOF was preserved after coating.(W. Zhang, Hu, Ge, Jiang, & Yu, 2014)
Polymer Coating	silica	ZrMOF	Water protection observed in a process too intense for most MOFs(Demin Liu, Huxford, & Lin, 2011)
Shell Ligand-Exchange	DMBIM	ZIF-8	Ligands on outer layers of the MOF are exchanged to form a shell, promoting water resistance(X. Liu et al., 2013)
Heat-treatment	Carbon-coating	MOF-5	Enhanced moisture resistance(S. J. Yang & Park, 2012)
Electrospinning	PAN	HKUST-1	Up to 80% loading and full accessibility by N_2 at 77 K(Rose, Böhringer, Jolly, Fischer, & Kaskel, 2011)
Electrospinning	PVP	ZIF-8	MOF inside fibers and full accessibility by N_2 at 77 K(Ostermann et al., 2011)
Electrospinning	PEO	ZIF-8	Embedded MOFs are covered and negligable N_2 uptake in MOF observed in dilute loading regime at 77 K(M. Armstrong, Balzer, Shan, & Mu, 2017a)

*abbreviations are used for polymers and ligands: PS = polystyrene, PVA = poly(vinyl alcohol), PDMS = polydimethylsiloxane, PAN = poly(acrylonitrile), PVP = poly(vinylpyrridine), DMBIM = dimethylbenzeimmidazole, PEO = poly(ethylene oxide)

Coating MOFs with electrospun polymer barriers allows selectivity and stability requirements for the sorbent composite to be decoupled from the MOF design, enabling a rational design process for meeting industrial requirements. The idea of creating adsorbents that separate gases based on kinetic selectivity rather than thermodynamic selectivity is not new; using selectivity in zeolites based on molecular sieving has been studied for some time.(Ruthven & Reyes, 2007) However, introducing the solution-diffusion mechanism over sorbent crystals is still relatively new and not well understood. Previous works have alluded to this mechanism, or mentioned its presence for both enhancing selectivity,(Ostermann et al., 2011) and hydrostability (Carné-Sánchez et al., 2015). To date, work has been based on proof-of-concept without a strong theoretical basis for material selection, a design criterion for selecting polymers to coat MOFs has not been determined, and the transport through these layers has not been studied.

In this chapter a model for the kinetics of adsorption on a core-shell composite is presented, the implications of this model on the kinetic selectivity between gases is presented, and case studies demonstrating that an excess selectivity is realized on these composites.

5.2. Models and Theory

5.2.1 Sorption thermodynamics. When sorption occurs such that the sorbent uptake quantity (***Q***) is sufficiently proportional to the pressure (***p***) or concentration (***C***), a linear isotherm may be used to represent the data given by:

$$Q = Sp \tag{5.1}$$

where ***S*** is the Henry's constant. The uptake of a composite may be modeled as a function of the mass fraction ($\boldsymbol{m_i}$) of each component if interfacial properties such as gaps or blockage are negligible:

$$Q = m_1 S_1 p + m_2 S_2 p \tag{5.2}$$

The selectivity of a preferred sorbate **a** over a non-preferential sorbate **b** ($\alpha_{a/b}$) may also be found when comparing single-component isotherms of different gases at the same temperature. This is commonly performed using the ideal adsorbed solution theory (IAST), which, when all components may be described by a linear isotherm, reduces to:(Walton & Sholl, 2015)

$$\alpha_{a,b} = \frac{S_a}{S_b} \tag{5.3}$$

This is the selectivity when the system is allowed to reach thermodynamic equilibrium.

5.2.2. Kinetics with finite element model (FEM). Fick's Laws of diffusion are commonly used to describe sorption kinetics,(John Crank, 1975) and may be expressed as:

$$J = -D\nabla C \tag{5.5}$$

$$\frac{\delta C}{\delta t} = -\nabla \mathrm{J} \tag{5.6}$$

respectively, where ***J*** is the flux, ***C*** is the concentration and ***D*** is the diffusivity of the gas inside the sorbent. For a 2D core-shell system in which a shell of length L_S leads to a core of length L_C (Figure 5.2.2.1),

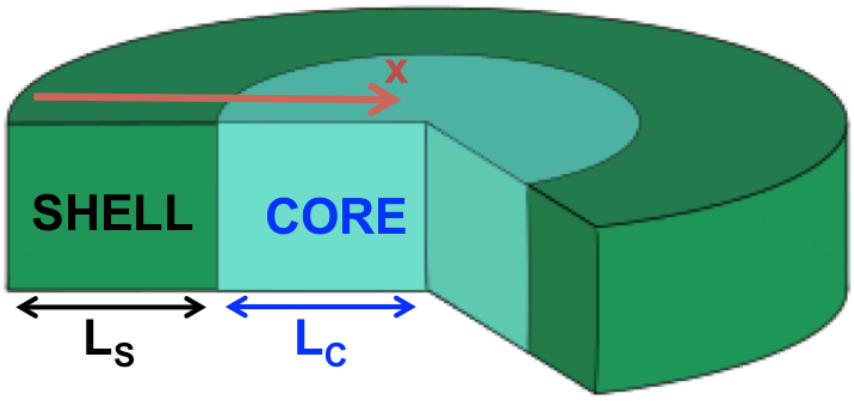

Figure 5.2.2.1. 2-D geometry considered in the COMSOL FEM method where the green represents the shell of length L_S, and the blue represents a core of length L_C along the x-axis.

the following boundary equations may be applied.

$C = S_S C_0$ $x = 0, t > 0$ (5.7a)

$C = 0$ $x > 0, t = 0$ (5.7b)

$\frac{\delta C}{\delta t} = D_S \frac{\delta^2 c}{\delta x^2}$ $0 < x < L_S$ (5.7c)

$\frac{\delta C}{\delta t} = D_C \frac{\delta^2 c}{\delta x^2}$ $x > L_S$ (5.7d)

$J = 0$ $x = L_S + L_C$ (5.7e)

$\mu_S = \mu_C$ $x = L_S$ (5.7f)

$D_S \frac{\delta C}{\delta x}\Big|_{L_S^-} = D_C \frac{\delta C}{\delta x}\Big|_{L_S^+}$ (5.7g)

where the last two terms express the continuity across the core-shell interface. $\boldsymbol{\mu_S}$ and $\boldsymbol{\mu_C}$ correspond to the chemical potential of the sorbent in either phase and the final boundary condition bounds the continuity of flow through the interface.(Jost, 1952) $\mathbf{S_S}$ refers to the Henry's constant of the shell, which is also commonly expressed as the solubility of the shell. Crank,(John Crank, 1975) Barrer,(Barrer, 1968) Jost,(Jost, 1952) and Carslaw(Carslaw & Jaeger, 1959) provide sets of particular solutions to some of these cases (described as laminates, heterogeneous sorbents, or dual-phase sorbents) with different sets of particular approximations. However, these solutions tend to become unwieldy and require iterative methods to solve, reducing their usefulness in developing predictive design criteria. For this reason, a finite-element-method is initially used to solve these equations in full to demonstrate the impact of important variables.

The total uptake at a particular time is found by solving EQ 6 at a particular $\boldsymbol{x}$ and integrating over time. A finite-element-method was used to solve and illustrate the uptake of the

core, the shell, and total sorbent uptake as a function of time in COMSOL, the conditions tested are given in Table 5.2.2.1 for each run.

Table 5.2.2.1.

COMSOL Finite-element-method trials performed in this chapter.

Trial	D_S (m^2/s)	D_C (m^2/s)	L_S (nm)	L_C (nm)
1	10^{-16}	10^{-10}	100	100
2	10^{-16}	10^{-15}	100	100
3	10^{-16}	10^{-16}	100	100
4	10^{-16}	10^{-17}	100	100
5	10^{-15}	10^{-10}	100	100
6	10^{-17}	10^{-10}	100	100
7	10^{-18}	10^{-10}	100	100
8	10^{-16}	10^{-10}	200	100
9	10^{-16}	10^{-10}	500	100
10	10^{-16}	10^{-10}	1000	100
11	10^{-16}	10^{-10}	100	400
12	10^{-16}	10^{-10}	100	600
13	10^{-16}	10^{-10}	100	1000
14	10^{-16}, 10^{-17}	10^{-10}	1	5000
15	10^{-16}, 10^{-17}	10^{-10}	5	5000
16	10^{-16}, 10^{-17}	10^{-10}	10	5000
17	10^{-16}, 10^{-17}	10^{-10}	50	5000
18	10^{-16}, 10^{-17}	10^{-10}	100	5000
19	10^{-16}, 10^{-17}	10^{-10}	500	5000
20	10^{-16}, 10^{-17}	10^{-10}	1000	5000

A representative example of these uptake curves from trial 1 is shown in Figure 5.2.2.2.

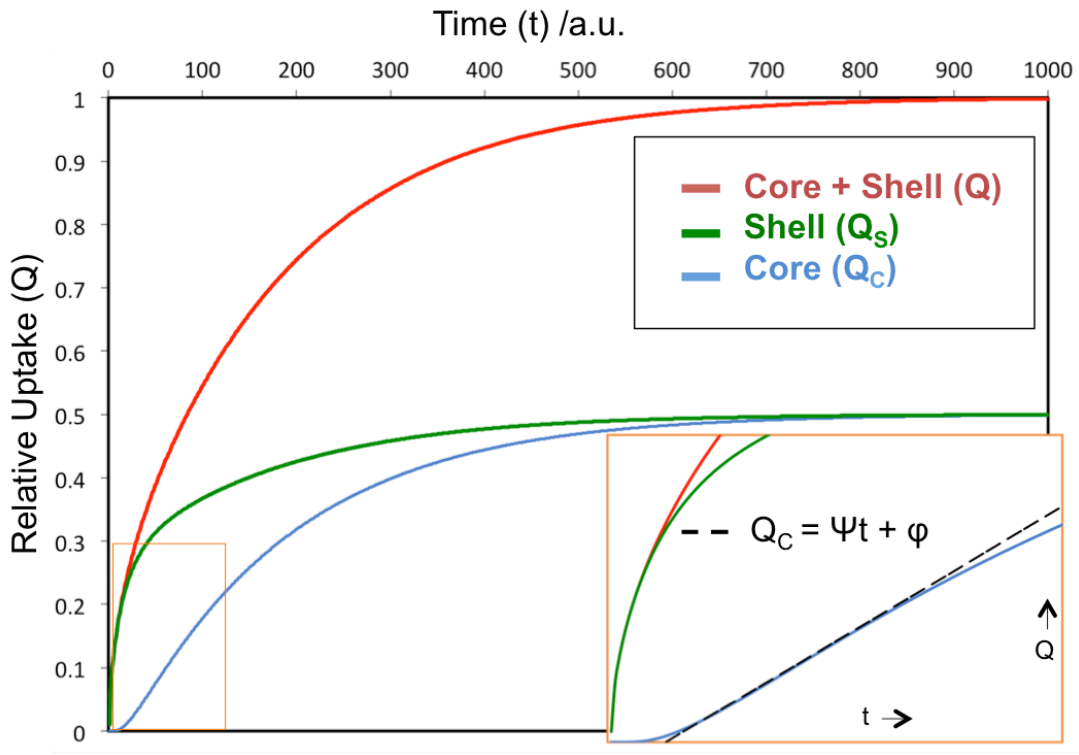

Figure 5.2.2.2. Example of uptake in a core-shell sorbent generated in COMSOL using Trial 1, where the red curve depicts the total uptake in the sorbent, the green curve represents uptake exclusively in the shell, and the blue curve represents uptake exclusively in the core. The inset image is a zoomed-in region bounded by the orange rectangle, and the black dashed line is an extrapolation of the linear uptake region in the core.

Three different regimes are observed in a dual phase core-shell sorbent: (i) exclusive shell uptake, (ii) linear core uptake, and (iii) asymptotic core uptake. There is an initial phase in which all of the uptake occurs in the shell, which may be defined as the lag-time ending at time $\boldsymbol{\varphi}$. This is followed by a phase where uptake in the core ($\boldsymbol{Q_c}$) may be approximated by a linear rate $\boldsymbol{\psi}$:

$$Q_C = \psi t + \varphi \tag{5.8}$$

Following the linear uptake in the core is a non-linear uptake region in which a maximum uptake is approached. The effects of changing $\boldsymbol{L_C}$, $\boldsymbol{L_S}$, $\boldsymbol{D_C}$, and $\boldsymbol{D_S}$ on these uptake regimes are shown in Figure 5.2.2.3.

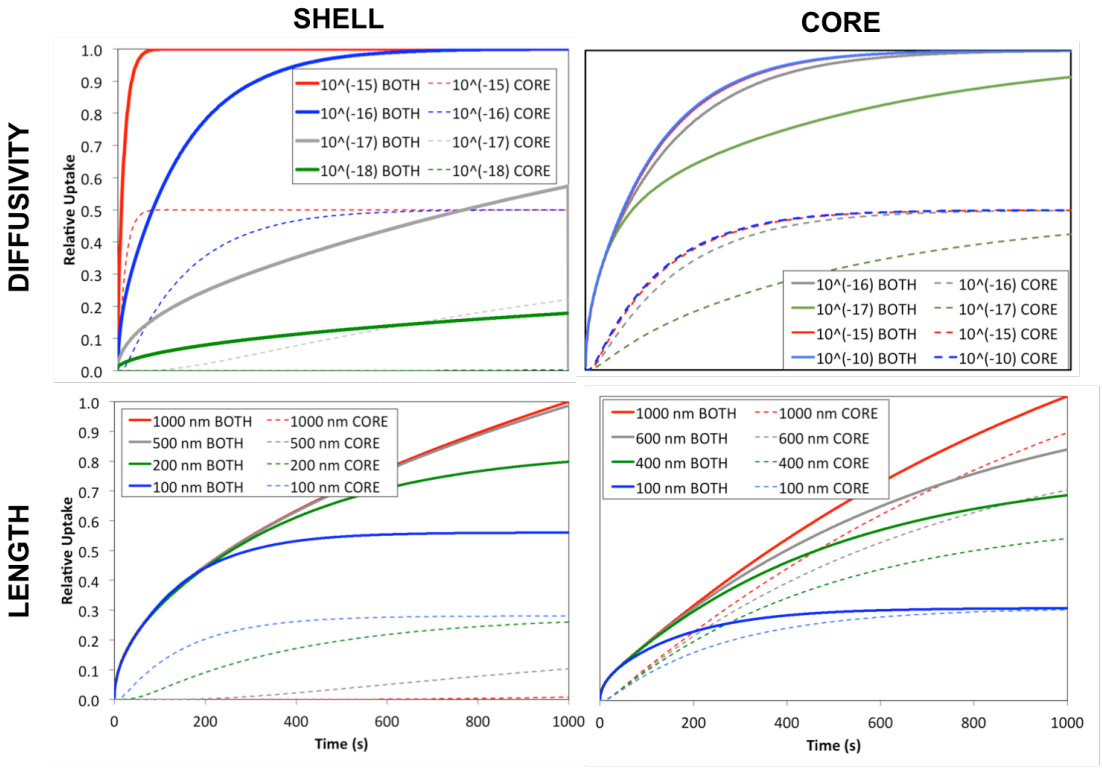

Figure 5.2.2.3. COMSOL kinetic uptake simulations in core-shell adsorbents at a variety of conditions for both the entire adsorbent (BOTH) and just in the core (CORE). Changes in the diffusivity of the shell include trials 1-4 from Table 5.2.2.1. Changes in the diffusivity of the core include trials 1 and 5-7 from Table 5.2.2.1. Changes in the length of the shell include trials 1 and 8-10 from Table 5.2.2.1. Changes in the length of the core include trials 1 and 11-13 from Table 5.2.2.1.

D_C has negligible influence as long as it is an order of magnitude larger than D_S. L_C primarily influences the length of linear uptake. Extending L_S or decreasing D_S increases both φ and linear uptake time while decreasing ψ.

By manipulating the contribution of the shell uptake and core uptake along with influences of the uptake phase, the selectivity may be manipulated. Selectivity was found by plotting the ratio of Q at different diffusivities as a function of time for two different L_S and L_C values (Figure 5.2.2.3).

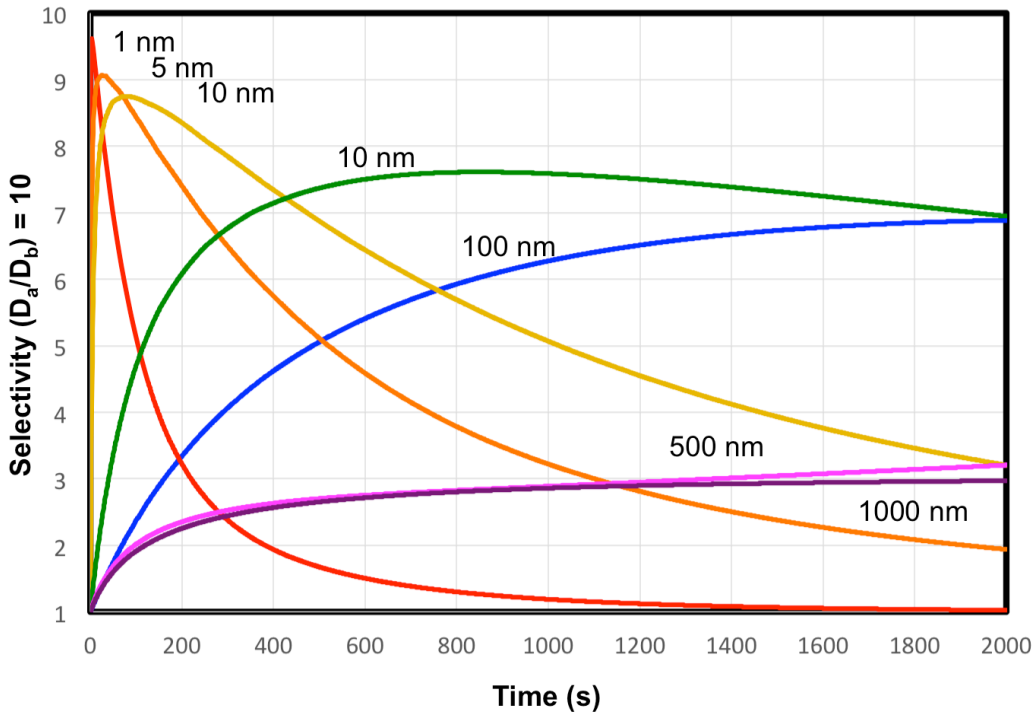

Figure 5.2.2.3. Selectivity as a function of time calculated in COMSOL for two gases with a D/D ratio of 10 in the shell. This data comes from trials 14-20 from Table 5.2.2.1. Each curve represents a different shell length (L_S = 1 (red), 5(orange), 10 (yellow), 50 (green), 100 (blue), 500 (indigo), 1000 (violet). The diffusivity of gas a in the shell ($\mathbf{D_{S,a}}$) is $1x10^{-16}$ cm^2/s and the diffusivity of gas b in the shell ($\mathbf{D_{S,b}}$) is $1x10^{-17}$. All other values are held constant for each test: L_{CORE}=5000 nm, C_0=1 mol/m^3, D_C =$1x10^{-10}$ cm^2/s.

Three selectivity limits may be seen from these plots, with one corresponding to a dominance of each different uptake phase. When the shell has the same uptake capacity as the core, diffusion into the shell dominates selectivity. This selectivity has the limit of a single-phase sorbent kinetic separation, which has an expected selectivity of:(Ruthven & Reyes, 2007)

$$\alpha_{a,b} = \frac{S_a}{S_b}\sqrt{\frac{D_a}{D_b}} \tag{5.9}$$

When the shell becomes negligibly small, the steady-state uptake by the core reservoir dominates the selectivity, where the **ψ** dictates the uptake rate, and selectivity approaches the ratio of these two slopes (called permeation selectivity):

$$\alpha_{a,b} = \frac{\gamma_a}{\gamma_b} = \frac{D_a}{D_b}\frac{S_a}{S_b} \tag{5.10}$$

When long times are observed and the final uptake phase dominates, the selectivity approaches thermodynamic selectivity (equation 5.4).

5.2.3 Kinetics with analytical solution. From the previous FEM simulations, we see that if $\mathbf{D_C/D_S}$ >10, that $\mathbf{D_C}$ has a negligible effect on the uptake because the sorbing gas is able to approach an equilibrium value in the core much faster than it is able to pass into the core from the shell (Figure 5.2.2.3): allowing us to consider a boundary condition in which the core is considered to be well-mixed at all times by dropping equation 5.7(d-f) and replacing them with the equation:

$$D\frac{\delta C}{\delta x} + \frac{L_S}{\eta}\frac{\delta C}{\delta t} = 0 \tag{5.11}$$

Since the motivation behind this work is to use the shell as a selective layer and the core as a reservoir, selecting a core material with much faster diffusivities than the shell may be expected. Therefore, if we are able to neglect the diffusivity in the core, we may instead model the core as a reservoir of capacity $\mathbf{Q_c}$ that maintains equal concentration throughout, allowing for an analytical solution that parallels work by Paul and DiBenedetto,(Paul & DiBenedetto, 1965) by using a sorbent instead of a reservoir and a more generalized integration. The full analytical solutions are provided in the supplementary information, and the important results are presented here.

The uptake of the composite may is given as:

$$Q = ApS_S L_S\left[1 - \frac{x}{L_S} + \frac{1}{\eta} - \sum_n \frac{2(\beta_n^2+\eta^2)\cos(\beta_n\frac{x}{L_S})}{\beta_n^2(\beta_n^2+\eta^2+\eta)} e^{\frac{-D_S\beta_n^2 t}{L_S^2}}\right] \tag{5.12}$$

Where **A** is the surface area of the shell, the $\boldsymbol{\beta_n}$ values represent the non-negative roots of the equation βtan(β)=η and

$$\eta = \frac{S_S}{S_C}\frac{AL_S}{V_C} = \frac{Q_{\infty,S}}{Q_{\infty,C}} \tag{5.13}$$

where $\mathbf{Q_{\infty,S}}$ is the maximum capacity of the shell and $\mathbf{Q_{\infty,C}}$ is the maximum capacity of the core. The total uptake, **Q**, is calculated when setting x=0, resulting in the cosine expression in equation 5.12 going to one. The uptake in the core ($\mathbf{Q_c}$) is solved for by setting $x=L_S$. A model exclusively for $\mathbf{Q_c}$ is important for defining the uptake regimes (i-iii), which subsequently allows the definition of design criteria for stability and selectivity.

The lag phase (**φ**) separating uptake phase (i) from phase (ii) may be approximated as:(Barrer, 1968)

$$\varphi = \frac{L_S^2}{6D_S} \tag{5.14}$$

The lag-phase is important in balancing core stability and selectivity. If the sorption cycle time is less than **φ**, the core should be protected from that component in the fluid stream. However, if this lag-phase is too large, desirable sorbates may not penetrate into the core as easily either, and productivity may be reduced.

After the lag phase the summation term in equation 5.12 will become negligible, and **ψ** from EQ 8 is expressed as:(Paul & DiBenedetto, 1965)

$$\Psi = \frac{ApS_SD_S}{L_S}\left[\frac{2(\beta_0^2+\eta^2)\cos(\beta_0)}{(\beta_0^2+\eta^2+\eta)}e^{\frac{-D_S\beta_0^2t}{L_S^2}}\right] = \frac{ApS_SL_S}{6\varphi}\left[\frac{2(\beta_0^2+\eta^2)\cos(\beta_0)}{(\beta_0^2+\eta^2+\eta)}e^{\frac{-\beta_0^2t}{6\varphi}}\right] \tag{5.15}$$

Where $\boldsymbol{\beta_0}$ is the first non-negative root of βtanβ=η. This term is linear when the term in the exponential is near zero, and we may define uptake region (ii) to occur after **φ** and before this exponential term influences **Ψ**. As an approximation it may be assumed that the function e^{-x} is linear until the exponential term x surpasses a value of 0.25 (however this term may be adjusted for desired tolerance). We may then define region (ii) as occurring from:

$$\varphi < t_{Linear\ Uptake\ (ii)} < \frac{6\varphi}{4\beta_0^2} \tag{5.16}$$

This criteria allows for the design of a sorbent for the time regimes: When undesirable sorbents are in phase (i) protection occurs, when both sorbents are in phase (ii) maximum relative selectivity occurs, and when a desirable sorbent is in phase (iii) maximum relative uptake occurs.

5.3 Conclusion

In sum, this simulation study and analytical model demonstrates that two major uptake advantages of using this dual-sorbent scheme with electrospun fibers may be expected. That (a) the thin fiber interface covering the MOF particles enabled by electrospinning may be used to increase kinetic selectivity. (b) That the kinetic bottle-necking of the polymer layer both dictates the time until a fluid reaches the sorbent through the characteristic lag-time and rate in which the sorbent fills. Increasing the lag-time before uptake by the particle is of particular importance if the polymer layer is being designed to block fluids from the core that will poison the sorbent such as water or sour gas over the time-scale of an absorption cycle; enhanced protection and sorbent lifetime may be expected.

CHAPTER 6.

MOF-EMBEDDED FIBER CASE STUDY I: EVIDENCE OF ENHANCED KINETIC CO_2/N_2 SELECTIVITY

6.1 Introduction

In this chapter, we aim to experimentally confirm that thin polymer layers are indeed wrapping particles embedded in these electrospun fibers with nano-scale coatings, and that enhanced selectivity may be observed relative to either the core or shell components individually as predicted by our previous first-principle derivations. To conduct this proof-of-concept test, we selected separation of carbon dioxide from nitrogen as the application; a separation that is highly desirable for the application of post-combustion carbon capture as well as direct air capture. Along with these applications, carbon dioxide and nitrogen are easy probe molecules to test experimentally.

Post-combustion carbon capture is an example of an application that promising and affordable MOFs are not stable enough to make an impact. For a sorbent to be used for post-combustion carbon capture, it must exhibit strong water stability, high CO_2 uptake at 1 bar above 40 °C and reasonably reject N_2 sorption to minimize the energy penalty of regeneration.(Drage et al., 2012) Although some MOFs demonstrate superior performance in CO_2 uptake, (including MgMOF-74 with a CO_2 capacity of 8.61 mmol/g)(Bao, Yu, Ren, Lu, & Deng, 2011) these same MOFs lack water stability and N_2 rejection.

In this section we fabricate ZIF-8 embedded fibers, explore their distribution inside of the fiber structure, and run preliminary tests that demonstrate the fibers have a higher selectivity at 3 minutes of adsorption time compared to either the pure ZIF-8 powder or pure fiber samples.

6.2 Materials Preparation

ZIF-8 was synthesized using Cravillon's method(Cravillon et al., 2011) as described previously. Two electrospinning suspensions were prepared. Each was composed of a 100 mg MAT and 100 mg PEO dissolved in 10 mL of dichloromethane. The first had 50 mg ZIF-8 suspended in solution (for a 20% ZIF-8 composite, called 1:1:0.5 MAT:PEO:ZIF-8 fibers), and the second had 200 mg ZIF-8 suspended in solution (for a 50% ZIF-8 composite, called 1:1:2 MAT:PEO:ZIF-8 fibers). Electrospun fibers were fabricated using an apparatus described previously.(M. R. Armstrong et al., 2015) 1:1:0.25 MAT:PEO:ZIF-8 and 1:1:2 MAT:PEO:ZIF-8 were prepared in a previous study by the same manner and more details and characterization are shown there.(M. R. Armstrong et al., 2016)

6.3 Results and Discussion

6.3.1. Materials. Images of the four materials tested in the adsorption tests are shown in Figure 6.3.1.1 including SEM images of ZIF-8 powder, pure 1:1 MAT:PEO fibers, and the composite 1:1:0.5 and 1:1:2 MAT:PEO:ZIF-8 fibers. TEM images of the composite fibers are also shown to demonstrate the internal morphology in Figure 6.3.1.2.

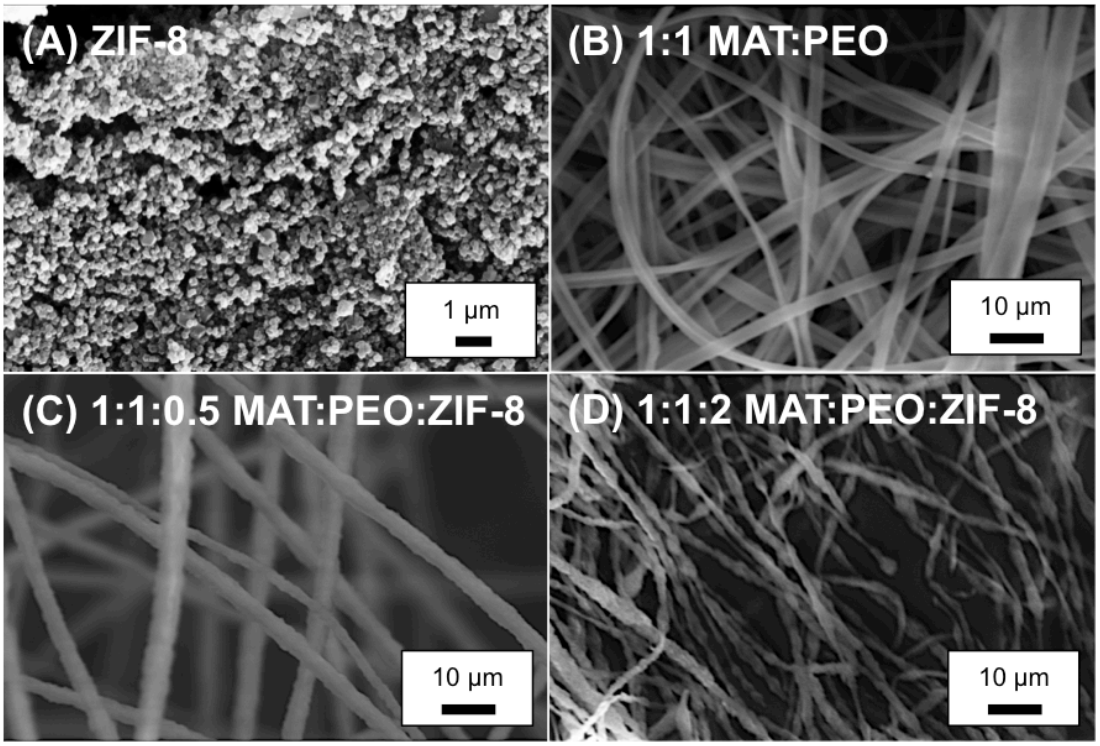

Figure 6.3.1.1. SEM image of (A) pure ZIF-8 powder, (B) 1:1 Matrimid:PEO, (C) 1:1:0.5 MAT:PEO:ZIF-8, and (D) 1:1:2 MAT:PEO:ZIF-8.

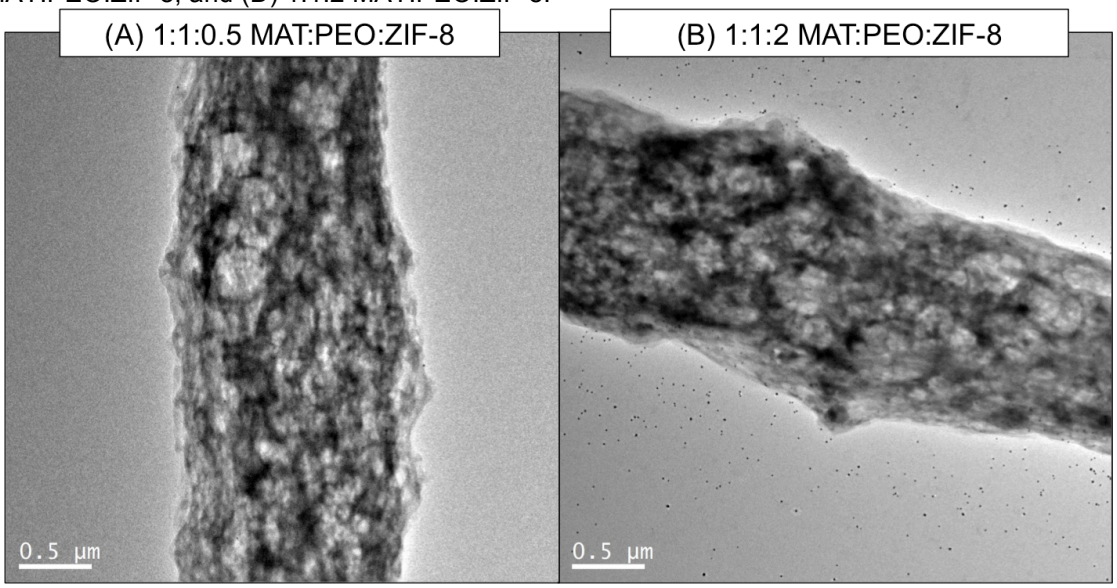

Figure 6.3.1.2. TEM image of (A) 1:1:0.5 MAT:PEO:ZIF-8 fibers and (B) 1:1:2 MAT:PEO:ZIF-8 fibers.

From these images it may be seen that the 1:1 MAT:PEO fibers and 1:1:0.5 MAT:PEO:ZIF-8 fibers are of similar diameters, but the 1:1:2 fibers are smaller. All fibers are

larger than the average 200 nm ZIF-8 particle size. ZIF-8 is seen embedded throughout the composite fibers in Figure 6.3.1.2, however, the 2D projection of these fibers does not accurately demonstrate how far from the surface these particles are. For this reason a tomogram was constructed over a segment of the 1:1:2 MAT:PEO:ZIF-8 fibers to understand how these particles load (Figure 6.3.1.3).

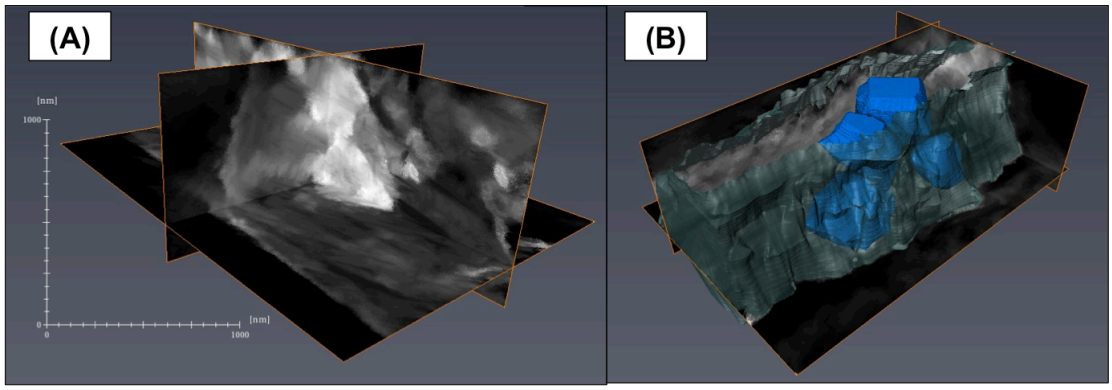

Figure 6.3.1.3. Tomogram and model constructed from series of HAADF TEM images of 1:1:0.5 MAT:PEO:ZIF-8 fibers over two tilt angles. (A) 3 representative slices of the tomogram in each plane where the bright areas represent ZIF-8 and the grey areas represent fiber. The scale bar spans 1000 nm along both the x and y-axis. (B) 3D reconstruction where representative ZIF-8 particles are modeled in blue and the fiber is represented with a transparent green.

Tomography was done along two perpendicular tilt axis each containing 89 images each from -55° to 55° spaced with the Saxton scheme. Tomograms were constructed and processed using IMOD software provided by the University of Colorado Boulder, and model was developed with FEI Avizo software from this tomogram using techniques from literature for nanoparticle reconstruction.(Ersen, Florea, & Hirlimann, 2015)

From the 3D TEM imaging we are able to measure the distance between the particle and the surface of the fiber where the polymer appears to extend out to wrap the particle. The thickness of the region between MOF and fiber surface is measured to reach minimums on the order of 10 nm.

6.3.2. Sorption isotherms and availability. In literature, multiple reports show isotherms of polymer coated MOFs in which isotherms demonstrate the expected shape with lower uptakes for

some gases when gases such as nitrogen diffuse through the polymer slower than the allowed equilibrium time.(Carné-Sánchez et al., 2015; Ostermann et al., 2011) The resulting isotherm demonstrate the selectivity based on a combined diffusivity and solubility factors as long as diffusivity is sufficiently independent of concentration and the sorption during dosing time does not exceed the uptake value of the next point. This method is used here. Isotherms were collected at 45 °C for each material with both CO_2 and N_2 up to 6 bar with a predefined maximum equilibrium time of 3 minutes. 3 minutes was chosen as the short equilibrium time since it falls within the typical optimum 100-200 seconds between vacuum swings during vacuum adsorption cycles as calculated by Susarla and coworkers.(Rajendran, Soon, Tan, Sue, & Lim, 2015) These isotherms are shown in Figure 6.3.2.1 along with their linear fit.

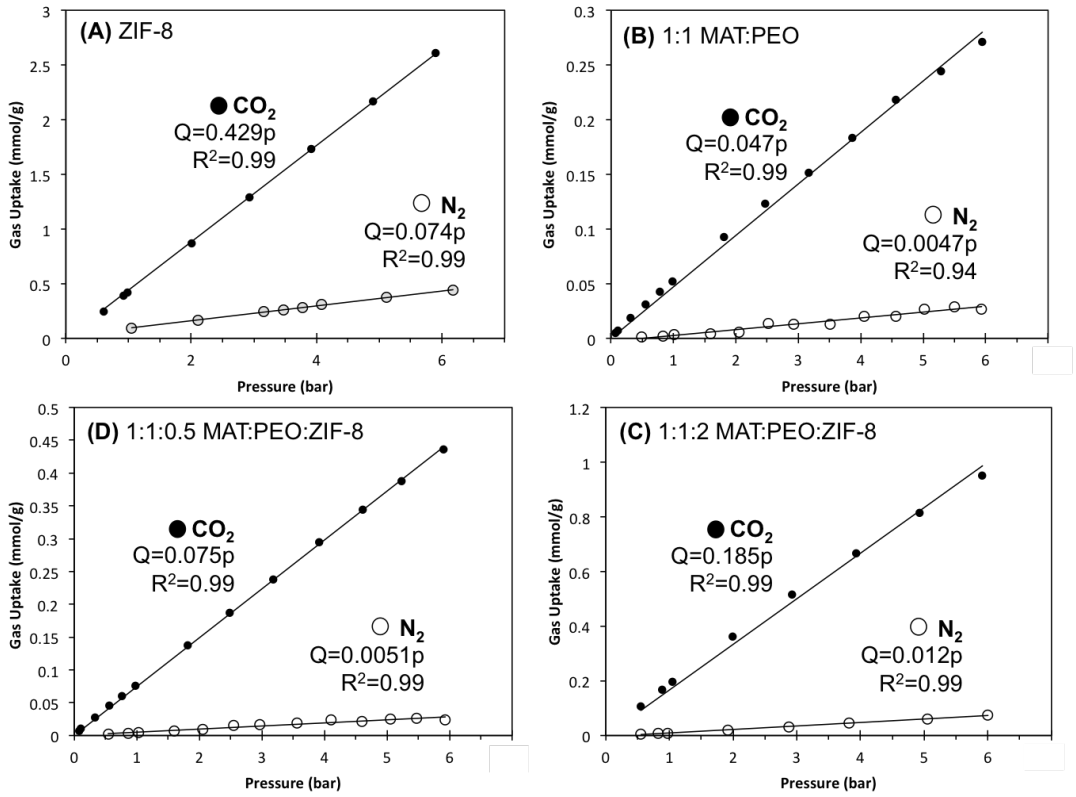

Figure 6.3.2.1. Kinetically suppressed isotherms for (A) ZIF-8, (B) 1:1 MAT:PEO fibers, (C) 1:1:2 MAT:PEO:ZIF-8 fibers and (D) 1:1:0.5 MAT:PEO:ZIF-8 fibers with a maximum of 3 minutes equilibrium time up to 6 bar pressure of either CO_2 or N_2.

In the range of pressures tested, each isotherm appears sufficiently straight and is fit to a linear isotherm (equation 5.1) with a strong correlation coefficient. The linear nature of the isotherms for pure ZIF-8 and the 1:1 MAT:PEO fibers are near those found in literature for CO_2 and N_2. ZIF-8 CO_2 isotherms are found to be linear until around 10 bar, where they begin to flatten due to pore filling, whereas N_2 isotherms appear linear up to at least 25 bar.(Z. Zhang et al., 2013) PEO appears to follow a linear isotherm up to 10 bar, where it begins to follow a convex path following a Flory-Huggins isotherm, whereas the nitrogen isotherm appears linear up to 20 bar.(Lin & Freeman, 2004) MAT isotherms have concave isotherms for both N_2 and CO_2 which have been fit to dual-site polymeric isotherms.(Scholes, Tao, Stevens, & Kentish, 2010) N_2 isotherms in MAT become non-linear at around 5 bar and CO_2 isotherms become non-linear around 2 bar.

The CO_2 uptake at 1 bar (calculated as **S**) for each material plotted against the $\alpha_{CO2/N2}$ in Figure 6.3.2.2.

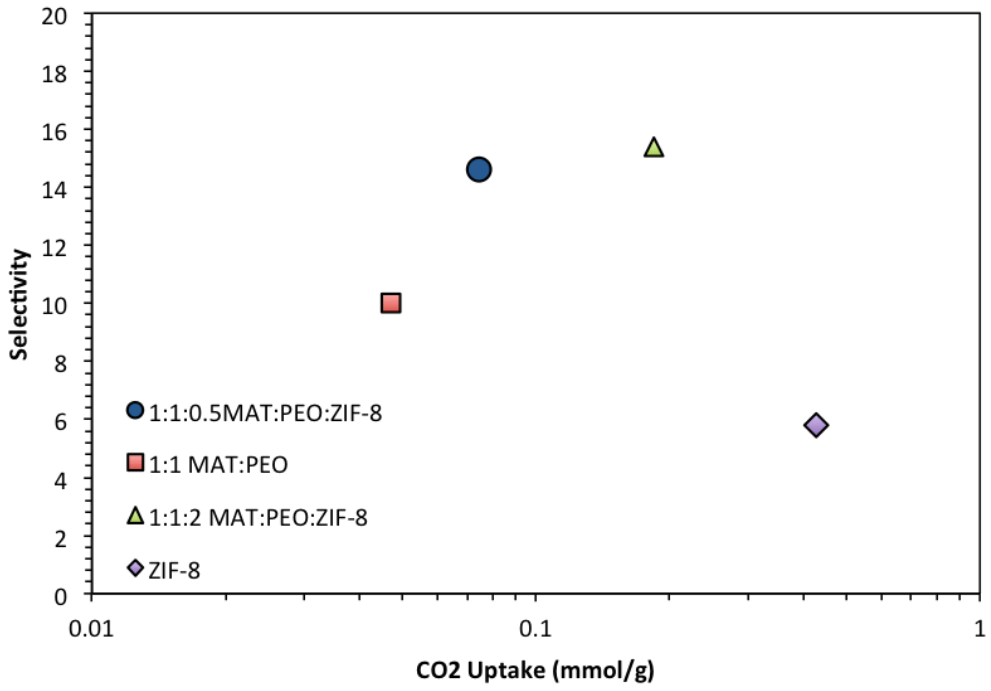

Figure 6.3.2.2. CO_2/N_2 selectivity plotted against CO_2 uptake for 1:1 MAT:PEO fibers (red square), 1:1:0.5 MAT:PEO:ZIF-8 fibers (blue circle), 1:1:2 MAT:PEO:ZIF-8 fibers (green triangle), and ZIF-8 (purple diamond).

The measured ZIF-8 selectivity at 3 minutes of equilibration match well with results for fully equilibrated isotherms in literature, where ZIF-8 experimental selectivity is between 5 and 6 and CO_2 uptake near 45°C and 1 bar is 0.45 mmol/g.(H. Huang et al., 2011) This is expected for ZIF-8 under 500 nm diameter at these conditions since, with diffusivities of 2×10^{-8} and 3×10^{-8} cm^2/s for CO_2 and N_2 respectively, uptake was found to be too rapid for experimental measurements with traditional techniques at 35°C,(C. Zhang et al., 2012) and may be expected to be even faster at 45°C.(John Crank, 1975) Also noteworthy is the fact that N_2 diffuses through ZIF-8 faster than CO_2, so any kinetic separations with pure ZIF-8 would result in a lower selectivity than the equilibrium state. Both pure CO_2 and N_2 isotherms for MAT and PEO isotherms found in literature are of the same order of magnitude as those found for the 1:1 MAT:PEO fibers,(Lin & Freeman, 2004; Scholes et al., 2010) suggesting that uptake is observed in both the MAT and PEO portions of the fibers, and nearly complete uptake is reached over the 3 min equilibrium time.

The MOF-embedded fibers both show an excess selectivity compared to either the pure MOF powder or the 1:1 MAT:PEO fibers. In both cases a larger percentage of the embedded ZIF-8 is used for CO_2 uptake at 3 minutes over N_2 (Figure 6.4.2.3); as predicted by the models presented in section 2. The ZIF-8 used in the 1:1:2 fibers is larger than in the 1:1:0.5 fibers for each gas. This is likely because those fibers have a smaller diameter and also may contain ZIF-8 to ZIF-8 passages inside the fiber as well- resulting in a statistically thinner polymer coating than in the 1:1:0.5 fibers.

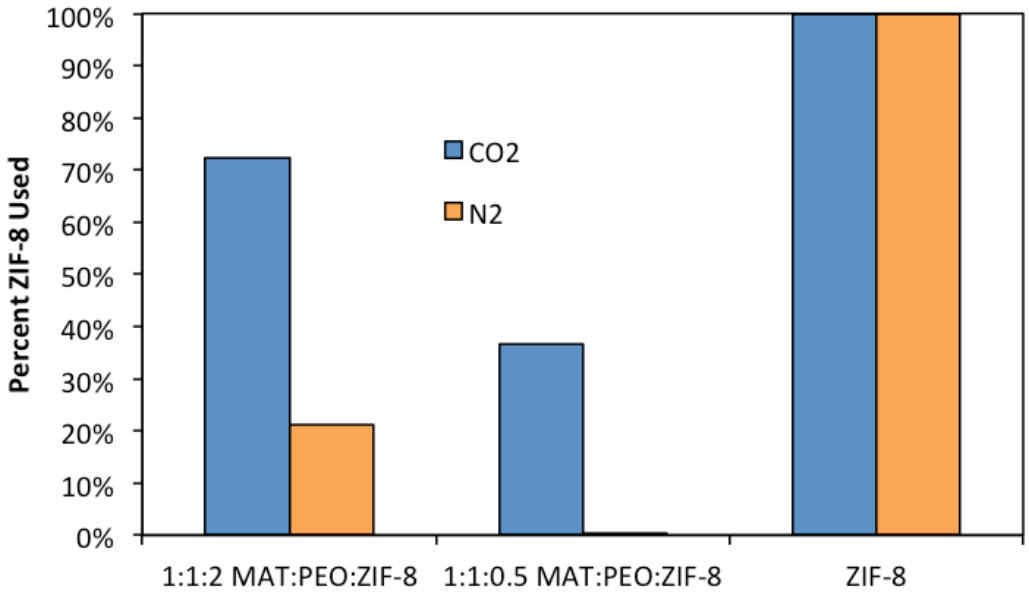

Figure 6.4.2.3. Histogram of approximate percentage ZIF-8 capacity used for CO_2 uptake (blue) and N_2 uptake (orange) for each ZIF-8 containing material studied over the three minute time-step sorption tests.

The percentage of ZIF-8 used was approximated by assuming nearly complete uptake in the polymer fiber, and dividing the resulting uptake by the full ZIF-8 uptake at the weight percent of ZIF-8 in the fibers.

6.4 Conclusion

A microscopy study showing that thin coatings over MOF materials may be made through the electrospinning process that may maximize the optimum selectivity regime, and adsorption studies were performed to demonstrate that selectivity/ uptake combinations unobtainable by either core or shell alone may be realized.

CHAPTER 7.

MOF-EMBEDDED FIBER CASE STUDY II: EVIDENCE OF HYDROTHERMAL MOF PROTECTION

7.1 Introduction

Incorporating open metal sites into metal-organic frameworks (MOFs) leads to elevated functionality in terms of uptake capacity. These open metal sites provide leading properties for hydrogen storage,(Suh, Park, Prasad, & Lim, 2011) carbon dioxide capture,(J. Liu, Thallapally, McGrail, Brown, & Liu, 2012) and methane storage(Peng et al., 2013) among porous materials. Even though MOFs with open metal sites (OMS), also called unsaturated metal sites (UMS), have flashed potential over a broad array of applications including gas storage and separation, they have yet to be used industrially.

Among other factors, the stability and cost of MOFs prohibit these materials from implementation in commercial applications.(Kumar, Vellingiri, Kim, Brown, & Manos, 2017) A link between these issues and the high functionality of MOFs are rooted in the coordination chemistry gluing MOFs together, a *functionality-stability-cost nexus*. This is because uncovering or strengthening open-metal binding sites that are also responsible for holding the framework together comes with a tradeoff in stability. These open sites catalyze a hydrolysis reaction that results in water entering the framework and breaking apart the metal-to-linker bonds.(Islas-jácome & González-zamora, 2017) This tradeoff has been well-documented for the removal of linkers in UiO-66 to uncover OMS,(Thornton, Babarao, Jain, Trousselet, & Coudert, 2016) metal-exchange to less-reactive species,(Jiao et al., 2015) partial blockage of open-metal sites,(H. Li et al., 2017) and the conclusion that increasing inertness of the metal-node increases hydrostability.(Qadir, Said, & Bahaidarah, 2015) Strategies to overcome this tradeoff by modifying the MOF structure include linker exchanges,(Jayachandrababu, Sholl, & Nair, 2017) complex ligand designs,(Y. Zhao et al., 2009) coatings,(Qian et al., 2017) and thermal treatment.(S. J. Yang & Park, 2012) Each of these strategies incorporates either multiple synthesis steps or

complex ligands that ultimately induce extra costs that appear to be too expensive for an industrial scale.

An alternate stage that may be exploited to address the functionality-stability-cost nexus is the shaping stage, where MOF powder is typically embedded in a highly permeable polymer substrate to form a process-ready material. Selecting a complementary polymer coating for the MOFs with OMS that attenuates water permeation could solve the stability issues of this class of MOFs, while allowing them to maintain their high functionality, while minimizing additional process expenses. To properly add both functionality and provide a process-ready composite, the shaping stage must result in a material that has both nano-scopic dimensions (mitigating resistance to gas uptake) while also properly supply macroscopic dimensions (to allow handling and implementation into a unit operation). In a previous work, we have demonstrated that electrospun fibers are able to handle both of these tasks.(M. Armstrong, Balzer, Shan, & Mu, 2017) Furthermore, work by Pimentel and coworkers demonstrated that MOF-containing fibers offer many benefits as a final shaped material including low pressure drop and high thermal heat transfer rates.(Lively, Leta, Derites, Chance, & Koros, 2011; Pimentel, Fultz, Presnell, & Lively, 2017)

In this work we demonstrate that MOF embedded electrospun fibers may be used to prevent hydroscopic degradation of MOFs with open metal sites. We use the MOF named HKUST-1 as a characteristic MOF with open-metal sites. HKUST-1 is well-documented to have high capacities for methane and carbon dioxide.(Peng et al., 2013) It is also known to undergo an irreversible hydrolysis reaction in the presence of humidity that degrades the framework over time.(Islas-jácome & González-zamora, 2017) The structure of this MOF is shown in Figure 7.1.1.

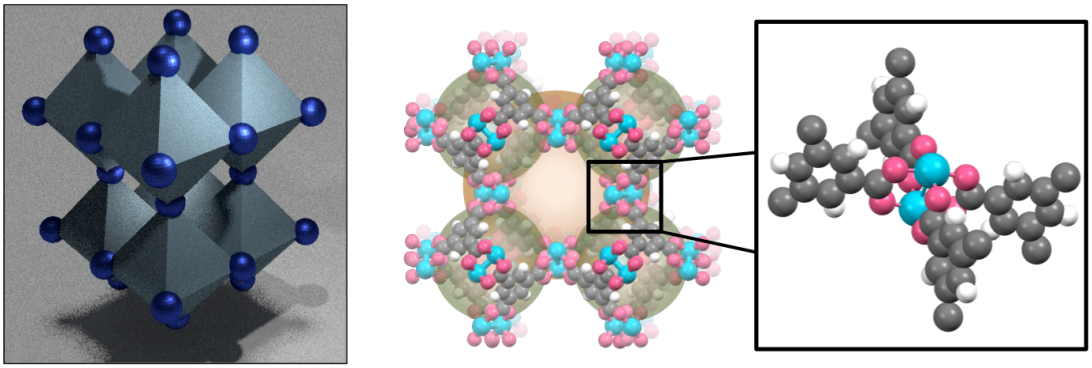

Figure 7.1.1. Geometric representation of HKUST-1 composed of pyramidal small-pore clusters and spherical metal clusters (left). Space filling model of HKUST-1 composed of carbon (grey), copper (blue), oxygen (red), and hydrogen (white) (middle). A segment of HKUST-1 demonstrating the paddle-wheel copper secondary building unit and coordinated trimesic acid ligands depicting two open-metal sites per metal cluster (right). The HKUST-1 crystal structure was provided by Mustafa and coworkers in the Cambridge Crystallographic Data Centre.(Mustafa, Breynaert, Bajpe, Martens, & Kirschhock, 2011)

HKUST-1 is embedded in polystyrene fibers near a 10% loading by mass for added hydrolytic protection. Polystyrene was selected because it has shown protective properties when coating HKUST-1 from water previously through a microcapusule technique.(Carné-Sánchez et al., 2015) A low loading was selected for this work to ensure that the MOF in the fibers was dilute enough to be entirely wrapped by polystyrene, since excessive loadings have shown to force MOF particles to the surface of fibers and into an unprotected state in previous work.(M. Armstrong, Balzer, Shan, et al., 2017)

From this work we see that when HKUST-1 is electrospun in polystyrene fibers that they are nearly all embedded inside the fiber, and that from SEM images the polymeric film covering the HKUST-1 particles is near 500 nm. Hydrothermal stability tests are performed on HKUST-1 powder and HKUST-1 embedded fibers showing that hydrolysis of HKUST-1 when embedded in fibers is much slower than the pure HKUST-1 powder alone.

7.2. Materials Preparation

HKUST-1 was synthesized via a sonochemical route we developed previously.(M. R. Armstrong, Senthilnathan, Balzer, et al., 2017) Three different fiber samples were made. Fine pure

polystyrene fibers were made from a solution of 2g PS in 10 mL DCM. Coarse pure PS fibers were made from a solution of 3g PS in 10 mL DCM. HKUST-1 embedded PS fibers were made from a solution of 2g PS with 200mg suspended HKUST-1 in 10 mL DCM. Each solution was spun in an electrospinning apparatus described previously,(M. R. Armstrong et al., 2015) at a working distance of 20 cm, a flow rate of 0.5 mL/min, and under a DC voltage of 15 kV. All samples were kept under vacuum at 100 °C overnight for activation. Digital images of the HKUST-1 powder and HKUST-1 embedded polystyrene fibers used in this study are shown in Figure 7.2.1.

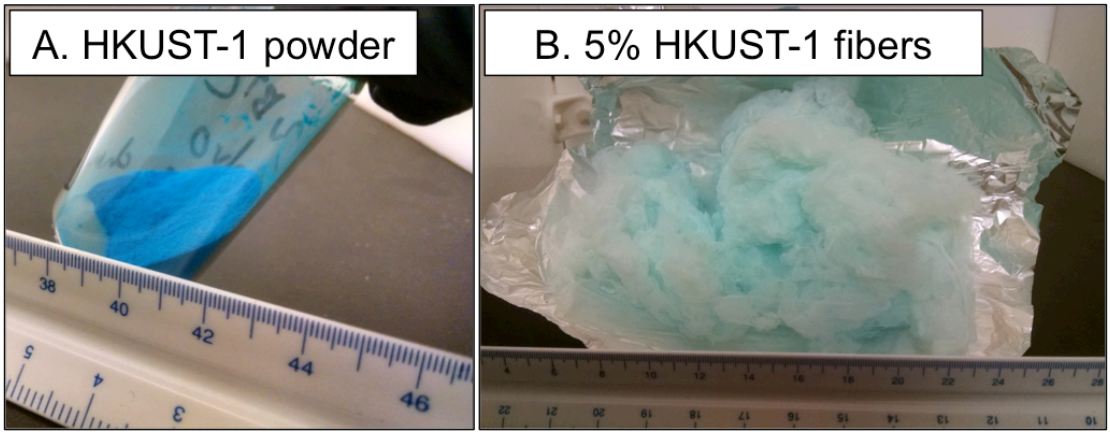

Figure 7.2.1. Images of (A) as-synthesized HKUST-1 powder and (B) HKUST-1 embedded polystyrene fibers.

7.3 Results and Discussion

Each of the synthesized samples are shown in Figure 7.3.1.

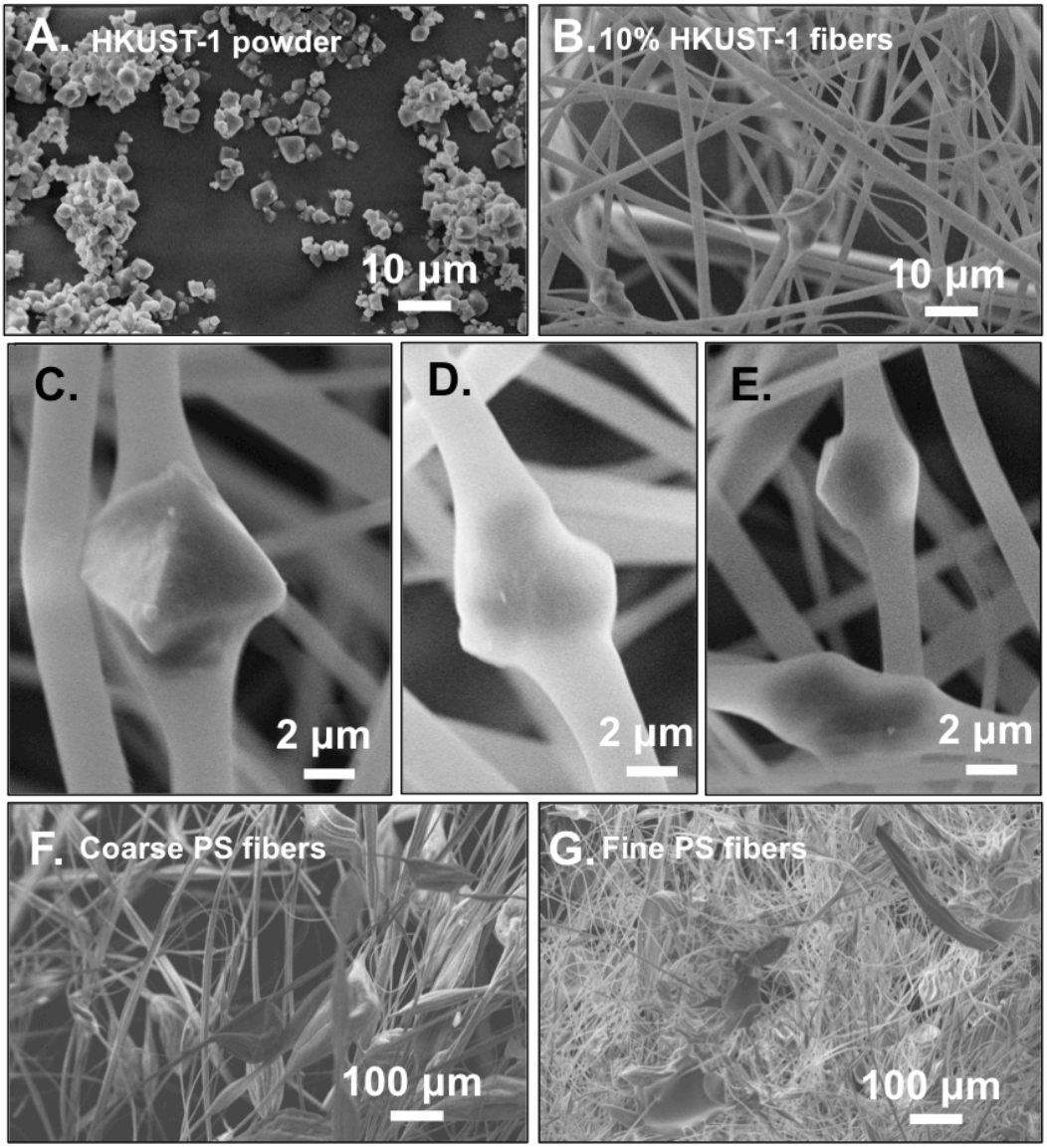

Figure 7.3.1. SEM images of (A) HKUST-1 powder, (B) HKUST-1 embedded polystyrene fibers, (C-E) higher magnifications of HKUST-1 embedded PS fibers, (F) coarse pure polystyrene fibers, and (G) fine pure polystyrene fibers.

The SEM images show that HKUST-1 has regular facets and an average crystal diameter of nearly 3 µm, which matches previous work.(M. R. Armstrong, Senthilnathan, Balzer, et al., 2017) The HKUST-1 embedded polystyrene fibers show that the fibers stretch to encapsulate the HKUST-1 fibers, which is in agreement with literature.(M. Armstrong, Balzer, Shan, et al., 2017) From Figure 7.3.1 (C-E) it may be observed that the coating over the particles is around 500 nm. The pure polystyrene fibers each have different diameters. The pure PS fibers in Figure 7.3.1 (F)

are called coarse fibers since they have a much larger average fiber diameter than the pure PS fibers in Figure 7.3.1 (G)- which are called fine PS fibers.

To confirm the loading of HKUST-1 in the polystyrene fibers thermal-gravimetric analysis (TGA) was run to confirm HKUST-1 loading in the fibers (Figure 7.3.2).

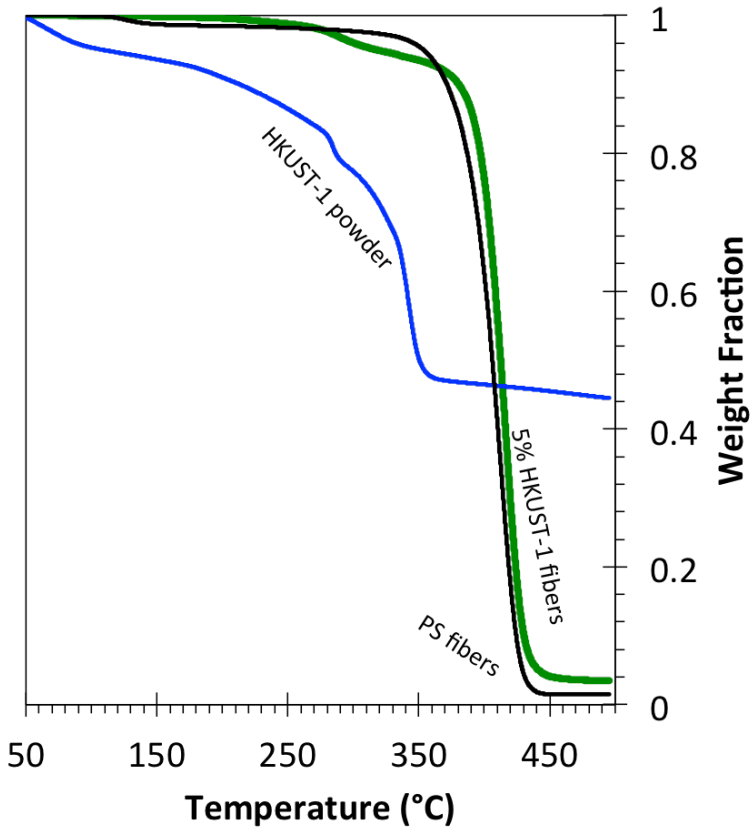

Figure 7.3.2. Thermal Gravimetric Analysis of HKUST-1 powder (blue), PS fibers (black), and 5% HKUST-1 fibers (green).

Polystyrene burns to 1.5 % of its original mass, HKUST-1 burns to 45% of its original mass, and therefore through interpolation it is approximated that the HKUST-1 embedded fibers have an HKUST-1 loading of 5 wt% since the final mass after burning is 3.5 %.

N_2 isotherms were taken at 77 K and CO_2 isotherm were taken at 273 K on pure HKUST-1 powder, HKUST-1 embedded polystyrene fibers, and the two different polystyrene fiber samples. These samples are shown in Figure 7.3.3.

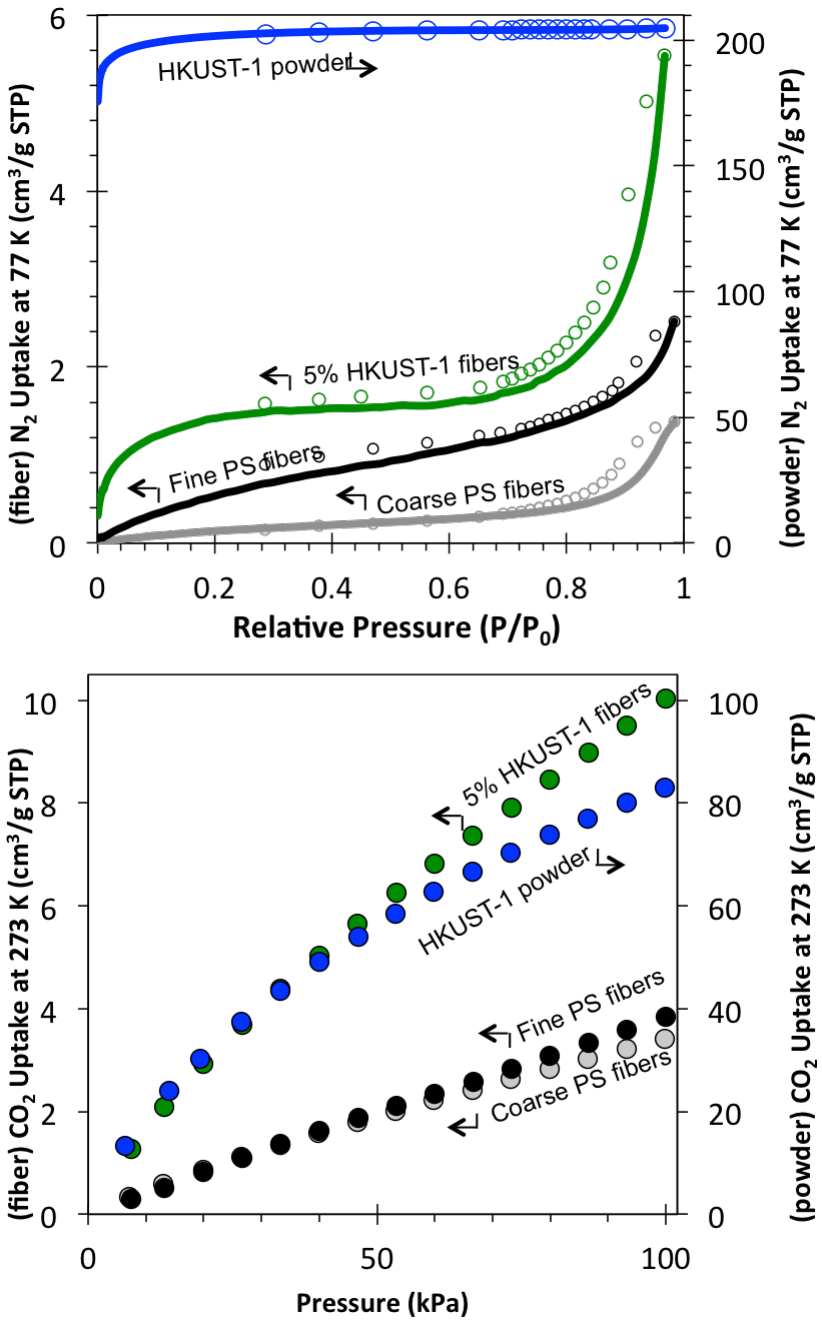

Figure 7.3.3. N_2 isotherms at 77 K (top) and CO_2 isotherms at 273 K (bottom) for as-synthesized samples including HKUST-1 powder (blue), HKUST-1 embedded polystyrene fibers (green), fine pure polystyrene fibers (black) and coarse pure polystyrene fibers (grey).

The resulting BET surface areas from the N_2 isotherms for these materials are 583 m^2/g for pure HKUST-1 powder, 5 m^2/g for the HKUST-1 impregnated fibers, 2.3 m^2/g for the fine PS

fibers, and 0.6 m^2/g for the coarse PS fibers. The fact that the surface area of the 5% HKUST-1 fibers are < 1% of the pure HKUST-1 powder, it is expected that nearly all HKUST-1 particles are embedded under a film of polystyrene as represented in the SEM images. The CO_2 isotherms show that the pure polystyrene samples take up nearly the same quantity of CO_2, demonstrating that CO_2 occurs primarily through an absorption mechanism since geometry does not appear to play a large role in uptake. This also suggests that CO_2 readily penetrates the fibers under these conditions. As a result of this an estimated negligible influence of geometry is assumed. it may be expected that the uptake of CO_2 in the HKUST-1 embedded fibers may be approximated through a weighted average between the weight percent of polystyrene and the weight percentage of HKUST-1 through the equation:

$$Q_{COMP.} = wt\%_{PS} Q_{PS} + wt\%_{HKUST} Q_{HKUST} \quad (7.1)$$

where Q_{COMP} is the CO_2 uptake of the entire composite, Q_{PS} is the CO_2 uptake of the polystyrene component, Q_{HKUST} is the CO_2 uptake of the HKUST-1 component, $wt\%_{PS}$ is the weight percentage of the polystyrene component in the composite, and $wt\%_{HKUST}$ is the weight percentage of the HKUST-1 component in the composite.

Using the weight fractions interpolated through TGA experiments, the approximate quantity of CO_2 uptake expected for this material is 7.7 cm^3/g STP as calculated by equation 7.1. This is in close agreement to the experimentally observed CO_2 uptake of 10 cm^3/g STP, demonstrating that the embedded HKUST-1 is readily available and negligibly damaged or blocked during the electrospinning process.

To analyze the hydrolysis rate of samples they are loaded into 50 mL Teflon-lined autoclaves on a raised platform over 10 mL of de-ionized water and placed in an oven at 100 °C for specified times. The HKUST-1 powder and HKUST-1 embedded fiber samples are always tested side-by-side for each given time step. CO_2 isotherms were also collected for the HKUST-1 containing samples at different humidity exposure times as shown in Figure 7.3.4.

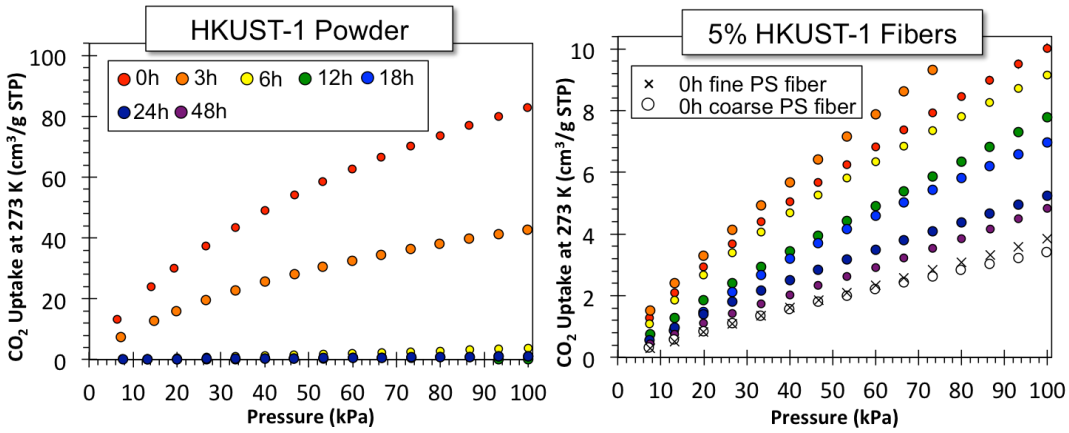

Figure 7.3.4. CO_2 isotherms after varying degrees of hydrothermal exposure including 0 h (red), 3 h (orange), 6 h (yellow), 12 h (green), 18 h (blue), 24 h (indigo), and 48 h (violet). The figure on the left shows CO_2 isotherms for pure HKUST-1 powder, and the figure on the right shows CO_2 isotherms for HKUST-1 impregnated fibers, along with CO_2 isotherms for pure PS fibers with 0 hour exposure.

The CO_2 capacity of the HKUST-1 embedded fibers actually increases at 3 hours, which is consistent with small water content loadings inside HKUST-1, where doubling of CO_2 capacity has been seen with 4% water loading.(Faheem, Jakubczak, Low, Willis, & Snurr, 2009) However, this trend quickly turns and the capacity starts to drop. The estimated hydrolysis fraction of the HKUST-1 embedded fibers and HKUST-1 powder at different time-steps and near 100 kPa is shown in Figure 7.3.5. Note that the data point at 3 hours for the HKUST-1 embedded fibers was estimated based on the prediction that an increase in CO_2 uptake results in a hydrolysis degree of around 4%. All other data points for fractional hydrolysis are represented by the equation:

$$Fractional\ Hydrolysis = 1 - Q(t)/Q_0 \tag{7.2}$$

where $Q(t)$ is the CO_2 uptake capacity after t hours of hydrothermal treatment and Q_0 is the initial CO_2 uptake capacity.

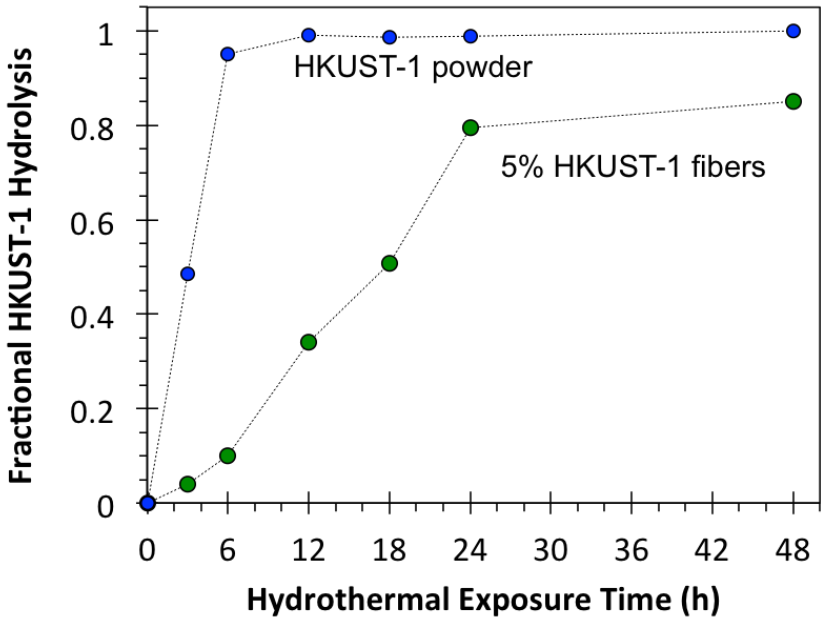

Figure 7.3.5. Approximated Fractional HKUST-1 hydrolysis versus hydrothermal exposure time for HKUST-1 embedded polystyrene fibers (green) and HKUST-1 powder (blue).

The pure HKUST-1 powder quickly loses CO_2 capacity. At 6 hours of moisture exposure the sample is nearly completely destroyed. This appears to be in agreement with similar studies, where a similar study by Carné-Sánchez and coworkers test HKUST-1 hydrothermal stability at room temperature and 80% relative humidity, and show a 56% loss in N_2 uptake at 8 hours.(Carne-Sanchez et al., 2015) The HKUST-1 embedded fibers show a slower hydrolysis rate than the pure HKUST-1 powder. This delayed loss confirms that these polystyrene fibers provide protection to the HKUST-1 particles by providing a barrier in which the moisture must overcome through a diffusion process before hydrolysis can occur.

7.4 Conclusion

HKUST-1 may be directly impregnated in polystyrene fibers during the electrospinning process by suspending sonochemically synthesized HKUST-1 powder in the polystyrene dope solution. It was confirmed that the final HKUST-1 loading was 5% by TGA. Nitrogen isotherms do not show the expected nitrogen uptake in these fibers, however, the carbon dioxide isotherms do.

This suggests that the particles are embedded under a layer of polystyrene in agreement with SEM images, and that the nitrogen is unable to penetrate this layer over the length of a nitrogen adsorption experiment. HKUST-1 powder and 5wt% HKUST-1 fibers are exposed to extreme hydrothermal conditions, and CO_2 uptake is measured at varying time steps. Nearly complete hydrolytic degradation of pure HKUST-1 powder is observed at 6 hours, but the rate of degradation in the 5wt% HKUST-1 impregnated fibers is slowed, and 20% CO_2 uptake capacity is still observed at 48 hours.

CHAPTER 8.

FABRICATING MOF-CONTAINING POROUS FIBERS THROUGH A SACRAFICIAL POLYMER REMOVAL STRATEGY

8.1 Introduction

In the previous chapters the focus was placed on developing tools, models, and proof-of-concept work for Type A- particle-embedded fibers. In this chapter the focus is now shifted to the development of Type C- particle containing porous fibers.

Relative to the other two types of fibers, Type C fibers are expected provide the highest particle loadings since both the external and internal fiber is used for anchoring sorbents. Furthermore, the pore network decreases the density of the fiber scaffold, ultimately increasing the weight percentage of sorbent loading. The introduction of pore networks also allows for accessibility to the internal sorbents while allowing for a structural polymeric scaffold that does not swell or disintegrate in the fluid stream.

In this chapter a methodology for fabricating Type C fibers is presented. In this work, we are the first to present a novel method for increasing the MOF to nanofiber ratio by electrospinning a two-polymer blend composed of the polyimide Matrimid 5218 and poly(ethylene oxide). The poly(ethylene oxide) is then removed, in a manner similar to that studied with pure polymeric fiber blends,(Bognitzki et al., 2001) leaving behind hierarchically porous Matrimid 5218 fibers containing impregnated MOF. The MOF used for this study was zeolitic immidazolate framework-8 (ZIF-8) due to its status as a leading archetypal MOF (as seen in Figure 2.2.2.1). From this study it is found that poly(ethylene oxide) can be successfully removed in polymer blends up to 50% poly(ethylene oxide) and leave behind ZIF-8 particles impregnated in the porous Matrimid fibers. The presented method is expected to be applicable to all MOF-nanofiber systems since specific chemical interactions between the two species are not vital to its success. Increasing the density of active sites and accessibility through a hierarchical pore structure by

selective polymer removal successfully meets these urgent demands required for MOF-impregnated nanofiber research to continue to grow.

8.2 Materials Preparation

ZIF-8 was synthesized using a room temperature synthesis described by Cravillon,(Cravillon et al., 2011) creating particles averaging 100 nm diameter as observed by SEM. Full characterization of ZIF-8 including powder SEM images, nitrogen isotherms at 77 K, and pore size distributions may be found in previous chapters.

Fibers were electrospun in dichloromethane solutions in mass ratios of 1:1:0, 3:1:0, 1:3:0, 1:1:0.25, and 1:1:1 MAT: PEO: ZIF-8. ZIF-8 was suspended in polymeric solutions in an analogous manner to mixed-matrix-membrane solution priming described by Song and coworkers,(Song et al., 2012) and the custom-designed electrospinning apparatus used is well described in previous work.(M. R. Armstrong et al., 2015) Because varying solution parameters were necessary, each solution was spun under different operating conditions to come as close to uniform 1 μm fibers as possible. Ranges of variables included flow rates between 0.05 and 0.2 ml/min, voltages between 10 and 25 kV, and working distances between 5 and 20 cm with aluminum foil as the grounded collector, and specific synthesis details may be found in the supplementary information as well. To wash samples, fibers were immersed in 15 mL methanol solutions and heated to 65 °C for 12 hours, until they were within 5% of the expected mass considering complete PEO removal. Samples were activated at 45 °C under vacuum for 100 hours before each FTIR or adsorption tests.

8.3. Results and Discussion

8.3.1. Matrimid-PEO electrospun fibers. Matrimid and PEO were electrospun in three different ratios by weight: 1:3, 1:1, and 3:1 MAT: PEO. Half of each sample was kept in tact and are either

referred to by just their mass ratios or as “as-synthesized.” The second half of each sample was washed in methanol to remove the PEO and referred to as “washed.” The washed fibers were repeatedly washed until the actual weight after PEO removal was within 5% of the theoretically predicted weight expected upon complete PEO removal. Each sample was examined with FTIR before and after washing to confirm PEO was the polymer removed, as seen in Figure 8.3.1.1.

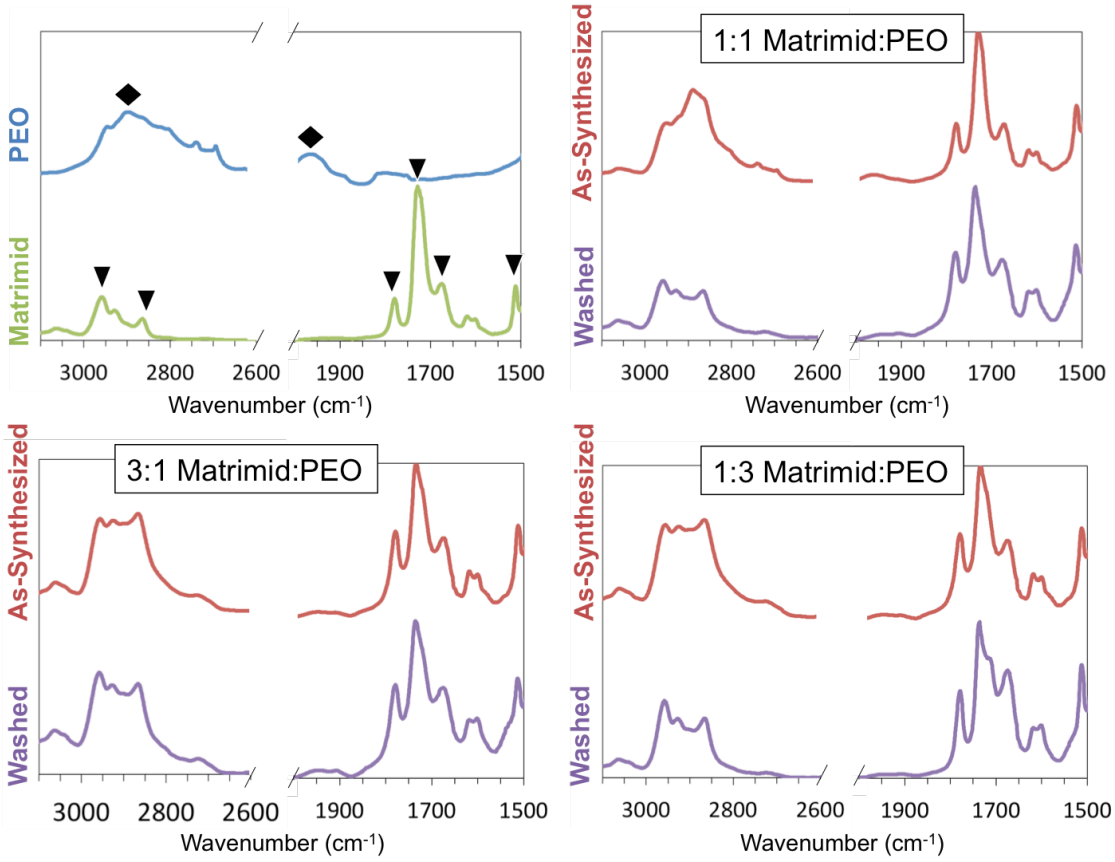

Figure 8.3.1.1. FTIR of pure Matrimid and pure PEO where diamonds represent PEO peaks at 2880 and 1950 cm^{-1} from left to right, and triangles represent Matrimid peaks at 2950, 2850, 1775, 1725, 1670, and 1508 cm^{-1} from left to right (top, left), 1:1 MAT:PEO before and after wash (top, right), 3:1 MAT:PEO before and after wash (bottom, left), and 1:3 MAT:PEO before and after washing (bottom, right). For each graph the Y-axis is presented in arbitrary absorbance units.

The FTIR patterns of each MAT:PEO ratio before and after PEO removal are shown along with the FTIR spectra of pure Matrimid and PEO in the top-left panel. These results show that PEO was almost entirely removed from each sample due to significant decreases in the peak at 2880 and 1950 cm^{-1} (corresponding to C-H stretching and asymmetric stretching,

respectively),(Ramesh, Yuen, & Shen, 2008) and remaining Matrimid peaks at 2950 and 2850 cm^{-1} (corresponding to C-H bending modes), 1775, 1725 and 1670 cm^{-1} (corresponding to C=O stretching asymmetrically, symmetrically, and C=O stretching on the benzophenone, respectively), and 1508 cm^{-1} (corresponding aromatic stretching).(Rahmani, Kazemi, Talebnia, & Khanbabaei, 2014)

Scanning electron microscopy (SEM) was used to visualize the fibers before and after PEO removal, and these images may be seen in Figure 8.3.1.2.

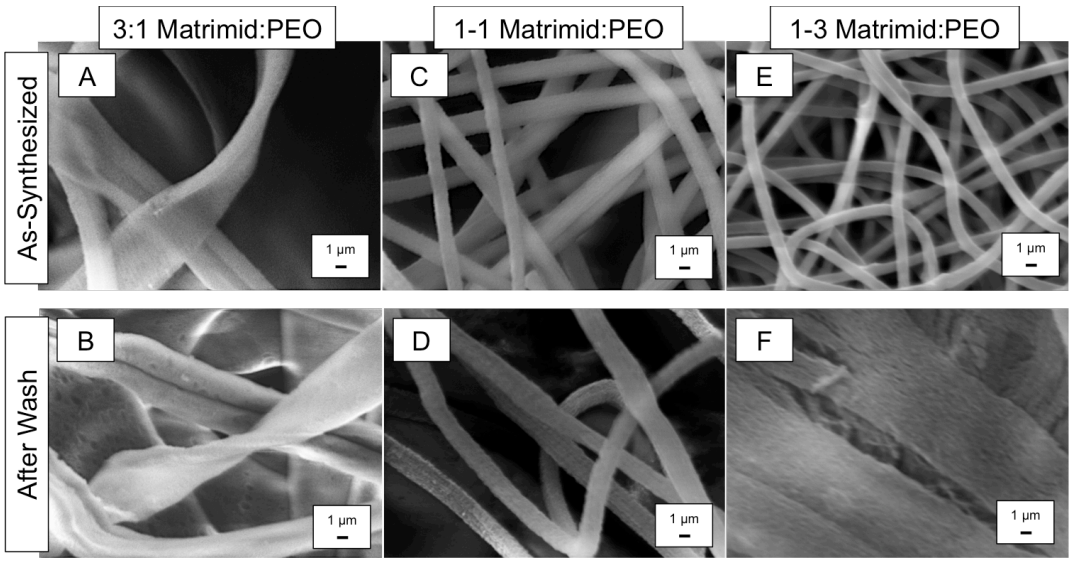

Figure 8.3.1.2. SEM images of Matrimid-PEO fibers before and after PEO removal, where the left images correspond to 75% Matrimid by weight fibers before washing, the middle images correspond to 50% Matrimid by weight fibers before washing, and the right images correspond to 25% Matrimid by weight fibers before washing. The top images each correspond to as-synthesized fibers and the bottom images correspond to fibers after PEO removal.

Each of the fibers after electrospinning had uniform diameters of nearly 1 µm, with the exception of the 3:1 MAT:PEO sample in which a larger range of diameters and morphologies including ribbons is observed with an average around 1 µm (Figure 8.3.1.2 A). After PEO removal porous fibers are observed in each sample (Figure 8.3.1.2 B, D, E), and the fiber size does not decrease for the 3:1 or 1:1 samples. The final morphology of the 1:3 sample is changed after PEO removal (Figure 8.3.1.2 F), likely due to the significant mass loss that occurs in the PEO removal step leading to a collapse of the fiber structure.

Digital images of the fiber 1 x 1 cm MAT:PEO nonwoven mats before and after washing may be seen in Figure 8.3.1.3 which complement the SEM images showing that the 3:1 and 1:1 MAT:PEO fibers show no visual signs of damage or change besides a slight hint of yellowing, while the 1:3 MAT:PEO fibers show significant deterioration after washing.

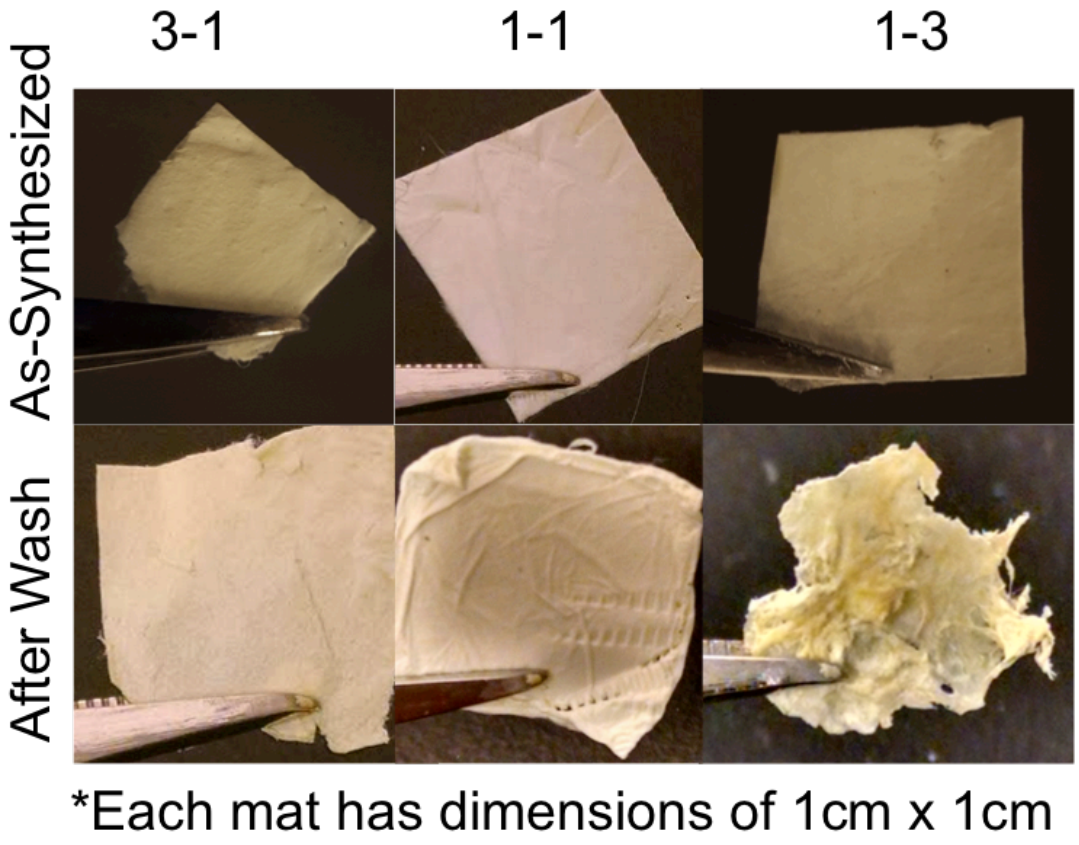

Figure 8.3.1.3. Optical images of each MAT:PEO fiber sample before and after washing. Each mat has original dimensions of 1cm × 1 cm.

By assuming that the fibers are cylinders and that the contributions of the top and bottom of the cylinder are negligible compared to the sides. The isotherms of the fibers along with a plot of theoretical surface area of dense fibers (as calculated with equation 2.2) and the calculated BET surface areas is shown in Figure 8.3.1.4.

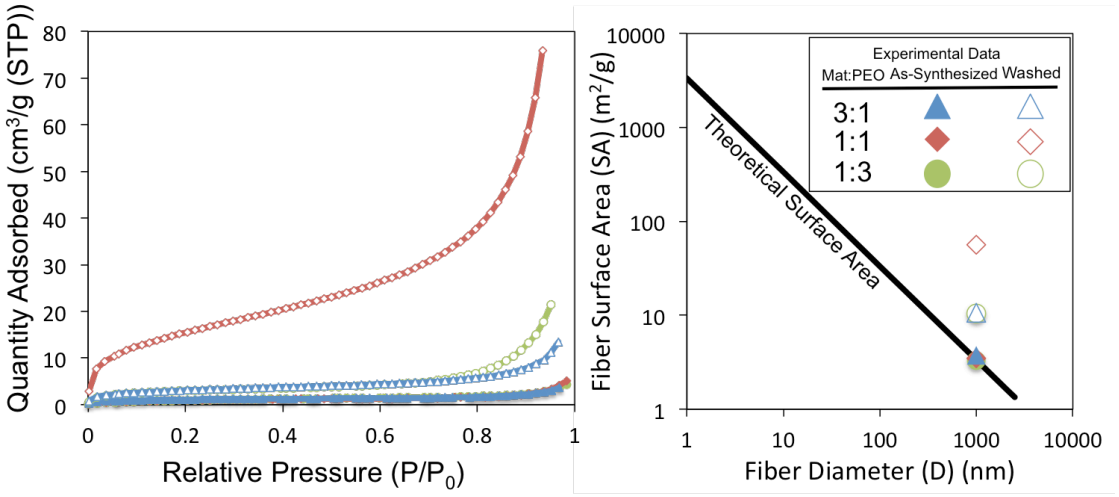

Figure 8.3.1.4. Isotherms of Matrimid/PEO electrospun fibers before and after PEO removal (left) and the calculated BET surface areas of each fiber plotted as a function of fiber diameter along with a line representing the theoretical surface area of a nonporous fiber with a density of 1.2 g/mL where all fibers before washing exhibit surface areas around 3 m^2/g, the 1:1 MAT:PEO fibers show a surface area of 56 m^2/g, and the 3:1 and 1:3 MAT:PEO fibers show surface areas of 10 and 11 m^2/g, respectively. (right).

This data shows that all three fibers before washing exhibit the expected surface area of a dense fiber of density 1.2 (density of Matrimid is 1.2 g/cm as reported by Huntsmann's technical data sheet). Washing the 1:1 MAT:PEO fibers exhibit a maximum observed surface area of 50 m^2/g among the samples tested, and both the 1:3 and 3:1 MAT:PEO fibers have lesser surface areas of around 10 m^2/g after PEO removal by washing. This shows that an ideal MAT:PEO ratio exists around 50:50. Based on BET images it is expected that fibers with small Matrimid content decompose when the PEO is pulled out, which is also corroborated by the early increase towards saturation in the washed 1:3 MAT:PEO isotherm that is likely caused by macropores formed when the Matrimid condenses into a film as seen in SEM and digital images. The fibers with high electrospun Matrimid content may also have a smaller surface area due to the fewer voids left behind after PEO removal.

In sum this section shows that PEO removal is an effective strategy for controlling and creating porous Matrimid fibers, and that if the Matrimid content is 50% or less that the fibers will retain their original diameters and structure while adding significant surface area enhancement

(>10x) due to the formation of pores. Removing the PEO from fibers that had originally been 1:1 MAT:PEO by weight show an optimum increase of surface area relative to the other mass ratios tested, therefore 1:1 MAT:PEO fibers were used exclusively for ZIF-8 impregnation studies.

6.3.2. ZIF-8 impregnated Matrimid-PEO fibers. ZIF-8 was suspended in 1:1 MAT:PEO (by weight) polymeric solutions and electrospun to create ZIF-8 impregnated nanofibers with two different ZIF-8 loadings (1:1:0.25 and 1:1:1 Mat:PEO:ZIF-8). The same PEO wash was performed on the ZIF-8 impregnated fibers, and Figure 8.3.2.1 shows SEM and TEM images of the fibers before and after washing.

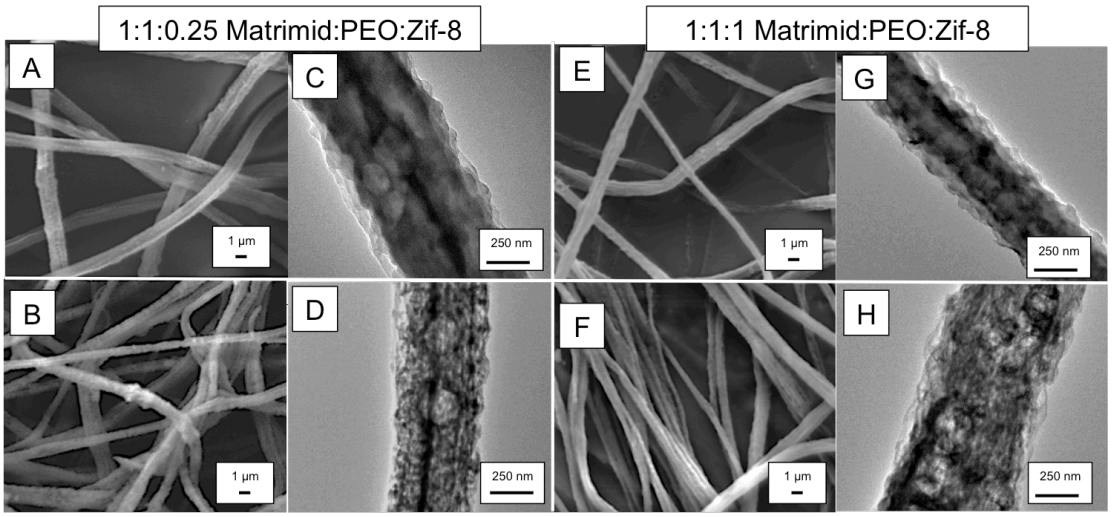

Figure 8.3.2.1. SEM images of 1:1:0.25 MAT:PEO:ZIF-8 fibers before PEO removal (A) and after PEO removal (B), TEM images of 1:1:0.25 MAT:PEO:ZIF-8 fibers before PEO removal (C), and after PEO removal (D). SEM images of 1:1:1 MAT:PEO:ZIF-8 fibers before PEO removal (E), and after PEO removal (F), TEM images of 1:1:1 MAT:PEO:ZIF-8 fibers before PEO removal (G), and after PEO removal (H).

These images show fibers with diameters between 250 nm and 1.5 um, and that after PEO removal the fiber structure is well maintained. TEM images of single fibers of around 0.5 um show impregnated hexagonal ZIF-8 particles throughout the fibers, and that they are clearly present after washing as well. The light hexagonal crystals were confirmed to be ZIF-8 particles by EDX displaying a strong concentration of zinc on these lighter hexagonal spots in contrast to the bulk darker fiber, which are shown in the supplementary information of the original

manuscript.(M. R. Armstrong et al., 2016) SEM images show an increase in the roughness of the fiber texture after washing in both 1:1:0.25 and 1:1:1 MAT:PEO:ZIF-8 ratios suggesting the addition of pores, which are apparent in the TEM images of washed fibers in which grainy patterns emerge throughout the fiber corresponding to an absence of polymer density in those areas.

FTIR was also carried out for these fibers as seen in Figure 8.3.2.2 over the wavenumbers 400 to 3400 cm^{-1} to ensure all of the distinct ZIF-8 bands are accounted for, the pure spectra for Matrimid, PEO, and Zif-8 may be seen in the supplementary information (ESI Fig S4).

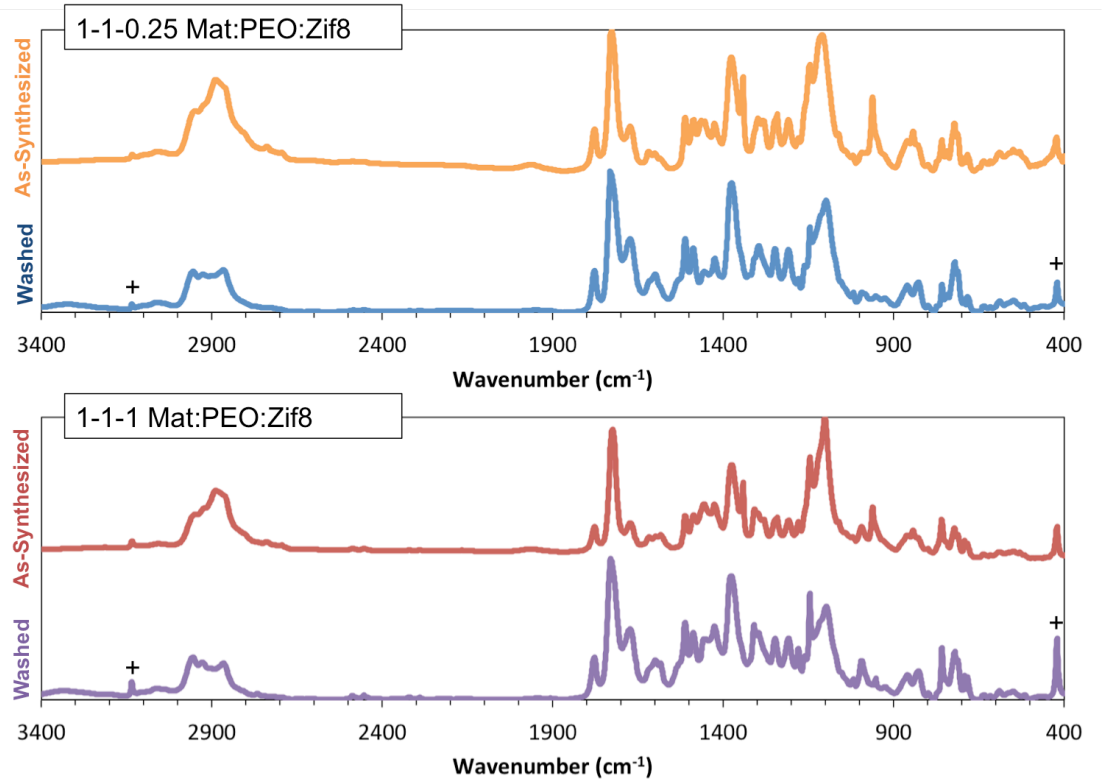

Figure 8.3.2.2. FTIR of 1:1:0.25 (top) and 1:1:1 (bottom) Mat:PEO:ZIF-8 before and after washing. The plus sign (+) represents peaks unambiguously associated with ZIF-8.

After washing until the fibers were within 5% of their expected theoretical weight assuming complete PEO removal, ZIF-8 peaks at 3130, and 420 cm^{-1} (corresponding to aromatic C-H stretch and Zn-N stretch, respectively)(Hu, Kazemian, Rohani, Huang, & Song, 2011) become more prevalent, PEO peaks are minimized, and the Matrimid peaks appear unchanged

for both 1:1:0.25 and 1:1:1 Mat:PEO:ZIF-8 mats. This further confirms that PEO removal was successful, and that the Zif-8 was not pulled out during wash cycles.

Adsorption isotherms collected of as-synthesized and washed ZIF-8 impregnated fibers collected using nitrogen porosimetry at 77K in Figure 8.3.2.3.

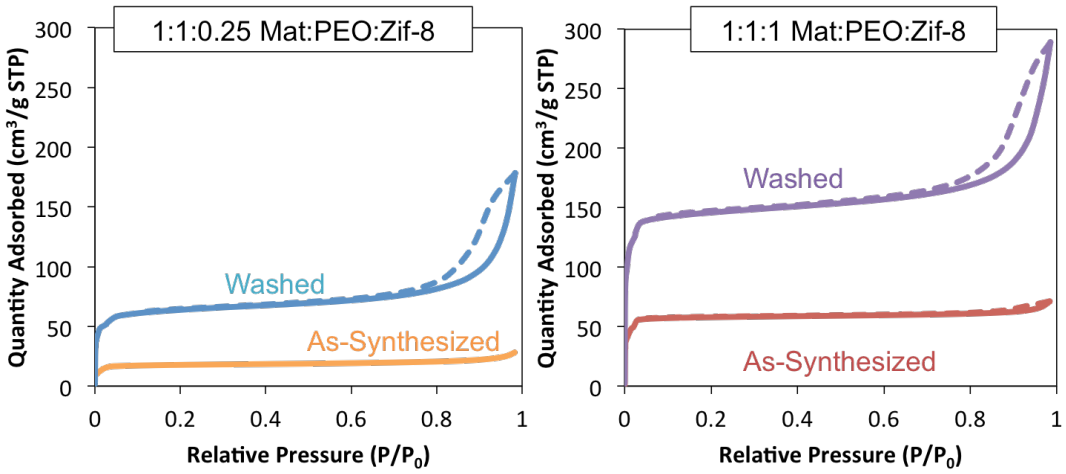

Figure 8.3.2.3. Nitrogen isotherms at 77K for 1:1:0.25 Mat:PEO:ZIF-8 fibers as-synthesized and after PEO removal by washing (left) and for 1:1:1 Mat:PEO:ZIF-8 fibers as-synthesized and after PEO removal by washing (right). The solid lines represent adsorption branches and the broken lines represent desorption branches.

The unwashed ZIF-8 impregnated fibers in each case introduce a large initial nitrogen uptake at relative pressures less than 0.1 indicative of a Type I microporous adsorbent with another slight increase at relative pressures above 0.9 induced by the fibers.

After washing the ZIF-8 impregnated fibers the initial nitrogen uptake increases due to both the decrease in polymer content relative to ZIF-8 by mass as well the increased initial uptake provided by porous fibers versus dense fibers.

The isotherms of the washed ZIF-8 impregnated fibers also take on the characteristic shape of the pure washed fiber isotherm for partial pressures greater than 0.1 including a shallow continuous increase from 0.1 to 0.8 relative pressure as well as an asymptotic increase as the nitrogen reaches saturation pressures.

These features confirm the existence of the anticipated hierarchical pore structures existing between the ZIF-8 pores and the large fiber pores induced by PEO removal.

The only differences that may be seen between the isotherms of 1:1:0.25 MAT:PEO:ZIF-8 fibers and the 1:1:1 MAT:PEO:ZIF-8 fiber are the sizes of the initial nitrogen uptake caused by the differences in ZIF-8 content, and aside from that difference the characteristic shape of the isotherms are consistent.

To further understand the pore structure of these materials, the pore size distribution was calculated using the Kelvin equation approximating each pore as cylindrical and using the Halsey film thickness approximation generated from the isotherms given in Figure 8.3.2.3.(Halsey, 1948) These pore structures are given in Figure 8.3.2.4.

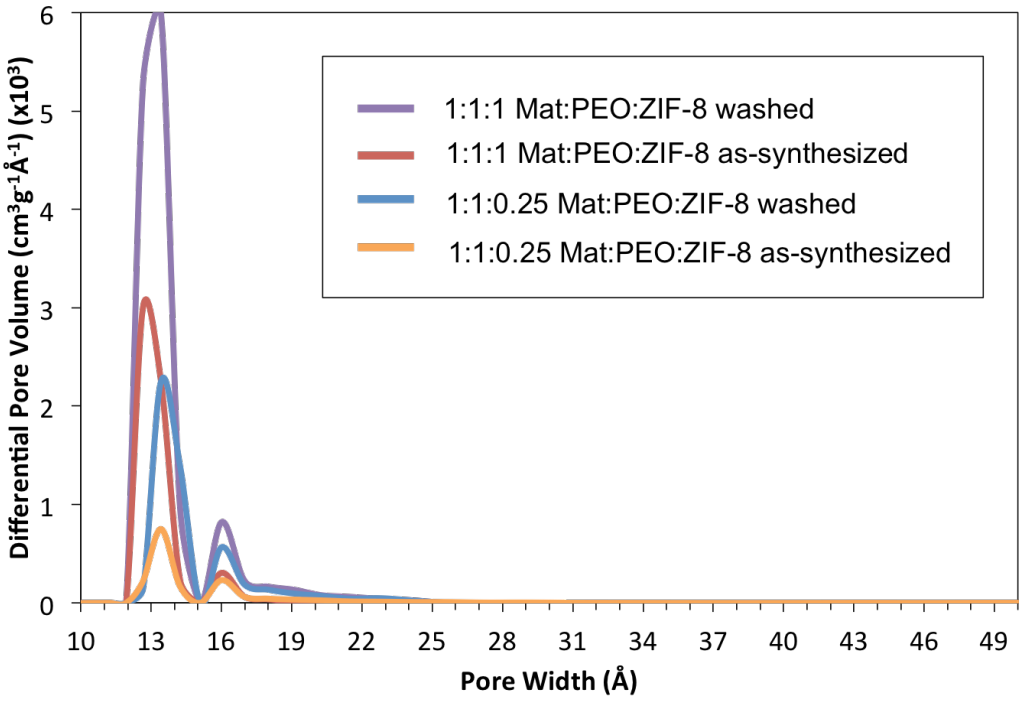

Figure 8.3.2.4. Differential pore volume as a function of pore width for 1:1:1 and 1:1:0.25 Mat:PEO:Zif-8 fibers as-synthesized and after washing to remove PEO.

The curves corresponding to ZIF-8 impregnated fibers before washing in each case consist of two sharp peaks with pore widths of 13 and 16 angstroms. This is consistent with results found in literature for pure ZIF-8 crystals,(Lu et al., 2012) and is a fingerprint result brought about from discrepancies between the theoretically assumed cylindrical pores and the actual spherical cavities in ZIF-8.

According to Figure 8.3.2.3 there are no pores larger than the expected ZIF-8 pores up to 50 angstroms for unwashed fibers, which is consistent with the flat isotherm found in Figure 8.3.2.4 as well as the absence of visible pores in the SEM images. After washing the pore volume associated with ZIF-8 for both 1:1:0.25 and 1:1:1 MAT:PEO:ZIF-8 fibers more than double, indicating that more ZIF-8 has been made available for nitrogen uptake since half the polymer has been removed. Also visible for both of the washed fibers is the introductions of pore volumes between 16 and 20 angstroms, which is attributed to the addition of pores on the polymer fibers.

Along with the pore volumes for ZIF-8 impregnated fibers before and after washing, the BET surface areas of these fibers were calculated from the isotherms in Figure 8.3.2.3, and these values are shown in Table 8.3.2.1. along with a summary of the pure fiber surface areas, pure ZIF-8, and the theoretically calculated surface areas where applicable.

Table 8.3.2.1.
Summary of the experimental BET surface area and theoretical surface area for fibers and ZIF-8.

Sample	MAT:PEO:ZIF-8 Mass Ratio		Experimental BET Surface Area	Theoretical BET Surface Area	Theoretical Surface Area Calculation
1	0-0-1		1659	1600	[(Park et al., 2006)]
2	3-1-0		4	4	Eq 2.2
3		Washed	10	-	-
4	1-1-0		4	4	Eq 2.2
5		Washed	56	-	-
6	1-3-0		4	4	Eq 2.2
7		Washed	11	-	-
8	1-1-0.25		70	177	Eq 8.1
9		Washed	225	365	Eq 8.2
10	1-1-1		322	533	Eq 8.1
11		Washed	583	828	Eq 8.2

The theoretical surface area (**$SA_{theoretical}$**) of unwashed ZIF-8 impregnated fibers was calculated assuming that the experimental surface areas of the fibers (**SA_{fiber}**) and the experimental surface area of ZIF-8 (**$SA_{ZIF\text{-}8}$**) were additive based on their mass fractions, and that all ZIF-8 was accessible with the equation:

$$SA_{Theoretical} = \frac{mass_{ZIF-8} SA_{ZIF-8} + mass_{fiber} SA_{fiber}}{mass_{total}} \quad (8.1)$$

The theoretical surface area for ZIF-8 impregnated washed fibers was calculated assuming that the PEO was completely removed as well as the only component removed, and that the surface area is additive based on the experimental surface area of pure washed fibers (**$SA_{WashedFiber}$**) (i.e. Sample 5 from Table 1) and **$SA_{ZIF\text{-}8}$** based on their mass fractions with the equation:

$$SA_{\square heoretical} = \frac{mass_{ZIF-8} SA_{ZIF-8} + mass_{WashedFiber} SA_{WashedFiber}}{mass_{total}} \quad (8.2)$$

In each case for ZIF-8 impregnated fibers the experimentally determined BET surface area falls short of the theoretically calculated surface area. This is expected to be caused by some of the ZIF-8 pores to be inaccessible to nitrogen uptake due to fiber blockage. This explanation is validated due to the more than double ZIF-8 pore volume accessible after washing as well as the larger-than-expected increase in surface area between washed and unwashed ZIF-8 impregnated fibers if this was not the case. The washed fibers, however, also do not reach the theoretical maximum surface area, and this may be due to some loss of ZIF-8 during washing, incomplete PEO removal contributing to the overall mass, or more blocked ZIF-8 pores.

These results successfully show that after removing PEO from ZIF-8 impregnated fibers, the ZIF-8 is retained, more ZIF-8 becomes accessible, the ZIF-8: fiber ratio is doubled, and that a hierarchical pore structure is created composed of ZIF-8 and fiber pores.

8.4 Conclusion

This chapter reports a new strategy to increase nanoparticle loading and porosity in electrospun composite fibers by washing away sacrificial components from a blended polymer precursor. Of the three ratios tested, porous Matrimid has an optimum porosity when Poly(ethylene oxide) (PEO) is removed from the fibers when a blend of 50% Matrimid and 50% PEO by weight is electrospun. Less PEO content leads to fewer voids left behind after PEO removal, and more PEO content leads to a loss of fiber structure after PEO removal. When the metal-organic-framework (MOF) zeolitic-immidazolate-framework-8 (ZIF-8) is suspended in the polymeric electrospinning solution, the resulting fibers contain impregnated ZIF-8. It is shown

that ZIF-8 suspensions of 20% and 50% by weight with respect to Matrimid result in a doubling of surface area and pore volume associated with ZIF-8 pores after PEO removal, proving that removal of blended PEO results in mats of a hierarchical porous fibers composed of both porous Matrimid fibers and the pores contributed by the impregnated ZIF-8. It also confirms that the process of electrospinning blends of highly soluble and low soluble polymers with impregnated nanomaterials followed by removal of the highly soluble polymer is a suitable scheme for designing composite nanofibers with elevated nanoparticle loadings. This technique is translatable to a variety of fields where the application of functional nanofibers are being studied including filtration, sensing, protective clothing, and catalysis.

CHAPTER 9.

PARTICLE-CONTAINING POROUS FIBER CASE STUDY: DIRECT AIR CAPTURE AS A COMPETITIVE APPLICATION FOR RESIN-CONTAINING POROUS FIBERS

9.1. Introduction

Direct air capture- the process of removing carbon dioxide directly from ambient air has the potential to become a powerful tool in combating climate change.(Sanz-Perez, Murdock, Didas, & Jones, 2016) Sorbents are currently being designed to accomplish this task including metal-organic frameworks,(Shekhah et al., 2014) activated carbon,(X. Shi, Xiao, Lackner, & Chen, 2016) and amine-tethered materials.(Choi, Gray, & Jones, 2011) Important characteristics of a sorbent for direct air capture include high uptake capacities, fast uptake rates, and an economically viable regeneration process.(Choi, Drese, Eisenberger, & Jones, 2011) Moisture swing absorption has proven to be a competitive direct air capture technique by balancing the energy cost of regeneration against the energy of evaporating water, which much like the famous desktop drinking bird heat engine, results in the overall appearance of a passive process.(Lackner, 2009) Furthermore, Yang has demonstrated that the kinetics of carbon dioxide capture on an ion-exchange resin embedded in a thin film through a moisture swing process are among the fastest direct air capture kinetics found in literature.(X. Shi, Li, Wang, & Lackner, 2017)

We demonstrate in this work that embedding an ion-exchange resin in an electrospun fiber matrix provides faster sorption kinetics than in commercially available film morphologies. A frequency response technique is developed and used to characterize the kinetic rate as a function of sinusoidal moisture concentration profiles. The porous fiber scaffold provides 90% IER accessibility, while the dense fiber scaffold only allows for only 50% IER accessibility. Overall, when considering both the uptake capacity and sorption kinetics in a metric called the average uptake per gram-hour, the IER-containing porous fiber scaffolds have the fastest uptake found in literature.

9.2. Theory

A first-order kinetic uptake model may be used in many cases to describe the uptake of a sorbate by a sorbent. This is accurate when there is only one type of active site collecting sorbate, and when both the uptake rate and solubility of the sorbate is independent of concentration. After a step-change the external sorbate concentration (or any other step-change in sorbate chemical potential), this uptake equation may be given as:

$$Q_t = Q_e e^{-\frac{t}{\tau}} \tag{9.1}$$

In this equation $\mathbf{Q_t}$ is the uptake at time **t**, $\mathbf{Q_e}$ is the uptake at equilibrium, and **τ** is the time constant. The time constant represents the time it takes for the sorbent to reach approximately 63.2% of its equilibrium value after a step change. The time to reach half of the equilibrium value is called the half-time ($\boldsymbol{\tau_{1/2,\bar{v}}}$). It is found from the equation: $\tau_{1/2,\bar{v}}$ = ln(2)× $\tau_{\bar{v}}$. Also, the first-order rate constant ($\mathbf{k_{\bar{v}}}$), as defined in the Legrengan uptake model, is given as the inverse of the time constant: $k_{\bar{v}} = (\tau_{\bar{v}})^{-1}$.

Water content in the air is expected to have a non-negligible impact on **τ** in the present system. Water swells the ion-exchange resin when it is absorbed. This causes a lubrication effect that allows molecules to pass through with less resistance than a dry resin. For this reason a term incorporating this effect must be used in the developed model.

To make a model for first-order uptake kinetics we use an analogous circuit that can be described as a single pole low pass-filter in signal processing (Figure 9.2.1).

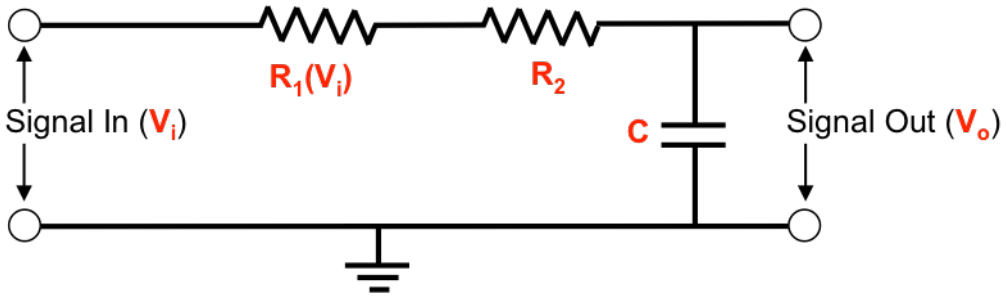

Figure 9.2.1. An analogous low pass filter where $\mathbf{V_i}$ is the signal in, $\mathbf{R_1}$ is a resistance that is dependent on $\mathbf{V_i}$ (to allow for the impact of water content on the uptake rate), $\mathbf{R_2}$ is a signal independent resistance, **C** is a capacitance, and $\mathbf{V_o}$ is the output signal.

The signal out (designated as $\mathbf{V_o}$ to draw parallels the commonly used voltage in electronics) may be expressed as a function of signal in ($\mathbf{V_i}$) as a voltage divider in terms of the impedence (**Z**) of each element in the circuit when considering a sinusoidal signal in:

$$\frac{V_o}{V_i} = \frac{Z_C}{Z_C + Z_{R1} + Z_{R2}} \tag{9.2}$$

The impedence of a resistor is defined as its resistance (Z_R=R), and the impedence of a capacitor is given by $Z_C=(i\omega C)^{-1}$, where **ω** is the signal angular frequency and **i** is $\sqrt{-1}$. This allows EQ 2 to be rewritten as:

$$\frac{V_o}{V_i} = \frac{1}{1 + i\omega C(R_1(V_i) + R_2)} \tag{9.3}$$

The intended signal will be a sinusoidal waveform that may be expressed as:

$$V = \bar{v} + Asin(\omega t + \phi) \tag{9.4}$$

where $\bar{\mathbf{v}}$ is the average signal (the offset), **A** is the amplitude, **ϕ** is the phase, and **t** is the time. If we assume that the amplitude is small such that $\bar{v}$>>Asin(ωt+ϕ) we can reassign $\mathbf{R_1}$ to be a function of only $\bar{\mathbf{v}}$ such that $R_1=R_1(\bar{v}_i)$. We can then define a time constant $\tau_{\bar{v}}$ = $C(R_1(\bar{\mathbf{v}}_i)+R_2)$ Since we are only interested in the magnitude of change, EQ 9.3 may be rewritten as:

$$\frac{A_o}{A_i} = \frac{1}{\sqrt{1+\omega^2\tau_{\bar{v}}^2}} \tag{9.5}$$

as a result of the relationship V=(VV*)$^{0.5}$.

By plotting the amplitude ratio as a function of changing **ω** on a log-log scale a Bode plot is constructed. An example is shown in Figure 9.2.2.

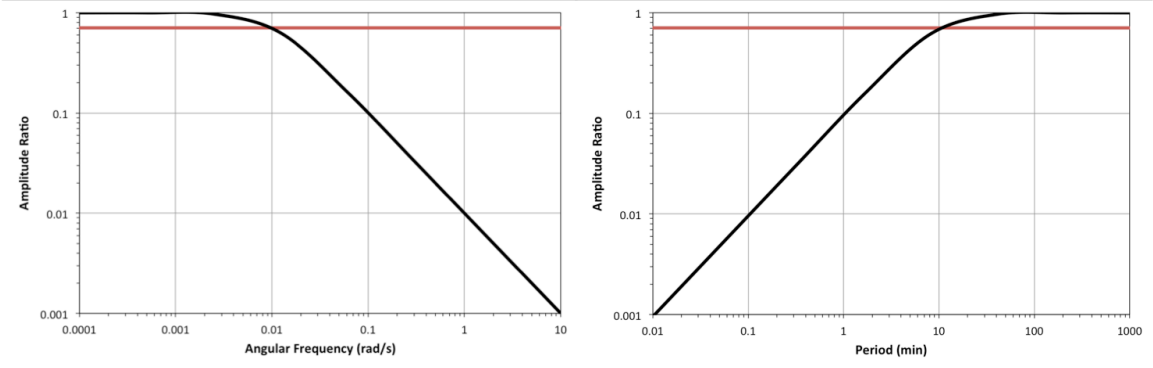

Figure 9.2.2. Examples of a Bode plot with $\tau_{\bar{v}}$= 100 rad/s. The left figure represents the traditional representation with angular frequency on the x-axis. The right figure contains a Bode plot with period on the x-axis.

$\boldsymbol{\tau_{\bar{v}}}$ may be found from this plot using the relationship:

$$\omega_{AR=0.7071} = \frac{1}{\tau_{\bar{v}}} \tag{9.6}$$

where $\boldsymbol{\omega_{AR=0.707}}$ is the angular frequency at which the amplitude ratio is equal to ($1/\sqrt{2}$), which is approximately 0.707. This is the traditional Bode plot used for filter analysis, however, plotting the period (**T**) on the x-axis provides a more intuitive figure for analysis of mass transfer kinetics. Rather than the intersection of 0.707 the first order rate constant $\mathbf{k_{\bar{v}}}$.

Furthermore, a consistency check to confirm the assumptions of a first-order reaction and that $\bar{v}$>>Asin(ωt+ϕ) may be found from the roll-off. The slope of this linear region must span 1 order of magnitude in frequency with 1 order of magnitude in amplitude ratio for a first order

system. The intercept of this linear region also intersects the amplitude ratio of 1 at the period associated with the time constant.

9.3 Materials and Methods

9.3.1. Moisture swing frequency response apparatus. The schematic of the Moisture/ Humidity Exchange Response Board (MotHER Board) is shown in Figure 9.3.1.1**.**

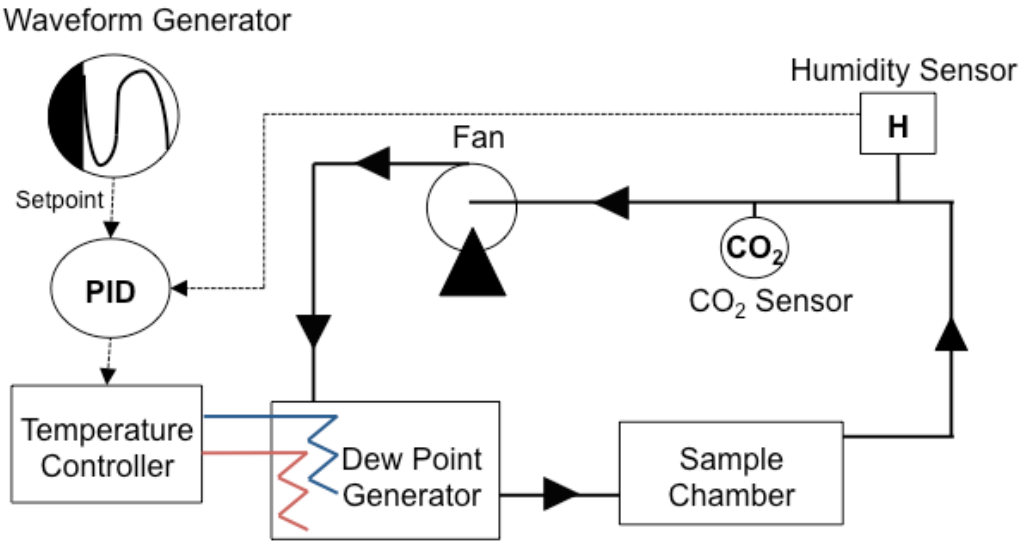

Figure 9.3.1.1. Schematic of **Mo**is**t**ure/ **H**umidity **E**xchange **R**esponse **Board** (i.e. MotHER Board).

The MotHER Board is an apparatus that exchanges moisture between a temperature controlled reservoir and the circulating air by changing the dew point. This humid air is circulated over a sample. Varying setpoint profiles may be used to set the humidity exchange profile. A waveform generator sends a setpoint as a function of time through a PID algorithm to a temperature controller. This temperature controller either heats or cools a dewpoint generator to control the humidity in a system containing a sample in which the air is circulated by a fan. A CO_2 sensor reads the CO_2 concentration in the system. A humidity sensor reads the humidity of the

system, and sends a feedback loop to the PID controller. The entire system has a closed volume of approximately 175 mL, and the air is circulated at a flowrate of 1 L/min.

This work exclusively uses a sinusoidal exchange profile to conduct frequency response tests as expressed by equation 9.5. When a moisture swing sorbent is placed in this apparatus, the water is taken up by the sorbent and CO_2 is displaced. When the moisture level in air drops, water desorbs from the sorbent and CO_2 is taken up. This generates a CO_2 sinusoidal uptake response that may be monitored by measuring the CO_2 concentration in the headspace over the sorbent. In this work we input various moisture sinusoidal waveforms and measure the output CO_2 response. By maintaining a constant moisture offset and amplitude while varying the period, the amplitude of the resulting CO_2 response may be measured at each period to generate Bode plots as demonstrated in Figure 9.2.2. Since the input is a moisture signal and the output is a CO_2 signal, the AR ratio must be adjusted from A_o/A_i to A_T/A_∞, which is the CO_2 concentration amplitude at a specified period over the maximum CO_2 concentration amplitude.

9.3.2. Material preparation. Two different ion exchange resins (IER) are used in this work as moisture swing sorbents. The first is a Type I strong base resin named Purolite resin A500, it was grinded to particle diameters between 44 and 74 μm and provided by Kilimanjaro Energy. The second ion exchange resin is a Type I strong base resin of particle size around 50 μm imbedded in a polypropylene binder film of 1 mm thickness at 50 weight percent IER provided by Snowpure LLC. It is called the commercial film in this work.

To form dense electrospun fiber scaffolds for the crushed IER, a solution containing 1.25 g crushed IER is suspended in a 10 mL n-n dimethylformamide (99.9%, Sigma Aldrich) solution with 1.25 g of dissolved polystyrene (M_w= 280,000, Sigma-Aldrich). This solution is spun at a flowrate of 0.25 mL/min with an applied voltage of 20 kV onto a grounded substrate 10 cm from the needle using a vertical apparatus described previously.(M. R. Armstrong et al., 2015)

To form porous electrospun fiber scaffolds for the crushed IER a method developed previously was used.(M. R. Armstrong et al., 2016) A solution containing 400 mg crushed resin is suspended in a 10 mL dimethylformamide solution containing a 400 mg polystyrene and 400 mg poly(ethylene oxide) (MV=400,000, Sigma Aldrich) blend. This solution is spun at a flowrate of 0.25 mL/min with an applied voltage of 20 kV onto a grounded substrate 10 cm from the needle using the same apparatus that was used to form dense fibers.

Each sample was vigorously stirred in a 50 molar NaOH aqueous solution to perform an ion exchange and subsequently washed in DI water. This step simultaneously removed the water-soluble filler polymer from the fibers composed of a polystyrene/ poly(ethylene oxide) blend. After moisture swing frequency response testing, each fiber sample was weighed; dissolved in dichloromethane (99.5%, VWR International), filtered, and dried; and then the residual ion-exchange resin was reweighed to determine the weight percentage of resin in the tested fibers. It was found that the dense fibers had a resin loading of 32.5 % after testing; the porous fibers had a resin loading of 34.5 % after testing. The discrepencies between the loading in the electrospinning dope and the final fibers may be due to either particles that are not connected to the fiber structure or weakly attached that are lost during the vigorous stirring or testing. Noteworthy is that although these values are similar, it is the porous fibers that have a slightly higher loading, which suggests that the additive removal did not cause more particle loss than the dense fibers.

The commercial resin is reported to have a 50 wt% resin loading. Each fiber sample fabricated in this work had scanning electron microscopy images taken on an FEI XL30 scanning electron microscope at an accelerating voltage of 10 kV after moisture swing analysis was finished.

9.4 Results and Discussion

9.4.1. SEM images of materials. Figure 9.4.1.1 shows the materials made for this study, IER embedded porous electrospun fibers and IER embedded dense electrospun fibers, along with the IER powder that was suspended in the electrospinning solution.

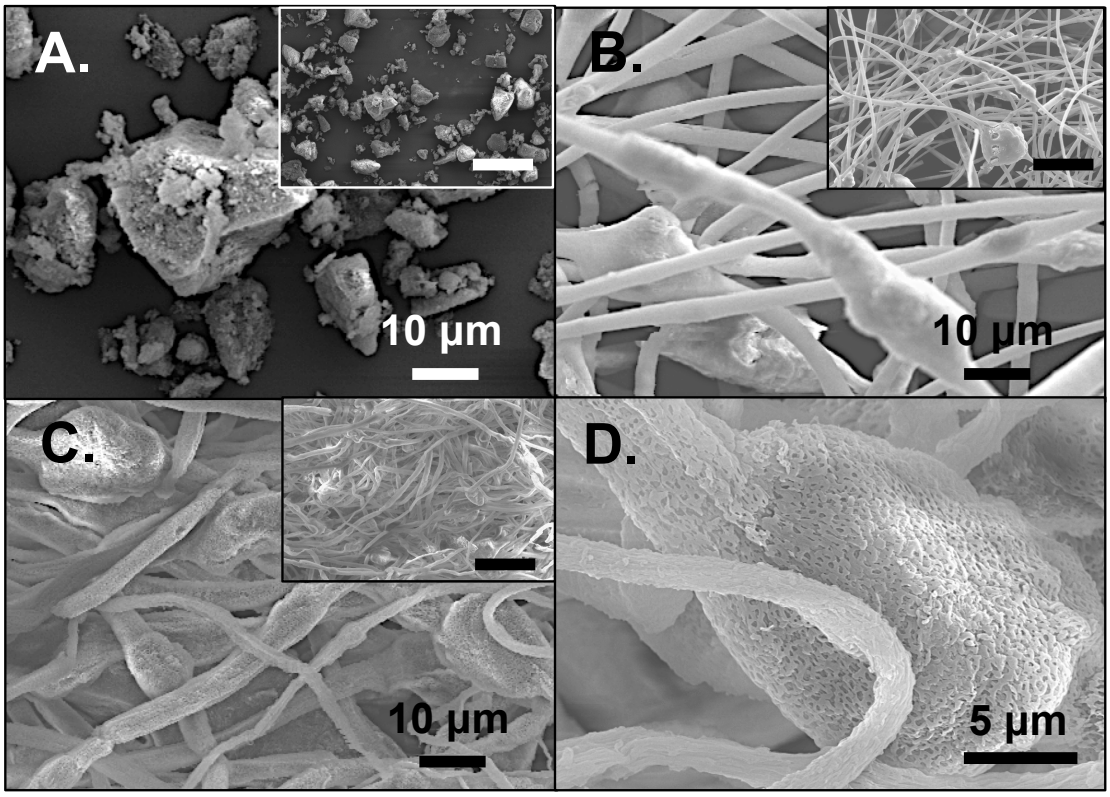

Figure 9.4.1.1. SEM images of (A) the IER particles, (B) IER particles embedded in dense electrospun fibers, (C) IER particles embedded in porous electrospun fibers, and (D) higher magnification image of IER particles embedded in porous electrospun fibers. Inset images each have a scale bar of 50 µm.

The images of the dense fiber show mostly smooth fibers, and many particles appear to be entirely embedded. Other resin particles appear to emerge at the surface, and in some cases the dense fiber appears to have some cracks or holes when wrapping some of the larger particles. The porous fiber scaffold appears to have a texture along all of the fibers, and from the higher magnification image in Figure 9.4.1.1(D) a pore network can be seen along the fibers.

9.4.2. Technique validation. To validate our instrumentation and approximations made during the derivation of our characteristic frequency response equation a film was tested that had been previously tested by Shi.(X. Shi et al., 2017) Variations in both offset and amplitude of the humidity profile were made at varying frequencies as shown in Figure 9.4.2.1.

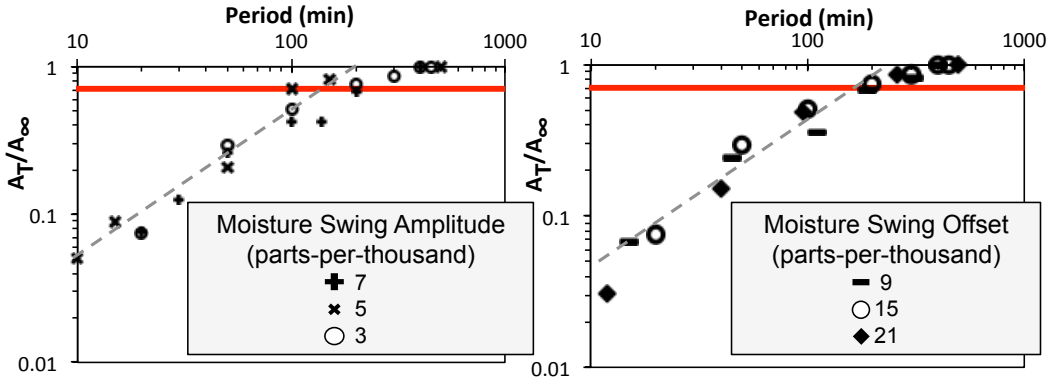

Figure 9.4.2.1. Moisture frequency response curves of carbon dioxide amplitude in the commercial film. The left chart has a constant offset of 15 parts-per-thousand with variable amplitude, and the right chart has constant amplitude of 3 parts-per-thousand and a variable offset. The red line represents an amplitude ratio of 0.707, and the dotted line represents an estimated first-order roll-off slope. A_f represents the carbon dioxide frequency response amplitude at the moisture swing frequency corresponding to the specified period, and A_∞ represents the carbon dioxide frequency response amplitude at the longest periods.

From these tests an apparent first-order response is seen over all samples tested based upon the agreement between the rolloff slope and the rolloff frequency. Each test also appears to demonstrate a similar rolloff frequency, suggesting that the uptake remains first-order regardless of moisture content- at least over the range and experimental precision of the test. The absorption half-time ($\mathbf{t_{1/2}}$) from these tests if found to be 138 ± 62 minutes from determining the value of τ graphically, and then solving for $\mathbf{t_{1/2}}$ with Eq 9.2. Previous experiments in literature made by Shi measured a half-time on this film of 107.5 minutes, which falls within this range. Although the precision of this technique appears low, due to the graphical nature of the technique it scales with

the inverse of the order of magnitude making it more precise over the shorter periods that will be used to characterize the new sorbent embedded fibers. Furthermore, smaller periods are expected to be more precise due to fewer environmental factors such as temperature changes in the room or small leaks.

9.4.3. Fiber scaffold characterization. Next, the same moisture swing profile was used to characterize the commercial film, dense IER-embedded electrospun fibers, and porous IER-embedded electrospun fibers. The results form these tests are shown in Figure 9.4.3.1.

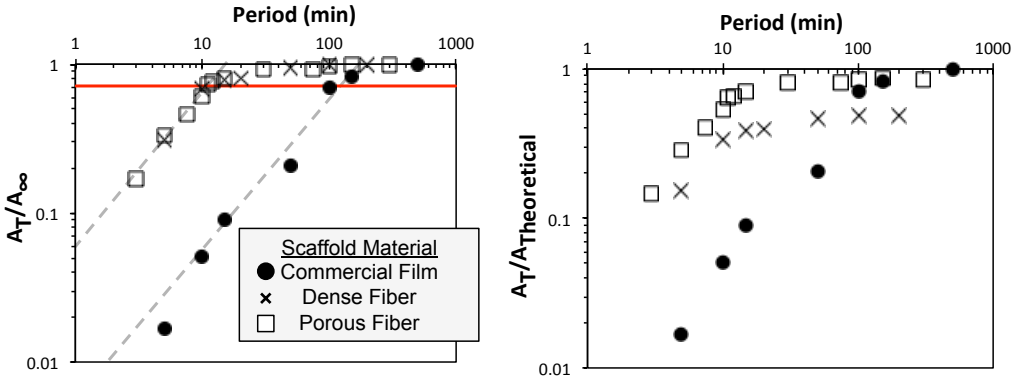

Figure 9.4.3.1. Moisture frequency response curves generated from carbon dioxide concentration response for the ion exchange resin embedded in the commercial film, porous fibers, and dense fibers. The sinusoidal moisture swing profile has amplitude of 5 parts-per-thousand and an offset of 15 parts-per-thousand in each case, with a variable frequency. In the figure on the left each material is normalized to its own maximum amplitude (A_∞), and in the figure on the right they are normalized the expected maximum amplitude if all the IER embedded in the fiber were available ($A_{Theoretical}$).

The half-time of sorption on IER embedded in each fiber scaffold is 10 ± 3 minutes. It can be seen that the uptake in the fiber samples is over an order of magnitude faster than the uptake in the commercial film, even though the exact same ion exchange resin is used. This demonstrates the incredible importance the binder has on the overall kinetic uptake of the sorbent. Both fiber samples have the same first order response, suggesting that all available particles

function by the same uptake pathway. Furthermore, it is confirmed that the technique precision is far more accurate at the lower periods.

The y-axis on the right-side graph on Figure 9.4.3.1 is reported as the actual CO_2 amplitude versus the maximum expected CO_2 amplitude expected if all particles in the particular sample are accessible (i.e. 32.5 wt% for dense fibers and 34.6 wt% for porous fibers). In the porous fiber scaffold 90% of the particles are accessible, and in the dense fiber only 50% of the particles are accessible. This demonstrates that the introduction of a pore networks throughout the fiber are beneficial for maximizing the exposure of particles.

Jones and coworkers suggested that a beneficial metric for comparing direct air capture sorbents is to plot their uptake versus sorption half-time. Some materials that their group had synthesized are plotted with data for the ion exchange resin embedded in films created by Shi, along with the materials tested in this work in Figure 9.4.3.2.

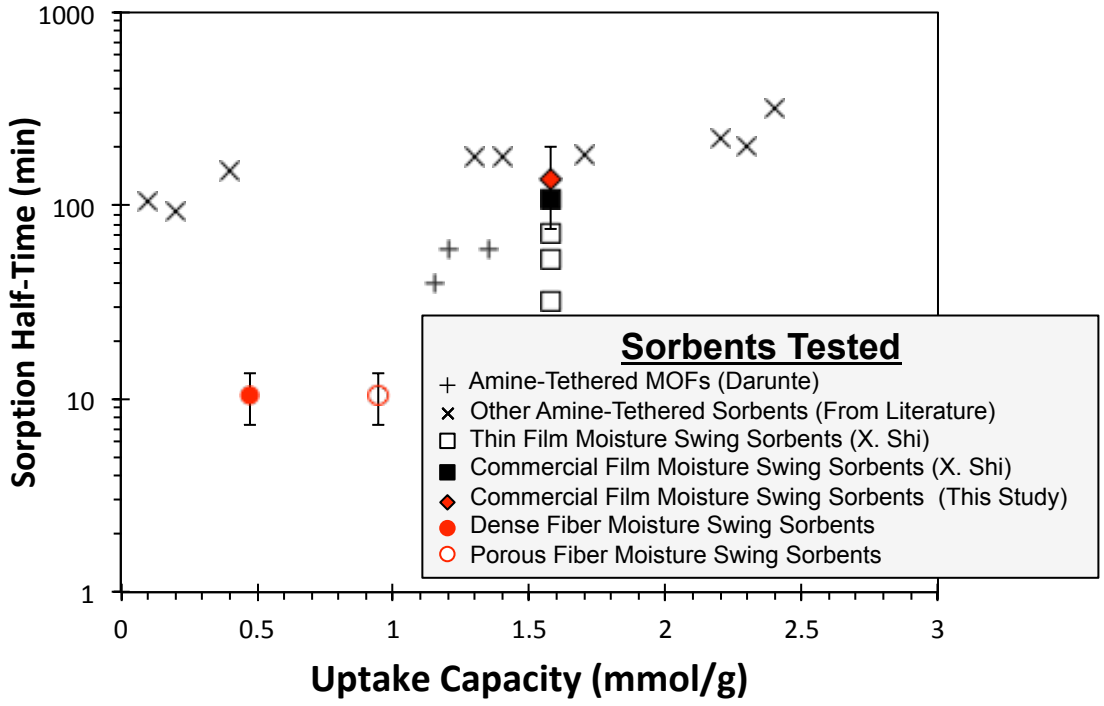

Figure 9.4.3.2. Various direct air capture sorbents plotted with sorption half-time versus uptake capacity. Amine-tethered MOFs come from work by Darunte,(Darunte, Oetomo, Walton, Sholl, &

Jones, 2016) and other amine-tethered sorbents come from other members of Jones's group,(Choi, Drese, et al., 2011; Choi, Gray, et al., 2011) thin film moisture swing sorbents come from Shi,(X. Shi et al., 2017) the commercial film was tested by Shi,(X. Shi et al., 2017) and the same commercial film was tested in this study for system validation. The dense fiber moisture swing sorbents and porous fiber moisture swing sorbents were each tested in this work.

In this study we did not directly measure the uptake capacity, however, because we used the same ion exchange resin studied by Shi, we assume that the capacity of the film is equivalent for the commercial film. The uptake capacities of the fiber samples are then estimated by their uptake in comparison to the commercial film. It may be observed that the fiber structures made in this work provide the fastest uptake kinetics observed in direct air capture sorbents to date. It also demonstrates that the fiber structure provides a much smaller resistance to uptake as compared to the film morphology, even though the exact same particles were used. These particles do not lead the field in uptake capacity, although higher loadings could be pursued.

Higher loadings of particle should be readily available in these electrospun scaffolds with further optimization of the fiber fabrication process. Higher loadings were pursued, and the appearance of good fibers immediately after electrospinning were visible for weight loadings up to 66%, however, these fibers slowly coalesce into mats and crumbled with time on the order of minutes. Our hypothesis for the cause of this is significant amounts of residual solvent left over in the insoluble resin that releases and dissolves the fiber structure. In future investigations it is expected that this problem may be mitigated with further processing such as an immediate quenching step in water bath after formation.

Nevertheless, even with reduced uptake capacities, the exceptional increase in sorption kinetics overcomes these issues. Ultimately the unifying metric that is of most important when considering uptake capacity and uptake rate is the average uptake per gram-hour ($\mathbf{\bar{Q}_{h,g}}$). This is approximated by the equation:

$$\bar{Q}_{h,g} = 60 * (0.5Q_t)/(2t_{\frac{1}{2}}) \quad (9.8)$$

where the factor 60 is added to convert from minutes to hours, the factor of 0.5 in front of Q_t is added since only half of the capacity is used, and the factor of 2 is added in front of the $\mathbf{t_{1/2}}$ to take into account desorption- using the approximation that desorption time is equal to sorption time. The data for each material tested in **Figure 9.4.3.2** is shown in **Figure 9.4.3.3** in terms of $\overline{\mathbf{Q}}_{\mathbf{h,g}}$.

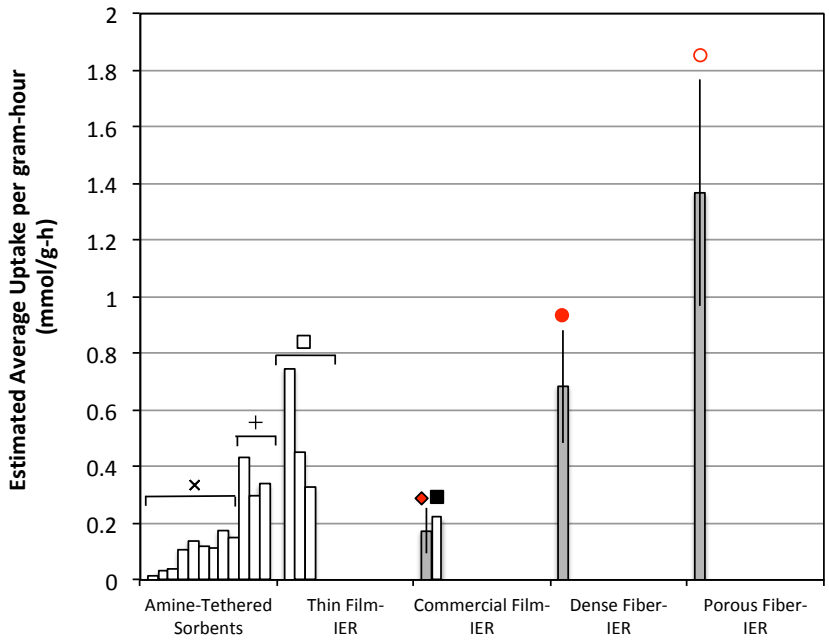

Figure 9.4.3.3. The estimated average uptake of carbon dioxide per gram-hour during direct air capture from sorbents found in literature (light boxes) and sorbents tested in this work (dark boxes). The symbols above each test correlate to the symbols used in Figure 9.4.3.2 for clarity.

Figure 9.4.3.2. shows that when the ion-exchange resin is embedded in a porous electrospun fiber scaffold, that it is able to capture CO_2 from ambient air faster than any other direct air capture sorbent to date. The drastic increase in uptake rate when switching from a film to fiber morphology may be explained by increasing the available surface of the resin particle. By allowing access to the particle from all sides, the effective distance fluid must diffuse through the particle is decreased. The results of this test are expected to be translatable to other sorption-based systems in other fluid streams as well.

9.5. Conclusion

In this work dense electrospun scaffolds and porous electrospun scaffolds were used for the immobilization of ion exchange resin particles for direct air capture. A moisture frequency response technique is used to characterize the uptake kinetics of these materials, along with a commercial film containing ion exchange resin. These results show that the kinetic rate of the commercial film is near that of work found in literature. 90% of particles are available for CO_2 sorption in the porous fiber scaffold, and only 50% are available in the dense fiber scaffold, demonstrating the advantages of solvothermal polymer additive removal (SPAR) induced pores. The kinetic uptake analysis of the fiber samples demonstrates field-leading kinetic uptakes, but a slight loss in uptake capacity. However, when considering the average uptake per gram-hour the porous electrospun scaffolds lead all direct air capture sorbents characterized in literature to date.

CHAPTER 10.

SUMMARY AND FUTURE WORK

10.1 Summary

In this work, two different design strategies for sorbent-containing electrospun fibers were developed. The first type of fiber structure presented was particle-embedded fibers. In this strategy, it was found that directly electrospinning sorbent suspensions in polymeric solutions led to sorbents that were coated in the fiber layer when the sorbent suspension was dilute. When the loading surpassed 33 weight percent particles began to appear on the surface of the fiber, which is hypothesized to be caused by a kinetic trapping effect. The second fiber formation strategy involves the removal of a soluble polymer additive from the spun fibers to introduce a pore network allowing access to imbedded fibers, which is expected to enable higher particle loadings and accessibility.

Type A fibers, particle-embedded electrospun fibers, are synthesized by directly spinning dilute suspensions of MOFs in polymeric solutions. MOF loadings are considered dilute when nearly all of the particles are embedded in the fiber. For the case of ZIF-8 in poly(ethylene oxide), this occurs at loadings less than 25 wt%. The externally exposed ZIF-8 is measured by nitrogen adsorption, and the total ZIF-8 concentration is measured by thermal gravimetric analysis. A model based on Fick's Laws is derived and validated against COMSOL models to demonstrate that these fibers may be used to observe excess selectivity when designed such that the polymer coating is selective towards a certain gas species, and the diffusivity through the MOF core is at least 10 times higher than the polymer coating. Two proof-of-concept studies are conducted to observe this phenomenon. In the first case, carbon dioxide and nitrogen isotherms are collected with pure ZIF-8, pure polymeric fibers, and ZIF-8 embedded fibers with maximum equilibrium times preset to 3 minutes so that a kinetic selectivity and uptake may be observed. From these results it is seen that the selectivity of the ZIF-8 embedded fibers is higher than both the pure ZIF-8 and the polymeric fibers. In the second proof-of-concept study HKUST-1 was embedded in

polystyrene fibers, and the carbon dioxide uptake capacity was shown to be preserved longer after exposure to water vapor versus the pure HKUST-1 particles.

Type C fibers, particle-containing porous fibers, were then developed by a polymer additive removal technique. ZIF-8 embedded in a blend of Matrimid and poly(ethylene oxide) polymers was electrospun, and the water-soluble poly(ethylene oxide) was removed. It was shown that the ZIF-8 remained behind in these fibers and a porous network was created where the poly(ethylene oxide) was removed. As a proof-of-concept study, an ion exchange resin (IER) was embedded in both a dense polystyrene fiber and a porous polystyrene fiber, and the uptake rate and IER accessibility was tested. During these tests it was observed that both the porous and dense fiber scaffold allowed the fastest uptake kinetics of any direct air capture sorbent measured to date, but that the porous fiber allowed over 90% IER accessibility while the dense structure only allowed 50% particle accessibility.

10.2. Future Work: Core-Shell Fibers

At the conclusion of this work, we have developed a theoretical model and material that both provide proof of enhanced selectivity and stability of core-shell fibers. However, we have not yet provided a model that predicts the actual properties of the materials we have made. This is because our model assumes a single pathway for adsorption; when in reality a large distribution of pathways exist (Figure 10.2.1).

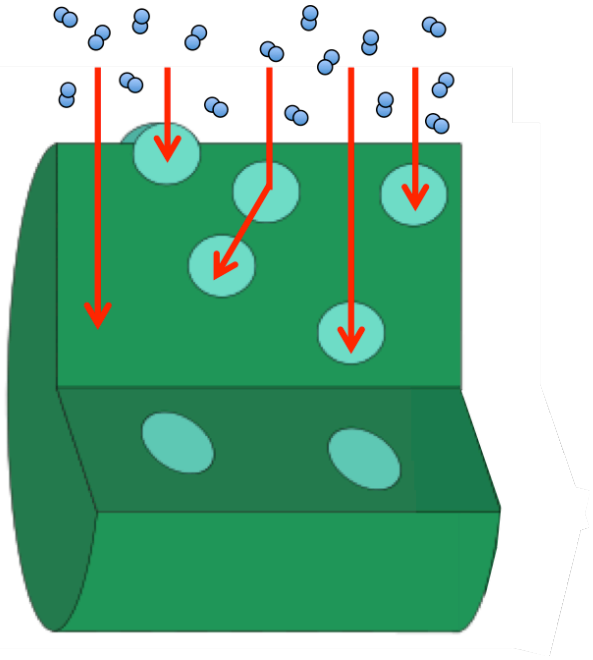

Figure 10.2.1. An illustration of some adsorption pathways that may exist in a particle-embedded fiber.

Two options exist to reconcile the model and material: make a more complex model or make a more complex material. In the first option, we may make a more complex model that solves for a distribution of pathways. There are two disadvantages to this route. It will require a more sophisticated characterization technique to solve for the distribution, and require a developed understanding of how to obtain such distributions. Also, this path also fails to address particles locating themselves on the surface after leaving the dilute regime. For this reason, an alternative strategy is suggested.

The second option for matching a predictive model to the material is to design a more sophisticated material that matches the current model. In this second generation material it would be ideal to maximize the particle loading, while making a material that exhibits a nearly cylindrical geometry that may be modeled as a single adsorption pathway. An idealized, realizable nanofiber morphology that is expected to match this criteria requires the direct electrospinning of a shell over a core material using a coaxial electrospinning setup as shown in Figure 10.2.2.

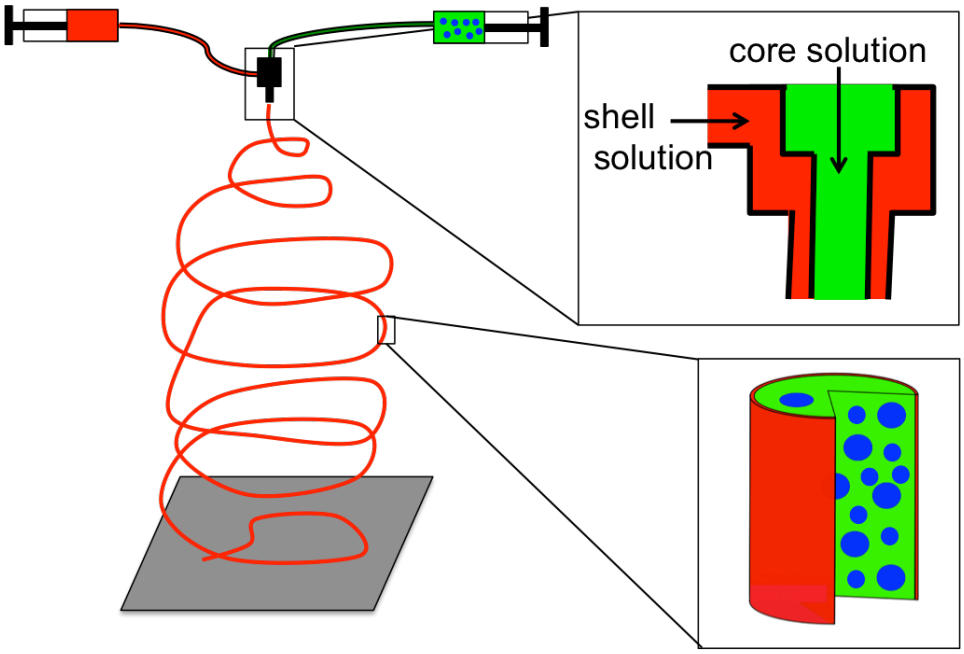

Figure 10.2.2. Coaxial electrospinning setup with 2 syringe pumps, a cross-section of the spinerette, and the fiber inset demonstrates the targeted fiber morphology.

Coaxial electrospinning has been successfully carried out by multiple other groups, for other purposes.(Qu & Guo, 2013) In our future work it would be ideal to use a shell solution composed of a protective barrier layer that also provides a strong structural support (such as Matrimid), and a core solution composed of a high particle loading, and a strong binder material that provides selectivity as well (such as poly(ethylene oxide)). Developing these materials, showing a tunable shell thickness, high loadings, and convergence between the material performance and predictive model would greatly enhance this technology. The mathematical model developed should also be solved for both cylindrical geometries (to solve for the case when d/D is small) and for spherical geometries for when d/D is large).

10.3. Future Work: Porous Fibers

In this work a methodology for preparing particle-containing porous fibers has been presented, and proof-of-concept work has shown these materials to be competitive as a shaping

material for kinetic uptake. Since the publication of chapter 8 in 2016, this method for increasing particle accessibility has been taken up by other groups as well for various separation-based applications. This includes work by Qin and coworkers, where catalysts for the destruction of water-borne biological contaminants are embedded in porous fibers and the catalytic activity and rate is nearly that of the pure catalyst.(D. Qin et al., 2017) The NSF-sponsored Nanotechnology-Enabled Water Treatment Center at Arizona State University is also pursuing this technology for embedding arsenic sorbents in fibers with preliminary success. In future work, new materials should be introduced to expand the scope of this technology.

Tradeoffs of pore structure, kinetics, and structural stability should be established. In our work we targeted the maximum pore volume, however, this likely came at the cost of mechanical stability. With maximum pore size we have seen incredibly fast kinetic uptake, yet Qin and coworkers observed satisfactory uptake rates while only removing 20% of the polymer in the fiber.

REFERENCES

Abràmoff, M. D., Magalhães, P. J., & Ram, S. J. (2004). Image processing with imageJ. *Biophotonics International*, *11*, 36–41. http://doi.org/10.1117/1.3589100

Agarwal, A., Raheja, A., Natarajan, T. S., & Chandra, R. S. (2012). Development of universal pH sensing electrospun nanofibers. *Sensors and Actuators B: Chemical*, *161*(1), 1097–1101. http://doi.org/https://doi.org/10.1016/j.snb.2011.12.027

Armstrong, M., Balzer, C., Shan, B., & Mu, B. (2017). Influence of Particle Size and Loading on Particle Accessibility in Electrospun Poly(ethylene oxide) and ZIF-8 Composite Fibers: Experiments and Theory, *33*(36), 9066–9072. http://doi.org/10.1021/acs.langmuir.7b01978

Armstrong, M., Balzer, C., Shan, B., & Mu, B. (2017). Influence of Particle Size and Loading on Particle Accessibility in Electrospun Poly (ethylene oxide) and ZIF-8 Composite Fibers : Experiments and Theory. *Langmuir*, *33*(36), 9066–9072. http://doi.org/10.1021/acs.langmuir.7b01978

Armstrong, M. R., Arredondo, K. Y. Y., Liu, C.-Y., Stevens, J. E., Mayhob, A., Shan, B., … Mu, B. (2015). UiO-66 MOF and Poly(vinyl cinnamate) Nanofiber Composite Membranes Synthesized by a Facile Three-Stage Process. *Industrial & Engineering Chemistry Research*, *54*, 12386–12392. http://doi.org/10.1021/acs.iecr.5b03334

Armstrong, M. R., Senthilnathan, S., Balzer, C. J., Shan, B., Chen, L., & Mu, B. (2017). Particle size studies to reveal crystallization mechanisms of the metal organic framework HKUST-1 during sonochemical synthesis. *Ultrasonics Sonochemistry*, *34*, 365–370. http://doi.org/10.1016/j.ultsonch.2016.06.011

Armstrong, M. R., Shan, B., Cheng, Z., Wang, D., Liu, J., & Mu, B. (2017). Adsorption and diffusion of carbon dioxide on the metal-organic framework CuBTB. *Chemical Engineering Science*, *167*, 10–17. http://doi.org/10.1016/j.ces.2017.03.049

Armstrong, M. R., Shan, B., Maringanti, S. V., Zheng, W., & Mu, B. (2016). Hierarchical Pore Structures and High ZIF-8 Loading on Matrimid Electrospun Fibers by Additive Removal from a Blended Polymer Precursor. *Industrial & Engineering Chemistry Research*, *55*(37), 9944–9951. http://doi.org/10.1021/acs.iecr.6b02479

Armstrong, M. R., Shan, B., & Mu, B. (2017). Microscopy Study of Morphology of Electrospun Fiber-MOF Composites with Secondary Growth. *MRS Advances*, *2*(46), 2457–2463. http://doi.org/10.1557/adv.201

Aziz, F., & Ismail, A. F. (2010). Preparation and characterization of cross-linked Matrimid membranes using para-phenylenediamine for O2/N2 separation. *Separation and Purification Technology*, *73*(3), 421–428. http://doi.org/10.1016/j.seppur.2010.05.002

Baerlocher, C., McCusker, L., & Olson, D. (2007). *Atlas of zeolite framework types* (Vol. 12). http://doi.org/10.1016/B978-044453064-6/50287-5

Balzer, C., Armstrong, M., Shan, B., Huang, Y., Liu, J., & Mu, B. (2018). Modeling Nanoparticle Dispersion in Electrospun Nanofibers. *Langmuir*, *34*(4), 1340–1346. http://doi.org/10.1021/acs.langmuir.7b03726

Balzer, C. J., Armstrong, M. R., Shan, B., & Mu, B. (2017). Composite MOF mixture as volatile organic compound sensor - A new approach to LMOF sensors. *Materials Letters*, *190*, 33–

36. http://doi.org/10.1016/j.matlet.2016.12.111

Bang, J. H., & Suslick, K. S. (2010). Applications of ultrasound to the synthesis of nanostructured materials. *Advanced Materials*. http://doi.org/10.1002/adma.200904093

Bansal, D., Meyer, B., & Salomon, M. (2008). Gelled membranes for Li and Li-ion batteries prepared by electrospinning. *Journal of Power Sources*, *178*(2), 848–851. http://doi.org/10.1016/j.jpowsour.2007.07.070

Bao, Z., Yu, L., Ren, Q., Lu, X., & Deng, S. (2011). Adsorption of CO 2 and CH 4 on a magnesium-based metal organic framework. *Journal of Colloid And Interface Science*, *353*(2), 549–556. http://doi.org/10.1016/j.jcis.2010.09.065

Barrer, R. M. (1968). Diffusion and Permeation in Heterogeneous Media. In J. Crank & G. S. Park (Eds.), *Diffusion in Polymers* (pp. 165–216). London: Academic Press Inc.

Basdogan, Y., & Keskin, S. (2015). Simulation and modelling of MOFs for hydrogen storage. *CrystEngComm*, *17*(2), 261–275. http://doi.org/10.1039/C4CE01711K

Batten, S. R., Champness, N. R., Chen, X., Garcia-martinez, J., Kitagawa, S., & Ohrstr, L. (2012). Coordination polymers , metal – organic frameworks and the need for terminology guidelines, 3001–3004. http://doi.org/10.1039/c2ce06488j

Batten, S. R., Champness, N. R., Chen, X., Garcia-martinez, J., Kitagawa, S., Öhrström, L., … Reedijk, J. (2013). Terminology of metal – organic frameworks and coordination polymers (IUPAC Recommendations 2013)*. *Pure Appl. Chem.*, *85*(8), 1715–1724.

Bechelany, M., Drobek, M., Vallicari, C., Abou Chaaya, A., Julbe, A., & Miele, P. (2015). Highly crystalline MOF-based materials grown on electrospun nanofibers. *Nanoscale*, *7*(13), 5794–802. http://doi.org/10.1039/c4nr06640e

Ben, T., Ren, H., Shengqian, M., Cao, D., Lan, J., Jing, X., … Zhu, G. (2009). Targeted synthesis of a porous aromatic framework with high stability and exceptionally high surface area. *Angewandte Chemie - International Edition*, *48*(50), 9457–9460. http://doi.org/10.1002/anie.200904637

Bhardwaj, N., & Kundu, S. C. (2010). Electrospinning: A fascinating fiber fabrication technique. *Biotechnology Advances*, *28*, 325–347. http://doi.org/10.1016/j.biotechadv.2010.01.004

Bigi, A., Cojazzi, G., Panzavolta, S., Rubini, K., & Roveri, N. (2001). Mechanical and thermal properties of gelatin films at different degrees of glutaraldehyde crosslinking. *Biomaterials*, *22*(8), 763–768. http://doi.org/10.1016/S0142-9612(00)00236-2

Bognitzki, M., Frese, T., Steinhart, M., Greiner, A., Wendorff, J. H., Schaper, A., & Hellwig, M. (2001). Preparation of fibers with nanoscaled morphologies: electrospinning of polymer blends. *Polymer Engineering and Science*, *41*(6), 982–989. http://doi.org/10.1002/pen.10799

Bordiga, S., Regli, L., Bonino, F., Groppo, E., Lamberti, C., Xiao, B., … Zecchina, A. (2007). Adsorption properties of HKUST-1 toward hydrogen and other small molecules monitored by IR. *Physical Chemistry Chemical Physics : PCCP*, *9*(21), 2676–85. http://doi.org/10.1039/b703643d

Brown, A. J., Johnson, J. R., Lydon, M. E., Koros, W. J., Jones, C. W., & Nair, S. (2012). Continuous polycrystalline zeolitic imidazolate framework-90 membranes on polymeric hollow fibers. *Angewandte Chemie (International Ed. in English)*, *51*(42), 10615–8.

http://doi.org/10.1002/anie.201206640

Cao, L., An, P., Xu, Z., & Huang, J. (2016). Performance evaluation of electrospun polyimide non-woven separators for high power lithium-ion batteries. *Journal of Electroanalytical Chemistry*, *767*, 34–39. http://doi.org/10.1016/j.jelechem.2016.01.041

Carne-Sanchez, A., Stylianou, K. C., Carbonell, C., Naderi, M., Imaz, I., & Maspoch, D. (2015). Protecting metal-organic framework crystals from hydrolytic degradation by spray-dry encapsulating them into polystyrene microspheres. *Advanced Materials*, *27*(5), 869–873. http://doi.org/10.1002/adma.201403827

Carné-Sánchez, A., Stylianou, K. C., Carbonell, C., Naderi, M., Imaz, I., & Maspoch, D. (2015). Protecting Metal-Organic Framework Crystals from Hydrolytic Degradation by Spray-Dry Encapsulating Them into Polystyrene Microspheres. *Advanced Materials*, *27*(5), 869–873. http://doi.org/10.1002/adma.201403827

Carslaw, H. S., & Jaeger, J. C. (1959). *Heat Conduction in Solids* (2nd ed.). Oxford University Press.

Cavka, J. H., Jakobsen, S., Olsbye, U., Guillou, N., Lamberti, C., Bordiga, S., & Lillerud, K. P. (2008). A new zirconium inorganic building brick forming metal organic frameworks with exceptional stability. http://doi.org/10.1021/ja8057953

Chawla, J., Kumar, R., & Kaur, I. (2015). Carbon nanotubes and graphenes as adsorbents for adsorption of lead ions from water: A review. *Journal of Water Supply: Research and Technology - AQUA*, *64*(6), 641–659. http://doi.org/10.2166/aqua.2015.102

Chen, L., Bromberg, L., Schreuder-Gibson, H., Walker, J., Alan Hatton, T., & Rutledge, G. C. (2009). Chemical protection fabrics via surface oximation of electrospun polyacrylonitrile fiber mats. *Journal of Materials Chemistry*, *19*(16), 2432. http://doi.org/10.1039/b818639a

Chen, W., Shi, L., Wang, Z., Zhu, J., Yang, H., Mao, X., … Yuan, S. (2016). Porous cellulose diacetate-SiO 2 composite coating on polyethylene separator for high-performance lithium-ion battery. *Carbohydrate Polymers*, *147*, 517–524. http://doi.org/10.1016/j.carbpol.2016.04.046

Choi, S., Drese, J. H., Eisenberger, P. M., & Jones, C. W. (2011). Application of amine-tethered solid sorbents for direct CO2 capture from the ambient air. *Environmental Science and Technology*, *45*(6), 2420–2427. http://doi.org/10.1021/es102797w

Choi, S., Gray, M. L., & Jones, C. W. (2011). Amine-tethered solid adsorbents coupling high adsorption capacity and regenerability for CO2 capture from ambient air. *ChemSusChem*, *4*(5), 628–635. http://doi.org/10.1002/cssc.201000355

Chung, G. S., Jo, S. M., & Kim, B. C. (2005). Properties of Carbon Nanofibers Prepared from Electrospun Polyimide. *Journal of Applied Polymer Science*, *97*, 165–170. http://doi.org/10.1002/app.21742

Chung, T. S., Chan, S. S., Wang, R., Lu, Z., & He, C. (2003). Characterization of permeability and sorption in Matrimid/C60 mixed matrix membranes. *Journal of Membrane Science*, *211*(1), 91–99. http://doi.org/10.1016/S0376-7388(02)00385-X

Collins, G., Federici, J., Imura, Y., Catalani, L. H., Collins, G., Federici, J., … Catalani, L. H. (2012). Charge generation , charge transport , and residual charge in the electrospinning of polymers : A review of issues and complications. *Journal of Applied Physics*, *44701*(111). http://doi.org/10.1063/1.3682464

Containing, F., & Rectangular, L. (1995). Hydrothermal Synthesis of a Metal-Organic Framework Containing Large Rectangular Channels. *Journal of the American Chemical Society*, *117*, 10401–10402. http://doi.org/10.1021/ja00146a033

Crank, J. (1975). *The Mathematics of Diffusion* (2nd ed.). Oxford University Press.

Cravillon, J., Nayuk, R., Springer, S., Feldhoff, A., Huber, K., & Wiebcke, M. (2011). Controlling zeolitic imidazolate framework nano- and microcrystal formation: Insight into crystal growth by time-resolved in situ static light scattering. *Chemistry of Materials*, *23*(8), 2130–2141. http://doi.org/10.1021/cm103571y

Dahi, A., Fatyeyeva, K., Langevin, D., Chappey, C., Rogalsky, S. P., Tarasyuk, O. P., & Marais, S. (2014). Polyimide/ionic liquid composite membranes for fuel cells operating at high temperatures. *Electrochimica Acta*, *130*, 830–840. http://doi.org/10.1016/j.electacta.2014.03.071

Darunte, L. A., Oetomo, A. D., Walton, K. S., Sholl, D. S., & Jones, C. W. (2016). Direct Air Capture of CO2 Using Amine Functionalized MIL-101(Cr), *101*, 4–11. http://doi.org/10.1021/acssuschemeng.6b01692

Daynes, H. A. (1920). The Process of Diffusion through a Rubber Membrane. *Proc. Roy. Soc. (London)*, *A97*, 286–307.

Department of Energy. (2005). *Materials for Separation Technologies : Energy and Emission Reduction Opportunities*.

Desantis, D., Mason, J. A., James, B. D., Houchins, C., Long, R., & Veenstra, M. (2017). Techno-economic Analysis of Metal − Organic Frameworks for Hydrogen and Natural Gas Storage. *Energy & Fuels*, (31), 2024–2032. http://doi.org/10.1021/acs.energyfuels.6b02510

Deserno, M., & Bickel, T. (2003). Wrapping of a spherical colloid by a fluid membrane. *Europhysics Letters*, *62*(5), 767–772. http://doi.org/10.1209/epl/i2003-00438-4

Dietrich, C., Angelova, M., & Pouligny, B. (1997). Adhesion of Latex Spheres to Giant Phospholipid Vesicles: Statics and Dynamics. *Journal de Physique II*, *7*(11), 1651–1682. http://doi.org/10.1051/jp2:1997208

Ding, B., Kim, H. Y., Lee, S. C., Lee, D. R., & Choi, K. J. (2002). Preparation and characterization of nanoscaled poly(vinyl alcohol) fibers via electrospinning. *Fibers and Polymers*, *3*(2), 73–79. http://doi.org/Doi 10.1007/Bf02875403

Do, D. D. (1998). *Adsorption Analysis: Equilibria and Kinetics*. Imperial College Press.

Doktycz, S. J., & Suslick, K. S. (1990). Interparticle collisions driven by ultrasound. *Science*, *247*(4946), 1067–1069. http://doi.org/10.1126/science.2309118

Dong, X., Liu, Q., & Huang, A. (2016). Highly permselective MIL-68(Al)/matrimid mixed matrix membranes for CO2/CH4 separation. *Journal of Applied Polymer Science*, *133*(22), 1–8. http://doi.org/10.1002/app.43485

Drage, T. C., Snape, C. E., Stevens, L. A., Wood, J., Wang, J., & Cooper, A. I. (2012). Materials challenges for the development of solid sorbents for post-combustion carbon capture. *Journal of Materials Chemistry*, *22*, 2815–2823. http://doi.org/10.1039/c2jm12592g

Ersen, O., Florea, I., & Hirlimann, C. (2015). Exploring nanomaterials with 3D electron microscopy. *Biochemical Pharmacology*, *18*(7), 395–408. http://doi.org/10.1016/j.mattod.2015.04.004

Faheem, S. A., Jakubczak, P., Low, J. J., Willis, R. R., & Snurr, R. Q. (2009). Enhanced CO2 Adsorption in Metal-Organic Frameworks via Occupation of Open-Metal Sites by Coordinated Water Molecules. *Chem. Mater.*, (13), 1425–1430.

Fang, J., Lin, T., Tian, W., Sharma, A., & Wang, X. (2007). Toughened electrospun nanofibers from crosslinked elastomer-thermoplastic blends. *Journal of Applied Polymer Science*, *105*(4), 2321–2326. http://doi.org/10.1002/app.26422

Francis, L., Maab, H., AlSaadi, a., Nunes, S., Ghaffour, N., & Amy, G. L. L. (2013). Fabrication of electrospun nanofibrous membranes for membrane distillation application. *Desalination and Water Treatment*, *51*(7–9), 1337–1343. http://doi.org/10.1080/19443994.2012.700037

Furukawa, S., Reboul, J., Diring, S., Sumida, K., & Kitagawa, S. (2014). Structuring of metal–organic frameworks at the mesoscopic/macroscopic scale. *Chem. Soc. Rev.*, *43*(16), 5700–5734. http://doi.org/10.1039/C4CS00106K

Guerrero, J., Rivero, J., Gundabala, V. R., Perez-saborid, M., & Fernandez-nieves, A. (2014). Whipping of electrified liquid jets, 21–25. http://doi.org/10.1073/pnas.1411698111

Guerrero, V. V., Yoo, Y., McCarthy, M. C., & Jeong, H.-K. (2010). HKUST-1 membranes on porous supports using secondary growth. *Journal of Materials Chemistry*, *20*, 3938. http://doi.org/10.1039/b924536g

Halsey, G. (1948). Physical Adsorption on Non-Uniform Surfaces. *Journal of Chemical Physics*, *16*, 931. http://doi.org/10.1063/1.1746689

Han, W., Nurwaha, D., Li, C., & Wang, X. (2014). Free Surface Electrospun Fibers : The Combined Effect of Processing Parameters. *Polymer Engineering & Science*. http://doi.org/10.1002/pen

Hem, S. L. (1967). The effect of ultrasonic vibrations on crystallization processes. *Ultrasonics*, *5*, 202–207. http://doi.org/10.1016/0041-624X(67)90061-3

Herm, Z. R., Wiers, B. M., Mason, J. a, van Baten, J. M., Hudson, M. R., Zajdel, P., … Long, J. R. (2013). Separation of hexane isomers in a metal-organic framework with triangular channels. *Science*, *340*(May), 960–4. http://doi.org/10.1126/science.1234071

Hirai, K., Furukawa, S., Kondo, M., Uehara, H., Sakata, O., & Kitagawa, S. (2011). Sequential Functionalization of Porous Coordination Polymer Crystals **. *Angewandte Chemie (International Ed. in English)*, *50*, 8057–8061. http://doi.org/10.1002/anie.201101924

Hoskins, B. F., & Robson, R. (1989). Infinite Polymeric Frameworks Consisting of Three Dimensionally Linked Rod-like Segments. *Journal of the American Chemical Society*, *111*(15), 5962–5964.

Howarth, A. J., Liu, Y., Li, P., Li, Z., Wang, T. C., & Farha, O. K. (2016). Chemical, thermal, and mechanical stabilities of metal-organic frameworks. *Nature Reviews Materials*, *1*(15018), 1–15. http://doi.org/10.1038/natrevmats.2015.18

Howarth, A. J., Liu, Y., Li, P., Li, Z., Wang, T. C., Hupp, J. T., & Farha, O. K. (2016). Chemical, thermal and mechanical stabilities of metal–organic frameworks. *Nature Reviews Materials*, *1*, 15018. Retrieved from http://dx.doi.org/10.1038/natrevmats.2015.18

Hu, Y., Kazemian, H., Rohani, S., Huang, Y., & Song, Y. (2011). In situ high pressure study of ZIF-8 by FTIR spectroscopy. *Chemical Communications (Cambridge, England)*, *47*(47), 12694–6. http://doi.org/10.1039/c1cc15525c

Hua, M., Zhang, S., Pan, B., Zhang, W., Lv, L., & Zhang, Q. (2012). Heavy metal removal from water/wastewater by nanosized metal oxides: A review. *Journal of Hazardous Materials*, *211–212*, 317–331. http://doi.org/10.1016/j.jhazmat.2011.10.016

Huang, H., Zhang, W., Liu, D., Liu, B., Chen, G., & Zhong, C. (2011). Effect of temperature on gas adsorption and separation in ZIF-8: A combined experimental and molecular simulation study. *Chemical Engineering Science*, *66*(23), 6297–6305. http://doi.org/10.1016/j.ces.2011.09.009

Huang, X. (2011). Separator technologies for lithium-ion batteries. *Journal of Solid State Electrochemistry*, *15*(4), 649–662. http://doi.org/10.1007/s10008-010-1264-9

Ibrahim, M. M., Hafez, S. A., & Mahdy, M. M. (2013). Organogels, hydrogels and bigels as transdermal delivery systems for diltiazem HCL. *Asian Journal of Pharmaceutical Sciences*, *8*(1), 46–54. http://doi.org/10.1016/j.ajps.2013.07.006

Islas-jácome, A., & González-zamora, E. (2017). Structure stability of HKUST-1 towards water and ethanol and their effects on its CO2 capture properties. *Dalton Transactions*, *46*, 9192–9200. http://doi.org/10.1039/c7dt01845b

Jaeger, H. M., & Nagel, S. R. (1992). Physics of the Granular State. *Science*, *255*(5051), 1523–1531. http://doi.org/10.1126/science.255.5051.1523

James, J. B., Wang, J., Meng, L., & Lin, Y. S. (2017). ZIF - 8 Membrane Ethylene / Ethane Transport Characteristics in Single and Binary Gas Mixtures. *Industrial & Engineering Chemistry Research*, *56*, 7567–7575. http://doi.org/10.1021/acs.iecr.7b01536

Jayachandrababu, K. C., Sholl, D. S., & Nair, S. (2017). Structural and Mechanistic Differences in Mixed-Linker Zeolitic Imidazolate Framework Synthesis by Solvent Assisted Linker Exchange (SALE) and de novo Routes. *Journal of the American Chemical Society*, *139*, 5906–5915. http://doi.org/10.1021/jacs.7b01660

Jiang, W., Liu, Z., Kong, Q., Yao, J., Zhang, C., Han, P., & Cui, G. (2013). A high temperature operating nanofibrous polyimide separator in Li-ion battery. *Solid State Ionics*, *232*, 44–48. http://doi.org/10.1016/j.ssi.2012.11.010

Jiao, Y., Morelock, C. R., Burtch, N. C., Moun, W. P., Hungerford, J. T., & Walton, K. S. (2015). Tuning the Kinetic Water Stability and Adsorption Interactions of Mg-MOF-74 by Partial Substitution with Co or Ni. *Industrial & Engineering Chemistry Research*, *54*, 12408–12414. http://doi.org/10.1021/acs.iecr.5b03843

Jin, R., Bian, Z., Li, J., Ding, M., & Gao, L. (2013). ZIF-8 crystal coatings on a polyimide substrate and their catalytic behaviours for the Knoevenagel reaction. *Dalton Transactions (Cambridge, England : 2003)*, *42*(11), 3936–40. http://doi.org/10.1039/c2dt32161k

Jost, W. (1952). *Diffusion in Solids, Liquids and Gases*. (E. Hutchinson, Ed.). New York, NY: Academic Press Inc.

Ju, H., McCloskey, B. D., Sagle, A. C., Wu, Y. H., Kusuma, V. A., & Freeman, B. D. (2008). Crosslinked poly(ethylene oxide) fouling resistant coating materials for oil/water separation. *Journal of Membrane Science*, *307*(2), 260–267. http://doi.org/10.1016/j.memsci.2007.09.028

Jung, K. H., & Ferraris, J. P. (2012). Preparation and electrochemical properties of carbon nanofibers derived from polybenzimidazole/polyimide precursor blends. *Carbon*, *50*(14), 5309–5315. http://doi.org/10.1016/j.carbon.2012.07.019

Kandiah, M., Nilsen, M. H., Usseglio, S., Jakobsen, S., Olsbye, U., Tilset, M., … Lillerud, K. P. (2010). Synthesis and stability of tagged UiO-66 Zr-MOFs. *Chemistry of Materials*, *22*(10), 6632–6640. http://doi.org/10.1021/cm102601v

Katz, M. J., Mondloch, J. E., Totten, R. K., Park, J. K., Nguyen, S. T., Farha, O. K., & Hupp, J. T. (2014). Simple and compelling biomimetic metal-organic framework catalyst for the degradation of nerve agent simulants. *Angewandte Chemie - International Edition*, *53*(Iii), 497–501. http://doi.org/10.1002/anie.201307520

Katz, M. J., Moon, S.-Y., Mondloch, J. E., Beyzavi, M. H., Stephenson, C. J., Hupp, J. T., & Farha, O. K. (2015). Exploiting parameter space in MOFs: a 20-fold enhancement of phosphate-ester hydrolysis with UiO-66-NH 2. *Chem. Sci.*, *6*(4), 2286–2291. http://doi.org/10.1039/C4SC03613A

Khan, N. A., & Jhung, S. H. (2009). Facile syntheses of metal-organic framework Cu3(BTC)2(H2O)3 under ultrasound. *Bulletin of the Korean Chemical Society*, *30*(12), 2921–2926. http://doi.org/10.5012/bkcs.2009.30.12.2921

Kim, K., Luu, Y. K., Chang, C., Fang, D., Hsiao, B. S., Chu, B., & Hadjiargyrou, M. (2004). Incorporation and controlled release of a hydrophilic antibiotic using poly(lactide-co-glycolide)-based electrospun nanofibrous scaffolds. *Journal of Controlled Release*, *98*(1), 47–56. http://doi.org/10.1016/j.jconrel.2004.04.009

Ko, F. K., & Wan, Y. (2014). *Introduction to Nanofiber Materials*. Cambridge, United Kingdom: Cambridge University Press.

Kornev, K. G. (2011). Electrospinning: Distribution of charges in liquid jets. *Journal of Applied Physics*, *110*(12), 1–6. http://doi.org/10.1063/1.3671629

Kuiper, S., Embrechts, A., Every, H. A., De Vries, T., & De Smet, L. C. P. M. (2013). Matrimid aerogels by temperature-controlled, solution-based crosslinking. *Macromolecular Materials and Engineering*, *298*(8), 868–875. http://doi.org/10.1002/mame.201200335

Kumar, P., Vellingiri, K., Kim, K., Brown, R. J. C., & Manos, M. J. (2017). Modern progress in metal-organic frameworks and their composites for diverse applications. *Microporous and Mesoporous Materials*, *253*(January 2016), 251–265. http://doi.org/10.1016/j.micromeso.2017.07.003

Lackner, K. S. (2009). Capture of carbon dioxide from ambient air. *European Physical Journal: Special Topics*, *176*(1), 93–106. http://doi.org/10.1140/epjst/e2009-01150-3

Langmuir, I. (1932). *Surface chemistry**.

Lee, Y.-R., Jang, M.-S., Cho, H.-Y., Kwon, H.-J., Kim, S., & Ahn, W.-S. (2015). ZIF-8: A comparison of synthesis methods. *Chemical Engineering Journal*, *271*, 276–280. http://doi.org/10.1016/j.cej.2015.02.094

Lee, Y., Kim, S., Kang, J. K., & Cohen, S. M. (2015). Photocatalytic CO2 reduction by a mixed metal (Zr/Ti), mixed ligand metal-organic framework under visible light irradiation. *Chem. Commun.*, *51*, 5735–5738. http://doi.org/10.1039/C5CC00686D

Li, H., Lin, Z., Zhou, X., Wang, X., Li, Y., Wang, H., & Li, Z. (2017). Ultrafast room temperature synthesis of novel composites Imi @ Cu-BTC with improved stability against moisture. *Chemical Engineering Journal*, *307*, 537–543. http://doi.org/10.1016/j.cej.2016.08.128

Li, J., Tian, W., Yan, H., He, L., & Tuo, X. (2016). Preparation and performance of aramid

nanofiber membrane for separator of lithium ion battery. *Journal of Applied Polymer Science*, *133*(30), 1–8. http://doi.org/10.1002/app.43623

Li, T., Sullivan, J. E., & Rosi, N. L. (2013). Design and Preparation of a Core − Shell Metal − Organic Framework for Selective CO 2 Capture. *Journal of the American Chemical Society*, *135*, 9984–9987.

Lin, H., & Freeman, B. D. (2004). Gas solubility, diffusivity and permeability in poly(ethylene oxide). *Journal of Membrane Science*, *239*(1), 105–117. http://doi.org/10.1016/j.memsci.2003.08.031

Liu, D., Huxford, R. C., & Lin, W. (2011). Phosphorescent Nanoscale Coordination Polymers as Contrast Agents for Optical Imaging **. *Angewandte Chemie (International Ed. in English)*, *50*, 3696–3700. http://doi.org/10.1002/anie.201008277

Liu, D., Ma, X., Xi, H., & Lin, Y. S. (2014). Gas transport properties and propylene/propane separation characteristics of ZIF-8 membranes. *Journal of Membrane Science*, *451*, 85–93. http://doi.org/10.1016/j.memsci.2013.09.029

Liu, J., Thallapally, P. K., McGrail, B. P., Brown, D. R., & Liu, J. (2012). Progress in adsorption-based CO $_2$ capture by metal–organic frameworks. *Chem. Soc. Rev.*, *41*, 2308–2322. http://doi.org/10.1039/C1CS15221A

Liu, L., Sanders, E. S., Johnson, J. R., Karvan, O., Kulkarni, S., Hasse, D. J., & Koros, W. J. (2013). Influence of membrane skin morphology on CO2/N2 separation at sub-ambient temperatures. *Journal of Membrane Science*, *446*, 433–439. http://doi.org/10.1016/j.memsci.2013.06.001

Liu, X., Li, Y., Ban, Y., Peng, Y., Jin, H., Bux, H., … Yang, W. (2013). Improvement of hydrothermal stability of zeolitic imidazolate frameworks. *Chem. Commun.*, *49*, 9140–9142. http://doi.org/10.1039/c3cc45308a

Lively, R. P., Leta, D. P., Derites, B. A., Chance, R. R., & Koros, W. J. (2011). Hollow fiber adsorbents for CO 2 capture : Kinetic sorption performance. *Chemical Engineering Journal*, *171*(3), 801–810. http://doi.org/10.1016/j.cej.2011.01.004

Lõpez-Maya, E., Montoro, C., Rodríguez-Albelo, L. M., Aznar Cervantes, S. D., Lozano-Pérez, A. A., Cenís, J. L., … Navarro, J. A. R. (2015). Textile/metal-organic-framework composites as self-detoxifying filters for chemical-warfare agents. *Angewandte Chemie - International Edition*, *54*(23), 6790–6794. http://doi.org/10.1002/anie.201502094

Lu, G., Farha, O. K., Kreno, L. E., Schoenecker, P. M., Walton, K. S., Van Duyne, R. P., & Hupp, J. T. (2011). Fabrication of metal-organic framework-containing silica-colloidal crystals for vapor sensing. *Advanced Materials*, *23*, 4449–4452. http://doi.org/10.1002/adma.201102116

Lu, G., Li, S., Guo, Z., Farha, O. K., Hauser, B. G., Qi, X., … Huo, F. (2012). Imparting functionality to a metal-organic framework material by controlled nanoparticle encapsulation. *Nature Chemistry*, *4*(4), 310–316. http://doi.org/10.1038/nchem.1272

Luo, C. J., Stoyanov, S. D., Stride, E., Pelan, E., & Edirisinghe, M. (2012). Electrospinning versus fibre production methods : from specifics to technological convergence. *Chem Soc Rev*, 4708–4735. http://doi.org/10.1039/c2cs35083a

Lyoo, W. S., Youk, J. H., Lee, S. W., & Park, W. H. (2005). Preparation of porous ultra-fine poly(vinyl cinnamate) fibers. *Materials Letters*, *59*(28), 3558–3562.

http://doi.org/10.1016/j.matlet.2005.06.027

Ma, Y., Li, L. B., Gao, G. X., Yang, X. Y., You, J., & Yang, P. X. (2016). Colloids and Surfaces A : Physicochemical and Engineering Aspects Ionic conductivity enhancement in gel polymer electrolyte membrane with N -methyl- N -butyl-piperidine-bis (trifluoromethylsulfonyl) imide ionic liquid for lithium ion battery, *502*(4), 130–138. http://doi.org/10.1016/j.colsurfa.2016.05.011

Majano, G., & Pérez-Ramírez, J. (2012). Room Temperature Synthesis and Size Control of HKUST-1. *Helvetica Chimica Acta*, *95*(11), 2278–2286. http://doi.org/10.1002/hlca.201200466

Majano, G., & Pérez-Ramírez, J. (2013). Scalable room-temperature conversion of copper(II) hydroxide into HKUST-1 (Cu3(btc)2). *Advanced Materials*, *25*(Ii), 1052–1057. http://doi.org/10.1002/adma.201203664

Miao, Y. E., Zhu, G. N., Hou, H., Xia, Y. Y., & Liu, T. (2013). Electrospun polyimide nanofiber-based nonwoven separators for lithium-ion batteries. *Journal of Power Sources*, *226*, 82–86. http://doi.org/10.1016/j.jpowsour.2012.10.027

Mondloch, J. E., Katz, M. J., Isley III, W. C., Ghosh, P., Liao, P., Bury, W., … Farha, O. K. (2015). Destruction of chemical warfare agents using metal–organic frameworks. *Nature Materials*, (March), 1–5. http://doi.org/10.1038/nmat4238

Mughal, A., Chan, H. K., Weaire, D., & Hutzler, S. (2012). Dense packings of spheres in cylinders: Simulations. *Physical Review E - Statistical, Nonlinear, and Soft Matter Physics*, *85*(5). http://doi.org/10.1103/PhysRevE.85.051305

Mustafa, D., Breynaert, E., Bajpe, S. R., Martens, J. a, & Kirschhock, C. E. a. (2011). Stability improvement of Cu3(BTC)2 metal-organic frameworks under steaming conditions by encapsulation of a Keggin polyoxometalate. *Chemical Communications (Cambridge, England)*, *47*, 8037–8039. http://doi.org/10.1039/c1cc12341f

Ordoñez, M. J. C., Balkus, K. J., Ferraris, J. P., & Musselman, I. H. (2010). Molecular sieving realized with ZIF-8/Matrimid mixed-matrix membranes. *Journal of Membrane Science*, *361*(1–2), 28–37. http://doi.org/10.1016/j.memsci.2010.06.017

Ostermann, R., Cravillon, J., Weidmann, C., Wiebcke, M., & Smarsly, B. M. (2011). Metal-organic framework nanofibers via electrospinning. *Chemical Communications (Cambridge, England)*, *47*, 442–444. http://doi.org/10.1039/c0cc02271c

Pai, C. L., Boyce, M. C., & Rutledge, G. C. (2011). Mechanical properties of individual electrospun PA 6(3)T fibers and their variation with fiber diameter. *Polymer*, *52*(10), 2295–2301. http://doi.org/10.1016/j.polymer.2011.03.041

Papporello, R. L., Miro, E. E., & Zamaro, J. M. (2015). Secondary growth of ZIF-8 films onto copper-based foils. Insight into surface interactions. *Microporous and Mesoporous Materials*, *211*, 64–72. http://doi.org/10.1016/j.micromeso.2015.02.049

Park, K. S., Ni, Z., Côté, A. P., Choi, J. Y., Huang, R., Uribe-Romo, F. J., … Yaghi, O. M. (2006). Exceptional chemical and thermal stability of zeolitic imidazolate frameworks. *Proceedings of the National Academy of Sciences of the United States of America*, *103*, 10186–10191. http://doi.org/10.1073/pnas.0602439103

Paul, D. R., & DiBenedetto, A. T. (1965). Diffusion in Amorphous Polymers. *Journal of Polymer Science Part C*, *10*(17), 17–44.

Peng, Y., Krungleviciute, V., Eryazici, I., Hupp, J. T., Farha, O. K., & Yildirim, T. (2013). Methane Storage in Metal − Organic Frameworks: Current Records, Surprise Findings, and Challenges. *Journal of the American Chemical Society*, *135*, 11887–11894. http://doi.org/10.1021/ja4045289

Pimentel, B. R., Fultz, A. W., Presnell, K. V, & Lively, R. P. (2017). Synthesis of Water-Sensitive Metal − Organic Frameworks within Fiber Sorbent Modules. *Industrial & Engineering Chemistry Research*, *56*, 5070–5077. http://doi.org/10.1021/acs.iecr.7b00630

Prozorov, T., Prozorov, R., & Suslick, K. S. (2004). High velocity interparticle collisions driven by ultrasound. *Journal of the American Chemical Society*, *126*(43), 13890–1. http://doi.org/10.1021/ja049493o

Qadir, N., Said, S. A. M., & Bahaidarah, H. M. (2015). Structural stability of metal organic frameworks in aqueous media – Controlling factors and methods to improve hydrostability and hydrothermal cyclic stability. *Microporous and Mesoporous Materials*, *201*, 61–90. http://doi.org/10.1016/j.micromeso.2014.09.034

Qian, X., Sun, F., Sun, J., Wu, H., Xiao, F., Wu, X., & Zhu, G. (2017). Imparting surface hydrophobicity to metal–organic frameworks using a facile solution-immersion process to enhance water stability for CO_2 capture. *Nanoscale*, *9*(5), 2003–2008. http://doi.org/10.1039/C6NR07801J

Qin, D., Lu, W., Zhu, Z., Li, N., Xu, T., Wang, G., & Chen, W. (2017). Free Channel Formation around Graphitic Carbon Nitride Embedded in Porous Polyethylene Terephthalate Nano fi bers with Excellent Reusability for Eliminating Antibiotics under Solar Irradiation. *Industrial & Engineering Chemistry Research*, *56*, 11151–11160. http://doi.org/10.1021/acs.iecr.7b02800

Qin, X.-H., & Wang, S.-Y. (2006). Filtration properties of electrospinning nanofibers. *Journal of Applied Polymer Science*, *102*(2), 1285–1290. http://doi.org/10.1002/app.24361

Qu, H., & Guo, Z. (2013). Coaxial electrospun nanostructures and their applications. *Journal of Materials Chemistry A*, (1996), 11513–11528. http://doi.org/10.1039/c3ta12390a

Raatz, M., Lipowsky, R., & Weikl, T. R. (2014). Cooperative wrapping of nanoparticles by membrane tubes. *Soft Matter*, *10*(20), 3570–7. http://doi.org/10.1039/c3sm52498a

Rahmani, M. R., Kazemi, a., Talebnia, F., & Khanbabaei, G. (2014). Preparation and characterization of cross-linked Matrimid membranes for CO2/CH4 separation. *Polymer Science Series B*, *56*(5), 650–656. http://doi.org/10.1134/S1560090414050108

Rajendran, A., Soon, L., Tan, C., Sue, J., & Lim, T. (2015). Energy and cost estimates for capturing CO 2 from a dry flue gas using pressure / vacuum swing adsorption. *Chemical Engineering Research and Design*, *102*, 354–367. http://doi.org/10.1016/j.cherd.2015.06.033

Ramesh, S., Yuen, T. F., & Shen, C. J. (2008). Conductivity and FTIR studies on PEO-LiX [X: CF3SO3-, SO42-] polymer electrolytes. *Spectrochimica Acta - Part A: Molecular and Biomolecular Spectroscopy*, *69*(2), 670–675. http://doi.org/10.1016/j.saa.2007.05.029

Rangel Rangel, E., Maya, E. M., Sánchez, F., de Abajo, J., & de la Campa, J. G. (2013). Gas separation properties of mixed-matrix membranes containing porous polyimides fillers. *Journal of Membrane Science*, *447*, 403–412. http://doi.org/10.1016/j.memsci.2013.07.051

Reneker, D. H., & Chun, I. (1996). Nanometre diameter fibres of polymer, produced by

electrospinning. *Nanotechnology*, *7*(3), 216–223. http://doi.org/10.1088/0957-4484/7/3/009

Reneker, D. H., & Yarin, A. L. (2008). Electrospinning jets and polymer nanofibers. *Polymer*, *49*(10), 2387–2425. http://doi.org/10.1016/j.polymer.2008.02.002

Rose, M., Böhringer, B., Jolly, M., Fischer, R., & Kaskel, S. (2011). MOF processing by electrospinning for functional textiles. *Advanced Engineering Materials*, *13*(4), 356–360. http://doi.org/10.1002/adem.201000246

Ruthven, D. M., & Reyes, S. C. (2007). Adsorptive separation of light olefins from paraffins. *Microporous and Mesoporous Materials*, *104*, 59–66. http://doi.org/10.1016/j.micromeso.2007.01.005

Sachse, A., Ameloot, R., Coq, B., Fajula, F., Coasne, B., De Vos, D., & Galarneau, A. (2012). In situ synthesis of Cu–BTC (HKUST-1) in macro-/mesoporous silica monoliths for continuous flow catalysis. *Chemical Communications*, *48*, 4749. http://doi.org/10.1039/c2cc17190b

Sakintuna, B., & Yürüm, Y. (2005). Templated porous carbons: A review article. *Industrial and Engineering Chemistry Research*, *44*(9), 2893–2902. http://doi.org/10.1021/ie049080w

Sander, J. R. G., Zeiger, B. W., & Suslick, K. S. (2014). Sonocrystallization and sonofragmentation. *Ultrasonics Sonochemistry*, *21*(6), 1908–1915. http://doi.org/10.1016/j.ultsonch.2014.02.005

Sanz-Perez, E. S., Murdock, C. R., Didas, S. A., & Jones, C. W. (2016). Direct Capture of CO2 from Ambient Air. *Chemical Reviews*, *116*(19), 11840–11876. http://doi.org/10.1021/acs.chemrev.6b00173

Sazali, N., Wan Salleh, W. N., Md Nordin, N. A. H., Harun, Z., & Ismail, A. F. (2015). Matrimid-based carbon tubular membranes: The effect of the polymer composition. *Journal of Applied Polymer Science*, *42394*, n/a-n/a. http://doi.org/10.1002/app.42394

Scholes, C. A., Tao, W. X., Stevens, G. W., & Kentish, S. E. (2010). Sorption of Methane, Nitrogen, Carbon Dioxide, and Water in Matrimid 5218. *Journal of Applied Polymer Science*, *117*, 2284–2289. http://doi.org/10.1002/app

Seol, W. H., Lee, Y. M., & Park, J. K. (2006). Preparation and characterization of new microporous stretched membrane for lithium rechargeable battery. *Journal of Power Sources*, *163*(1 SPEC. ISS.), 247–251. http://doi.org/10.1016/j.jpowsour.2006.02.076

Shan, B., James, J. B., Armstrong, M. R., Close, E. C., Letham, P. A., Nikkhah, K., … Mu, B. (2018). Influences of Deprotonation and Modulation on Nucleation and Growth of UiO-66 : Intergrowth and Orientation. *Journal of Physical Chemistry C*, *122*, 2200–2206. http://doi.org/10.1021/acs.jpcc.7b11012

Shan, B., Yu, J., Armstrong, M. R., Wang, D., & Mu, B. (2017). A Cobalt Metal-Organic Framework with Small Pore Size for Adsorptive Separation of CO 2 Over N 2 and CH 4. *AIChE Journal*, *63*, 4532–4540. http://doi.org/10.1002/aic

Shekhah, O., Belmabkhout, Y., Chen, Z., Guillerm, V., Cairns, A., Adil, K., & Eddaoudi, M. (2014). Made-to-order metal-organic frameworks for trace carbon dioxide removal and air capture. *Nature Communications*, *5*(May), 1–7. http://doi.org/10.1038/ncomms5228

Shen, X., & Yan, B. (2015). Polymer hybrid thin films based on rare earth ion-functionalized MOF: photoluminescence tuning and sensing as a thermometer. *Dalton Trans.*, *44*(4), 1875–1881. http://doi.org/10.1039/C4DT03213F

Sherwood, T. K. (1959). Mass Transfer Between Phases.

Shi, C., Zhang, P., Chen, L., Yang, P., & Zhao, J. (2014). Effect of a thin ceramic-coating layer on thermal and electrochemical properties of polyethylene separator for lithium-ion batteries. *Journal of Power Sources*, *270*, 547–553. http://doi.org/10.1016/j.jpowsour.2014.07.142

Shi, X., Li, Q., Wang, T., & Lackner, K. S. (2017). Kinetic analysis of an anion exchange absorbent for CO 2 capture from ambient air. *PLoS ONE*, *12*(6), 1–12.

Shi, X., Xiao, H., Lackner, K. S., & Chen, X. (2016). Capture CO2 from Ambient Air Using Nanoconfined Ion Hydration. *Angewandte Chemie - International Edition*, *55*(12), 4026–4029. http://doi.org/10.1002/anie.201507846

Shin, Y. M., Hohman, M. M., Brenner, M. P., & Rutledge, G. C. (2001). Experimental characterization of electrospinning: the electrically forced jet and instabilities. *Polymer*, *42*(25), 09955–09967. http://doi.org/10.1016/S0032-3861(01)00540-7

Sholl, D. S., & Lively, R. P. (2016). Seven Chemical Separations to Change the World. *Nature*, *532*, 435–437.

Snyder, M. a., Lee, J. A., Davis, T. M., Scriven, L. E., & Tsapatsis, M. (2007). Silica nanoparticle crystals and ordered coatings using lys-sil and a novel coating device. *Langmuir*, *23*(34), 9924–9928. http://doi.org/10.1021/la701063v

Song, Q., Nataraj, S. K., Roussenova, M. V., Tan, J. C., Hughes, D. J., Li, W., … Sivaniah, E. (2012). Zeolitic imidazolate framework (ZIF-8) based polymer nanocomposite membranes for gas separation. *Energy & Environmental Science*, *5*(8), 8359. http://doi.org/10.1039/c2ee21996d

Sridhar, S., Veerapur, R. S., Patil, M. B., Gudasi, K. B., Aminabhavi, T. M. (2007). Matrimid Polyimide Membranes for the Separation of Carbon Dioxide from Methane. *Journal of Applied Polymer Science*, *106*, 1585–1594.

Stoeger, J. A., Choi, J., & Tsapatsis, M. (2011). Rapid thermal processing and separation performance of columnar MFI membranes on porous stainless steel tubes. *Energy & Environmental Science*, *4*(9), 3479. http://doi.org/10.1039/c1ee01700d

Stranger, Jon, Tucker, Nick, and Staiger, M. (2009). *Electrospinning*. Smithers Rapra.

Subbiah, T., Bhat, G. S., Tock, R. W., Parameswaran, S., & Ramkumar, S. S. (2005). Electrospinning of nanofibers. *Journal of Applied Polymer Science*, *96*, 557–569. http://doi.org/10.1002/app.21481

Suh, M. P., Park, H. J., Prasad, T. K., & Lim, D. (2011). Hydrogen Storage in Metal - Organic Frameworks. *Chemical Reviews*, (112), 782–835. http://doi.org/10.1021/cr200274s

Sun, S.P., Chung, T.S., Lu, K.J., Chan, S. Y. (2014). Enhancement of Flux and Solvent Stability of Matrimid Thin-Film Composite Membranes for Organic Solvent Nanofiltration. *American Institute of Chemical Engineers Journal*, *60*(10), 3626–3633.

Sung, S.-J., Cho, K.-Y., Hah, H., Lee, J., Shim, H.-K., & Park, J.-K. (2006). Two different reaction mechanisms of cinnamate side groups attached to the various polymer backbones. *Polymer*, *47*(7), 2314–2321. http://doi.org/10.1016/j.polymer.2006.02.003

Tan, E. P. S., & Lim, C. T. (2006). Mechanical characterization of nanofibers - A review. *Composites Science and Technology*, *66*(9), 1099–1108. http://doi.org/10.1016/j.compscitech.2006.03.001

Tan, J., Bennett, T. D., & Cheetham, A. K. (2010). Chemical structure, network topology, and porosity effects on the mechanical properties of Zeolitic Imidazolate Frameworks. *Proceedings of the National Academy of Sciences of the United States of America*, *107*(22), 9938–9943. http://doi.org/10.1073/pnas.1003205107/-/DCSupplemental.www.pnas.org/cgi/doi/10.1073/pnas.1003205107

Terech, P., & Weiss, R. G. (1997). Low Molecular Mass Gelators of Organic Liquids and the Properties of Their Gels. *Chemical Reviews*, *97*(97), 3133–3160. http://doi.org/10.1021/cr9700282

Thommes, M., Kaneko, K., Neimark, A. V., Olivier, J. P., Rodriguez-Reinoso, F., Rouquerol, J., & Sing, K. S. W. (2015). Physisorption of gases, with special reference to the evaluation of surface area and pore size distribution (IUPAC Technical Report). *Pure and Applied Chemistry*, *87*(9–10), 1051–1069. http://doi.org/10.1515/pac-2014-1117

Thornton, A. W., Babarao, R., Jain, A., Trousselet, F., & Coudert, F. (2016). Defects in metal-organic frameworks: a compromise between adsorption and stability? *Dalton Trans.*, *45*, 4352–4359. http://doi.org/10.1039/c5dt04330a

Tin, P. S., Chung, T. S., Liu, Y., Wang, R., Liu, S. L., & Pramoda, K. P. (2003). Effects of cross-linking modification on gas separation performance of Matrimid membranes. *Journal of Membrane Science*, *225*(1–2), 77–90. http://doi.org/10.1016/j.memsci.2003.08.005

Torquato, S., Truskett, T. M., & Debenedetti, P. G. (2000). Is Random Close Packing of Spheres Well Defined? *Physical Review Letters*, *84*(10), 2064–2067. http://doi.org/10.1103/PhysRevLett.84.2064

Tranchemontagne, D. J., Mendoza-Cortes, J. L., O'Keeffe, M., & Yaghi, O. M. (2009). Secondary building units, nets and bonding in the chemistry of metal-organic frameworks. *Chem Soc Rev*, *38*(5), 1257–1283. http://doi.org/10.1039/b817735j

Trappe, V., Prasad, V., Cipelletti, L., Segre, P. N., & Weitz, D. a. (2001). Jamming phase diagram for attractive particles. *Nature*, *411*(6839), 772–775. http://doi.org/10.1038/35081021

Vanherck, K., Vandezande, P., Aldea, S. O., & Vankelecom, I. F. J. (2008). Cross-linked polyimide membranes for solvent resistant nanofiltration in aprotic solvents. *Journal of Membrane Science*, *320*(1–2), 468–476. http://doi.org/10.1016/j.memsci.2008.04.026

Vaughan, O. (2014). Porous by design. In M. Montoya, A. Moscatelli, & A. Taroni (Eds.), *Nature Milestones in Crystallograpny* (p. 1). Nature Publishing Group. http://doi.org/10.1038/nature13371

Vintiloiu, A., & Leroux, J.-C. (2008). Organogels and their use in drug delivery - A review. *Journal of Controlled Release*, *125*(3), 179–92. http://doi.org/10.1016/j.jconrel.2007.09.014

Vondran, J. L., Sun, W., & Schauer, C. L. (2008). Crosslinked, electrospun chitosan–poly(ethylene oxide) nanofiber mats. *Journal of Applied Polymer Science*, *109*(2), 968–975. http://doi.org/10.1002/app.28107

Walton, K. S., & Sholl, D. S. (2015). Predicting Multicomponent Adsorption: 50 Years of the Ideal Adsorbed Solution Theory. *AIChE Journal*, *61*(9), 2757–2762. http://doi.org/10.1002/aic.14878

Walton, K. S., & Snurr, R. Q. (2007). Applicability of the BET method for determining surface areas of microporous metal-organic frameworks. *Journal of the American Chemical Society*, *129*(27), 8552–6. http://doi.org/10.1021/ja071174k

Wang, S., Wang, J., Cheng, W., Yang, X., Zhang, Z., Xu, Y., … Fang, M. (2015). A Zr metal–organic framework based on tetrakis(4-carboxyphenyl) silane and factors affecting the hydrothermal stability of Zr-MOFs. *Dalton Trans.*, *44*(17), 8049–8061. http://doi.org/10.1039/C5DT00421G

Wee, L. H., Lohe, M. R., Janssens, N., Kaskel, S., & Martens, J. A. (2012). Fine tuning of the metal–organic framework Cu3(BTC)2 HKUST-1 crystal size in the 100 nm to 5 micron range. *Journal of Materials Chemistry*, *22*(27), 13742. http://doi.org/10.1039/c2jm31536j

Wu, X., Oleschuk, R. D., & Cann, N. M. (2012). Characterization of microstructured fibre emitters: in pursuit of improved nano electrspray ionization performance. *Analyst*, *137*(18), 4150–4161. http://doi.org/10.1039/c2an35249d

Xu, Y., Wen, Y., Wu, Y. N., Lin, C., & Li, G. (2012). Hybrid nanofibrous mats with remarkable solvent and temperature resistance produced by electrospinning technique. *Materials Letters*, *78*, 139–142. http://doi.org/10.1016/j.matlet.2012.03.016

Xu, Y., Wen, Y., Zhu, W., Wu, Y. N., Lin, C., & Li, G. (2012). Electrospun nanofibrous mats as skeletons to produce MOF membranes for the detection of explosives. *Materials Letters*, *87*, 20–23. http://doi.org/10.1016/j.matlet.2012.07.076

Yang, J., Dai, Y., Zhu, X., Wang, Z., Li, Y., Zhuang, Q., … Gu, J. (2015). Metal–organic frameworks with inherent recognition sites for selective phosphate sensing through their coordination-induced fluorescence enhancement effect. *J. Mater. Chem. A*, *3*(14), 7445–7452. http://doi.org/10.1039/C5TA00077G

Yang, Q., Wiersum, A. D., Jobic, H., Guillerm, V., Serre, C., Llewellyn, P. L., & Maurin, G. (2011). Understanding the thermodynamic and kinetic behavior of the CO2/CH4 gas mixture within the porous zirconium terephthalate UiO-66(Zr): A joint experimental and modeling approach. *Journal of Physical Chemistry C*, *115*, 13768–13774. http://doi.org/10.1021/jp202633t

Yang, S. J., & Park, C. R. (2012). Preparation of highly moisture-resistant black-colored metal organic frameworks. *Advanced Materials*, *24*, 4010–4013. http://doi.org/10.1002/adma.201200790

Yarin, A. L., & Reneker, D. H. (2001). Taylor Cone and Jetting from Liquid Droplets in Electrospinning of Nanofibers. *Journal of APplied Physics*, *90*(9), 4836–4846. http://doi.org/10.1063/1.1408260

Yi, W., Huaiyu, Z., Jian, H., Yun, L., & Shushu, Z. (2009). Wet-laid non-woven fabric for separator of lithium-ion battery. *Journal of Power Sources*, *189*(1), 616–619. http://doi.org/10.1016/j.jpowsour.2008.09.078

Zeiger, B. W., & Suslick, K. S. (2011). Sonofragmentation of molecular crystals. *Journal of the American Chemical Society*, *133*, 14530–3. http://doi.org/10.1021/ja205867f

Zhang, C., & Koros, W. J. (2015). Zeolitic Imidazolate Framework-Enabled Membranes: Challenges and Opportunities. *Journal of Physical Chemistry Letters*, *6*(19), 3841–3849. http://doi.org/10.1021/acs.jpclett.5b01602

Zhang, C., Lively, R. P., Zhang, K., Johnson, J. R., Karvan, O., & Koros, W. J. (2012). Unexpected Molecular Sieving Properties of Zeolitic Imidazolate Framework-8. *The Journal of Physical Chemistry Letters*, *3*, 2130–2134.

Zhang, S. S. (2007). A review on the separators of liquid electrolyte Li-ion batteries. *Journal of Power Sources*, *164*(1), 351–364. http://doi.org/10.1016/j.jpowsour.2006.10.065

Zhang, W., Hu, Y., Ge, J., Jiang, H., & Yu, S. (2014). A Facile and General Coating Approach to Moisture/Water-Resistant Metal − Organic Frameworks with Intact Porosity. *Journal of the American Chemical Society*, *136*, 16978–16981. http://doi.org/10.1021/ja509960n

Zhang, Y.-B., Furukawa, H., Ko, N., Nie, W., Park, H. J., Okajima, S., … Yaghi, O. M. (2015). Introduction of Functionality, Selection of Topology, and Enhancement of Gas Adsorption in Multivariate Metal–Organic Framework-177. *Journal of the American Chemical Society*, *137*, 2641–2650. http://doi.org/10.1021/ja512311a

Zhang, Z., Xian, S., Xia, Q., Wang, H., Li, Z., & Li, J. (2013). Enhancement of CO2 Adsorption and CO2/N2 Selectivity on ZIF-8 via Postsynthetic Modification. *AIChE Journal*, *59*(6), 2195–2206. http://doi.org/10.1002/aic

Zhao, Y., Liu, L., Zhang, W., Sue, C., Li, Q., Miljanic, O. S., … Stoddart, J. F. (2009). Rigid-Strut-Containing Crown Ethers and [2]Catenanes for Incorporation into Metal–Organic Frameworks. *Chemistry - A European Journal*, *15*, 13356–13380. http://doi.org/10.1002/chem.200902350

Zhao, Z., Ma, X., Li, Z., & Lin, Y. S. (2011). Synthesis, characterization and gas transport properties of MOF-5 membranes. *Journal of Membrane Science*, *382*(1–2), 82–90. http://doi.org/10.1016/j.memsci.2011.07.048

Zhou, C., Wang, Q., & Wu, Q. (2012). UV-initiated crosslinking of electrospun poly(ethylene oxide) nanofibers with pentaerythritol triacrylate: Effect of irradiation time and incorporated cellulose nanocrystals. *Carbohydrate Polymers*, *87*, 1779–1786. http://doi.org/10.1016/j.carbpol.2011.09.095

APPENDIX A

LIST OF PUBLICATIONS

The following is a list of publications adapted for use in this thesis (Table A1). The primary chapter the publication is present in is given, however, elements of each of these articles have been moved to the introduction (Chapter 1), the background (Chapter 2), or the materials and methods section (Chapter 3).

Table A1.
A list of publications adapted for this manuscript

Chapter	Original Article Title	Journal/ Progress	Year
4	Influence of Particle Size and Loading on Particle Accessibility in Electrospun Poly(ethylene oxide) and ZIF-8 Composite Fibers: Experiments and Theory	Langmuir	2017
5,6	Polymer Coating on Metal-Organic Framework Particles by Electrospinning for Core-Shell Sorbents with Improved Adsorption Properties: Experiments and Theory	In review	2018
7	Prolonged HKUST-1 Functionality Under Extreme Hydrothermal Conditions by Electrospinning Polystyrene Fibers as A New Coating Method	In review	2018
8	Hierarchical Pore Structures and High ZIF-8 Loading on Matrimid Electrospun Fibers by Additive Removal From a Blended Polymer Precursor	I&ECR	2016
9	Porous Electrospun Mats Made With the SPAR Technique As An Ideal Scaffold for Low Uptake Resistance And Accessibility To Embedded Direct Air Capture Sorbents	In review	2018

A list of publications adapted and attached in the Appendix (Table A2). In some of these Appendix papers other authors have made significant writing contributions, and the sections in which I was only a minor author have been omitted. In appendix B I had developed the ideas, theories, and was the principal writer. C. Balzer and S. Senthilnathan performed a significant portion of the experimental work, and C. Balzer performed the ImageJ analysis. The article in appendix D was co-first authored by K. Yuriar-Arredondo, who provided substantial input throughout the appendix chapter presented.

Table A2.
A list of publications adapted for the appendix.

Appendix	Original Article Title	Journal/ Progress	Year
B	Particle Size Studies to Reveal Crystallization Mechanisms of the Metal Organic Framework HKUST-1 During Sonochemical Synthesis	Ultrasononics Sonochemistry	2017
C	UiO-66 MOF and Poly(vinyl cinnamate) Nanofiber Composite Membranes Synthesized by a Facile Three-Stage Process	I&ECR	2015
D	Nanofiber-Based Matrimid Organogel Membranes For Battery Separator	Journal of Membrane Science	2018

Other first author work includes a publication in MRS Advances,(M. R. Armstrong, Shan, & Mu, 2017) which is similar to a conference proceedings that publishes work in progress. This work was omitted because it exclusively contains a microscopy study, and is not by itself a stand-alone work. Another first-author work focuses on the adsorption and diffusion of CO_2 on the MOF CuBTB.(M. R. Armstrong, Shan, Cheng, et al., 2017) In this work each author contributed significantly to different portions of the manuscript.

Co-authored work primarily includes collaborations with B. Shan and C. Balzer. Work with C. Balzer included help with developing the original ideas, consulted during experimentation, and helped in preparing the final draft.(C. J. Balzer, Armstrong, Shan, & Mu, 2017)(C. Balzer et al., 2018) Work with B. Shan included consulting during experimentation and theory development, occasional experimental support, and help with preparing the final draft of manuscripts.(Shan, Yu, Armstrong, Wang, & Mu, 2017)(Shan et al., 2018)

APPENDIX B

PARTICLE SIZE STUDIES TO REVEAL CRYSTALLIZATION MECHANISMS OF THE METAL-ORGANIC FRAMEWORK HKUST-1 DURING SONOCHEMICAL SYNTHESIS

B1. Introduction

Metal organic framework (MOF) crystals have shown promise in many different applications such as separations,(Herm et al., 2013) adsorption,(Y.-B. Zhang et al., 2015) and catalysis(Y. Lee, Kim, Kang, & Cohen, 2015) due in part to their highly tunable functional groups. The initial particle size of crystals plays a vital role in overall performance for these applications. For example, emphasis on seed crystal size in gas separations has been highly studied for growing membranes,(Snyder, Lee, Davis, Scriven, & Tsapatsis, 2007) and in catalysis many reactions are shown to occur at the crystal surface since diffusion into the pores is a rate-limiting step.(Mondloch et al., 2015) Continuous high-throughput methods to produce small MOF crystals of nearly uniform size are a necessary step for any of these processes to become commercially feasible. Currently in the separation field, gas membranes are being made through a dip-coating method, but these MOF seeds are grown in small batches and take over 24 hours to crystallize.(Defei Liu, Ma, Xi, & Lin, 2014) In the kinetics field, MOFs are being used to break down nerve agents, but the reaction is shown to happen on the outer surface of the MOF, and much of the porous crystal is not being used.(Katz et al., 2014) This catalytic process could be improved by making smaller crystals than currently being produced to increase the effective surface area.

Sonochemical synthesis is a potential technique that may meet each of these demands due to the relatively small particle sizes it produces with a high reaction rate compared to other techniques,(Y.-R. Lee et al., 2015) in which liter scale bulk quantities of different MOFs have already been demonstrated.[9] A few previous scale-up(Majano & Pérez-Ramírez, 2013) and size control(Majano & Pérez-Ramírez, 2012; Wee, Lohe, Janssens, Kaskel, & Martens, 2012) investigation has been performed on HKUST-1, however the methods used are unlikely to synthesize other MOFs due to their temperature restrictions and dependence on solvents, severely limiting extension of these investigations to other MOFs. In addition, a study of the effect of multiple variables on particle size and particle size distribution is not found in literature, although Khan et al do a study on BET surface area and morphology of sonochemically

synthesized HKUST-1.(Khan & Jhung, 2009) To complete a thorough investigation of these parameters, the MOF HKUST-1 ($(C_{18}H_6Cu_3O_{12})_n$) was selected because it has been highly studied for many different applications ranging from the previously mentioned applications in membrane separations(V. V. Guerrero, Yoo, McCarthy, & Jeong, 2010) and catalysis,(Sachse et al., 2012) as well as many others including sensing(Lu et al., 2011) and gas adsorption(Bordiga et al., 2007). The variables studied were chosen due to their potential relevance in the scale up of the sonochemical synthesis method for continuous operation and increased volumes to evaluate whether or not a sonochemical reactor would be a viable solution to this issues, and find what potential issues may arise. Along with a particle size analysis, the mechanisms for these processes are of key importance to make this technology scalable to different throughputs, and translatable to other MOFs.

Inside a sonochemical reactor, many inter-correlated regimes exist with different phenomena at each that result in different crystal growth mechanics in regards to MOFs. Three primary regimes may be outlined to describe sonochemical reactions: the first are hot spots generated by cavity implosions characterized by instances of temperatures exceeding 5000 K, and pressures as high as 1000 bar;(Bang & Suslick, 2010) the second regime is the area immediately surrounding these hot spots where the shockwaves produced by the hot spots induce high sheer forces in the fluid; and finally the third important regime is the bulk fluid where the shockwaves produced by the hot spots are negligible where the fluid reaches an equilibrium temperature between heat generated by the hot spots and the reactor surroundings. Because of these three regimes governed by very different physical phenomena, there is little understanding of how to scale up this promising technology. Pioneering work in ultrasound chemistry by Suslick and coworkers has defined three significant growth steps that are expected to be significant for our purposes: crystal initiation, crystal propagation, and crystal fracture (sonofragmentation).(Sander, Zeiger, & Suslick, 2014) Determining the significance of each of these events inside the three regimes of a sonochemical reaction is the first fundamental step necessary to understand how to scale up these reactors, and this work uses the synthesis of HKUST-1 to locate where these

phenomena occur by systematically studying the particle sizes and particle size distributions of HKUST-1 synthesized under varying conditions.

The results found in this study fit trends that would be expected from plausible competitive mechanisms including crystal initiation at instances of super-saturation caused in the shockwave region, crystal growth following the kinetics of traditional crystallization models, and sonofragmentation causing crystal fracture at the shockwave-particle interface.

B2. Materials and Methods

B2.1. Chemicals. Copper (II) Nitrate ($(CuNO_3)_2 \cdot 6H_2O$, 98%), trimesic acid (BTC, 98%), dimethyl formamide (DMF, 99.9%), and ultra-pure water (H_2O, 99.9%), and ethanol (EtOH, sigma, 99.8%) were purchased from Sigma Aldrich and used without any further purification.

B2.2. MOF Synthesis. The standard synthesis studied used a QSonica Q500 (500 watt max power and 20 kHz frequency) sonicator running for 30 minutes at 60% amplitude with a ½" sonicator tip placed into a 20 mL glass screw-top vial containing a solution of 12 mL DMF and 6 mL water, 300 mg copper (II) nitrate, and 300 mg BTC. Systematic changes to this recipe were made as described in the results section. The precursor mixture was a clear blue colored solution before the sonochemical synthesis. After sonication 46 kJ had been added to the solution, and it had nucleated becoming a turbid slurry. After the reaction, tiny crystals were filtered out from the solution, rinsed by passing acetone over the filtrate, dried in air overnight, and collected into glass vials for the characterization.

Solvothermal synthesis was carried out in the autoclave oven at a temperature of 100 °C for 12 hours with the solution mixture containing 500 mg BTC, 500 mg Copper (II) Nitrate, 7.5mL ethanol, 7.5mL of DMF and 15 mL Water. After the reaction, the mixture is filtered, dried in air overnight and collected.

B2.3. Characterization. Powder x-ray diffraction (PXRD) was performed with a P'Analytical x-ray diffractometer at 40 kV with Cu-K α radiation and a nickel filter. Scanning electron microscopy (SEM) was performed with a Zeiss electron microscope after gold plating. Nitrogen porosimetry was carried out to find BET surface area on a Micrometrics Tristar II porosimeter at 77K.

B2.4 Computational analysis. SEM images were converted to high contrast, black and white images with ImageJ,(Abràmoff, Magalhães, & Ram, 2004) and the total area of each particle was measured through comparison with the scale bar provided by the SEM image. The average diameter of each particle in the image was calculated through the conversion area = $0.785(\text{diameter})^2$ The minimum sample size for each measurement was greater than 100.

B3. Results

B3.1. MOF characterization. Figure B1 contains an SEM image of the product as well as its powder X-ray diffraction (PXRD) compared to the literature.

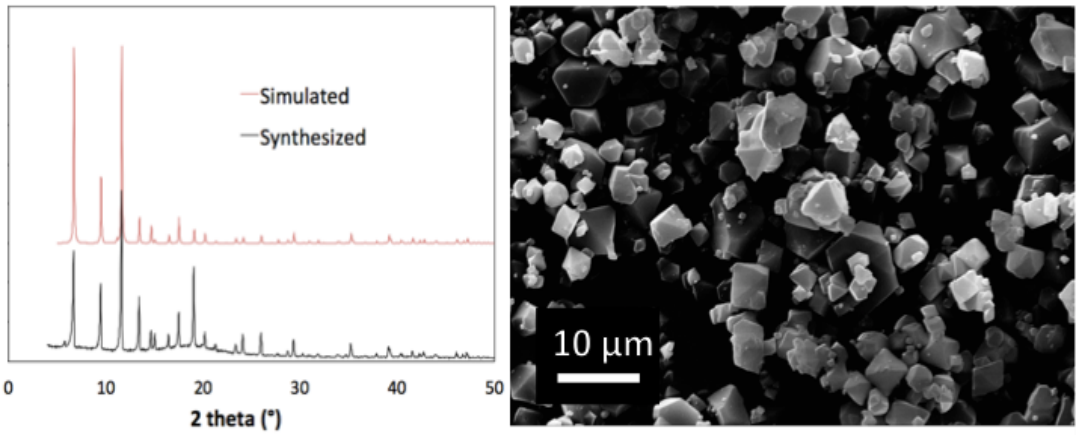

Figure B1. Comparison of simulated HKUST-1 PXRD pattern generated from single crystal data to experimentally collected PXRD patterns from the standard sonochemical synthesis recipe used in this work (left). SEM image of sonochemically synthesized HKUST-1 (right).

The product at these standard conditions had a BET surface area of 850 cm^2/g. The BET surface area and the SEM image visually confirms that crystalline particles of relatively uniform particle size were produced. The SEM images and conditions for each of the other reactions may be found in Figure B2.

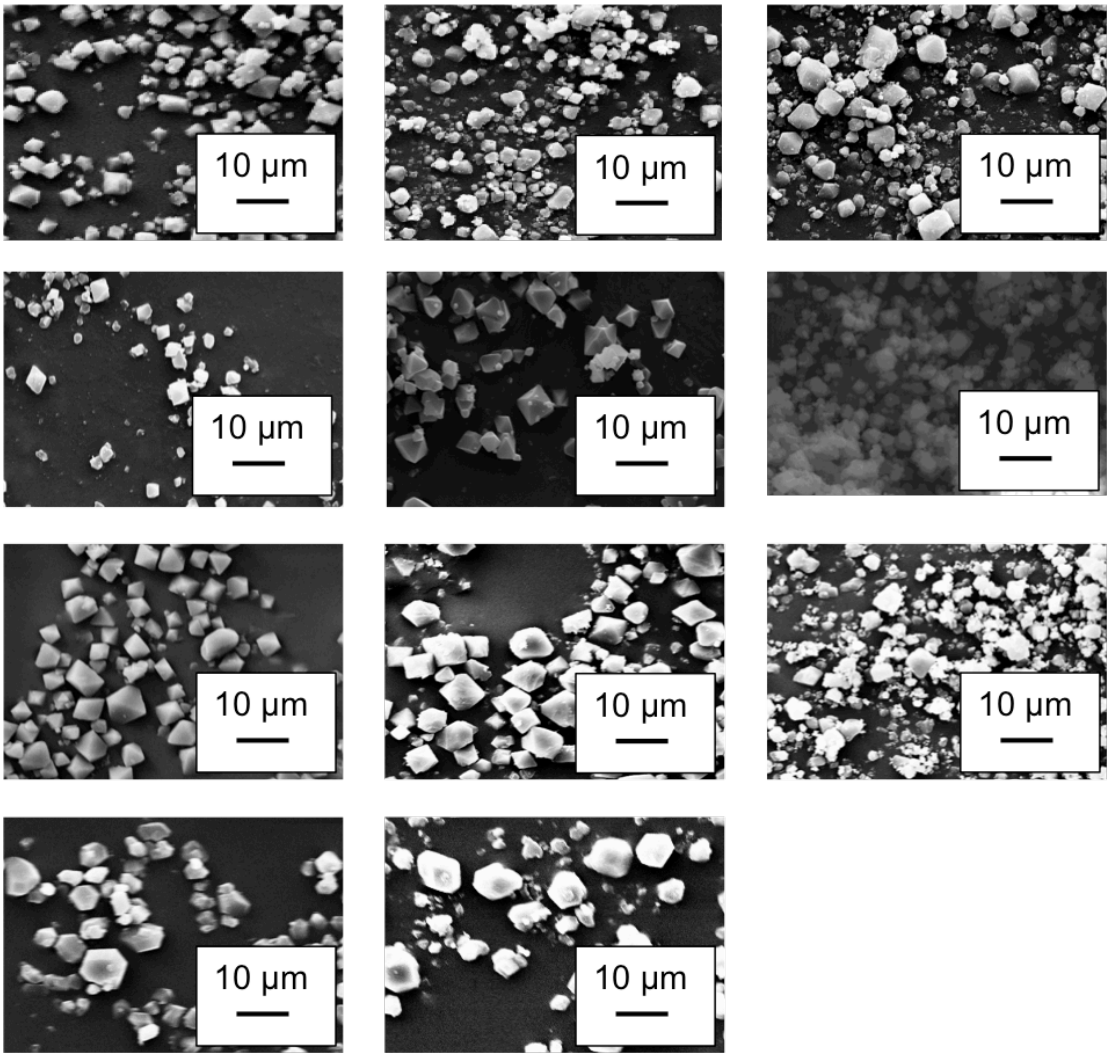

Figure B2. Row 1: SEM images of HKUST-1 synthesized using standard recipes with a condenser for 10, 30, and 60 minute, respectively (from right to left). Row 2: Changes in amplitude at 40% (left), 80% amplitude (middle), and 100 % amplitude (right). Row 3: Synthesis in 100 mL beaker (left), and with ¼" tip and a Qsonica Q125 sonicator (middle). Changes in solvent ratio 15:3 DMF: water (right), Row 4: half reactant concentration (left) and double reactant concentration (right).

From Figure B1, it can be seen that the powder X-ray diffraction peaks line up with the spectra simulated from single crystal x-ray diffraction patterns supplied by Mustafa and coworkers.(Mustafa et al., 2011) Other PXRD patterns from this work compared to the standard synthesis presented in Figure B2 may be found in Figure B3, and Table B1 contains a legend for the Figure B3.

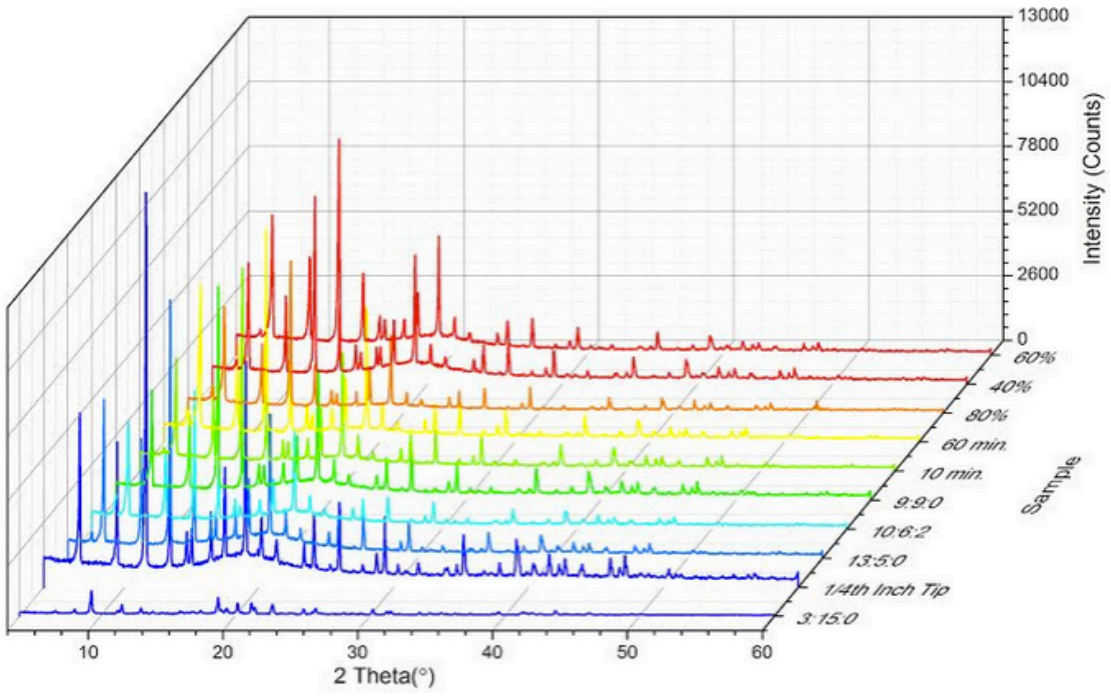

Figure B3. PXRD spectra for selected samples from the main body of the text to show crystals were all HKUST-1. Table B1 provides a legend to convert from sample name in this figure to figures in the text.

Table B1.
Legend for Figure B3

Sample name in Fig 3	Corresponding Fig in main text	Description of Sample
60%	Fig B1	Standard Synthesis
10 min	Fig B2	10 min reaction time
60 min	Fig B2	60 min reaction time
40%	Fig B3	40% amplitude
80%	Fig B3	80% amplitude
1/4 Inch Tip	Fig B3	¼” sonicator tip size
13:5	Fig B3	13:5 DMF to water ratio
9:9	Fig B3	9:9 DMF to water ratio
3:15	Fig B3	3:15 DMF to water ratio

B3.2. Effect of reaction time. The time dependence of particle size was studied at different time intervals as seen in left panel of Figure B4. Relative yield as a function of time and the energy delivered to the solution and yield as a function of time is also provided in the right panel of Figure B4. It can be seen that the particle sizes maintain a steady mean initially, but start to drop as a function of time after 30 minutes.

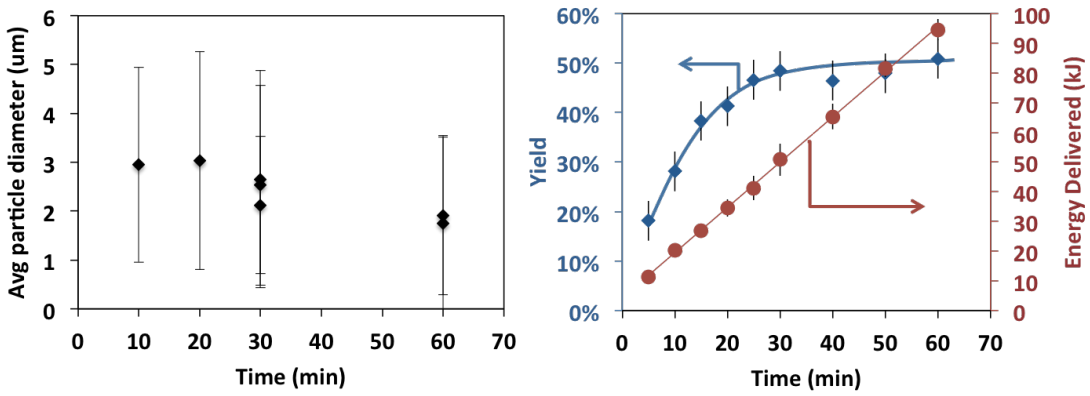

Figure B4. Particle size and standard deviation of HKUST-1 sonochemical synthesis as a function of time (left). HKUST-1 yield and energy delivered by the sonicator as a function of time (right).

B3.3. Effects of ultrasound amplitude, solvent compositions, reactant concentration, and sonicator tip size. Figure B5 shows the effects of changes in amplitude percentage, solvent composition, reactant concentration, and sonicator tip size. Changes in amplitude percentage demonstrate a characteristic inverse parabola where particle sizes increase with a maxima of 80% amplitude. The particle size increases with decreasing DMF: water ratio, however ratios dominated by either DMF or water do not form a crystalline product. The size of sonicator tip does not strongly influence the particle size; however increases in tip size do decrease the standard deviation of the particles. Reactant concentration also had little effect on the overall average particle diameter.

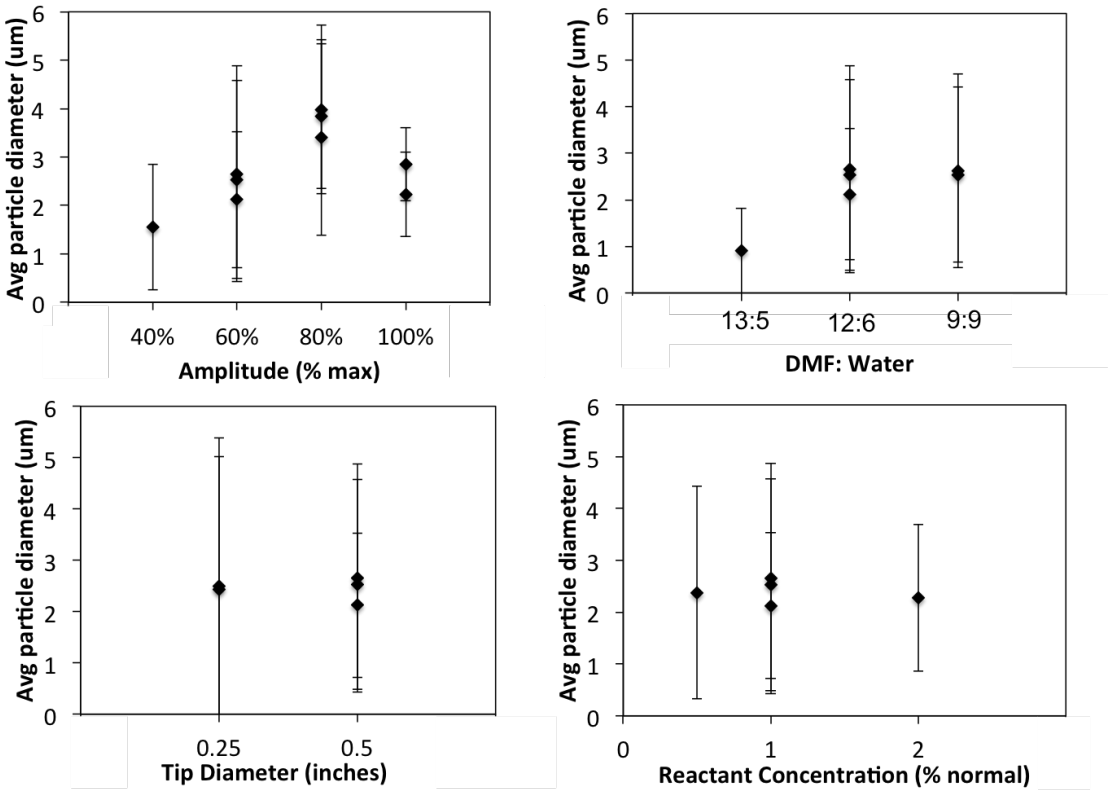

Figure B5. The dependence of average particle diameter and particle size distributions on changing sonication tip amplitudes (top, left), DMF to water ratios (top, right), changing tip diameters (bottom, left), and reactant concentrations (bottom, right).

B3.4. Effect of sonicating solvothermally grown MOFs without precursor. HKUST-1 was grown solvothermally to much larger sizes than producible by sonochemistry and sonicated for 30 minutes in 12 mL DMF and 6 mL water. The SEM image of these crystals before and after sonication along with sonochemically synthesized HKUST-1 for comparison and a mean average particle size comparison showing a significant drop in particle size is shown in Figure B6.

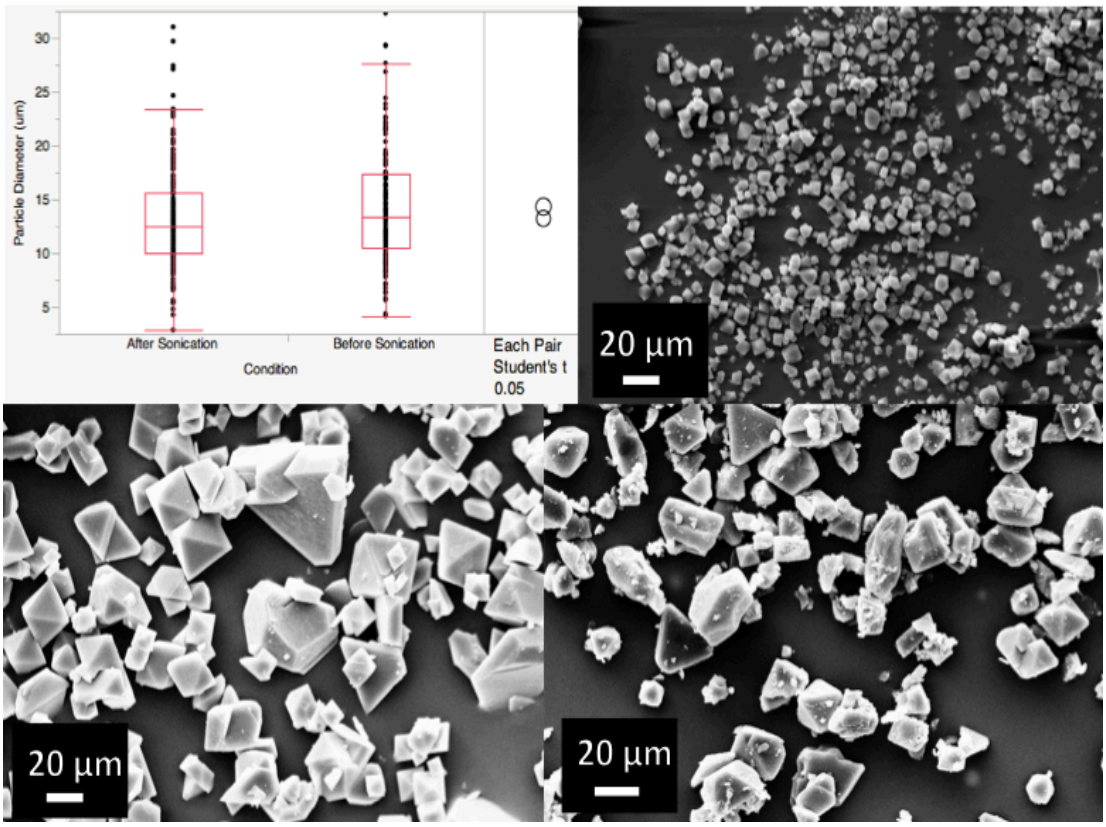

Figure B6. SEM image of HKUST-1 grown solvothermally (bottom, left), solvothermally synthesized HKUST-1 after 30 minutes of sonication (bottom, right), and sonochemically synthesized HKUST-1 after 30 minutes (top, right), along with a Student's T test showing a statistical difference between the mean diameters of the powder before and after sonication (top, left).

The difference of the SEM image before and after sonication show small fragments devolving off of the crystal which were not measured for the particle size analysis. The solution after sonofragmentation was centrifuged and a digital image of the solution was taken as seen in Figure B7 showing a clear solution with HKUST-1 particles clearly separated from solution.

Figure B7. Optical image of HKUST-1 solution after the sonofragmentation study outlined in section 3.4 showing and after centrifugation to collect the residual HKUST-1 suspension at the bottom. The image depicts a clear solution lacking any visual evidence of a blue tint, which suggests that HKUST-1 dissolving in the solution is not a primary factor resulting in the decreasing particle size.

The absence of a blue tint in the reaction solution confirms that the particles size drop was not from crystals dissolving.

B3.5. Effect of reactor size. Figure B8. shows changes in reactor volume when switching from the standard 20 mL vial containing 18 mL of reaction solution to a standard 100 mL Thermo Scientific beaker containing 54 mL of a proportional reaction solution on the left panel. The right panel of Fig. 5 depicts a visual representation of sound waves propagating though solutions of geometries proportional to our reaction conditions using COMSOL Multiphysics to solve for the Helmholtz equation and boundary conditions.

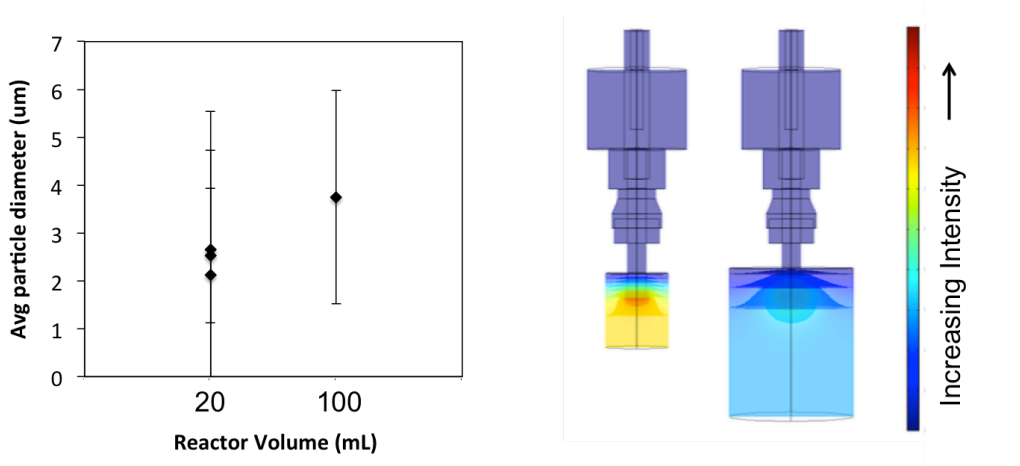

Figure B8. Effect of changing reactor size on particle sizes and distribution (left). Visual representation of the Helmholtz equation modeling sound wave propagation in two different sized vessels showing differences in wave dissipation using COMSOL Multiphysics with the equivalent radiation energy at the sonicator tip (right).

B3.6. Effect of temperature. In Figure B9, the temperature was studied in two different ways: without temperature control in the left panel and with a controlled reaction solution temperature of 10 °C in the right panel. Monitoring the temperature directly from the reaction solution with different ratios of DMF and water in the 20 mL vial all behave the same with a rapid rise to 100 °C and maintaining that temperature throughout the reaction. When the 100 mL beaker was used the reaction solution temperature rapidly rose to 85 °C and maintained that temperature throughout instead. When the reaction was run at 10 °C it appears that no reaction occurred, and when filtered no product was collected. The right panel of Figure B9 contains digital images that show the resulting reaction solution after a reaction at 10 °C for 10 minutes, after a reaction solution is allowed to raise to 100 °C for 10 minutes, and a solution before reaction, where the lack of turbidity and pale blue color indicates that a negligible amount of reaction occurred.

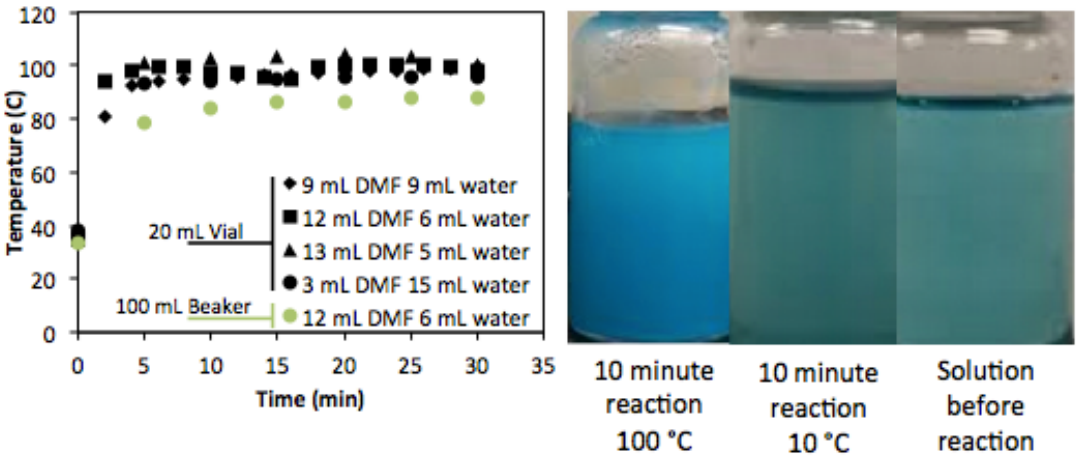

Figure B9. Reaction solution temperature as a function of time for reaction occurring in 100 mL beaker with a DMF: water ratio of 12:6 (green circle) and reactions in a 20 mL vial (black) at DMF: water ratios of 9:9 (diamond), 12:6 (square), 13:5 (triangle), and 3:15 (circle) (left). Digital image of vials containing reaction after 10 minutes of sonochemical reaction without temperature control, 10 minutes of sonochemical reaction when the reaction solution temperature is reduced to 10 °C, and the reaction solution before sonication (right).

B4. Discussion

B4.1. Trends in particle size and particle size distribution. Significant trends seen in particle sizes after systematically changing variables include a constant size as a function of time until a significant drop after half an hour as seen in Figure B2, a bell-shaped curve in amplitude and a change with solvent ratios as seen in Figure B3. Changes in standard deviations are found when dropping tip size (Figure B3) or increasing the size of the reactor (Figure B5) without much change in the mean size. Results from the particle size analysis show that the key factors in designing sonochemical reactors for MOF synthesis should be solvent choices rather than process parameters for determining a specific average particle size, and smaller reactors with larger tips should be used to reduce the particle size distribution. The reasons for these trends will be discussed in the mechanism discussions in parts 4.2 through 4.4. The cause for changing particle sizes and distributions found from changing reactor sizes seen in Figure B5 remains unclear due to multiple changing variables including different bulk temperature (Figure B6) and changing ratios of bulk fluid to shockwave region as seen in the Helmholtz model showing that as

the reactor increases there is more bulk phase for the particles to explore away from the reactive shockwaves (Figure B5). Effects of changing reactor sizes remain one of the greater challenges with scaling up this technology. Overall, it is found that minimal size control is available by changing operating parameters, but consistent results and trends are found that allow insights into potential mechanisms, and with a further understanding of the MOF crystallization mechanism in a sonochemical reactor controllable size control may be realizable through reactor system design.

B4.2. Crystal initiation. Crystal Initiation in the reactor is expected to take place due to spontaneously induced super-saturation in either the shockwave region or the implosion region of the sonochemical reactor.(Sander et al., 2014)(Hem, 1967) This places crystal initiation in either shockwave regions surrounding bubble implosions, or inside the bubble implosions themselves. If crystal initiation were to occur inside the shockwave region, intuitive kinetics where reaction rate increases with temperature would apply. If crystal initiation occurred in bubble implosions the opposite would hold true since bubble implosions release more energy at lower temperatures due to decreases in solvent vapor pressure inside the reactors attenuating the implosion. Since the reaction did was unable to proceed in an ice bath as seen in Figure B6, it is clear that crystal initiation must occur in the shockwave region through the aid of the mechanical frictional forces associated with this regime. These results suggest that crystal initiation results from activation by the shockwave region.

B4.3. Sonofragmentation. Suslick and co-workers showed that fragmentation and particle annihilation could occurs in sonochemical reactor with metal particles by inter-particle collisions in studies in 1990(Doktycz & Suslick, 1990) and 2004.(Prozorov, Prozorov, & Suslick, 2004) Later another study was done on molecular crystals showing that the main source of sonofragmentation is induced in these materials by shockwave-particle interactions.(Zeiger & Suslick, 2011) In Figure B4 sonofragmentation is shown to have a significant effect inside the

sonochemical reactor due to an observed decrease in crystal size and fragments of MOF crystal visible in the SEM image which is in good agreement to this previous work in literature. This phenomenon also is confirmed by trends found in other studies in this work. Particle size drops beginning to occur at the inflection point of the yield versus time at 30 minutes due to reactants no longer providing a large driving force for the growth of the crystals, and a drop in maximum particle size due to changes in amplitude after 80% amplitude caused by the potential increase in shockwaves in the solution providing more driving force for particle size decrease than at lower amplitude levels. From this these results it is clear that a competitive destructive mechanism exists, and this work along with mentioned previous studies suggests that it is sonofragmentation.

B4.4. Crystal propagation. For crystal propagation, we propose that HKUST-1 growth follows similar kinetics to traditional crystallization mechanics until sonofragmentation becomes a significant factor. This approximation is presumed accurate after taking into account the visible facets and growth patterns observed in the SEM image in Figure B1 assuming growth in a pillared fashion where each incoming molecule attaches on top of another molecule already set on the crystal. Strong agreement between this model and experimental data through differences in particle size with differences in equilibrium surface energies from changing solvent ratios and free reactants seen in Figure B3, and changes in equilibrium size with different amounts of reactants as a function of time seen in Figure B2. Simple crystal growth models fit the crystal propagation of this system until destructive forces become significant.

B5. Conclusion

Results of the sonochemical synthesis of the metal-organic-framework HKUST-1 found from this work show that observations in particle size trends and related experiments may be explained with competitive growth and deconstruction models. Crystal initiation is likely to occur in spontaneous super-saturation points along the shockwaves generated by bubble implosion sites,

however are unlikely to occur in the implosion sites themselves. Crystal growth follows trends expected in traditional crystallization models in areas of high concentrations of reactant and relatively lower energy levels, however when reactant concentration drops or energy levels increase sonofragmentation becomes a significant factor in which the shockwaves fracture HKUST-1 crystals.

Variables concerning the crystallization of HKUST-1 have been systematically altered during sonochemical synthesis and particle sizes have been reported based on SEM analysis. Factors including sonication amplitude and solvent choice were seen to be primary factors contributing to particle size, sonicator tip size and reactor size were seen as primary factors contributing to particle size distribution, and time was found to less impact relative to other parameters studied and a much more significant effect on yield.

APPENDIX C

UiO-66 MOF AND POLY(VINYL CINNAMATE) NANOFIBER COMPOSITE MEMBRANES SYNTHESIZED BY A FACILE THREE-STAGE PROCESS

C1. Introduction

Metal organic framework (MOF) crystals have been extensively studied for many applications such as sensing,(J. Yang et al., 2015) catalysis,(Katz et al., 2015) separations,(Defei Liu et al., 2014) and gas storage(Basdogan & Keskin, 2015) in part due to their high surface area(Walton & Snurr, 2007) and tunability.(Shen & Yan, 2015) Limitations to MOF materials include the low stabilities of a majority of these crystals and the fact that nanometer to micrometer powder is sometimes not ideal for specific applications. Zirconium based MOFs (ZrMOF) are becoming more popular,(Kandiah et al., 2010) due in part to their superior stability relative to MOFs based on other metals,(Wang et al., 2015) since the archetypal ZrMOF, UiO-66 (also called Zr-BDC), was synthesized.(Cavka et al., 2008) To make MOF based materials suitable for applications, work has been done to grow the crystals on various substrates such as porous stainless steel,(Stoeger, Choi, & Tsapatsis, 2011) metal alloys,(Z. Zhao, Ma, Li, & Lin, 2011) and polymeric hollow-tube membranes.(Brown et al., 2012) Recently, nanofibers have been introduced as a platform for growing MOF crystals on.(Xu, Wen, Zhu, et al., 2012) Plastic nanofibers are a promising material themselves due to their own high versatility in many fields such as sensing,(Agarwal, Raheja, Natarajan, & Chandra, 2012) protective clothing,(L. Chen et al., 2009) and separations.(X.-H. Qin & Wang, 2006) Exciting proof of concept work has been reported showing MOF impregnated nanofibers electrospun, followed by controlled secondary growth of the MOFs on the fibers leading to interesting morphologies such as full membranes(Xu, Wen, Zhu, et al., 2012) and two-dimensional strings of nanofibers completely covered in a thin layer of MOF crystals.(Bechelany et al., 2015)

Currently, nano-composite MOF/ nanofiber materials face one large limitation preventing their utilization in the broad array of applications in which secondary growth is desirable: to fabricate nanofibers they must be dissolved in a solvent for electrospinning, and for secondary growth they must be placed in a solvent, and usually heated above 100 °C, for extended periods of time to grow the MOF crystals. The conditions required for MOF secondary growth are generally too extreme for the nanofibers, leading to dissolution or contraction of the nanofibers. Because of

this, only a handful of MOFs have been successfully grown on nanofibers including CuBTC,(Xu, Wen, Zhu, et al., 2012) MIL-53-NH_2,(Bechelany et al., 2015) and Zif-8.(Jin, Bian, Li, Ding, & Gao, 2013) Others have been grown by using the fibers as a sacrificial layer.(Xu, Wen, Zhu, et al., 2012) Successfully choosing polymers with high thermal stability, high chemical stability for a solution required to grow ZrMOFs, and yet a high solubility for a separate solvent is nearly impossible. Any polymer candidate that seems possible would require extremely harsh conditions and solvents that may deteriorate the MOF seed crystals. Instead, modification of the nanofibers after electrospinning presents itself as a more promising path. Some nanofibers have been cross-linked already including a polystyrene derivative(Xu, Wen, Wu, Lin, & Li, 2012) and poly(ethylene oxide).(Vondran, Sun, & Schauer, 2008) Some nanofibers have even been successfully cross-linked using ultraviolet light such as unsaturated polyester,(Fang, Lin, Tian, Sharma, & Wang, 2007) poly(ethylene oxide),(Zhou, Wang, & Wu, 2012) and poly(vinyl cinnamate) (PVCi).(Lyoo, Youk, Lee, & Park, 2005) Crosslinking via ultraviolet light provides potential as a way to increase chemical and thermal stability of nanofibers under mild conditions without sacrificing nanofiber structure.

In this work, the commercially available polymer PVCi is electrospun, and the changes in structure, chemical stability, and thermal stability induced by ultraviolet crosslinking on these nanofiber mats are investigated. Then, for the first time, a ZrMOF is grown via solvothermal secondary growth on these electrospun mats to form various topologies. At latter growths, continuous UiO-66 membranes with PVCi scaffolding for structural support are observed and tested for gas permeation properties. This novel process is also translatable to other MOFs requiring strong solvents and temperatures, as well as any other polymers that can be electrospun and cross-linked under mild conditions.

C2. Experimental

C2.1. Chemicals and supplies. Dimethyl formamide (DMF), acetic acid, and dichloromethane (DCM) were each purchased from Fischer Scientific, zirconium chloride ($ZrCl_4$) and terepthalic

acid (BDC) were purchased from Sigma-Aldrich, poly(vinyl cinnemate) (PVCi) was purchased from Polysciences INC., the gases nitrogen, argon, helium, and sulphur tetraflouride were purchased from Praxair, and stainless steel mesh, needles, and tubing for electrospinning were purchased from McMaster-Carr. All chemicals and materials were used without further processing.

C2.2. UiO-66 seed synthesis. Solvothermal reactions were carried out in a Teflon lined autoclave by mixing 0.357 g of $ZrCl_4$ and 0.254 g of terephthalic acid in 21 mL of dimethylformamide (DMF) and 8.6 mL of acetic acid. The mixture solution was heated at 120 °C for 24 h, then slowly cooled to room temperature yielding the white color crystals. The synthesized sample was obtained by filtration, and dried in air for 24 h before use.

C2.3. Nanofiber synthesis. Solutions of 10 wt.% PVCi/DCM with 100 mg of UiO-66 crystals were prepared and stored in darkness at room temperature until use.

PVCi and PVCi with UiO-66 samples were fed through a metallic needle by a syringe pump (New Era Pump Systems, Inc.) at the rate of 3 and 4.2 ml h^{-1}, respectively. A voltage of 22 kV (Gamma High Voltage Research) was applied between the spinneret and the collector with a distance of 6 cm at room temperature. The spun-nanofibers mats were collected and dried at room temperature for 24 h.

C2.4. UV irradiation. For photo-crosslinking, the electrospun PVCi mats were irradiated with ultraviolet (UV) light for 30, 60, and 120 minutes. The PVCi with UiO-66 solution was UV irradiated for 3 h. The irradiation of nanofibers was carried out by a UVM-28 EL Series UV Lamp (UVP, LLC, CA, USA) emitted a light intensity of 2000 μW/cm² at a wavelength of 302 nm at room temperature. The mats were place under UV light with a distance of 4 cm from the lamp head. An initial 15 min time period was allotted for the lamp to warm up before exposing to nanofibers.

C2.5. Secondary growth. Photo-cross-linked PVCi with UiO-66 mats were cut to fit inside 100 mL Teflon lined autoclaves and filled with a solution of 0.115 g of $ZrCl_4$ and 0.083 g of terephthalic acid in 35 mL of DMF. Samples were heated at 100° and 80 °C for 12 h. The membranes were collected from the autoclave and allowed to slowly cool. The procedure was repeated 3 and 4 times at 100 °C and 80 °C, respectively. Final membranes were washed multiple times with DMF to remove any excess UiO-66.

C2.6. Characterization. Nanofibers stability was tested by exposing the PVCi mats to air and DMF; nanofibers and DMF were sealed in a 50 mL Teflon lined autoclave and nanofibers exposed to air were placed in a petri dish. Samples were kept at room temperature, 80 and 120 °C for 24 h, then slowly cooled to room temperature. Analysis of the mats was conducted by using digital photographs taken by MicroCapture Pro microscope, (Celestron).

The surface morphologies of gold-coated electrospun PVCi fibers were observed by a scanning electron microscope (SEM, Zeiss).

Powder X-ray diffraction (PXRD) analysis of the UiO-66 and secondary growth samples were performed using an X-ray diffractometer (P'ANalytical) at 40 kV with a Cu-Kα X-ray tube with a nickel filter.

A BET surface analyser (Micrometrics TriStar II 3020) was used to measure nitrogen adsorption–desorption isotherm on samples that underwent solvent-exchange by immersion in acetone for 24 h while replacing the solution 3 times and activating under vacuum for 12 h.

C3. Results and Discussion

C3.1. Poly(vinyl cinnamate) crosslinking and stability. Electrospun PVCi mats were cross-linked for 30, 60, and 120 minutes under ultraviolet irradiation, and the FTIR patterns of each sample is shown in Figure C1 along with the cross-linking scheme of PVCi monomers.

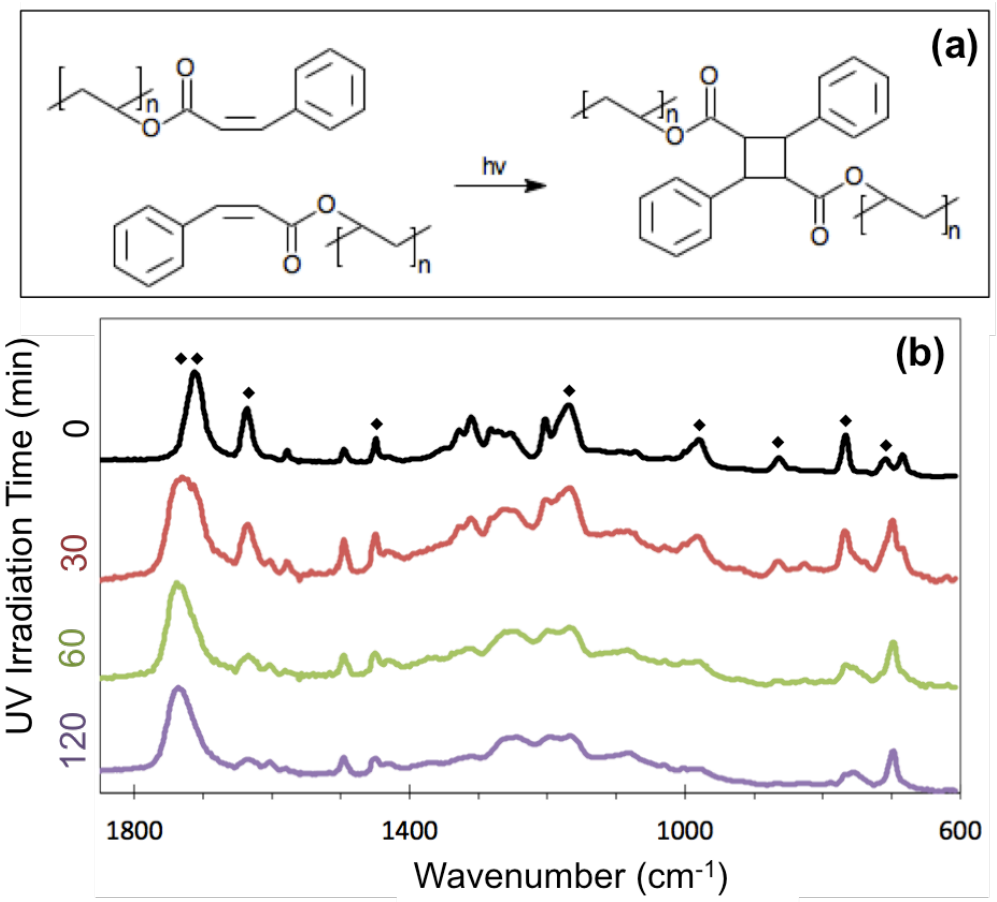

Figure C1. PVCi crosslinking mechanism via ultraviolet irradiation (a). FTIR absorbance for pure PVCi nanofiber irradiation times of 0, 30, 60, and 120 minutes stacked and normalized to each spectra's maximum intensity (c). The (♦) annotation denotes the wavenumbers 1734, 1712, 1636, 1450, 979, 864, 767, 709, and 698 cm^{-1} from left to right.

The reaction between PVCi monomers is a photo-induced [2+2] cycloaddition reaction between two cinnamate side-groups forming a cyclic carbon bond from the C=C bond in the cinnamate group.(Sung et al., 2006) Notable patterns seen in this data are a shift in the large peak at 1712 cm^{-1} to 1734 cm^{-1} corresponding to unsaturated and saturated C = O stretching vibrations, respectively. Both of these peaks appear to be present at 30 minutes of crosslinking, but by 60 minutes the peak at 1734 cm^{-1} appears to be dominant. These results are consistent with those of previously characterized PVCi cross-linked nanofibers.(Lyoo et al., 2005) The FTIR spectra also showed peaks at: 1636 cm^{-1}, caused by oscillation of coupled double bonds of C = C types; 1167 cm^{-1} corresponding to C = C – H interactions; and peaks of the range 979 – 709 cm^{-1}

are also related to the presence of = CH bonds. These peaks can be seen decreasing with increasing irradiation time. A strong peak representative of – C-H bend at 698 cm^{-1} can also be seen in each of the three cross-linked spectra. These changes confirm the absence of carbon double bonds in the final PVCi molecule and validate the effectiveness of the ultraviolet cross-linking process.

Before impregnating PVCi with UiO-66, stability tests were performed on the PVCi nanofibers to confirm that the cross-linking was capable of providing insoluble supports for the secondary growth through the formation of extended polymer networks generated from bonds between polymer chains. To test these materials non-cross-linked fibers as well as fibers that have been cross-linked for 30, 60, and 120 minutes were placed into ovens for 24 hours while still on the stainless steel mesh. Half of the samples were left in air to test the temperature stability, and half of the samples were submerged in 10 mL of DMF to test solvent compatibility. Table C1 depicts the results, where a check mark denotes the presence of nanofibers on the stainless steel mesh after the test, and an x represents no nanofibers on the stainless steel mesh after the test.

Table C1.
Crosslinked PVCi Stability Test

			Ambient Air	10 mL DMF		
Temp (°C)	25	80	120	25	80	125
PVCi unmodified	✓	✓	✓	✗	✗	✗
PVCi 30 min UV	✓	✓	✓	✓	✓	✓
PVCi 60 min UV	✓	✓	✓	✓	✓	✓
PVCi 120 min UV	✓	✓	✓	✓	✓	✓

*Unmodified nanofibers and fibres cross-linked for various times were exposed to the specified conditions for 24 hours. A (✓) denotes fibres remaining after the test and an (✗) denotes no fibres remaining after the test.

This table shows that the PVCi must undergo some degree of cross-linking to withstand any DMF exposure at all, and that between 30 minutes and 120 minutes of cross-linking the fibers become insoluble in DMF up to at least 120 °C, which was chosen as the maximum temperature studied since it is at the upper end of what is typical for MOF synthesis. The fact that multiple degrees of cross-linking provide enough protection against strong solvents like DMF

suggests that polymer properties such as stiffness and toughness may be optimized for particular applications when using this technique due to the large window of acceptable degrees of cross-linking that these different times are shown to correspond to in Figure C1. Since the degree of cross-linking of the PVCi nanofibers can be determined by the intensity of the peaks, and is also time dependent; the strength of the nanofibers can be optimized to satisfy specific applications' requirements.

The cross-linking of fibers shows that it can strengthen the fibers chemical and temperature stability; adding other variables, which can determine other benefits of cross-linking the nanofibers, can do more tests. Including purposes like MOF secondary growth, this technique may be used for many other applications such as strengthen the polymer equipment or clothing that are frequently in contact with chemicals, and working under higher temperature environment.

C3.2. UiO-66 secondary growth. UiO-66 seeds were synthesized and suspended in solutions of PVCi in DCM, To achieve the nearly complete cross linking desired for the secondary growth of UiO-66, a 3 hour UV irradiation time was carried out to achieve a similar degree of cross linking as the 2 hour time for pure PVCi nanofibers according to FTIR. It is hypothesized that the longer times required to cross link MOF impregnated nanofibers relative to pure nanofibers is because of the increased average distance between PVCi functional groups caused by the presence of MOFs impregnated in the fibres, and a smaller amount of available crosslinking sites available because of this spacing. After crosslinking, UiO-66 secondary growths were performed at 100 °C and 80 °C, and every 12 hours the samples were dried and placed into a fresh growth solution until the final membranes were produced. Samples were analysed at each time step to study the affects of each temperature and each growth. Figure C2 shows the FTIR patterns of each growth recorded.

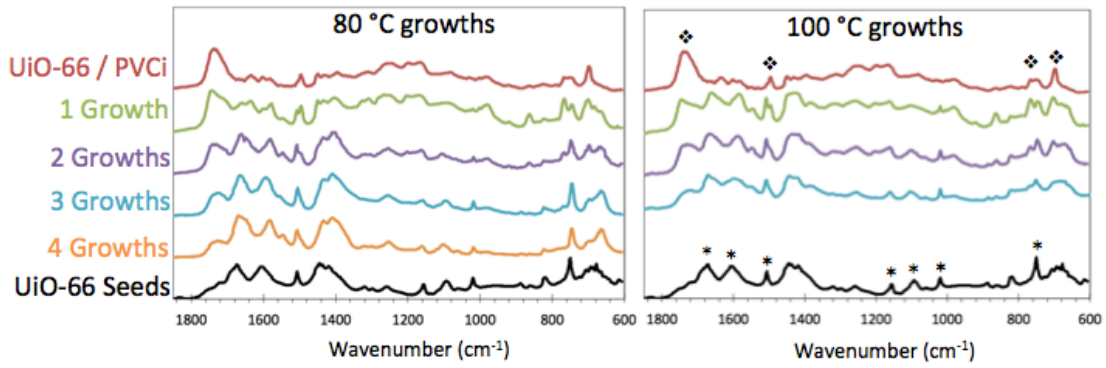

Figure C2. Normalized and stacked FTIR absorbance spectra of the UiO-66 seeds as well as UiO-66 impregnated PVCi membranes at after crosslinking and at each reported stage of secondary growth. The reference symbol (*) denotes peaks are major peaks attributed to UiO-66 seed absorbance at 1675, 1607, 1507, 1157, 1094, 1020, and 750 cm^{-1}, and (❖) denotes major peaks that are attributed to cross-linked PVCi at 1737, 1498, 754, and 698 cm^{-1}.

From the FTIR peaks it can be seen that the peaks representative of the UiO-66 crystal pattern increase with increasing growths. The stability of the PVCi fibres at increased temperature and prolonged chemical exposure times is reaffirmed in Fig. 3 by the absence of a doublet or peak shift at 1737 cm^{-1}, which would indicate the breaking of cross linking bonds. Systematic decreases in representative PVCi peaks across the FTIR spectra occur as well at 1737, 1498, 754, and 608 cm^{-1}, while peaks provided by the UiO-66 seeds steadily become more prominent with growths at 1675, 1507, 1157, 1094, 1020, and 750 cm^{-1}.

Figure C3 shows PXRD patterns performed on membranes of each time step to monitor the synthesis of UiO-66 at each interval. These intervals each show an increase in crystallinity as the UiO-66 crystals emerge and engulf the PVCi fibres, and the final pattern for each temperature are compared to a simulated PXRD pattern from single crystal XRD data provided by Cavka et. al.(Cavka et al., 2008)

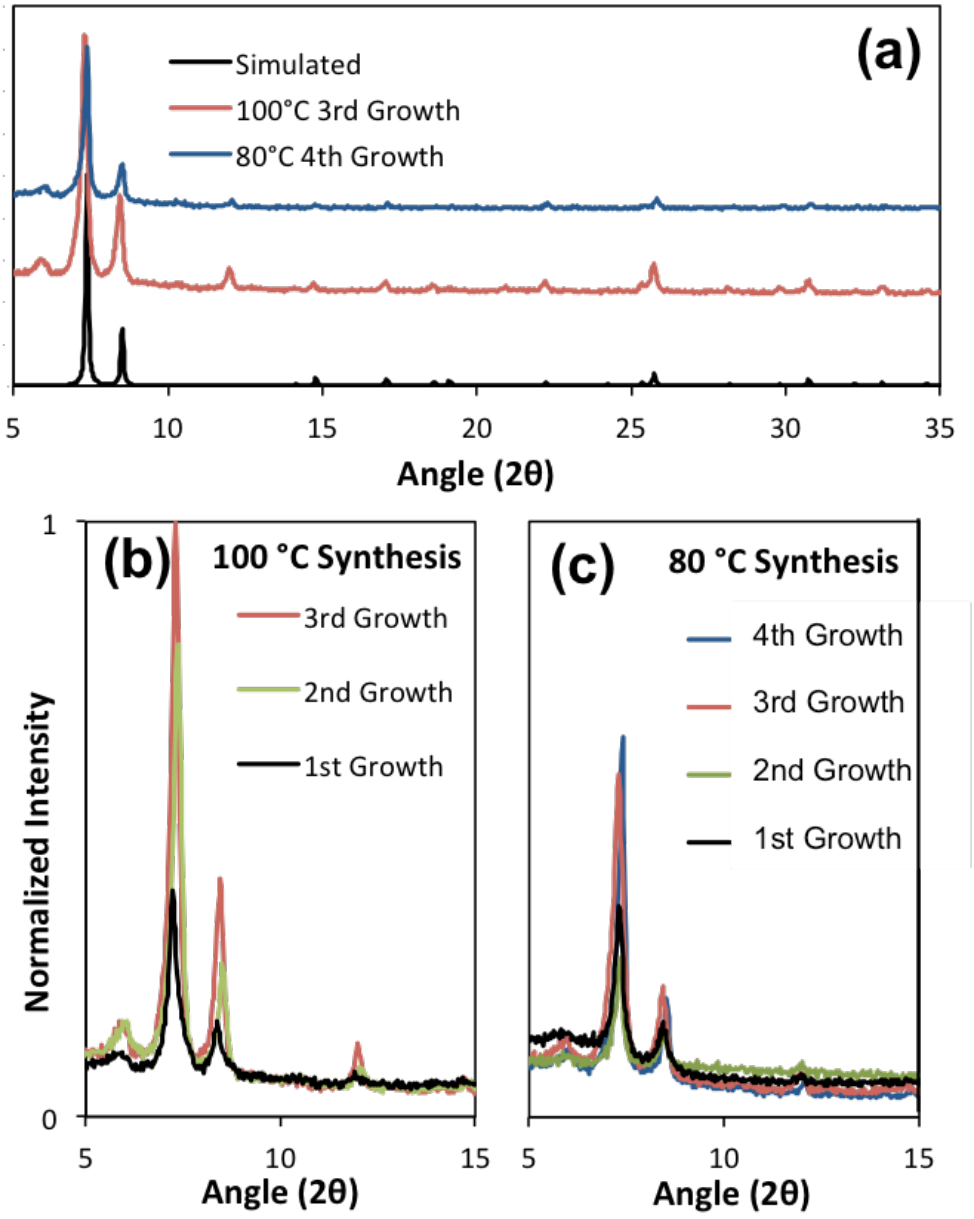

Figure C3. PXRD patterns comparing the final membranes for both 80 °C and 100 °C compared to a simulated pattern for pure UiO-66 powder (a). PXRD patterns of membranes after each 12 hour growth period for 100 °C (b) and 80 °C (c) synthesis temperatures normalized to the maximum intensity found from the 3rd growth at 100 °C.

The peaks from the membranes match the peaks of the simulated pattern with the addition of a peak near 12 2θ, which was also present in the UiO-66 seed crystals. The relative

background intensities of the stainless steel mesh to UiO-66 peak heights cannot be correlated to the thickness of the membrane since the mesh is not a single uniform layer, and the positioning of the sample in the X-ray diffractometer will have a significant impact on this peaks height. The sharp peaks at later growths and lack of peaks that do not correspond to UiO-66 or the steel mesh in the PXRD helps confirm that high crystallinity UiO-66 membranes with low impurity are produced by this method.

Scanning electron images were taken of each sample after PXRD analysis, and the results can be seen and compared in Figure C4. Images in (a) and (i) show fibres immediately after cross-linking, at lower magnifications the well distributed nonwoven mat commonly attributed to the electrospinning method is observed,(Bhardwaj & Kundu, 2010) and at high magnifications some agglomerates of UiO-66 particles can be seen sticking out of smooth fibres with fibres diameters well below 10 μm. Images (e) and (j) show the fibres after 1 growth at 80 °C with the fibres well intact, and looking similar to the fibres before growth. The increased magnification of (j) shows the small MOF particles start to grow and emerge from the PVCi fibres. Subsequent growths at both 80 °C (images (e) through (h)), and 100 °C (images (b) through (d)) show UiO-66 particles growing larger, and the third growth at 100 °C (images (d), (k), and (l)) show a membrane dominated by UiO-66 with the shape of a few fibres near the surface of the membrane. Intermediate growths of UiO-66 on these fibres show great flexibility in designing composite membranes, where variables such as flexibility, flux, and surface area may be manipulated by selecting the degree of UiO-66 growth for various applications such as protective clothing and sensors. However, this work is focused on the analysis and characterization of the final growth and its applicability as a gas membrane.

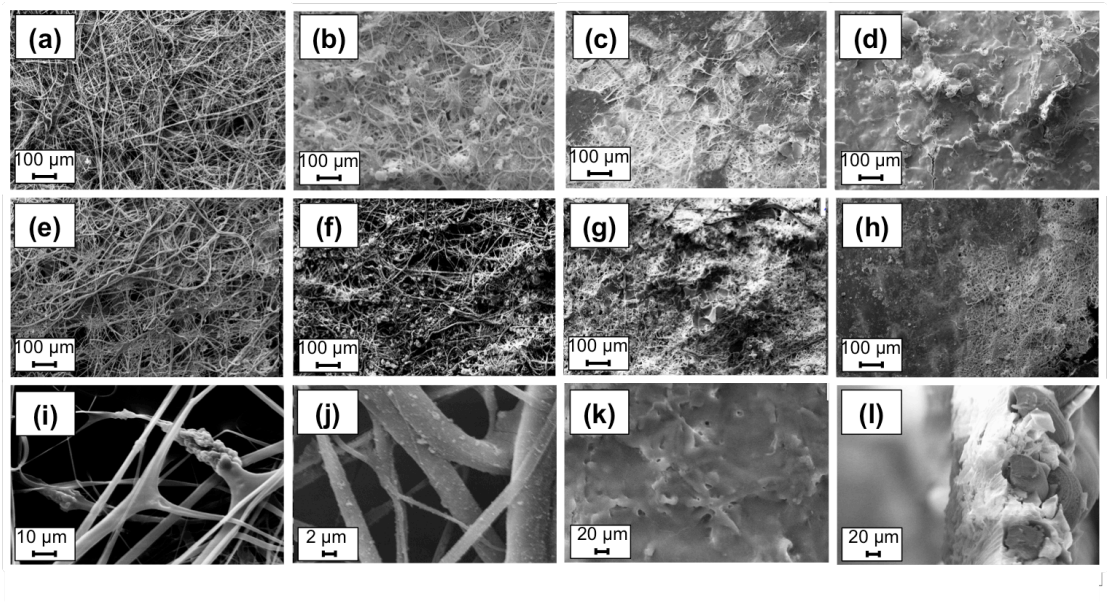

Figure C4. SEM images of: PVCi fibers with embedded UiO-66 crystals after UV crosslinking (a), the PVCi/ UiO-66 membrane after 1 growth at 100 °C (b), after a 2nd growth at 100 °C (c), a 3rd growth 100 °C (d), after a 1st growth at 80 °C (e), a 2nd growth at 80 °C (f), a 3rd growth at 80 °C (g), a 4th growth at 80 °C (h), a higher magnification of PVCi fibers with embedded UiO-66 crystals after UV crosslinking (i), a higher magnification of the 1st growth at 80 °C (j), a higher magnification of the 3rd growth at 100 °C (k), and a cross-sectional image of the 3rd growth at 100 °C (l).

C3.3. Membrane characterization. The final membrane at 100 °C is predominantly defect-free, and the crosscut image at higher magnifications in image (j) shows a thickness a little larger than 20 µm. Control over membrane thickness and defects is expected to be readily tuneable through increased MOF/ nanofiber loading ratios in the initial electrospinning solution or decreased MOF size to increase MOF nucleation points, in the electrospinning stages by controlling the thickness of the mat electrospun, or changes of secondary growth conditions such as MOF precursor concentration, reaction time, and temperature. Some boundaries and non-uniformities can be seen on the surface of the fully grown sample, especially in (k), however these irregularities and grain boundaries do not appear to propagate the through the entire membrane.

The final growth of the membrane was analysed with nitrogen porosimetry and compared to activated UiO-66 seed crystals. These isotherms along with a digital image of the final membrane can be seen in Figure C5.

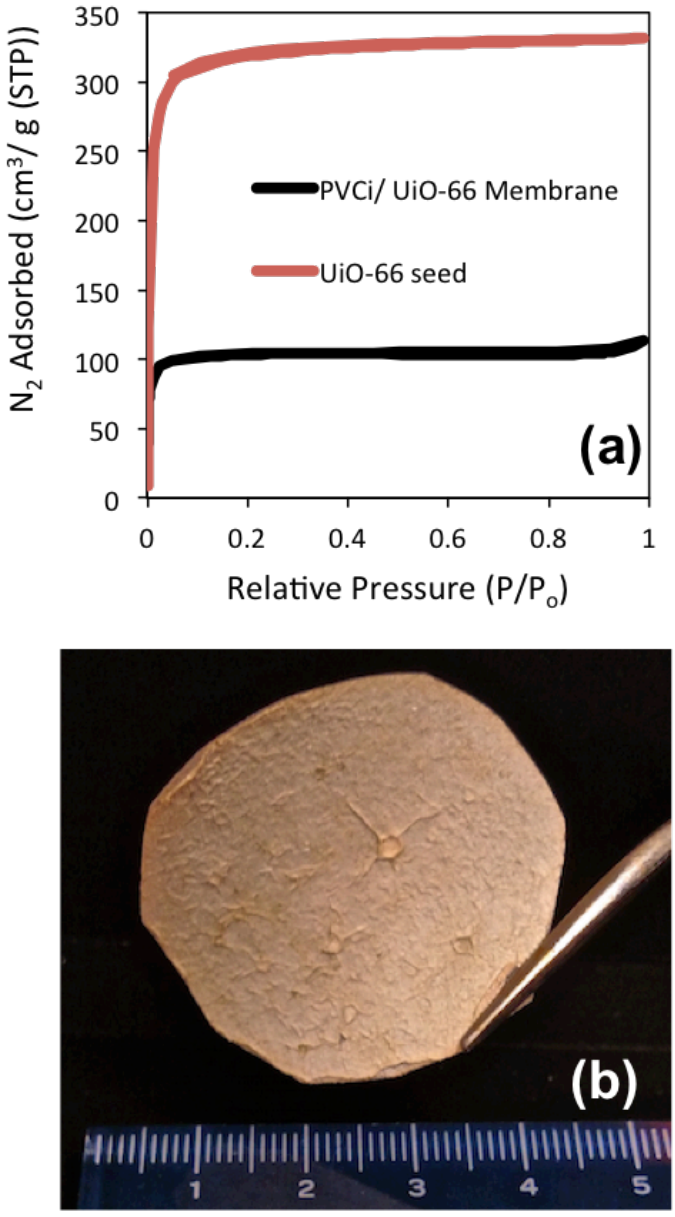

Figure C5. Isotherm of membrane after 3rd growth at 100 °C showing a BET surface area of 430 ± 1 m^2/g and the UiO-66 seeds with a BET surface area of 1188 ± 15 m^2/g (a). Digital image of membrane after 3rd growth at 100 °C after 3 washes with DMF, ruler units are cm (b).

Figure C5 shows a type 1 isotherm indicative of a microporous material for the UiO-66/ PVCi nanofiber composite membrane with a slight increase near the saturation pressure that may have resulted from mesoporous grain boundaries or pockets within the membrane. However, the isotherm does show reversible adsorption due to the absence

of hysteresis. The BET surface area of the membrane was found to be 430 ± 1 m^2/g. The UiO-66 seed isotherm shows a strong type I isotherm and has a BET surface area of 1188 ± 15 m^2/g, which compares favourably with literature values for the surface area of 1067 m^2/g reported by Yang et. al.(Q. Yang et al., 2011)

C4. Conclusions

This appendix introduces a three-part process for enabling the secondary growth of MOFs previously unavailable for growth on electrospun nanofibers. Poly(vinyl cinnamate) (PVCi) is electrospun, crosslinked via UV irradiation, and tested for chemical stability. Then, UiO-66 seeds are suspended in the electrospinning solution and UiO-66 impregnated PVCi nanofibers are synthesized. These fibers are then cross-linked and UiO-66/ PVCi composite membranes are grown through solvothermal secondary growth. The growth of these membranes are monitored at both 80 °C and 100 °C, and the final, continuous UiO-66 membrane supported by PVCi scaffolding was analysed by SEM, and nitrogen porosimetry. Discussions of many variables available for manipulating the final properties of the membrane are discussed such as membrane thickness and nanofiber toughness.

APPENDIX D

NANOFIBER-BASED MATRIMID ORGANOGEL MEMBRANES FOR BATTERY SEPARATOR

D1. Introduction

Electrospinning is an old technology that had remained dormant as an area of research until recently, with great interest generated by the surge in applications of nanotechnology.(Subbiah, Bhat, Tock, Parameswaran, & Ramkumar, 2005) Fibers produced from electrospinning are tunable from nanometers in diameter to several micrometers.(Reneker & Chun, 1996) This highly tunable fiber diameter along with tunable morphologies and the ability to use virtually any soluble polymer to produce fibers has been stimulating research interest in many fields including liquid separations, sensors, tissue scaffolding, and air filters.(Bhardwaj & Kundu, 2010) Another promising field for nanofiber-based materials are as separators for lithium-ion batteries.(Miao, Zhu, Hou, Xia, & Liu, 2013)'(Cao, An, Xu, & Huang, 2016) Nevertheless, an unfortunate drawback preventing this technology from further applications is the necessity of using soluble polymers, leading to an inherent inability to use unmodified nanofibers for applications requiring strong solvents. Nanofiber mats possess properties that would allow these materials to excel in applications involving strong solvents such as organic solvent filtrations, battery separators, and membrane distillation with higher chemical resistances. A handful of studies have shown the cross-linking of polymers to increase chemical resistance and application durability such as poly(vinyl cinnamate) for growth of zirconium-based metal-organic frameworks,(M. R. Armstrong et al., 2015) poly(ethylene oxide) for oil/water separation,(Ju et al., 2008) and poly(Vinyl alcohol) for microscaled-particles filters.(Ding, Kim, Lee, Lee, & Choi, 2002) However, these works either only introduce water resistance, or are composed of polymers that are not as commercially desirable as other materials.

Porous organogel membranes (POMs) with high surface area by incorporating a crosslinking step to electrospun mats should increase the tunability and functionality of the electrospun polymer mats just as crosslinking does to traditional polymeric gels. In this work, Matrimid 5218 (hereafter simply referred to as Matrimid), a highly-produced, commercial available polymer, was selected for electrospinning, which is a crosslinkable polymer from the polyimide family that has been electrospun for a variety of applications including fuel cell membranes,(Dahi et al., 2014)

membrane distillation,(Francis et al., 2013) and as carbon nanofiber precursors.(G. S. Chung, Jo, & Kim, 2005) The incredibly versatile Matrimid resin in a traditionally casted film form is studied and used commercially for many applications including gas separation(Dong, Liu, & Huang, 2016; L. Liu et al., 2013; Rangel Rangel, Maya, Sánchez, de Abajo, & de la Campa, 2013) and solvent filtration membranes.(Sun, S.P., Chung, T.S., Lu, K.J., Chan, 2014) However, although Matrimid has been crosslinked in a film form,(Tin et al., 2003)'(Kuiper, Embrechts, Every, De Vries, & De Smet, 2013) notably for organic solvent nanofiltration applications,(Vanherck, Vandezande, Aldea, & Vankelecom, 2008) and has been electrospun,(Francis et al., 2013)'(G. S. Chung et al., 2005)'(Bansal, Meyer, & Salomon, 2008)'(Jung & Ferraris, 2012) the two techniques have not been combined, and resulting properties have not been determined.

Proven versatility and commercial-scale production of Matrimid makes it a natural and potentially archetypal polymer for electrospinning and crosslinking as the technology evolves and matures. For this reason, this work focuses on the crosslinking of electropun Matrimid mats with para-xylylenediamine to produce a series of POMs. Organogels are fluid-filled structures as predominantly contain an organic continuous phase. By forming a three-dimensional crosslinking network, polymers have the ability to retain organic solvents and create semi-solid systems.(Ibrahim, Hafez, & Mahdy, 2013; Terech & Weiss, 1997; Vintiloiu & Leroux, 2008) Key properties concerning application and design of Matrimid gels are analyzed for multiple crosslinking densities including stability tests and gel swelling. Matrimid nanofiber mats are then used as a battery separator. The separator is one of the most critical parts of lithium ion batteries, which separates the positive and negative electrodes to prevent electrical short circuits while permitting free flow of lithium ions and isolating electronic flow.(W. Chen et al., 2016; J. Li, Tian, Yan, He, & Tuo, 2016; Seol, Lee, & Park, 2006; S. S. Zhang, 2007) Commercially, polyethylene (PE), polypropylene (PP), or their blends, are used as separators in lithium ion batteries.(J. Li et al., 2016; C. Shi, Zhang, Chen, Yang, & Zhao, 2014) The poor thermal stability of these polyolefin porous membranes leads to thermal shrinkage when used under elevated temperatures: generating safety concerns.(X. Huang, 2011; Yi, Huaiyu, Jian, Yun, & Shushu, 2009) On the

other hand, safety and cycle life of the battery are affected by the required use of very thin and highly porous separators because their mechanical strength is reduced.

In order to satisfy these needs, battery separators can be designed and obtained from non-woven membranes as they have more alternatives in compositions and structure than polyolefin (PE, PP) membranes.(Yi et al., 2009) Non-woven separators obtained by electrospinning are characterized by high porosity and large pore size.(S. S. Zhang, 2007) Moreover, studies made in electrospun polyimide nanofibers show an exciting superior thermal stability and mechanical and electrochemical performance when used as separators for lithium ion batteries.(Jiang et al., 2013; Miao et al., 2013)

The polyimide Matrimid has a glass transition temperature of 338 ^{o}C,(T. S. Chung, Chan, Wang, Lu, & He, 2003) and a degradation temperature of 465 ^{o}C,(Aziz & Ismail, 2010) which can effectively avoid the short circuits caused by the shrinkage of the conventional separators at high temperature of 150^{0}C.(Miao et al., 2013) Based on these chemical properties, Matrimid nanofibers are placed in an electrolyte solution composed of the strong solvent $LiPF_6$ in EC-DEC-DMC, and 20 charge/ discharge cycles are ran to further confirm the synthesized Matrimid POM are capable of continued performance in strong-solvent systems.

D2. Materials and Methods

D2.1. Preparation of Matrimid nanofiber organogel. Solutions of 12 w/w% Matrimid/DMF were prepared and fed through a metallic needle by a syringe pump (New Era Pump Systems, Inc. NY, USA) at the rate of 0.6 ml h^{-1}. A 5-cm circular 100 mesh 304 stainless steel filter was used as a collector. A voltage of 22 kV (Gamma High Voltage Research) was applied between the spinneret and the collector with a distance of 23 cm at room temperature. To obtain test samples with structures matched as much as possible, all electrospun nanofibrous mats were produced from 0.12 mL of the electrospinning solution, except for the membranes used for the battery test which

were produced from 1.2 mL of the Matrimid/DMF solution in order to increase the thickness. The spun-nanofibers mats were collected and stored at room temperature until use.

Crosslinking modification was performed as reported by Tin et al.(Tin et al., 2003) Crosslinking reagent solutions of 10% (w/v) para-xylenediamine/methanol were prepared. Electrospun Matrimid membranes were immediately washed with fresh methanol after 0.5, 3, 12, 24, and 72 hours to quench the crosslinking reaction and remove residual reagents. Samples were dried at room temperature overnight before tests.

D2.2. Characterization. The IR spectra of membranes were obtained at room temperature by a Nicolet iS50 FT-IR with a DTGS detector (Thermo Scientific, USA). Each image is an average of 100 scans in the range 1900-600 cm^{-1}, a background was taken immediately preceding each measurement.

SEM images were taken on a Zeiss EVO MA 10at 18.00 kV. The non-metallic samples were sputtered with gold and placed on copper tape for analysis.

Optical Profilometry was carried out with a 20x lense on a ZeScope Optical Profilometer machine. The tape substrate was considered level and the data was normalized to its slope. To prepare samples, each was pressed onto flat double sided copper tape intended for SEM, and attached to glass substrate. The fibers were carefully saturated in acetone and dried to set the fibers flat over the copper tape.

D2.3 Mechanical and stability tests. The DMA (Dynamic Mechanical Analysis) test used a Discovery HR2 Hybrid Rheometer (TRIOS software - TA Instruments) testing each sample in triplicate with a crosshead speed of 50 μm/s. Sample preparation was carried out using the method described by Tan et al.(E. P. S. Tan & Lim, 2006)

The stability of the nanofibers was tested by exposing the Matrimid mats to air and DMF; nanofibers exposed only to air were placed in a Petri dish, while nanofibers and DMF were sealed in a 50 mL Teflon lined autoclave. Samples were kept at room temperature, 100 °C, and 150 °C for 24 h, and then slowly cooled to room temperature. Analysis of the mats was conducted by using digital photographs taken by a MicroCapture Pro microscope (Celestron).

D2.4 Battery test. Matrimid membranes that underwent a 3-day crosslinking modification were tested as battery separators. These membranes were placed in a vacuum drying chamber at 75 ^{0}C overnight to get rid of crosslinking reagent residual before being used to assemble the cells.

The separators were sufficiently soaked in a liquid electrolyte consisting of 1.0 M $LiPF_6$ in ethylene carbonate (EC)-diethyl carbonate (DEC)-dimethyl carbonate (DMC) (4/2/4 by weight) in an argon-filled glove box. The electrolyte soaked separators were sandwiched between a natural graphite anode and a $LiCoO_2$ cathode of 4 cm^2 in area and assembled into blocking-type cells. A BT2000 Battery Test Equipment (Arbin Instruments, TX, USA) was used to evaluate the C-rate capability and cycling performance of the cells. For the measurement of cycling performance, the cells were cycled at a constant charge/discharge current density of 0.1C/0.1C for 20 cycles under a voltage range between 2.5 and 4.2 V.

The thermal shrinkage of the Matrimid separators was determined by measuring the change in area of 1 cm^2 – separator that underwent heat treatment at 120, 150, 170, 180, 190, and 200^{0}C for 0.5 h. The shrinkage percent was calculated using the following equation (S_0 and S stand for the area of separator before and after heat treated, respectively):

$$Shrinkage\ \% = \frac{S_0 - S}{S_0} \times 100 \qquad \text{(D.1)}$$

D3. Results and Discussion

D3.1 Matrimid crosslinking and mechanical strength.

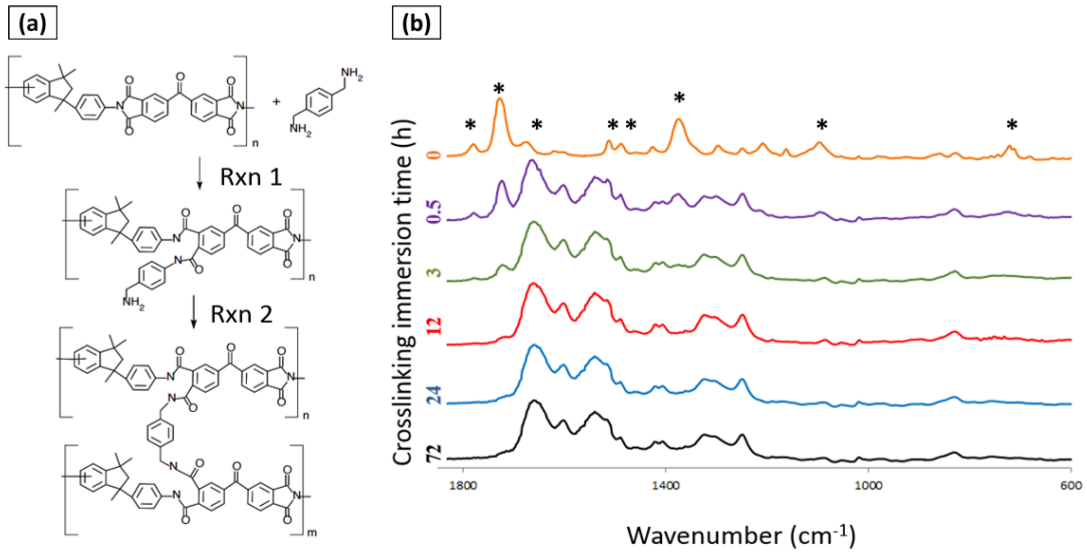

Figure D1. Matrimid crosslinking mechanism via solvent immersion (hydrogen atoms on Matrimid structure omitted for clarity) (a)**.** FTIR absorbance for pure Matrimid nanofibers solution immersion times of 0, 0.5, 3, 12, 24, and 72 hours stacked and normalized to each spectra's maximum intensity (b). The (*) annotation denotes the wavenumbers 1780, 1728, 1674, 1511, 1488, 1375, 1096, 721 cm^{-1} from left to right.

Electrospun Matrimid mats were crosslinked for 0, 0.5, 3, 12, 24 and 72 hours through room temperature solution immersion. Figure D1a shows a two-part reaction scheme for the crosslinking of Matrimid; amino groups in para- xylylenediamine attack the imide functional groups of Matrimid. FTIR peaks after varying crosslinking times are shown in Figure D1b.

The pure Matrimid film exhibited peaks at 1780, 1728, 1674, 1511, 1488, 1375, 1096, 721 cm^{-1}. Asymmetric and symmetric C=O stretching vibrations in the imide groups are represented, respectively, by the bands observed at 1780 and 1728 cm^{-1}. Both of these peaks appear to be present at 0.5 and 3 hours of crosslinking, but by 12 hours the peak at 1780 cm^{-1} has disappeared and the absorption band observed at 1728 cm^{-1} is almost undefined. The 1674 cm^{-1} peak is assigned to the benzophenone C=O stretching mode. The bands at 1510 and 1488 cm^{-1} are for the aromatic stretching of the para-disubstituted phenyl group. The bands observed at 1375 cm^{-1} proved the presence of aliphatic C–H bending vibration and/or C–N stretching of the

imide groups; this peak showed a decrease in its intensity with increasing immersion time. The 1096 cm^{-1} absorption bands are for the stretching modes of the C–N–C of the imide 5-membered ring, while the aromatic bending vibration is present at 721 cm^{-1}.

The cross-linking network in Matrimid can be detected from the appearance of amide groups.(Aziz & Ismail, 2010) The characteristic amide peaks are at 1662 cm^{-1} (C=O symmetric stretch of amide groups) and 1540 cm^{-1} corresponding to stretching of C–N and/or bending of N–H of CONH groups. Both peaks appeared and increased in their intensities with increasing immersion time. The formation of new amide groups confirms that the reaction successfully occurred and indicates that the cross-linking in Matrimid is a time-dependent process. These results are consistent with those of previously characterized Matrimid crosslinked films.(Aziz & Ismail, 2010; Ordoñez, Balkus, Ferraris, & Musselman, 2010; Rahmani et al., 2014; Sazali, Wan Salleh, Md Nordin, Harun, & Ismail, 2015; Sridhar, S., Veerapur, R. S., Patil, M. B., Gudasi, K. B., Aminabhavi, 2007)

The intensities of the FTIR peaks at 1728 and 1674 cm^{-1} were obtained from the respective spectra of each crosslinking time (CLT): 0, 0.5, 3, 12, and 72 h. The intensity ratio (IR) between both peaks (1674 cm^{-1}/1728 cm^{-1}) was calculated. This procedure was repeated three times using three different samples of each CLT and a final average for each CLT was reported. The final crosslinking determination was calculated considering 0 h of CLT as 0 % relative crosslinking degree (RCLD), while 72 h of CLT was set as 100 % RCLD. RCLD for 0.5, 3, and 12 h of CLT (X sample) were interpolated according to the following formula, while results are shown in Figure D2.

$$Relative\ Crosslinking\ Degree\ of\ x\ h\ CLT\ sample = \left(\frac{Average\ of\ IR\ at\ X\ h\ CLT - Average\ of\ IR\ at\ 0\ h\ CLT}{Average\ of\ IR\ at\ 72\ h\ CLT - Average\ of\ IR\ at\ 0\ h\ CLT}\right) \times 100 \quad (D.2)$$

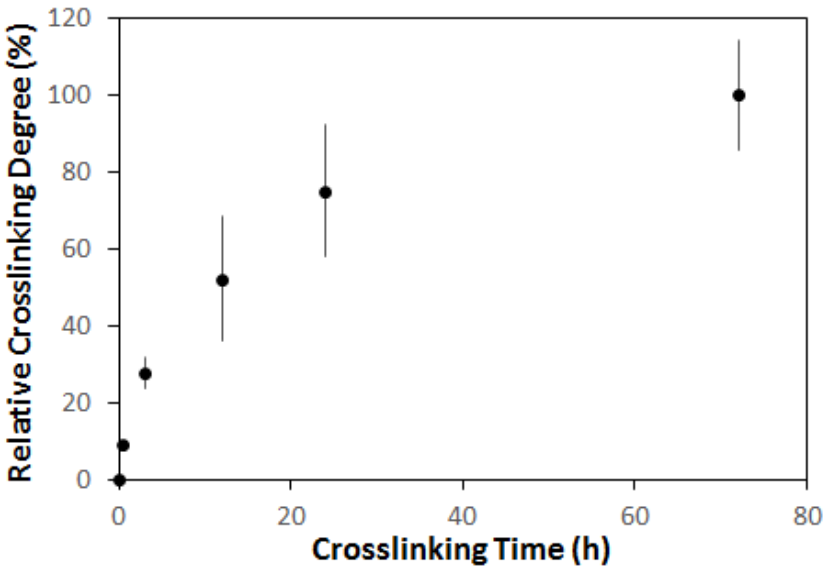

Figure D2. Correlation between relative crosslinking degree (% RCLD) and crosslinking time (h CLT).

Tin et al.(Tin et al., 2003) crosslinked 2 w/w% Matrimid/DCM casted films for 61 days. After this time, it can still be seen both interest peaks of Matrimid, at 1727 and 1674 cm^{-1}. This demonstrates that the crosslinking effect is incomplete since Matrimid active sites are still available. Therefore, it can be concluded that the electrospinning method for more efficient crosslinking results in less time brought about by the drastically larger surface area provided by fiber mats. SEM and digital pictures were taken for the mats before crosslinking, after 30 minutes of crosslinking, and after 3 days of crosslinking. Results are shown in Figure D3.

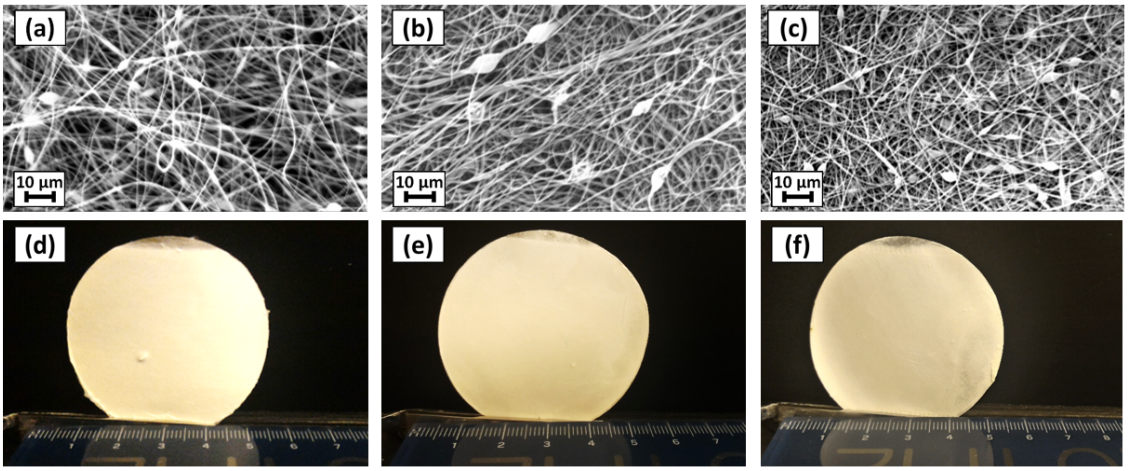

Figure D3. SEM images of: pure Matrimid fibers (a), Matrimid fibers after 3 hours of crosslinking (b), after 72 hours (c); digital image of pure Matrimid membrane (d), after 3 hours of crosslinking (e) and after 72 hours (f), ruler units are in cm.

Images in Figure D3(a-c) show Matrimid fibers at 0, 3, and 72 hours after the crosslinking reaction, respectively, at a magnification of 1500x in which uniformly distributed nonwoven mats are observed. This phenomenon is commonly attributed to the electrospinning method.(Bhardwaj & Kundu, 2010) Images (d) to (f) show optical images of Matrimid fibers after 0, 3, and 72 hours of crosslinking time. The fibers are intact after the crosslinking procedure; no physical change is perceived as the mats show the same uniform, cream color.

Optical profilometry results (from the original files supporting information) showed an average thickness value of 30 µm for each membrane represented in Figure D3, concluding that the thickness of the mats did not increase as the crosslinking time increased.

To confirm the degree of crosslinking with time, tensile strength tests were performed and the Young's Modulus was calculated from stress-strain curves.

Strain was calculated by:

$$\varepsilon = \frac{(l - l_0)}{l_0} \qquad \text{(D.3)}$$

where ε is the engineering strain, l_0 is the initial distance between the taped portion of the fibers (0.5 cm), and l is the distance between the taped portions of fiber at a given time.

Stress was calculated with:

$$\sigma = \frac{P}{A_0} \tag{D.4}$$

where σ is the engineering stress, P is the applied load, and A_0 is the original cross-sectional area found with the equation:

$$A_0 = \frac{Wt}{\rho} \tag{D.5}$$

where W is the width of the sample, t is the thickness found by optical profilometry, and ρ is the average fiber density across the cross-sectional area found by the difference between volumes of a nanofiber sample before and after dissolving into a dense thin film. Ultimate Tensile Strength (UTS) values are the highest engineering stresses obtained using equation D.4.

When tensioning the sample there is an initial non-linear region before the elastic regime that is attributed to the fibers aligning and taking in slack before the true elastic regime is observed and these initial points are neglected when measuring the Young's Modulus (E) as the slope of the elastic region in the stress-strain curve.

Higher crosslinking times (and therefore higher crosslinking degrees) lead to stiffer fibers (higher Young's modulus values).(Bigi, Cojazzi, Panzavolta, Rubini, & Roveri, 2001) Good agreement between the changes in Young's Modulus versus crosslinking time and FTIR experiments is shown in Figure D4. The crosslinking effect rigidifies the polymer chain due to the formation of crosslinked networks and hydrogen bonds, this also leads to the filling in the inter-chain spaces rearranging the free volume distribution.(Papporello, Miro, & Zamaro, 2015)

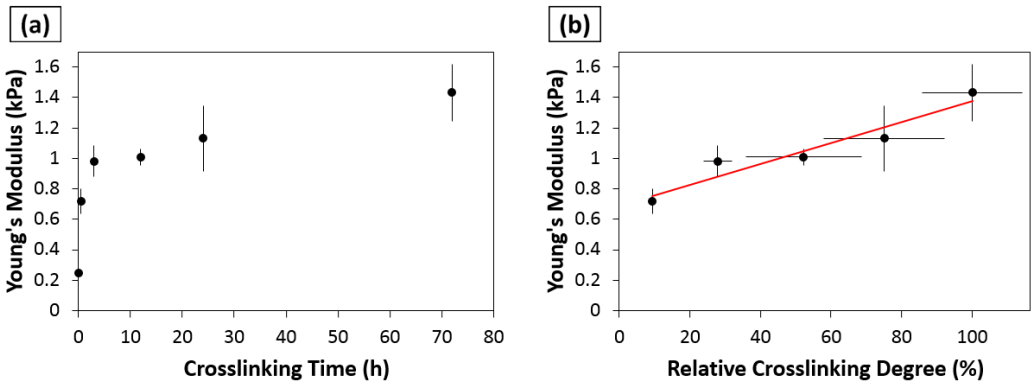

Figure D4. Young's Modulus (kPa) and Crosslinking time (in h) relation (a) and Young's Modulus (in kPa) and Crosslinking time (h) relation. Best fit line: $y = 0.0069x + 0.6893$ and $R^2 = 0.9190$ (b).

This result is consistent with previous FTIR analysis, further validating the technique used to monitor the crosslinking reaction via FTIR.

The Matrimid membrane that was crosslinked for 24 h showed the highest standard deviation (1.13±0.2143 kPa) (Figure D4a). High standard deviation values are common for electrospun mats due to uncertainties in film thicknesses, in agreement with others found in literature including poly(trimethyl hexamethylene terephthalamide) (43.7±14.9 MPa).(Pai, Boyce, & Rutledge, 2011) In glutaraldehyde crosslinked gelatin films, the Young's Modulus (Pa) and concentration (wt%) relation has shown the same behavior as in Figure D4a.(Bigi et al., 2001) A linear relation between the Young's Modulus and the RCLD was determined (R^2=0.9190) (Figure D4b).

Higher UTS values of the Matrimid samples are obtained as the crosslinking processing time increases, as it can be seen in Figure D5. Based on previous results (DMA test, FTIR), it was expected that the 100% RCLD Matrimid membrane (3 days of crosslinking time) showed the highest TS (7.3 kPa). But even for samples that underwent the crosslinking modification for very short time, the difference from 0% RCLD to 10 % RCLD (which corresponds to 0h and 0.5 h of crosslinking time, respectively) is notable as UTS values increased 3.4 kPa. It is also important to highlight that this UTS increase is neither proportional nor constant to CL time, as UTS values

reached a maximum at 100 % RCLD. The curve behavior of the UTS results showed in Figure D5 is consisted to the crosslinking determination trend seen in Figure D2.

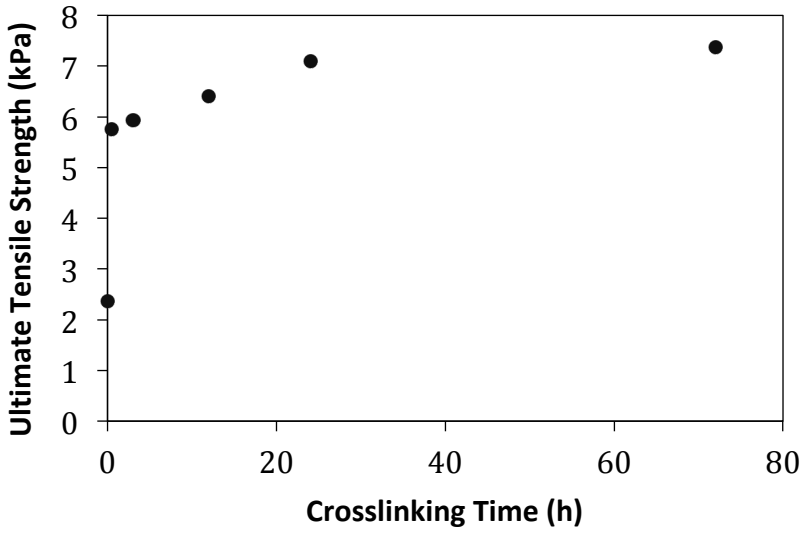

Figure D5. Correlation between tensile strength (kPa) and crosslinking time (h).

3.2. Solvent stability and interactions. SEM images of each sample after the final 3 days of DMF immersion are shown in Figure D6. Fiber structures still remain, even after minimal crosslinking as seen in the high magnification 10% sample in the top, left image of Figure D6. However a clear trend at lower magnifications can be seen with the most significant changes seen at lower degrees of crosslinking, but after a full 3 days of crosslinking no visible changes occur after 3 days of immersion in DMF.

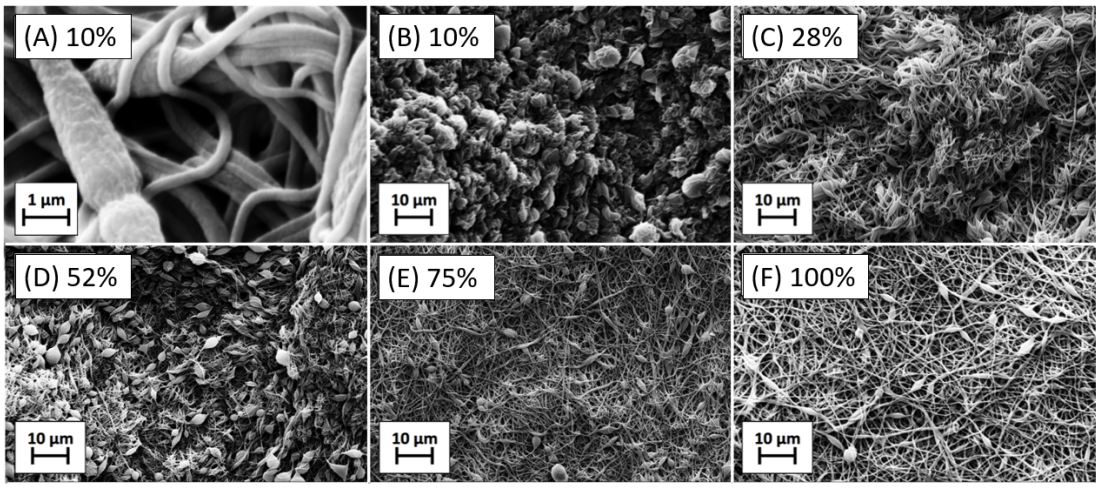

Figure D6. SEM images of Matrimid fibers at different crosslinking degree after 3 days of immersion in DMF including 10% (A and B), 28% (C), 52% (D), 75% (E), and 100% (F). Image (A) was taken at a magnification of 13000x and images (B-F) were taken at 1500x magnification.

At a magnification of 1500x in Figure 6b, fibers with 10% crosslinking degree seemed to be destroyed, nevertheless, at higher magnifications (Figure D6a), it can be seen that there are still fibers. At a 100% crosslinking degree, fibers appear completely intact in DMF after 3 days immersion with a comparison between the SEM images before and after crosslinking in Figure D3 and Figure D6, respectively.

Samples were also tested for thermal solvent resistance. Table D1 shows the response of each fibrous mat after immersion in DMF for 24 hours at varying temperatures. A plus sign (+) depicts fibers remaining after the test by visual inspection, and a minus sign (-) depicts visible fiber loss. DMF was used as the solvent for the thermal stability test as it was the solvent used for the electrospinning solution. Matrimid is soluble in DMF as shown in the first row of Table D1. With the crosslinking modification, pure Matrimid fibers start showing resistance to DMF at room temperature. A minimum of 50% RCLD is needed in order for the fibers to resist DMF at 100 and 150 ^{0}C. The results confirm the effectiveness of the crosslinking modification to improve solvent resistances at increased temperatures. The solvothermal resistance property these fibers shown can be used for synthesis of materials that involve harsh temperature conditions.

Table D1:

Crosslinked Matrimid Stability Test

Relative Crosslinking Degree (% RCLD)	Temperature (^{o}C)		
	25	100	150
0	-	-	-
10	+	-	-
28	+	+	-
50	+	+	+
75	+	+	+
100	+	+	+

Pure and crosslinked Matrimid nanofibers were immersed in 10 mL of DMF and exposed to the specified temperature conditions for 24 hours. A (+) and a (-) denotes fibers and no fibers remaining after the test, respectively.

D3.3. Performance as battery separator. In order to investigate the thermal-resistance properties of Matrimid, a thermal shrinkage test is conducted using Matrimid nanofibers that were crosslinked for three days. By measuring the dimensional change in area of these membranes after heat treatment for 30 min, no shrinkage occurred at temperature up to 180^{o}C (Figure D7). With further increase of temperature, the membrane starts show shrinkage of 9.75 and 19% at 190 ^{o}C and 200 ^{o}C, respectively. Compared to the commonly used pure PE separator, which losses its dimensional stability starting at 110 ^{o}C and has a thermal shrinkage of 63.5% at temperature of 145 ^{o}C,(C. Shi et al., 2014) Matrimid separators demonstrated a significant improvement in terms of excellent thermal resistance up to 180^{o}C.

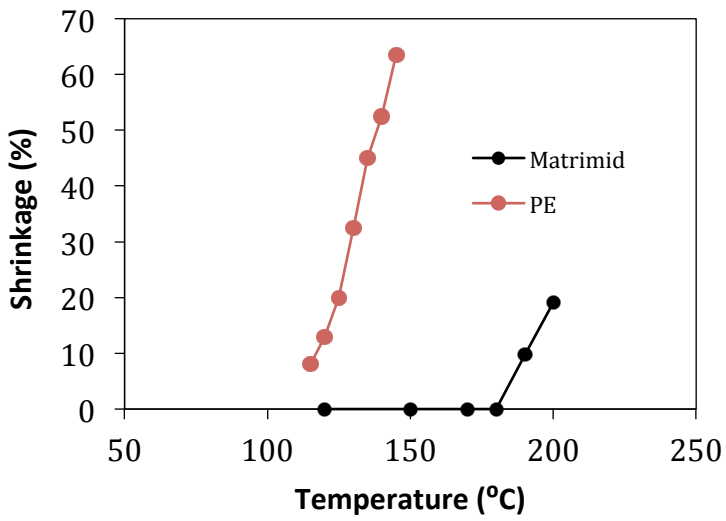

Figure D7. Correlation between relative shrinkage percent (%) and temperature (°C). The orange and black line correspond to polyethylene (PE) and Matrimid, respectively.

To confirm that these organogel nanofiber mats may be used in strong solvent systems, they were tested as a separator in a lithium ion battery. In the tested system, the Matrimid mat was soaked in the strong solvent $LiPF_6$ in EC-DEC-DMC: a solvent that readily dissolves unmodified Matrimid. Cycle performance of the $LiCoO_2$/graphite block-cell with 100% RCLD of Matrimid membrane as separator is evaluated and presented in Figure D8a along with images of the fiber mat after the test was performed (Figure D8). Cells were charged to 4.2 V and discharged to 2.5 V at current rate 0.1C/0.1C.

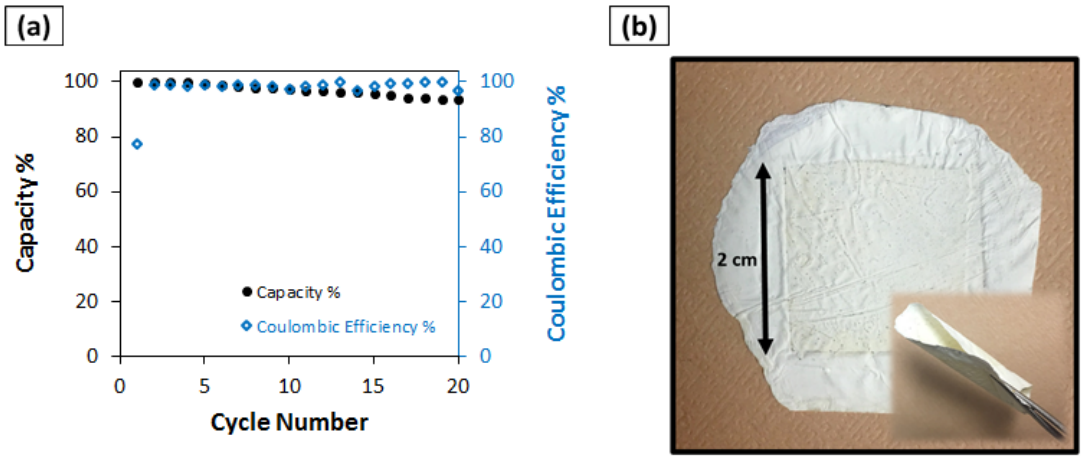

Figure D8. Cycle performance of the battery assembled with Matrimid membrane as separator. The batteries were cycled at 0.1C for 20 cycles (a). Digital image of the Matrimid membrane separator after being tested for 20 cycles.

The discharge capacity of cells decreased slightly with cycling because of the change of cell internal resistance. As the cycle number increased, physical changes occurred in the active materials and interfaces.(J. Li et al., 2016) Nevertheless, a discharge capacity above 93% is obtained during the first 20 cycles. The initial change of Coulombic efficiency can be explained by the reversibility of lithium ion deintercalation.(Ma et al., 2016) Charge-discharge curves at varying rates, the rate performance, and electrochemical impedance spectroscopy are shown in the supplementary information of the original article.

The Matrimid membrane is adhered to the electrodes during cycling and it prevents the leakage of the electrolyte. Other polymers such as aramid has also been tested as battery separators and has shown excellent mechanical properties and superior thermal stability, which improve the safety of lithium ion batteries.(J. Li et al., 2016) The stability of a separator is fundamental in the highly oxidizing and reducing environments encountered in Li-ion batteries at electrode-electrolyte interfaces.(X. Huang, 2011) The Matrimid membrane tested as separator material showed thermal and chemical stability against the electrolyte and electrode materials, as it also retained its mechanical strength and flexibility and it was not degraded. This resulting

application demonstrated for the first time that Matrimid organogels can be used in strong solvent systems (Figure D8b).

D4. Conclusion

Matrimid-based porous organogel membrances (POMs) were obtained by electrospinning and a room-temperature crosslinking modification, which has been carried out on the nanofibers by immersing the electrospun mats in p-xylenediamine/methanol solutions.

During the crosslinking modification process, the imide functional groups of Matrimid were converted to amide functional groups. These chemical changes were monitored by FTIR, which showed that the crosslinking process of Matrimid in POMs can be completed in 3 days compared to 2 months required in a thin-film structure. Mechanical and thermal properties were largely improved with crosslinking modification. Based on SEM images it can be concluded that the crosslinked and electrospun mats retained their physical structure as nanofibers after DMF immersion.

For the first time, Matrimid is electrospun and chemical crosslinked to form POMs. The initial performance evaluation as separators in Li-ion batteries demonstrated their potential to be used in strong-solvent systems as the mats retain their structural stability after being in contact to the electrolyte ($LiPF_6$ in EC-DEC-DMC) for three weeks of testing.

APPENDIX E

SUPPORTING INFORMATION FOR MATHEMATICAL MODEL

E1. Analytical Model

An analytical model is developed and explained here based on the observation that the core appears to reach equilibrium concentration values fast relative to the shell when the diffusivity in the core is approximately 10x larger than diffusivity in the shell. With this approximation we may treat the core as a large reservoir at equal concentration throughout at any time. This approximation allows us to readily solve the boundary condition requiring equal activity at the shell/ core interface by explicitly stating the concentration in the core as a function of $\mathbf{Q_t}$ neglecting any concentration gradients inside the core. This model is based on Fick's laws, and the integration of the concentration at a given time to find $\mathbf{Q_t}$ at a given x coordinate in the system:

$$Q_t = \int_0^t J dt = A \int_0^t -D \frac{\delta C}{\delta x} dt \quad \text{(E1)}$$

For this model we move from the 2-dimensional case treated with the COMSOL model to a 3-dimensional case where the sorbent is treated as two flat sheets in parallel with the outer flat sheet representing the shell and the inner sheet representing the core.

To describe uptake in this dual-phase sorbent, we assume that the diffusion coefficient in the core is sufficiently larger than the diffusion coefficient in the shell such that the concentration in the core is nearly uniform. With this approximation we may define the concentration at the interface in the shell as

$$C_{Ls} = S_S p^{eff} \quad \text{(E2)}$$

and in combination with the linear isotherm for the core, given as:

$$C = S_C p = \frac{Q_t}{V_C} \quad \text{(E3)}$$

we can rewrite equation C_{Ls} as:

$$C_{Ls} = \frac{S_S}{S_C} \frac{Q_{t(x=Ls)}}{V_C} \quad \text{(E4)}$$

Differentiating this expression we get:

$$\frac{\delta C}{\delta t} = \frac{-S_S D_S}{S_C} \frac{A}{V_C} \frac{\delta C}{\delta x} \quad \text{(E5)}$$

This can be rearranged to

$$D\frac{\delta C}{\delta x}+\frac{L_S}{\eta}\frac{\delta C}{\delta t}=0 \quad \text{(E6)}$$

where:

$$\eta=\frac{S_S}{S_C}\frac{Al_S}{V_C}=\frac{Q_{\infty,S}}{Q_{\infty,C}} \quad \text{(E7)}$$

Equation E6 may be used as the boundary condition at the core-shell interface, along with previously defined boundary conditions from the main chapter to describe this system:

C=0	t<0	all x	(E8a)
$C=S_S p_0$	t>0	x=0	(E8b)
$\frac{\delta C}{\delta t}=D_S\frac{\delta^2 c}{\delta x^2}$	0 > x > L_S		(E8c)

Using a Laplace expansion, Carlsaw and Jaeger(Carslaw & Jaeger, 1959) provide a general solution to this type of partial differential equation in terms of dimensionless quantities that are readily converted from conduction to diffusion through the concept of equivalent circuits. This results in the equation:

$$C=C_\infty\left[1-\sum_n\frac{2(\beta_n^2+\eta^2)\sin(\beta_n\frac{x}{L_S})}{\beta_n(\beta_n^2+\eta^2+\eta)}e^{\frac{-D_S\beta_n^2 t}{L_S^2}}\right] \quad \text{(E9)}$$

where $\boldsymbol{\beta_n}$ represents the positive roots of the equation $\beta_n\tan(\beta_n)=\eta$. This is an equivalent solution to this equation given by Paul and DiBenedetto for diffusion with a different dimensionless parameter **η** for applications in membrane characterization.(Paul & DiBenedetto, 1965)

Taking the derivative δC/δx, this equation becomes:

$$\frac{\delta C}{\delta x}=-S_S p\sum_n\frac{2(\beta_n^2+\eta^2)\cos(\beta_n\frac{x}{L_S})}{L_S(\beta_n^2+\eta^2+\eta)}e^{\frac{-D_S\beta_n^2 t}{L_S^2}} \quad \text{(E10)}$$

where C_∞ is expressed as $S_S p$ as a result of Henry's Law. Then, integrating with equation E1, this becomes:

$$Q=-AD_S\left[Const+pS_S\sum_n\frac{2(\beta_n^2+\eta^2)\cos(\beta_n\frac{x}{L_S})}{L_S(\beta_n^2+\eta^2+\eta)}\frac{L_S^2}{D_S\beta_n^2}e^{\frac{-D_S\beta_n^2 t}{L_S^2}}\right] \quad \text{(E11)}$$

By defining the maximum uptake over the section of composite being solved for with the boundary condition $Q=ApS_SL_S(1-x/L_S+1/\eta)$ at $t=\infty$ this becomes:

$$Q = ApS_S L_S \left[1 - \frac{x}{L_S} + \frac{1}{\eta} - \sum_n \frac{2(\beta_n^2+\eta^2)\cos(\beta_n \frac{x}{L_S})}{\beta_n^2(\beta_n^2+\eta^2+\eta)} e^{\frac{-D_S \beta_n^2 t}{L_S^2}}\right] \quad \text{(E12)}$$

When solving for x= 0, we arrive at the uptake over the entire composite:

$$Q = ApS_S L_S \left[1 + \frac{1}{\eta} - \sum_n \frac{2(\beta_n^2+\eta^2)}{\beta_n^2(\beta_n^2+\eta^2+\eta)} e^{\frac{-D_S \beta_n^2 t}{L_S^2}}\right] \quad \text{(E13)}$$

and when solving for x=L_S, we arrive at the uptake of the core alone ($\mathbf{Q_C}$).

$$Q_C = ApS_S L_S \left[\frac{1}{\eta} - \sum_n \frac{2(\beta_n^2+\eta^2)\cos(\beta_n)}{\beta_n^2(\beta_n^2+\eta^2+\eta)} e^{\frac{-D_S \beta_n^2 t}{L_S^2}}\right] \quad \text{(E14)}$$

This analytical model strongly correlates to the COMSOL simulation; Figure E1 compares the COMSOL model of trial 1 against the prediction from this model.

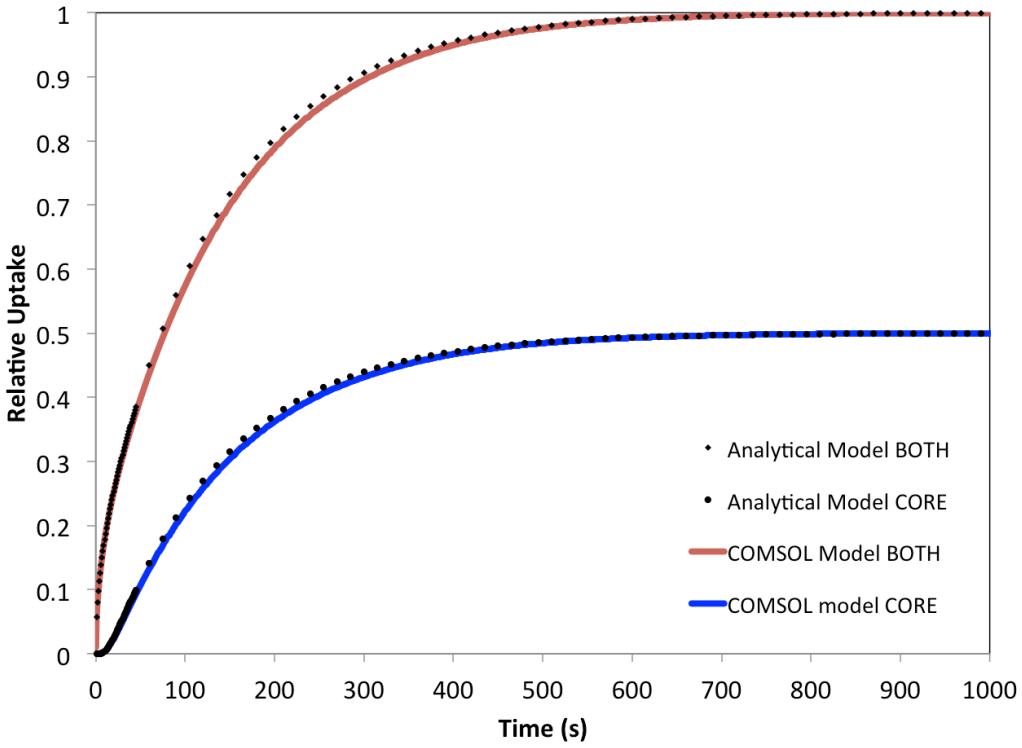

Figure E1. Comparison of the COMSOL model trial 1 and the same variables in the analytical model using the first 6 positive roots of the equation $\beta_n \tan(\beta_n)=1$. Uptake in the total composite is given by EQ E13 (diamond) and compared to COMSOL model (red). Uptake in the core is given by EQ E14 (circle) and compared to the COMSOL model (blue).

Next we work towards defining the linear uptake regime. To do this we define the term m such that m=n+1 and $\beta_m = \beta_n+1$, and then express Equation E14 as:

$$Q_C = ApS_S L_S \left[\frac{1}{\eta} - \frac{2(\beta_0^2+\eta^2)\cos(\beta_0)}{\beta_0^2(\beta_0^2+\eta^2+\eta)} e^{\frac{-D_S\beta_0^2 t}{L_S^2}} - \sum_{m=1} \frac{2(\beta_m^2+\eta^2)\cos(\beta_m)}{\beta_m^2(\beta_m^2+\eta^2+\eta)} e^{\frac{-D_S\beta_m^2 t}{L_S^2}}\right] \quad \text{(E15)}$$

where β_0 is the first non-negative root of $\beta_{m+1}(\tan\beta_{m+1})=\eta$ such that m=0. It is then evident that the first exponential term describes the uptake in the core, and the summation term balances this first exponential out by providing a lag time. For convenience of discussion we set **W** and **Y** such that:

$$W = ApS_S L_S \left[-\frac{2(\beta_0^2+\eta^2)\cos(\beta_0)}{\beta_0^2(\beta_0^2+\eta^2+\eta)} e^{\frac{-D_S\beta_0^2 t}{L_S^2}}\right] \quad \text{(E16)}$$

$$Y = ApS_S L_S \left[-\sum_{m=1} \frac{2(\beta_m^2+\eta^2)\cos(\beta_m)}{\beta_m^2(\beta_m^2+\eta^2+\eta)} e^{\frac{-D_S\beta_m^2 t}{L_S^2}}\right] \quad \text{(E17)}$$

This is illustrated in Figure E2:

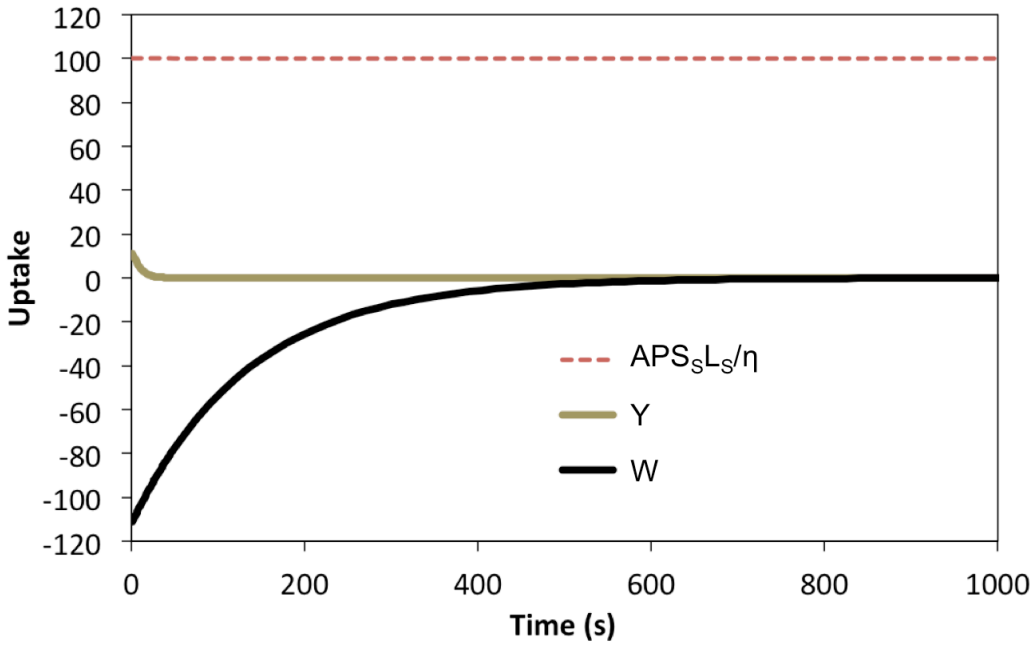

Figure E2. A plot illustrating the contribution of variables on EQ E15. The black curve represents W and the brown line represents Y and the dashed red line represents the maximum uptake term.

From this illustration, it is clear that 1/η determines the maximum capacity at the given external gas concentration since all other terms go to 0, that **W** describes the uptake in the core after the lag phase and that **Y** corrects **W** for the lag phase. To describe a straight line through this

function (to describe the uptake in the core during the second uptake phase, $\mathbf{Q_{C,ii}}$), we define $e^{mx} \approx mx$ for low values of **x** to describe the exponential in **W**, and assume that the exponential in **Y** is unimportant after the lag-time. This results in the linear approximation:

$$Q_{C,ii} = ApS_S L_S \left[\frac{2(\beta_0^2+\eta^2)\cos(\beta_0)}{(\beta_0^2+\eta^2+\eta)}\left(\frac{D_S t}{L_S^2}\right) - \sum_{m=1}\frac{2(\beta_m^2+\eta^2)\cos(\beta_m)}{\beta_m^2(\beta_m^2+\eta^2+\eta)}\right] \quad \text{(E19)}$$

The x-intercept of this curve then represents the lag time (**φ**), and the slope represents the uptake rate during the linear uptake region. This is demonstrated in Figure E3.

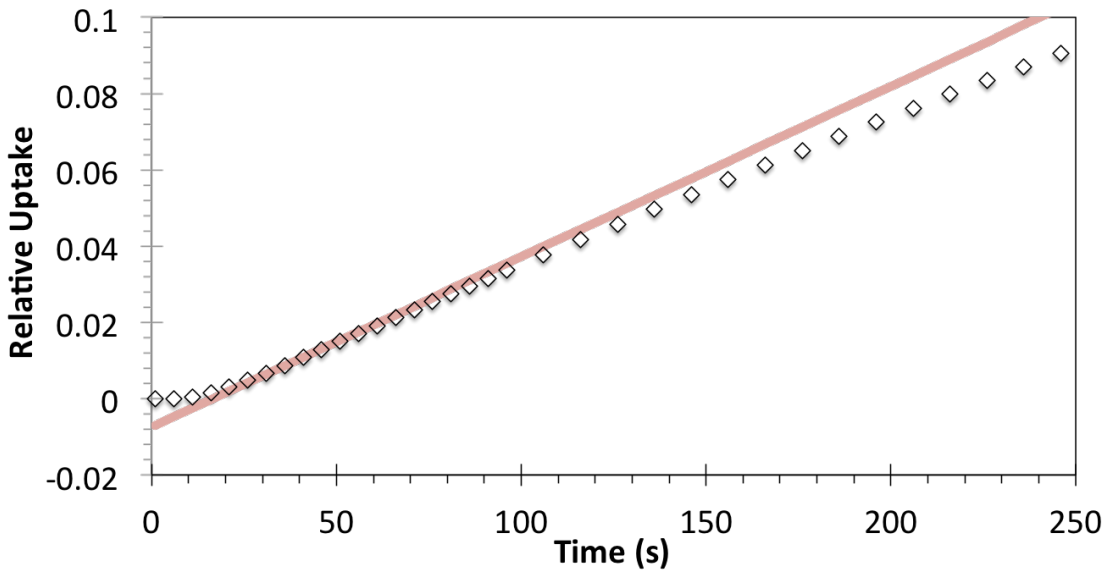

Figure E3. Comparison of analytical solution for the equivalent parameters as COMSOL trial 13 (diamonds) and the overlaying linear approximation given by EQ E18.

To find the lag time (**φ**), we solve EQ S18 for t when Q=0

$$\varphi = \left[\frac{L_S^2}{D_S}\right]\left[\frac{(\beta_0^2+\eta^2+\eta)}{(\beta_0^2+\eta^2)\cos(\beta_0)}\sum_{m=1}\left(\frac{(\beta_m^2+\eta^2)\cos(\beta_m)}{\beta_m^2(\beta_m^2+\eta^2+\eta)}\right)\right] \quad \text{(E19)}$$

This represents the transition between the first uptake phase (phase i) and the second uptake phase (phase ii). This equation is important if calculating $\mathbf{D_S}$ from experimental data in an approach similar to that of Daynes for the permeation test of polymer films. However, as seen in FIG S1 the effect of the core may be considered unimportant. We may then alternatively approximate the lag-time as that of a similar composite with an infinite capacity in the core- an equivalent to Daynes system. In the limit of an infinite core capacity $\eta = 0$, β_0 goes to 0, β_K goes

to nπ, and with the identities $\lim_{\beta_0 \to 0}\left(\frac{\beta_0^2+(\beta_0 tan(\beta_0))^2+\beta_0 tan\beta_0}{\beta_0^2+(\beta_0 tan(\beta_0))^2}\right) = 2$ and $\sum_{m=1}\left(\frac{\cos(n\pi)}{n^2}\right) = \frac{-\pi^2}{12}$ this lag time becomes:

$$\varphi = \frac{L_S^2}{6D_S} \tag{E20}$$

which is equivalent to that found by Daynes and Barrer for testing polymeric films for permeance.(Barrer, 1968; Daynes, 1920) Equation E20 is taken as the transition region between phase (i) and phase (ii). Barrer provides time-lag calculations for other geometries as well,(Barrer, 1968) for a cylinder:

$$\varphi = \frac{(R_S^2+R_C^2)\ln\left(\frac{R_S}{R_C}\right)-(R_S^2-R_C^2)}{4D_S \ln\left(\frac{R_S}{R_C}\right)} \tag{E21}$$

where R_S and R_C represent the radius of the shell and core respectively. For a sphere:

$$\varphi = \frac{(R_S-R_C)^2}{6D_S} \tag{E22}$$

The slope (**Ψ**) then describes the uptake rate of the linear region:

$$\frac{\delta Q_{C,ii}}{\delta t} = \Psi = \frac{ApS_S D_S}{L_S}\left[\frac{2(\beta_0^2+\eta^2)\cos(\beta_0)}{(\beta_0^2+\eta^2+\eta)}\right] \tag{E23}$$

which is a linear extrapolation of **W**, the component of Equation E16 that defines uptake in the core after the lag phase. Therefore we can define the end of the linear uptake region as the time the linear approximation breaks down, as an approximation we can estimate this to be when the time reaches t=0.25*m from e^{-mt} since the slope of the linear regression through the function e^{mx} is near 10% of the approximation of Equation E18. This results in an apparent linear region defined as:

$$t = t_{(phase\ ii)\rightarrow(phase\ iii)} = \frac{0.25L_S^2}{D_S\beta_0^2} = \frac{6\varphi}{4\beta_0^2} \tag{E24}$$

Like the lag-phase, when the limit of infinite core capacity is used this turns into the uptake rate provided by Daynes in his solution for the permeance test of polymer films.